



**MSc Physics and Astronomy**  
Track: Gravitational, Astro- and Particle Physics

Master Thesis

---

# Multi-Wavelength Modeling of Blazar Jets

## A Study of Leptonic and Lepto-Hadronic Emission in Single- and Multi-Zone Frameworks

---

by

**Scott Visser**  
**14487055 (UVA)**

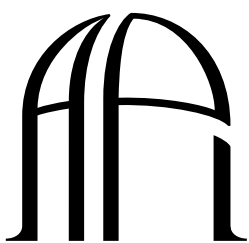
*August 9, 2024*  
*60 ECTS*  
*September 2023 - August 2024*

*Supervisors:*

Prof. Dr. Sera Markoff  
Dr. Foteini Oikonomou  
Dr. Matteo Lucchini

*Examiners*

Prof. Dr. Sera Markoff  
Dr. Shin'ichiro Ando



---

**ANTON PANNEKOEK  
INSTITUTE**



GRavitation AstroParticle Physics Amsterdam



# Contents

<b>1</b>	<b>Introduction</b>	<b>1</b>
1.1	The Mystery of Cosmic Rays . . . . .	1
1.1.1	The Cosmic Ray Spectrum . . . . .	2
1.1.2	The (Possible) Origin of Cosmic Rays . . . . .	3
1.1.3	Multi-Messenger Astronomy . . . . .	5
1.2	Black Holes . . . . .	7
1.2.1	Black Hole Accretion . . . . .	9
1.2.2	Relativistic Black Hole Jets . . . . .	11
1.2.3	Active Galactic Nuclei . . . . .	12
1.2.4	X-ray Binaries . . . . .	18
1.3	The Spectral Components of Accreting Black Holes . . . . .	19
1.3.1	The Accretion Disk . . . . .	19
1.3.2	Jet Formation and Acceleration . . . . .	21
1.3.3	Synchrotron Emission . . . . .	22
1.3.4	Inverse Compton Scattering . . . . .	26
1.4	Hadronic Interactions . . . . .	32
1.4.1	Proton-Proton Collisions . . . . .	32
1.4.2	Proton-Photon Collisions . . . . .	34
1.4.3	Synchrotron and IC Emission by Protons and Secondary Particles . . . . .	35
1.5	Standard Modelling Techniques for Blazars . . . . .	36
1.5.1	Single-Zone Jet Models . . . . .	36
1.5.2	BHJet: A Leptonic, Multi-Zone Jet Model . . . . .	39
1.6	Thesis Outline . . . . .	44
<b>2</b>	<b>Multi-Wavelength SED Modelling of Blazars</b>	<b>46</b>
2.1	Blazar Sources . . . . .	46
2.1.1	TXS 0506+056 . . . . .	47
2.1.2	PKS 1424-418 . . . . .	49
2.2	Extra-Galactic Background Light Attenuation . . . . .	51
<b>3</b>	<b>Multi-Zone Modeling of Blazar SEDs with BHJet</b>	<b>55</b>
3.1	Fixing Model Parameters for Blazar Sources . . . . .	55
3.2	Degenerate Thermal Electron Temperature for Blazars . . . . .	57
3.3	SED Fitting Strategy . . . . .	60

3.4	Leptonic Multi-Zone SED Fit for TXS 0506+056 . . . . .	61
3.5	Leptonic Multi-Zone SED Fits for PKS 1424-418 . . . . .	64
3.5.1	Joint Fit of the Quiescent and Flaring State of PKS 1424-418 . . . . .	67
<b>4</b>	<b>Multi-Zone Modelling of Blazar SEDs with HadJet</b>	<b>71</b>
4.1	HadJet: A Lepto-Hadronic Multi-Zone Jet Model . . . . .	71
4.1.1	Modifications to the HadJet Code . . . . .	72
4.2	Lepto-Hadronic Multi-Zone SED Fit for TXS 0506+056 . . . . .	73
4.3	Lepto-Hadronic Multi-Zone SED Fits for PKS 1424-418 . . . . .	77
<b>5</b>	<b>Single-Zone vs Multi-Zone Modelling of Blazar SEDs</b>	<b>82</b>
5.1	Comparing the Single-Zone Version of BHJet to AM3 . . . . .	82
5.2	Leptonic Single-Zone SED Modelling of Blazar SEDs . . . . .	85
5.2.1	Leptonic Single-Zone SED Fit for TXS 0506+056 . . . . .	86
5.2.2	Leptonic Single-Zone SED Fits for PKS 1424-418 . . . . .	89
5.3	Lepto-Hadronic Single-Zone Modelling of Blazar SEDs . . . . .	94
5.3.1	Lepto-Hadronic Single-Zone SED Fit for TXS 0506+056 . . . . .	94
5.3.2	Lepto-Hadronic Single-Zone SED Fits for PKS 1424-418 . . . . .	98
5.4	Reflective Analysis and Broader Implications . . . . .	102
<b>6</b>	<b>Summary and Conclusions</b>	<b>104</b>
<b>A</b>	<b>SED Data of All Sources</b>	<b>122</b>
A.1	SED Data After the Flare of TXS 0506+056 in 2017 . . . . .	122
A.2	SED Data for PKS 1424-418 . . . . .	123
A.2.1	PKS 1424-418: Archival Data . . . . .	123
A.2.2	PKS 1424-418: Alpha Epoch . . . . .	124
A.2.3	PKS 1424-418: Gamma Epoch . . . . .	125
A.2.4	PKS 1424-418: Delta Epoch . . . . .	125
A.2.5	PKS 1424-418: Eta Epoch (Flare) . . . . .	126
<b>B</b>	<b>Jet Model Parameters</b>	<b>128</b>
B.1	Parameters of BHJet and HadJet . . . . .	128
B.2	Parameters of OneZone_lep and OneZone_lephad . . . . .	130



# List of Figures

1.1	The CR spectrum as observed with various detectors. The CR spectrum covers more than 10 orders of magnitude in energy flux and extends between 1 GeV( $10^9$ eV) and 100 EeV ( $10^{20}$ eV) in particle energy. The different components are indicated in the plot with protons (p), electrons ( $e^-$ ), positrons ( $e^+$ ), antiprotons ( $\bar{p}$ ) and photons ( $\gamma$ ) composing the GeV-to-TeV energy regime. In this regime, the combined CR flux of all particles as measured by AMS-02 and CREAM is shown as the full green and red lines, respectively. Protons and heavier nuclei provide the most energetic part of the spectrum. The data were compiled by <a href="#">Evoli (2023)</a> . . . . .	2
1.2	Measured fluxes of the diffuse astrophysical backgrounds of $\gamma$ -rays (green) observed by Fermi-LAT, neutrinos (blue) observed by IceCube, and ultra-high energy cosmic rays (red) observed by the Pierre Auger Observatory and the Telescope Array. Figure from <a href="#">Ackermann et al. (2022)</a> . . . . .	6
1.3	Galactic sky position and 0.1-100 GeV flux of the Fermi-LAT 4FGL-DR2 point sources (colored dots), overlaid on the list of the 70 track-type neutrino detections by the IceCube observatory (black filled ellipses). The map is shown in the Mollweide projection. The equator is plotted as a purple continuous line, and the blazars TXS 0506+056 and PKS 1502+106 are marked on the map. Figure from <a href="#">Kun et al. (2022)</a> . . . . .	6
1.4	The shadow of the SMBH at the center of the elliptical galaxy M87 as observed during the 2017 and 2018 campaign. Image from <a href="#">The Event Horizon Telescope Collaboration 2024</a> . . . . .	7
1.5	Artist's impression of an AGN with two bipolar relativistic jets. These jets are launched by the SMBH and inflate to giant radio lobes at either end. Image from ESA/C. Carreau/ATG Medialab. . . . .	12
1.6	A schematic diagram for radio-loud AGN (not to scale). The central BH is surrounded by a luminous accretion disk. Broad emission lines are produced in clouds orbiting above the disk and perhaps by the disk itself. A thick dusty torus obscures the broad-line region from transverse lines of sight. A hot corona above the accretion disk may also play a role in producing the hard X-ray continuum. Narrow lines are produced in clouds farther from the central source. Radio jets, shown here as the diffuse jets characteristic of low-luminosity radio sources, emanate from the region near the BH, initially at relativistic speeds. Image from <a href="#">Urry &amp; Padovani (1995)</a> . . . . .	13

---

1.7	Geometry to explain the relativistic Doppler effect caused by the difference in arrival time due to light travel time. Figure from Rybicki & Lightman (1979) . . . . .	14
1.8	Beaming of the emission produced by a source moving at relativistic speeds. As the speed increases towards the speed of light, more and more radiation will be beamed in the direction in which the source is moving, rather than being isotropically emitted. Figure adapted from <a href="https://math.ucr.edu/home/baez/physics/Relativity/SR/Spaceship/spaceship.html">https://math.ucr.edu/home/baez/physics/Relativity/SR/Spaceship/spaceship.html</a> . . . . .	15
1.9	The Doppler/beaming factor of a source with different Lorentz factors as a function of viewing angle. Highly relativistic sources can have large beaming factors as they get more closely aligned with the line of sight. Image credit: M. Lucchini	16
1.10	Example of a typical double-humped blazar SED with the multi-wavelength (MWL) data of the blazar Mrk 501 in 2009. One sees a fit to the data using a simple synchrotron self-Compton model and a black body contribution from the surrounding galaxy. Figure from Baring et al. (2017). . . . .	17
1.11	The Fundamental Plane of Black Hole activity, showing the correlation between radio and X-ray luminosities and black hole mass. Figure from Plotkin et al. (2012). . . . .	19
1.12	Spectra of a steady optically thick accretion disk radiating locally as a black-body, for disks with different ratios of $R_{\text{out}}/R_{\text{in}}$ . The frequency is normalized to $k_b T_{\text{in}}/h$ . Figure from Frank et al. (2002). . . . .	20
1.13	Emitted synchrotron spectrum by a powerlaw distribution of particles that transitions from the optically thick to optically thin regime at $\nu = \nu_{\text{SSA}}$ ( $\nu_t = \nu_{\text{SSA}}$ in the figure). Figure from Ghisellini (2013). . . . .	24
1.14	Flat radio spectrum from an isothermal jet. The colored lines indicate the spectrum from different cylindrical regions of the jet, with lighter colors indicating larger distances from the BH. The black line is the sum of all jet segments which results in the flat spectrum. Image credit: M. Lucchini. . . . .	26
1.15	Ratio of the quantum mechanical Klein-Nishina to classical Thomson cross section. Figure from Ghisellini (2013). . . . .	26
1.16	The geometry of Inverse Compton scattering as observed in the observer frame on the left. The geometry as observed in the co-moving frame of the electron can be seen on the right. Figure from Rybicki & Lightman (1979). . . . .	27
1.17	Thermal Comptonization spectrum in the saturated regime, in which the total spectrum (blue line) is the sum of multiple scattering orders (red lines). The slope of the spectrum is set by the energy gain and fraction of escaping photons. The cut-off at higher energies reflects the maximum attainable photon energy which is determined by the electron energy. Figure from Ghisellini (2013). . . . .	30
1.18	The particle distributions for the products of pp/p $\gamma$ collisions between accelerated protons and cold protons/photons. The protons follow a powerlaw with a spectral index $p = 2.2$ that ranges from 1 GeV to 60 TeV. The distributions of $\gamma$ -rays ( $\gamma$ ), muon neutrinos ( $\nu_\mu$ ) and secondary electrons (e) cut off at the maximum energy of the accelerated protons. Image credit: D. Kantzas. . . . .	34
1.19	Geometry of a single-zone jet model. . . . .	37

1.20 Geometry of the <code>BHJet</code> model. . . . .	40
2.1 SED of TXS 0506+056 collected in the two weeks after the detection of neutrino event IceCube-170922A coinciding with a $\gamma$ -ray flare. Data was retrieved from Keivani et al. (2018). . . . .	48
2.2 <i>Fermi</i> /LAT light curve for PKS 1424-418 from August 4, 2008 to January 1, 2015. A Bayesian block analysis was performed on the data by Krauß et al. (2016) and is shown in dark gray. The horizontal pink line shows the average flux over the full light curve. Blocks with sufficient data for a broadband SED are shown in color and are labeled with Greek letters. Figure from Krauß et al. (2016). . . . .	49
2.3 MWL SEDs of PKS 1424-418 with the logarithmic flux as a function of logarithmic frequency. The left panel shows SEDs of the epochs $\alpha$ , $\gamma$ and $\delta$ where PKS 1424-418 is in a quiescent state. The right panel shows the epoch $\eta$ during which the source is in a flaring state. The data was retrieved from Krauß et al. (2016). . . . .	50
2.4 The optical depth for photon-photon pair production as a function of the incoming photon energy (in TeV) for four different EBL models. The figure shows the optical depth for redshifts ( $z_{\text{red}}$ ) 0.01, 0.5, 1.0 and 2.0. The gray dashed line represents $\tau_{\gamma\gamma} = 1.0$ where the flux is attenuated by a factor $1/e$ . The optical depth data was retrieved from Domínguez et al. (2011), Gilmore et al. (2012), Franceschini & Rodighiero (2017) and Finke et al. (2022). . . . .	53
2.5 The fit for the $\alpha$ epoch of PKS 1424-418 as obtained for the joint fit in Section 4.3. The full lines represent the model without accounting for EBL attenuation and the dashed lines represent the case where EBL attenuation is taken into account. The spectral components that are affected by EBL attenuation are also shown. . . . .	54
3.1 Fits with <code>BHJet</code> for the $\alpha$ epoch of PKS 1424-418 for two different electron temperatures. The left panel shows a fit with $T_e = 200$ keV and the panel on the right uses $T_e = 1000$ keV. The full black line shows the sum of all components which are shown as: non-thermal synchrotron in blue, non-thermal IC in orange, black body spectra from the disk (green) and torus (red), thermal synchrotron in purple and the thermal IC component in brown. . . . .	58
3.2 We show the 2D-posterior distributions with the electron temperature $T_e$ on the x-axis and the parameters for the jet power ( $N_j$ ) and the magnetization at the acceleration region ( $\sigma_{\text{acc}}$ ) on the y-axis from left to right, respectively. The best-fit values are marked by a red cross. . . . .	59
3.3 Fit of the flaring state of TXS 0506+056 in 2017 with <code>BHJet</code> together with the residuals in the lower panel. All components of the SED are shown as well as the sum of them which fits the SED data. . . . .	61

---

3.4	Corner plot with posterior distributions for the fit of the TXS 0506+056 SED with <b>BHJet</b> . In the plot, the model parameters for the jet power $N_j$ , the dissipation region $z_{\text{diss}}$ , the magnetization at the dissipation region $\sigma_{\text{acc}}$ and $f_{\text{sc}}$ are shown. . . . .	63
3.5	Fits with <b>BHJet</b> for all epochs of PKS 1424-418 together with their residuals in the lower panels. Left: the $\alpha$ epoch in blue, $\gamma$ in green and $\delta$ in red. Right: the $\eta$ (flaring) epoch in black. The contribution of the accretion disk for each epoch is shown by the dashed lines. . . . .	65
3.6	Corner plot with posterior distributions for the fit of the $\alpha$ epoch of PKS 1424-418 with <b>BHJet</b> . In the plot, the model parameters for the jet power $N_j$ , the dissipation region $z_{\text{diss}}$ , the magnetization at the dissipation region $\sigma_{\text{acc}}$ and $f_{\text{sc}}$ are shown. . . . .	66
3.7	Joint fit with <b>BHJet</b> for the epochs $\alpha$ and $\eta$ of PKS 1424-418 which represent a quiescent and a flaring state of the source respectively. The contribution of the accretion disk for each epoch is shown by the dashed lines. The residuals for the fits of both epochs are shown in the lower panel. . . . .	67
3.8	Corner plot with posterior distributions for the joint fit of $\alpha$ and $\eta$ epochs of PKS 1424-418 with <b>BHJet</b> . In the plot, the model parameters for the jet power $N_j$ , the dissipation region $z_{\text{diss}}$ , the magnetization at the dissipation region $\sigma_{\text{acc}}$ and $f_{\text{sc}}$ are shown. . . . .	69
4.1	Fit of the flaring state of TXS 0506+056 in 2017 with <b>HadJet</b> together with the residuals in the lower panel. All components of the SED are shown as well as the sum of them which fits the SED data. . . . .	74
4.2	Corner plot with posterior distributions for the fit with <b>HadJet</b> of the TXS 0506+056 SED. In the plot, the model parameters for the jet power $N_j$ , the dissipation region $z_{\text{diss}}$ , the magnetization at the dissipation region $\sigma_{\text{acc}}$ , $f_{\text{sc}}$ and the non-thermal proton fraction $f_{\text{nth, p}}$ are shown. . . . .	75
4.3	Joint fit with <b>HadJet</b> for the epochs $\alpha$ and $\eta$ of PKS 1424-418 which represent a quiescent and a flaring state of the source respectively. The contribution of the accretion disk, secondary synchrotron emission and pion decay for each epoch is shown by the dark green, yellow, and blue/green dashed lines, respectively. The residuals for the fits of both epochs are shown in the lower panel.. . . . .	78
4.4	Corner plot with posterior distributions for the joint fit of $\alpha$ and $\eta$ epochs of PKS 1424-418 with <b>HadJet</b> . In the plot, the model parameters for the jet power $N_j$ , the dissipation region $z_{\text{diss}}$ , the magnetization at the dissipation region $\sigma_{\text{acc}}$ , $f_{\text{sc}}$ and the non-thermal fraction of protons $f_{\text{nth, p}}$ are shown. . . . .	80
5.1	Comparison of the results with <b>AM<sup>3</sup></b> and <b>OneZone_1ep</b> for a simple SSC scenario. . . . .	85

5.2	Fits of the flaring state of TXS 0506+056 in 2017 with <code>OneZone_lep</code> together with the residuals in the lower panel. All components of the SED are shown as well as the sum of them which fits the SED data. The left-hand panel shows the fit with the parameters obtained from the median of all parameter posteriors. The right-hand panel shows the fit using the parameters that result in the lowest reduced $\chi^2$ . . . . .	86
5.3	Corner plot with posterior distributions for the fit of the TXS 0506+056 SED with <code>OneZone_lep</code> . In the plot, the model parameters for the radius of the emission region $R$ , the magnetic field strength $B$ , the electron number density $n_e$ and the maximum Lorentz factor $\gamma_{\max}$ are shown. . . . .	88
5.4	Joint fit with <code>OneZone_lep</code> for the epochs $\alpha$ and $\eta$ of PKS 1424-418 which represent a quiescent and a flaring state of the source respectively. The contribution of the accretion disk for each epoch is shown by the dashed lines. The residuals for the fits of both epochs are shown in the lower panel. . . . .	90
5.5	Corner plot with posterior distributions for the joint fit of $\alpha$ and $\eta$ epochs of PKS 1424-418 with <code>OneZone_lep</code> . The model parameters for the radius of the emission region $R$ , the magnetic field strength $B$ , the electron number density $n_e$ and the maximum Lorentz factor $\gamma_{\max}$ are shown. . . . .	92
5.6	Fits of the flaring state of TXS 0506+056 in 2017 with <code>OneZone_lephad</code> together with the residuals in the lower panel. All components of the SED are shown as well as the sum of them which fits the SED data. The left-hand panel shows the fit with the parameters obtained from the median of all parameter posteriors. The right-hand panel shows the fit using the parameters that result in the lowest reduced $\chi^2$ . . . . .	95
5.7	Corner plot with posterior distributions for the fit of the TXS 0506+056 SED with <code>OneZone_lephad</code> . In the plot, the model parameters for the radius of the emission region $R$ , the magnetic field strength $B$ , the electron number density $n_e$ and the maximum Lorentz factor $\gamma_{\max}$ are shown. . . . .	97
5.8	Joint fit with <code>OneZone_lephad</code> for the epochs $\alpha$ and $\eta$ of PKS 1424-418 which represent a quiescent and a flaring state of the source respectively. The contribution of the accretion disk for each epoch is shown by the dashed lines. The residuals for the fits of both epochs are shown in the lower panel. . . . .	98
5.9	Corner plot with posterior distributions for the joint fit of $\alpha$ and $\eta$ epochs of PKS 1424-418 with <code>OneZone_lephad</code> . The model parameters for the radius of the emission region $R$ , the magnetic field strength $B$ , the electron number density $n_e$ and the maximum Lorentz factor $\gamma_{\max}$ are shown. . . . .	101



# List of Abbreviations

**$\Lambda$ CDM**  $\Lambda$  Cold Dark Matter ( $\Lambda$  is the cosmological constant)

**ADAF** Advection Dominated Accretion Flow

**AGN** Active Galactic Nucleus

**AM<sup>3</sup>** The Astrophysical Multi-Messenger Modeling code

**BH** Black Hole

**BHXB** Black Hole X-ray Binary

**BLR** Broad Line region

**BP** Blandford-Payne

**BZ** Blandford-Znajek

**CMB** Cosmic Microwave Background

**CR** Cosmic Ray

**DT** Dusty Torus

**EBL** Extragalactic Background Light

**EC** External Compton

**EHT** Event Horizon Telescope

**EM** Electromagnetic

**eV** Electron Volt

**FP** Fundamental Plane

**FSRQ** Flat Spectrum Radio Quasar

**GR** General Relativity

**GRB** Gamma-ray Burst

**GRMHD** General Relativistic Magneto- Hydrodynamics

**GZK** Greisen-Zatsepin-Kuzmin

**IC** Inverse Compton

- IR** Infra-red
- ISCO** Innermost Stable Circular Orbit
- ISIS** Interactive Spectral Interpretation System
- KN** Klein-Nishina
- LAT** Large Area Telescope
- LLAGN** Low Luminosity Active Galactic Nucleus
- MCMC** Markov-Chain Monte Carlo
- MWL** Multi-Wavelength
- p $\gamma$**  proton-photon
- pp** proton-proton
- RIAF** Radiatively Inefficient Accretion Flow
- SED** Spectral Energy Distribution
- SMBH** Supermassive Black Hole
- SSA** Synchrotron Self-Absorption
- SSC** Synchrotron Self-Compton
- TANAMI** Tracking Active Galactic Nuclei with Austral Milliarcsecond Interferometry
- TDE** Tidal Disruption Event
- UHECR** Ultra High Energy Cosmic Ray
- UV** Ultra-Violet
- VHE** Very High Energy
- VLBI** Very Long Baseline Interferometry
- XRB** X-Ray Binary



# Acknowledgements

I would like to express my gratitude to everyone that helped and supported me during my MSc thesis. First of all, I would like to thank my supervisor Prof. Dr. Sera Markoff for guiding me through this project and helping me in every aspect of being a scientist. Your mentorship during this year has really taught me important things about science, science education and life in general, and motivated me even more to pursue a career in science.

I would also like to thank my second supervisor Dr. Foteini Oikonomou who enthusiastically embraced the idea of working together and of me coming to Trondheim. You helped me settle in and made me feel welcome during my one-month stay. I am really grateful for this great experience and for all the people I met during my trip.

I must give special thanks to my other second supervisor, Dr. Matteo Lucchini, who really helped me with understanding the models and everything about blazars. You never refused to help me with any question or problem I encountered. Without your guidance and motivation, I would not have been able to get as far in my project as I have come. I think every MSc student would wish for a supervisor like you.

Then, I would like to thank Volkert van der Willigen en the Amsterdams Universiteitsfonds for making the Volkert van der Willigen grant available for GRAPPA MSc students working on their thesis. The plan to work together with Dr. Foteini Oikonomou and her research group was already there, but this grant allowed me to actually visit and cooperate more intensively. This one-month trip was a great experience and really helped me grow both as a scientist and as a person.

In addition, I want to thank Dr. Dimitrios Kantzas for helping me understand to hadronic parts of the code and viewing things from a different perspective. Even though I mostly bothered you with naive questions or new bugs in the code, you were always open to talk and help me figure things out.

Moreover, I would like to thank all members of the Jetset research group this year. Marin, Leòn, Rittick, Ruby and Subhrat, thank you for the coffee breaks, insightful discussions, endless distraction and the support you gave me during this year. Without you, I would not have liked this time as much as I have enjoyed it now. It is up to you now, to keep the group spirit alive!

To my girlfriend, Lilian, thank you for always being supportive and listening to me complaining about everything that went wrong during this year. You always helped me forget about my struggles and motivated me to work on a solution.

Finally, I would like to thank my parents for their support during my studies over the past six years. They always trusted and supported me in every decision I made. Even though explaining to you what I do is not always easy, your curiosity and admiration really make me feel like I am the smartest, and most amazing person in the world.



## Abstract

The recent detection of astrophysical neutrinos temporally coincident with  $\gamma$ -ray flares from blazars has led to an increased interest in these sources. Blazars are supermassive black holes at the center of galaxies with a relativistic jet of matter closely aligned with our line of sight. These jets, which can extend to the size of entire galaxies and move at nearly the speed of light, produce non-thermal radiation across the electromagnetic spectrum through synchrotron and inverse Compton emission. The alignment of blazars jets leads to a significant enhancement of the observed flux due to relativistic beaming such that they can outshine entire galaxies by a million times.

While blazars themselves are interesting objects to study, the simultaneous observation of  $\gamma$ -ray flares and neutrinos suggests an intimate connection between blazars and the astrophysical backgrounds of  $\gamma$ -rays, neutrinos and cosmic rays. This link implies that blazars might be the source of these astrophysical backgrounds whose origin is unknown. To produce these backgrounds, the relativistic jet in blazars need to accelerate not only electrons, but also protons and heavier nuclei, leading to hadronic interactions in which  $\gamma$ -rays and neutrinos can be produced. The accelerated hadrons will then stream through the Universe providing the cosmic ray background.

Generally, the multi-wavelength emission produced by blazar jets is crucial for studying the physical conditions, the emitting particle distribution and the acceleration mechanisms within these jets. In order to explain their multi-wavelength emission, different approaches exist—from simpler single-zone to more complex multi-zone geometries, and from purely leptonic to incorporating lepto-hadronic interactions—there is no consensus on the best method.

Advances in computing power now allow for the development of detailed multi-zone geometries, but this requires a good understanding of the different approaches. In this study, we conducted a comprehensive comparison of single- and multi-zone black hole jet models by fitting the multi-wavelength emission of blazars TXS 0506+056 and PKS 1424-418. Our results show that tracking the entire evolution of the jet yields statistically better fits and offer deeper insights into the launching, evolution, and particle acceleration processes of the jet. Including the hadronic interactions of protons allows to lift degeneracies present in while preserving the overall jet conditions. The same behavior was seen for the single-zone geometry, where lepto-hadronic fits were better constrained and showed no degeneracies. While blazars are extreme astrophysical objects, this study showed that multi-zone models can explain these objects while requiring less extreme conditions and provide more accurate fits.



# Chapter 1

## Introduction

### 1.1 The Mystery of Cosmic Rays

Since the dawn of humankind, electromagnetic radiation (light) has been our main “messenger” of the Universe. Observations with just the naked eye allowed our ancestors to not only explore the cosmos, but also to start discovering some of the fundamental laws that govern the physical processes within it. Observations were taken to the next stage by using mirrors and lenses which eventually led to the magnificent telescopes we have today. These telescopes not only amplify the light that comes from the Universe but they also allow us to study other wavelengths of electromagnetic radiation with great precision. The capacity to study astrophysical light in wavelengths across the electromagnetic spectrum has revealed countless phenomena in the Universe. However, light is not the only type of messenger that we see coming from outer space. Nowadays, astronomy has entered the age of multi-messenger astronomy with detections of Cosmic Rays (CRs), neutrinos and gravitational waves. These new messengers can help us unravel the mysteries of unknown astrophysical processes and grant a deeper understanding of the processes that are already known (e.g. [Branchesi 2016](#); [Mészáros et al. 2019](#)).

Observing light in wavelengths other than the optical regime started with the detection of radio waves coming from the Universe in the 1930s ([Jansky 1933](#)). However, before these observations highly energetic, electrically charged particles with an extraterrestrial origin, called Cosmic Rays, had already been detected by Theodor Wulf ([Wulf 1909](#)). Wulf used a so-called electrometer to detect charged particles at the top and bottom of the Eiffel tower. At the time, it was theorized that the Earth’s surface would be a source of radiation, and therefore the levels of radiation should decrease at higher altitudes. However, he found that the radiation levels did not decrease as quickly as expected. Physicists realized that they had to take their experiments further up in order to understand these observations. If the particles were extraterrestrial, they would perhaps increase in number at even higher altitudes. At the time, performing these measurements was only possible with manned hot air balloon flights which was a dangerous venture. The scientist that performed these measurements and presented conclusive evidence for the existence of CRs was Victor Hess. He concluded that there has to be an extraterrestrial source of radiation that cannot be coming from the sun ([Hess 1912](#)).

More than a century after the discovery of CRs, humanity has managed to observe the CR spectrum over more than 10 orders of magnitude in flux, and over 10 orders of magnitude in particle energy as shown in Fig. [1.1](#). These observations have allowed us to start putting constraints on their origin, behavior and energy, but there are several significant open questions in the field. The astrophysical source or sources have not been unambiguously identified, the fraction of CRs that is extra-galactic is unclear and the physical mechanism to accelerate these particles is highly debated (e.g. [Blandford et al. 2014](#); [Gabici et al. 2019](#); [Adamo et al. 2022](#)).

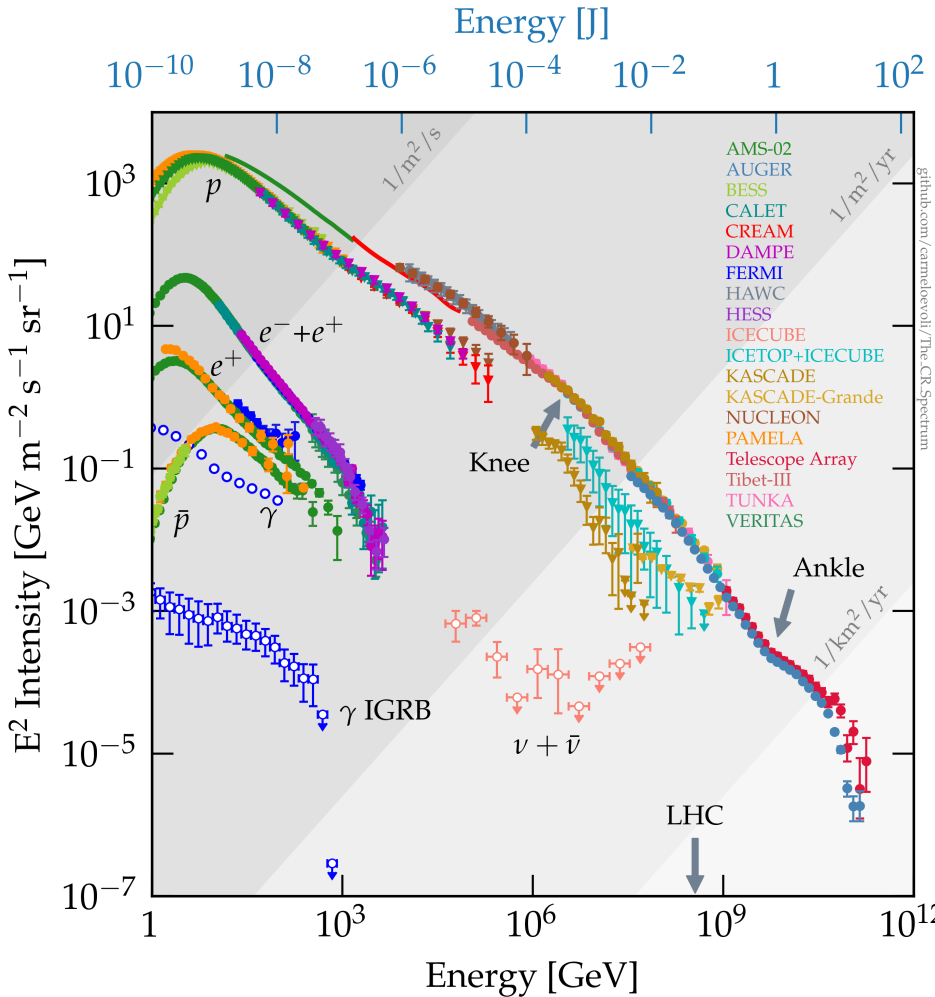


FIG. 1.1 – The CR spectrum as observed with various detectors. The CR spectrum covers more than 10 orders of magnitude in energy flux and extends between 1 GeV( $10^9$  eV) and 100 EeV ( $10^{20}$  eV) in particle energy. The different components are indicated in the plot with protons ( $p$ ), electrons ( $e^-$ ), positrons ( $e^+$ ), antiprotons ( $\bar{p}$ ) and photons ( $\gamma$ ) composing the GeV-to-TeV energy regime. In this regime, the combined CR flux of all particles as measured by AMS-02 and CREAM is shown as the full green and red lines, respectively. Protons and heavier nuclei provide the most energetic part of the spectrum. The data were compiled by [Evoli \(2023\)](#).

### 1.1.1 The Cosmic Ray Spectrum

Our current understanding of CRs can be best explained by studying the characteristics of their energy spectrum. Fig. 1.1 shows the observed CR flux as a function of particle energy, where the different colors correspond to the different detectors that have been used to collect these measurements. In a logarithmic plot, the CR spectrum has the shape of a powerlaw where the slope is also referred to as the spectral index. Whereas thermal radiation from bodies in thermodynamic equilibrium will lead to black body spectra, is the powerlaw shape strong evidence for a non-thermal origin of CRs. There are some distinct transitions in the CR

spectrum where the spectral index changes. These breaks are referred to as the “knee” at  $10^{15}$  eV (PeV) and the “ankle” around  $5 \times 10^{18}$  eV (5 Eev). Up to the “knee” the CR spectrum has a spectral index of  $s = 2.7$ , which softens to  $s = 3.1$  up to the “ankle” (Kulikov & Khristiansen 1959), and At 5 Eev the spectrum hardens again to  $s = 2.7$  (Bird et al. 1993). These breaks are thought to be associated to a change in source type, but this remains an open question (e.g. Coleman et al. 2023).

Besides the shape of the CR spectrum, we also have limited information about the composition of the spectrum. The low-energy CRs around  $\sim 10^9$  eV (GeV) are dominated by protons with a detected flux of about  $1 \text{ m}^{-2} \text{ s}^{-1}$  (Aguilar et al. 2015a,b). Up to an energy of  $10^{13}$  eV (10 TeV) we also detect electrons, positrons and antiprotons together with gamma-rays (Aguilar et al. 2014a,b, 2016). The flux of these low-energy CRs varies in time because they are affected by the partial shielding effects of the solar wind caused by the variable solar activity. We have learned that the solar wind is also responsible for the relatively lower flux of electrons and positrons, and the cutoff around 1-2 TeV (Forbush 1938; Simpson 1954; Aguilar et al. 2019a,b).

In contrast, protons extend all the way up to the “knee” at 1 PeV. At these energies the incoming flux is about  $1 \text{ m}^{-2} \text{ yr}^{-1}$  such that the statistics are significantly worse compared to the low-energy regime (Abbasi et al. 2013; Apel et al. 2013). Such a low detection rate makes it increasingly difficult to identify the type of particle that is detected, and what this means for the composition of the CR spectrum. Therefore, the composition for energies above the “knee” is highly uncertain and experiments indicate that the spectrum becomes dominated by ions, mostly by iron and maybe even heavier nuclei (e.g. Thoudam et al. 2016; Kang & Haungs 2024).

### 1.1.2 The (Possible) Origin of Cosmic Rays

Despite having observed the CR spectrum over a vast range in energy, the origin continues to remain unknown. Nevertheless, the spectral features in the spectrum and the particle composition can aid us in setting the requirements for a source. Firstly, the most energetic CRs reach extraordinarily high energies of  $E \geq 10^{21}$  eV. In order for this to be thermal radiation, this would require astrophysical environments with a temperature of  $T \geq 10^{24}$  K. Even in the most extreme astrophysical environments we know of, such temperatures are absolutely unreachable. Together with the powerlaw shape of the CR spectrum, this is firm evidence for a non-thermal origin of these particles.

The second key feature of CRs is that they are electrically charged. This observation has helped us understand that CRs are not only coming from outside the solar system, but even from outside our Galaxy. The Universe is filled with magnetic fields and electrically charged particles will follow the magnetic field lines because of the Lorentz force. Therefore, CRs will remain confined in their acceleration sites if the local magnetic field is strong enough and the particles do not have enough energy to escape. CRs will only be able to escape when the size of their acceleration region is close to or smaller than the gyroradius of the particle. This gyroradius (Larmor radius) is given by:

$$r_{\perp} = \frac{E}{ZqB}, \quad (1.1)$$

where  $E$  is the total energy of the particle,  $Z$  is the atomic number or charge,  $q$  is the fun-

damental unit of electric charge and  $B$  is the magnetic field strength. Requiring the typical size of the acceleration region to be less than or equal to the gyroradius is known as the Hillas criterion ([Hillas 1984](#)) which can be written as:

$$E \leq Z \left( \frac{B}{1 \mu\text{G}} \right) \left( \frac{R}{1 \text{ pc}} \right) \text{PeV.} \quad (1.2)$$

This criterion can be used to get an estimate of the maximum energy that CRs can obtain in a system with size  $R$  and magnetic field strength  $B$ . Using the Hillas criterion, we can estimate for a certain CR energy whether it has a galactic or extra-galactic origin.

As discussed in Section [1.1.1](#), the CR spectrum has a feature called the “ankle” around 5 EeV where the spectral index hardens from 3.1 to 2.7. This feature is often interpreted as the transition from a galactic component to a component of extra-galactic origin. For example, for a typical magnetic field strength of  $1 \mu\text{G}$  and CRs with energies on the order of 1 EeV, we see that equation [1.2](#) requires the acceleration site to have a size of at least  $10^6$  pc which suggests an extra-galactic origin. For comparison, the diameter of the Milky Way is about 26.8 kpc ([Goodwin et al. 1998](#)). The extra-galactic origin has also been confirmed by a bipolar anomaly on the sky that points away from the Galactic plane as seen by both the Pierre Auger Observatory in Argentina and the Telescope Array in the United States ([Pierre Auger Collaboration 2017](#); [Telescope Array Collaboration 2020](#)).

Having established that the origin of the highest energy CRs is extra-galactic, there are several astrophysical systems that are often suggested to be the origin of these CRs. The relativistic outflows launched by Active Galactic Nuclei (AGN; e.g. [Kazanas & Ellison 1986](#); [Murase et al. 2012](#); [Petropoulou et al. 2015](#); [Rodrigues et al. 2018](#)) and gamma-ray bursts (GRBs; e.g. [Levinson & Eichler 1993](#); [Waxman 1995](#); [Mészáros 2006](#); [Tamborra & Ando 2015](#)), have strong enough local magnetic fields that can accelerate CRs to the highest observed energies without violating the Hillas criterion. However, these two types of systems cannot explain the entire extra-galactic component of the CR spectrum while also accounting for other observational constraints such as the extra-galactic  $\gamma$ -ray and neutrino fluxes ([Batista et al. 2021](#)).

For relativistic jets in AGN, the Hillas energy requires large kinetic or magnetic powers which favours regions in the jet where large amounts of energy are dissipated. Additionally the observed ultra-high energy cosmic ray (UHECR) composition seems to imply a charge-dependent maximum energy of the accelerator which implies modest radiation densities so that sufficient intermediate mass nuclei can escape (e.g. [Kimura et al. 2018](#); [Rodrigues et al. 2021](#)). However, if neutrinos and UHECRs are to be produced in the same region, sufficient radiation densities are needed for efficient neutrino production (e.g. [Biehl et al. 2018](#)). Thus, producing both CRs and neutrinos in the same region of the jet seems to require contradictory conditions, and the high baryonic loading factor to match observations is energetically challenging requiring kinetic energies well beyond the sub-Eddington regime. Quantitatively, stacking limits show that the most prominent contribution of high luminosity blazars can account for at most 17% to the diffuse neutrino flux ([Huber 2019](#)). Alternatively, theoretical uncertainties for the working mechanisms of GRBs and the ill constrained statistics for neutrino detections lead to tight constraints on the neutrino and UHECR production in GRBs ([IceCube Collaboration 2016](#)). Therefore, additional sources are needed with candidates such as starburst galaxies, galaxy clusters, mergers of compact objects, and tidal disruption events (TDEs) that contribute to

the total observed extra-galactic CR and neutrino flux (e.g. Palladino & Winter 2018; Gabici et al. 2019).

There are two major problems with finding the source of UHECRs. The most straight-forward problem is that CRs are charged and are deflected by the magnetic fields in our galaxy and in the inter-galactic medium as they travel towards Earth. Our limited understanding of the magnetic field topology in the Galaxy effectively makes it almost impossible to determine the exact direction from where they came (e.g. Parker 1967; Reichherzer et al. 2022; Lazarian et al. 2023). From a theoretical point of view, it is difficult to find a mechanism that can accelerate these UHECRs. We believe that relativistic shocks in the systems mentioned above are the most likely mechanism. Simulations have shown that if micro-turbulence is triggered at these shocks, then Fermi acceleration can develop (Spitkovsky 2008; Pelletier et al. 2009). Nevertheless, UHECR acceleration is limited by the inability of turbulence at the shock to grow quickly enough to large enough scales and is only able to accelerate particles up to orders of magnitude below the EeV scale (e.g. Batista et al. 2021).

### 1.1.3 Multi-Messenger Astronomy

Reconciling the source of UHECRs seems to elude both theory and observation, but the era of multi-messenger astronomy provides us with a means of combining multiple astrophysical probes to obtain a complementary picture of their sources (see Guépin et al. 2022 for a review). For example, there is the Large Area Telescope (LAT) on the Fermi Gamma-ray Space Telescope<sup>1</sup> to detect  $\gamma$ -rays. This telescope covers the entire sky every three hours and it has been operating since 2008 providing continuous monitoring of the  $\gamma$ -ray sky. Another source of information are astrophysical neutrinos for which we need gigantic detectors, like the IceCube observatory<sup>2</sup>, to compensate for the low interaction cross section of neutrinos (Formaggio & Zeller 2012). The IceCube observatory is an in-ice Cherenkov light detector of  $1 \text{ km}^3$  in the ice of Antarctica with thousands of photomultipliers. These photomultipliers collect the light emitted by the particle showers initiated by incoming high-energy neutrinos, and help us reconstruct their energy and arrival direction.

In Fig. 1.2 we see the diffuse backgrounds of  $\gamma$ -rays, neutrinos and CRs with their flux as a function of particle/photon energy. All three backgrounds have a very similar flux, but their energies differ and span about 10 orders of magnitude. These comparable flux levels suggest a common origin of these three backgrounds. Therefore, we can use these backgrounds to provide complementary information, and overcome the limitations of CRs (e.g. Fornasa & Sánchez-Conde 2015; Ackermann et al. 2022).

The fact that the fluxes of the astrophysical backgrounds in Fig. 1.2 are comparable is not the only reason that we suspect a relation between them. Fig. 1.3 compares the  $\gamma$ -ray sky to the direction of neutrinos detected by IceCube. For every astrophysical neutrino, their source position is reconstructed and this correlates with one or multiple known gamma  $\gamma$ -ray sources. More specifically, we see that some neutrinos overlap with  $\gamma$ -ray producing AGN. Therefore, the IceCube collaboration has tried to statistically connect the detected neutrinos to the AGN catalogues that we currently have (IceCube Collaboration 2018a; IceCube collaboration 2022; Abbasi et al. 2023).

---

<sup>1</sup><https://fermi.gsfc.nasa.gov/>

<sup>2</sup><https://icecube.wisc.edu/>

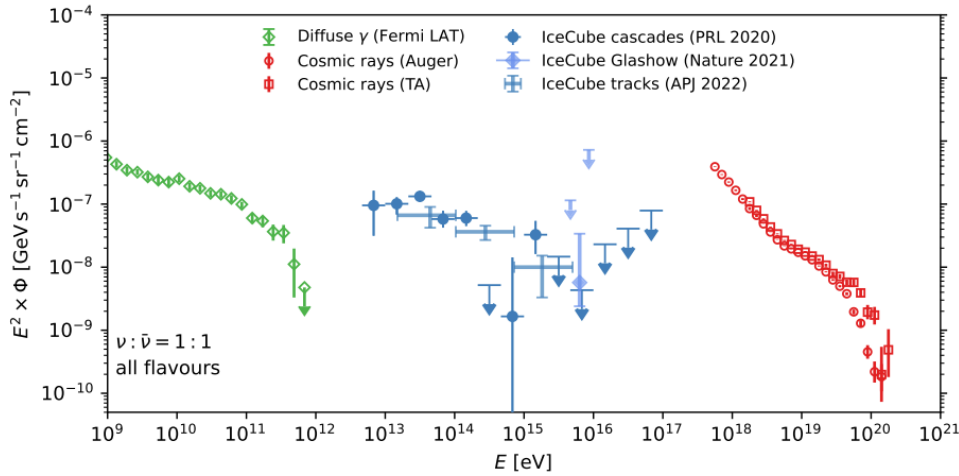


FIG. 1.2 – Measured fluxes of the diffuse astrophysical backgrounds of  $\gamma$ -rays (green) observed by Fermi-LAT, neutrinos (blue) observed by IceCube, and ultra-high energy cosmic rays (red) observed by the Pierre Auger Observatory and the Telescope Array. Figure from [Ackermann et al. \(2022\)](#).

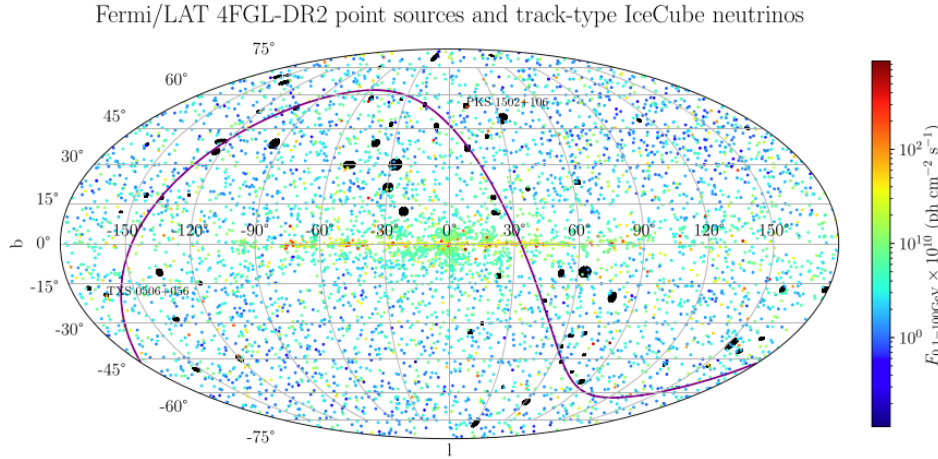


FIG. 1.3 – Galactic sky position and 0.1-100 GeV flux of the Fermi-LAT 4FGL-DR2 point sources (colored dots), overlaid on the list of the 70 track-type neutrino detections by the IceCube observatory (black filled ellipses). The map is shown in the Mollweide projection. The equator is plotted as a purple continuous line, and the blazars TXS 0506+056 and PKS 1502+106 are marked on the map. Figure from [Kun et al. \(2022\)](#).

Ever since the first detection of a neutrino event (IceCube-170922A) temporally coincident with a  $\gamma$ -ray flare coming from the blazar TXS 0506+056 in 2017 ([IceCube Collaboration 2018a](#)), there has been a debate on the physical mechanism that produces these neutrinos. The main idea is that the increased neutrino flux is connected to  $\gamma$ -ray flares ([Murase et al. 2018; Oikonomou et al. 2019](#)) which can be tested observationally. However, others have suggested that the increased flux can only occur for  $\gamma$ -ray dark blazars ([Halzen et al. 2019; Reimer et al. 2019; Halzen & Kheirandish 2020; Kun et al. 2023](#)). The first detections implied a correlation between astrophysical neutrinos and blazars, but this idea has been challenged by a recent

detection of a neutrino coming from the direction of NGC 1068, a prototype Seyfert II galaxy ([IceCube collaboration 2022](#)). While both these scenarios can be tested with observations, it remains important to study all scenarios from both a theoretical and a modelling point of view.

## 1.2 Black Holes

Black holes are one of the most fascinating objects out there in the Universe. The theory of General Relativity (GR) predicts that these objects exist and they are, somewhat surprisingly, characterized by only three quantities: mass, spin and electrical charge ([Israel 1967](#)). BHs are defined as a region in spacetime where gravity is so strong that not even electromagnetic (EM) radiation can escape ([Wald 1984](#)). Only a sufficiently compact mass can deform spacetime such that the density and gravitational force become infinitely large in what is called a singularity ([Hawking & Ellis 1973](#)). The boundary region, or event horizon, of a BH is defined as the radius from which EM radiation cannot escape and this is the part that is actually black. This radius is called the Schwarzschild radius ([Schwarzschild 1916](#)), and is defined as  $R_S = 2GM_{\text{BH}}/c^2$  where G is the gravitational constant,  $M_{\text{BH}}$  is the mass of the BH and c is the speed of light.

Schwarzschild was the first to propose the existence of BHs as a solution to the Einstein field equations of GR. The so-called ‘Schwarzschild metric’ described a neutral, non-spinning BH which is the most basic description for a BH. In 1963, Roy Kerr found the analytical solution for a rotating BH with the corresponding ‘Kerr metric’ ([Kerr 1963](#)). A few years later, this was expanded to also include electrical charge and was named a ‘Kerr-Newman’ BH ([Newman et al. 1965](#)), and is the most general solution for a BH. However, we do not expect real BHs to be charged since it would quickly neutralize by accreting charge of the opposite sign.

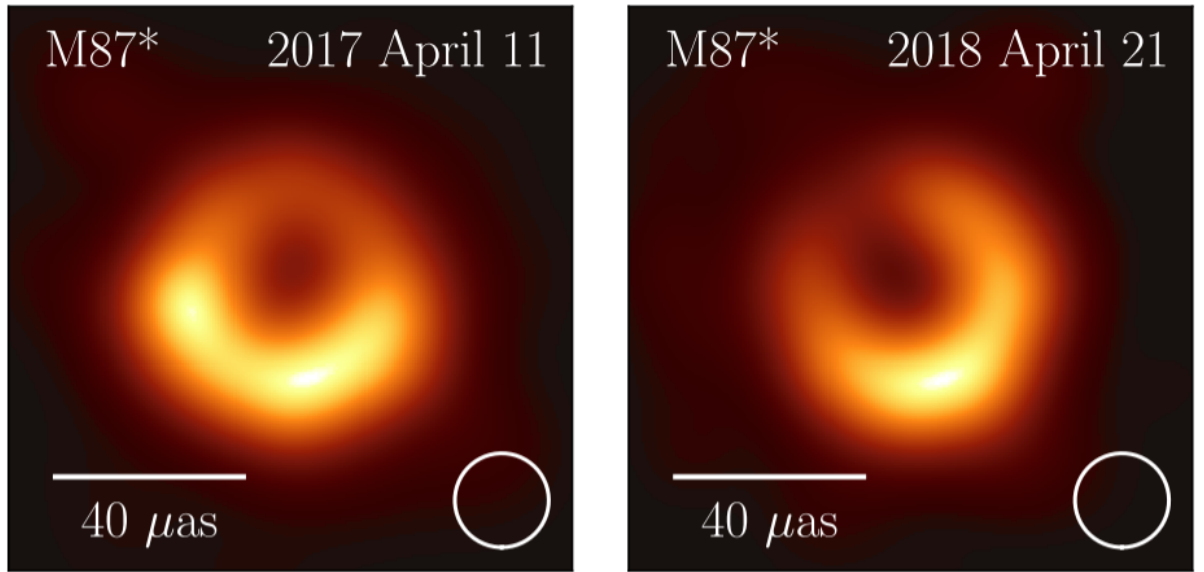


FIG. 1.4 – The shadow of the SMBH at the center of the elliptical galaxy M87 as observed during the 2017 and 2018 campaign. Image from [The Event Horizon Telescope Collaboration 2024](#).

After the prediction by Schwarzschild, the first evidence of their existence was found in the early 1970s when the X-ray source Cygnus X-1 was discovered ([Webster & Murdin 1972](#); [Bolton 1972](#); [Thorne & Price 1975](#)). Since then, more evidence has been collected by studying the proper motion of stars orbiting the supermassive black hole (SMBH) at the center of the Milky Way ([Ghez et al. 1998](#); [Eckart & Genzel 1996](#)), and through dynamical modelling of stellar and gas dynamics within the radius of influence of a BH (e.g. [Kormendy & Ho 2013](#)). However, the detection of a BH merger event using gravitational waves was the first direct evidence that BHs exist ([LIGO Scientific Collaboration and Virgo Collaboration 2016](#)). Nowadays, we are even able to take direct images of SMBHs at the center of galaxies as demonstrated by the Event Horizon Telescope (EHT) collaboration for Sagittarius A\* ([The Event Horizon Telescope Collaboration 2022](#)) and M87\* ([The Event Horizon Telescope Collaboration 2024](#), see Fig. 1.4).

Based on their mass, BHs can be divided into two main categories. There are the *Stellar mass black holes* with masses between  $\sim 3$  and  $\sim 100 M_{\odot}$  (e.g. [van den Heuvel 1992](#); [Fender & Belloni 2012](#); [Tetarenko et al. 2017](#)), where  $M_{\odot}$  is the solar mass. Secondly, there is the group of *supermassive black holes* which have masses ranging from  $\sim 10^5$  to  $\sim 10^{10} M_{\odot}$ . There is also the proposed class of *intermediate mass black holes*, but their existence has not been confirmed to date and we only have some potential candidates (e.g. [Fiorito & Titarchuk 2004](#); [Farrell et al. 2009](#); [Takekawa et al. 2019](#)).

Stellar mass BHs are the end products of the lives of massive stars. Once the fuel for nuclear fusion is depleted, the star can no longer counteract the gravitational force and maintain hydrostatic equilibrium which results in the core collapsing in on itself. This core collapse will lead to a supernova and if the star is massive enough, nothing can prevent the core from collapsing further into a BH. Crucially, many massive stars are part of a binary system where the companion star can survive the supernova explosion. In some cases, the BH can start accreting material from its stellar companion, and the system will form a black hole X-ray binary (BHXB; see e.g. [McClintock & Remillard 2004](#)).

When such a BHXB evolves further, the stellar companion will eventually also deplete its fuel. In that case, the star will either form a neutron star or a stellar mass black hole if it is massive enough. Thereby, the binary evolution will result in a neutron star-BH or a BH-BH binary which will slowly spiral towards each other as they lose gravitational potential energy in the form of gravitational waves. Ultimately, once the system has lost enough energy there will be a merger event leading to the production of strong gravitational waves that can be detected with the various gravitational wave detectors on Earth ([LIGO Scientific Collaboration and Virgo Collaboration 2016](#); [Marchant & Bodensteiner 2023](#)).

On the other side of the mass scale are the SMBHs, and it is thought that there is at least one SMBH in the centre of every galaxy ([Volonteri 2012](#)). There are some exceptions such as some dwarf galaxies that contain none or galaxies that contain more than one after galaxies have merged (e.g. [Satyapal et al. 2017](#)). Unlike stellar mass BHs, the origin of SMBHs is unknown and the mechanisms to create such extremely massive objects are poorly understood. Observations imply that these objects must have been present at very early times in the Universe and the details of their creation is one of the main open questions in modern astrophysics (e.g. [Volonteri 2010](#); [Volonteri et al. 2021](#)). Studying BHs is crucial both for fundamental physics and for understanding a large variety of astrophysical systems and phenomena as well as the evolution of the Universe.

### 1.2.1 Black Hole Accretion

Black holes cannot be observed directly since they do not emit any detectable form of radiation. However, we can learn more by studying the gravitational interactions of BHs with their environment. Firstly, there is the gravitational pull on other objects such that these orbit the BH. The gravitational interaction of the BH only teaches us about its mass and the distance between the BH and the affected object. More interesting is the process where BHs can accrete surrounding gas or merge with stars or other compact objects like BHs or neutron stars. In general, this is called the accretion of matter and it plays a crucial role in our understanding of BHs (e.g. [Narayan & Quataert 2005](#)).

Matter that is accreted onto a BH will form an accretion disk because this is the only way to effectively lose angular momentum before it can fall into the BH (e.g. [Abramowicz & Fragile 2013](#)). As the matter loses angular momentum, it will get closer and closer to the BH. The in-falling material will gain energy by extracting gravitational potential energy from the system. For some material with mass  $m$  gravitationally attracted to a BH with mass  $M_{\text{BH}}$  and radius  $R$  this can be described as

$$\Delta E_{\text{acc}} = \frac{GM_{\text{BH}}m}{R}. \quad (1.3)$$

The extracted potential energy can be converted into a power output of the accretion flow. Power is defined as the amount of energy flowing out of the system per unit time, and we can use the accretion rate for this. Under the assumption of steady state accretion, the accretion rate is given by  $\frac{dm}{dt} = \dot{m}$ . The accretion rate can be understood as the amount of mass per unit time that is crossing the event horizon of the BH. Using the accretion rate, the outgoing accretion luminosity (power) is given by

$$L_{\text{acc}} \equiv \frac{d\Delta E}{dt} = \frac{GM_{\text{BH}}\dot{m}}{R}. \quad (1.4)$$

The derivation above assumes that all available gravitational potential energy is converted into luminosity. In reality this will not happen since the BH will directly accrete material and radiation, never allowing it to escape the system. Therefore, we define an accretion “efficiency” that parametrizes the amount of energy that is able to escape the system. This efficiency is defined as

$$\eta \equiv \frac{L_{\text{acc}}}{\dot{m}c^2} = \frac{GM_{\text{BH}}}{Rc^2}, \quad (1.5)$$

such that the accretion luminosity becomes  $L_{\text{acc}} = \eta \dot{m}c^2$ , with  $0 \leq \eta \leq 1$ .

In order to estimate the efficiency of accretion process, we need to estimate the maximum possible energy that can be extracted from the in-falling material. Using equation 1.3 we can deduce that more gravitational potential energy will be liberated as material gets closer to the BH. However, it is generally thought that energy can only escape the system as long as it does not cross the Innermost Stable Circular Orbit (ISCO) at the radius  $R_{\text{ISCO}}$ . The ISCO is the smallest possible orbit at which a test particle can stably orbit a massive object before it will be accreted in the Kerr metric. Any inward perturbation at the ISCO will quickly grow in radial velocity such that matter or radiation is not able to escape the gravitational pull of the BH. Therefore, the ISCO is typically considered to be the inner edge of the accretion flow. For the

simplest case of a non-spinning BH,  $R_{\text{ISCO}} = 3R_S = 6GM_{\text{BH}}/c^2$ . Interestingly, there are recent ideas that it is possible to see emission produced by material within the ISCO (Mummary et al. 2024). Considering the scenario of material reaching the ISCO for a non-spinning BH, the maximum accretion efficiency is

$$\begin{aligned}\eta &= \frac{\text{maximum extractable gravitational potential energy}}{\text{rest mass energy}} \\ &= \frac{GM_{\text{BH}}m/2R_{\text{ISCO}}}{mc^2} \approx \frac{1}{12} = 0.08,\end{aligned}\quad (1.6)$$

where the extra factor of 2 is inserted because this Newtonian analysis is accurate up to a factor of  $\sim 2$  when compared to the solution found in GR.

For a spinning BH in the Kerr metric, we need to factor in the angular momentum of the BH. A complete derivation can be found in Frank et al. (2002), and the final analytical solution is given by (Bardeen 1973)

$$R_{\text{ISCO}} = m \left\{ 3 + A_2 \mp [(3 - A_1)(3 + A_1 + 2A_2)]^{1/2} \right\} \quad (1.7)$$

where  $A_1 = 1 + (1 - a^2/m^2)^{1/3} [(1 + a/m)^{1/3} + (1 - a/m)^{1/3}]$ ,  $A_2 = \sqrt{3a^2/m^2 + A_1^2}$ ,  $a$  is the angular momentum per unit mass of the BH, and the upper sign refers to particles orbiting in the same direction as the rotation of the BH. Hence, the general expression for the maximum accretion efficiency as a function of angular momentum is given by

$$\eta = 1 - \left[ R_{\text{ISCO}} - 2m \pm a \sqrt{\frac{m}{R_{\text{ISCO}}}} \right] \left[ R_{\text{ISCO}} - 3m \pm 2a \sqrt{\frac{m}{R_{\text{ISCO}}}} \right]^{-1/2}, \quad (1.8)$$

which can reach up to  $\sim 40\%$  for a particle co-rotating with the BH and having the maximum allowed angular momentum of  $a = m$ . For comparison, the process of nuclear fusion of hydrogen to helium, which powers most of the light produced by stars in the Universe, has an energy conversion efficiency of “only” 7%. It becomes evident that BHs can liberate large amounts of gravitational potential energy providing extreme astrophysical environments.

The luminosity emitted by an accreting BH is theoretically not only limited by the maximum extractable gravitational potential energy, but also by the radiation pressure exerted by the emitted radiation. When the gravitational force  $F_G$  is balanced by the radiation pressure  $F_{\text{rad}}$ , the accretion flow is halted such that the accretion rate, and thus the luminosity drops. The limiting luminosity for which this happens is known as the Eddington luminosity and is defined by

$$L_{\text{Edd}} \equiv \frac{GM_{\text{BH}}m_p 4\pi c}{\sigma_T} \approx 1.3 \times 10^{38} \left( \frac{M_{\text{BH}}}{M_{\odot}} \right) \text{erg s}^{-1}, \quad (1.9)$$

where  $m_p$  is the proton rest mass and  $\sigma_T \equiv \frac{8\pi q^4}{3m^2 c^4}$  is the Thomson cross section for a particle with mass  $m$  and electrical charge  $q$ . Interestingly, the Eddington luminosity only depends on the mass of the BH and it forms a self-regulating process in which a too high accretion rate is inhibited by the radiation pressure. This limit only applies if we consider steady spherically symmetric accretion, but it does allow for direct comparison of observed luminosities for sources across the mass scale ranging from stellar mass BHs to SMBHs.

### 1.2.2 Relativistic Black Hole Jets

Both theoretical and observational work have demonstrated that accretion is almost always associated with outflows of matter (e.g. Shakura & Sunyaev 1973; Urry & Padovani 1995; McKinney 2006; Yuan & Narayan 2014; Fender & Gallo 2014) such that a fraction of the in-falling material will not reach the BH, but is ejected from the system. Outflows can be divided into two groups: winds (e.g. Königl 2006; King & Pounds 2015) and jets (e.g. Fender 2003; Fender & Gallo 2014; Romero et al. 2017). Jets are highly collimated and have relativistic speeds ( $\Gamma \geq 1$ ), where  $\Gamma$  is the Lorentz factor of the outflow, while winds are un-collimated and have sub-relativistic speeds ( $\Gamma \approx 1$ ). Furthermore, jets are generally more common in sources with low accretion rates, whereas winds are often seen in high accretion rate systems.

Jets are believed to be a universal phenomenon in the Universe across a wide range of BH masses (Belloni 2010), but also in other compact objects such as TDEs (e.g. Zauderer et al. 2011; Cendes et al. 2021), GRBs (e.g. Band et al. 1993; Mészáros 2002; Kumar & Zhang 2015), and even accreting neutron stars (e.g. van den Eijnden et al. 2018; van den Eijnden et al. 2021). In the case of BHs, these bipolar jets are associated with the accretion disk surrounding the BH and the predominant idea is that they are driven by the enormous rotational energy of the system. Through magneto-hydrodynamic mechanisms, angular momentum of the in-falling material is evacuated through the poles by means of jets, such that the rest of the material can fall into the gravitational potential well.

While all astrophysical objects with jets are interesting in their own right, the main advantage when studying BHs is that they can mostly be described by their mass and this means that they are scale invariant (Falcke et al. 1995; Heinz & Sunyaev 2003; Merloni et al. 2003; Falcke et al. 2004; Plotkin et al. 2012). Scale invariance means that the properties of the system like the jet power and the extent of the jet, scale with the BH mass, but the overall behavior remains the same. For example, both small and massive BH jets can remain collimated up to  $10^9 R_g$ , where  $R_g = R_S/2 = GM_{BH}/c^2 \approx 1.5 \times 10^5 (\frac{M_{BH}}{M_\odot})$  cm is the gravitational radius. For SMBHs with masses up to  $10^9 M_\odot$  this translates to Mpc scales (Waggett et al. 1977) as illustrated by Fig. 1.5, whereas for X-Ray Binaries (XRBs) this translates to sub-pc scales (Mirabel & Rodríguez 1994). Despite the fact that the actual scales vary significantly, their behavior can be described by a single quantity.

A typical observational feature of jets is their flat or slightly inverted radio emission (see e.g. Fender et al. 1997). This characteristic arises from a conically expanding jet, where we observe superimposed radiation from synchrotron self-absorption (SSA) by a non-thermal electron population (Blandford et al. 1979). As the jet expands, the particle number density and the magnetic field strength decrease causing the self-absorption frequency to be inversely proportional to the distance from the BH. For XRBs the transition from optically thick to optically thin emission occurs in the infrared (IR) to X-ray frequency regime, but for AGN this occurs in the sub-mm wavelength band. This transition corresponds to a spectral break and is thought to originate from the first particle acceleration region in the jet where thermal electrons near the BH are accelerated into a powerlaw distribution (Markoff et al. 2001, 2003). Section 1.3 will give a more detailed overview of all the spectral components of BH jets.

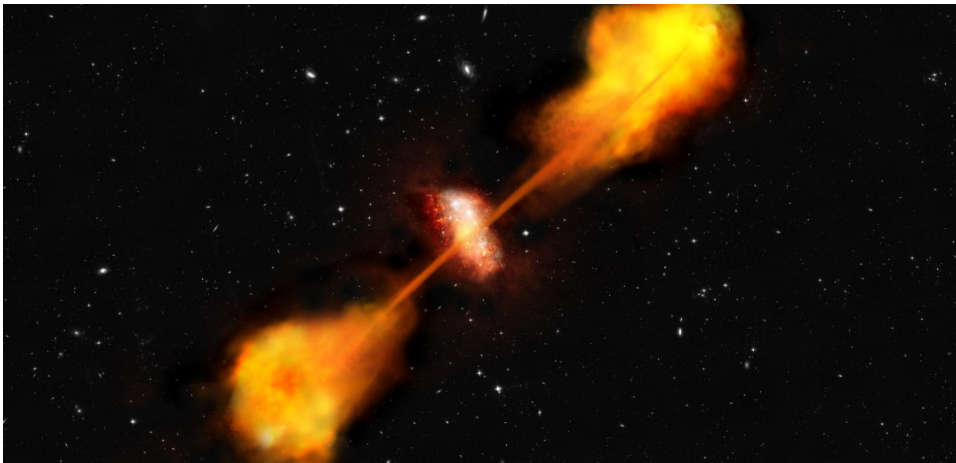


FIG. 1.5 – Artist’s impression of an AGN with two bipolar relativistic jets. These jets are launched by the SMBH and inflate to giant radio lobes at either end. Image from ESA/C. Carreau/ATG Medialab.

### 1.2.3 Active Galactic Nuclei

As discussed in Section 1.2, there is a SMBH in the center of practically every galaxy. If these objects actively accrete matter, these galactic centers become active and they are called *Active Galactic Nuclei* or AGN. AGN can have immense luminosities and emit radiation across the entire electromagnetic spectrum, from radio waves to  $\gamma$ -rays (see e.g. [Padovani et al. 2017](#); [Blandford et al. 2019](#) for reviews of AGN). The first observation of a jetted AGN was reported in 1918 when [Curtis \(1918\)](#) described the kiloparsec-scale jet of the M87 radio galaxy as “a curious straight ray...apparently connected with the nucleus by a thin line of matter.”. At the time, people did not realize that these objects are extra-galactic until Maarten Schmidt measured the redshift of 3C 273 using its optical spectrum. He estimated a redshift of  $z_{\text{red}} = 0.158$ , meaning that this source must be extra-galactic ([Schmidt 1963](#)). Based on the measured flux of 3C 273 and its distance with respect to Earth, based on the redshift, this object must have a bolometric luminosity comparable to that of an entire galaxy ( $L_{\text{bol}} = 10^{46} - 10^{47} \text{ erg s}^{-1}$ ). The only way to produce such powerful emission is through accretion onto a compact central object that converts gravitational potential energy into high energy emission.

More studies followed and after slightly more than a century of research, the current paradigm for radio-loud AGN can be best explained with Fig. 1.6. This paradigm is based on the unification scheme of radio-loud AGN by [Urry & Padovani \(1995\)](#). The scheme aims to explain the different classes of AGN by proposing that they all have the same structure, but we are looking at them from different angles. The most direct consequence is that we have to take the presence of clouds of gas around the SMBH into account. The broad line region (BLR) and dusty torus (DT) orbit the BH and can obscure the source. Moreover, these regions absorb disk and jet emission at certain frequencies and will lead to absorption lines in the emitted spectrum. The different velocities of these clouds relative to us will lead to broadening of these lines caused by the Doppler effect ([Seyfert 1943](#)). Gas that is further away from the BH, moves slower so the broadening will become less. Hence, the name BLR for the region close to the BH and narrow line region as we move further out.

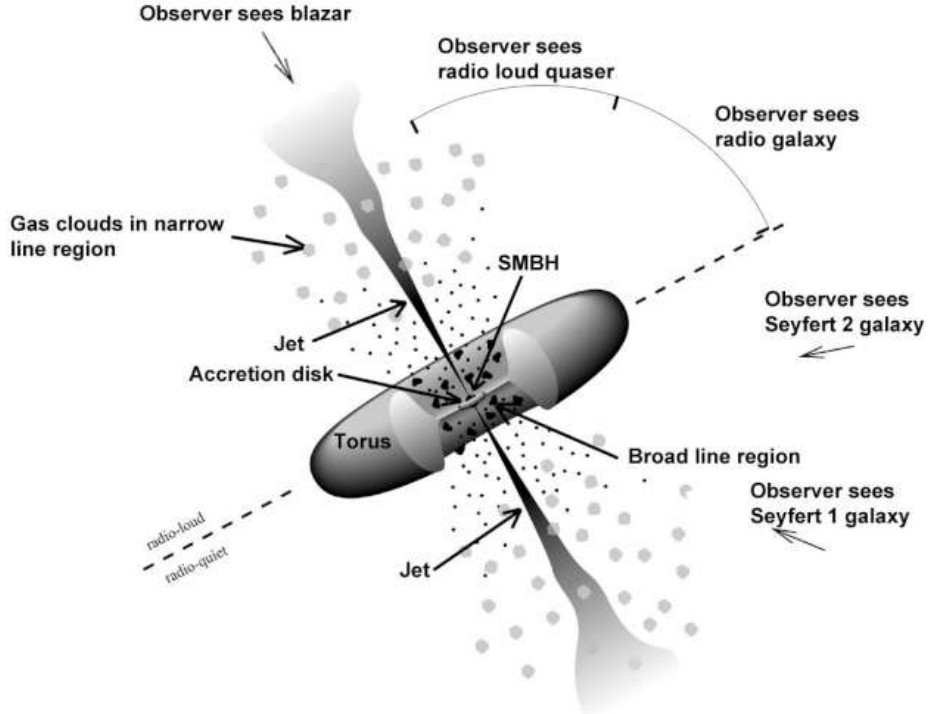


FIG. 1.6 – A schematic diagram for radio-loud AGN (not to scale). The central BH is surrounded by a luminous accretion disk. Broad emission lines are produced in clouds orbiting above the disk and perhaps by the disk itself. A thick dusty torus obscures the broad-line region from transverse lines of sight. A hot corona above the accretion disk may also play a role in producing the hard X-ray continuum. Narrow lines are produced in clouds farther from the central source. Radio jets, shown here as the diffuse jets characteristic of low-luminosity radio sources, emanate from the region near the BH, initially at relativistic speeds. Image from [Urry & Padovani \(1995\)](#).

In the past five decades, more classifications of AGN have been made leading to an entire zoo of AGN classes (see e.g. [Padovani 2017](#) for a full list). Except for their orientation, the seemingly different classes are due to changes in the host galaxy and its environment, the accretion rate (e.g. [Heckman & Best 2014](#)), and the presence of strong jets (e.g. [Hardcastle & Croston 2020](#)). Especially for different accretion rates, the slowly accreting sources can be named ‘jetted’, ‘radio-loud’ and ‘low excitation galaxy’ compared to ‘non-jetted’, ‘radio-quiet’ and ‘high excitation galaxy’ which all arise from studying AGN in different wavelengths. The accretion rate of the system can also be used to divide the population of low-redshift AGN into the categories “radiative mode” and “jet mode” (e.g. [Heckman & Best 2014](#)).

**Radiative mode** AGN have luminosities of  $L/L_{\text{Edd}} \geq 0.01$  and are associated with higher accretion rates. The higher accretion rate leads to an accretion disk which is geometrically thin and optically thick such that it peaks in the extreme ultraviolet (UV) through the visible part of the EM spectrum. This state shows wind-driven AGN feedback, which can have a significant influence on the co-evolution of the AGN and its host galaxy.

**Jet mode** AGN have luminosities of  $L/L_{\text{Edd}} \leq 0.01$  and are associated with relatively

low accretion rates. In this case, lower accretion rates will lead to a geometrically thick, radiatively inefficient accretion disk in the regions close to the BH. It is thought that these advection-dominated or radiatively-inefficient accretion flows (ADAFs/RIAFs) are needed to launch relativistic jets ([Yuan & Narayan 2014](#)). Namely, the thicker, puffed up disk helps in collimating the jet. Again, AGN feedback can play an important role and in some cases, these collimated jets could even affect the evolution of entire galaxy clusters if they stay collimated up to large enough scales.

The two AGN modes explained above show that both are associated with outflows of matter reaching up to galactic scales. Either through wind or jetted outflows, the energy radiated away from an AGN can heat up and/or remove cold gas reservoirs in its host galaxy, effectively halting the process of star formation. This coupling to the surrounding medium is called AGN feedback and it is a crucial component of galaxy evolution ([Brüggen & Kaiser 2002](#); [Di Matteo et al. 2005](#)). Notably, the jetted AGN outflows can reach even larger scales, thereby influencing galaxy cluster and cosmological structure formation. Therefore, accounting for the effects of AGN feedback is crucial in modern cosmological simulations to regulate the cooling in dense galaxy environments, and to sufficiently control the efficiency of star formation for massive galaxies (e.g. [Schaye et al. 2014](#); [Dubois et al. 2016](#); [Naab & Ostriker 2017](#)).

### Relativistic Beaming in Relativistic Jets

When looking at jet emission it is crucial to consider the effects of relativistic beaming. Relativistic beaming refers to the effects of special relativity on the observed emission of an object moving at a velocity close to the speed of light. When we observe an extended source that is moving at relativistic velocities, we have to consider effects like length contraction, time dilation and the transformation properties of velocities between different frames of reference. From special relativity, we know that length and time intervals change as we switch between different frames of reference. Neglecting light travel time, distances will contract as  $\Delta x = \Gamma^{-1} \Delta x'$ , where  $\Gamma \equiv (1 - v^2/c^2)^{-1/2}$  is the Lorentz factor of the source for an object moving at velocity  $v$ . In the case of time dilation, this will lead to  $\Delta t = \Gamma \Delta t'$  with the primed quantities corresponding to the co-moving frame and the unprimed quantities to the observer frame.

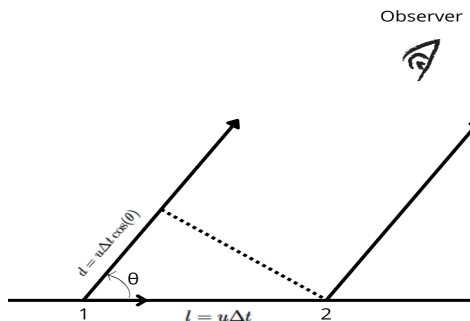


FIG. 1.7 – Geometry to explain the relativistic Doppler effect caused by the difference in arrival time due to light travel time. Figure from [Rybicki & Lightman \(1979\)](#).

More specifically, for an extended source, moving at a velocity close to the speed of light we have to consider the light travel time to the observer. Let us consider the geometry in Fig.

[1.7](#) and assume a continuously emitting source that is moving at a velocity  $u$  along the x-axis. The light emitted at point 1 will have to travel a distance  $d = u\Delta t \cos(\theta)$  to ‘catch up’ with the light emitted at point 2 at a distance  $l = u\Delta t$ . The different distances lead to a difference in arrival times expressed as

$$\Delta t_A = \Delta t - \frac{d}{c} = \Delta t \left( 1 - \frac{u \cos(\theta)}{c} \right) = \Delta t' \Gamma \left( 1 - \frac{u \cos(\theta)}{c} \right) \equiv \Delta t'_A / \delta, \quad (1.10)$$

where we defined the **Doppler factor** as  $\delta \equiv \frac{1}{\Gamma(1-\beta \cos(\theta))}$  with  $\beta \equiv u/c$ . Since frequency is the reciprocal of time, we have  $\nu = \delta\nu'$  which is important when studying the radiative emission of any astrophysical source.

In special relativity, one can show that directions of velocities (angles), also change between different frames of reference. Let us consider the angle  $\theta$  between the direction of the emitted photon and the jet velocity vector. For this we can use the *aberration formula*

$$\tan(\theta) = \frac{u_{\perp}}{u_{\parallel}} = \frac{u' \sin(\theta')}{\Gamma(u' \cos(\theta') + v)}, \quad (1.11)$$

where  $v$  is the velocity of the observer. If we set  $u' = c$ , then  $\sin(\theta) = \sin(\theta')/\delta$  and  $\cos(\theta) = \frac{\cos(\theta')-\beta}{1+\beta \cos(\theta')}$ . These relations show that isotropic radiation in the co-moving frame, is highly beamed in the direction of motion when seen by an observer at rest. This effect becomes stronger as the source moves at higher velocities and the resulting beaming pattern is illustrated in Fig. 1.8. Consequently, sources moving at relativistic velocities will appear more or less bright depending on the viewing angle.

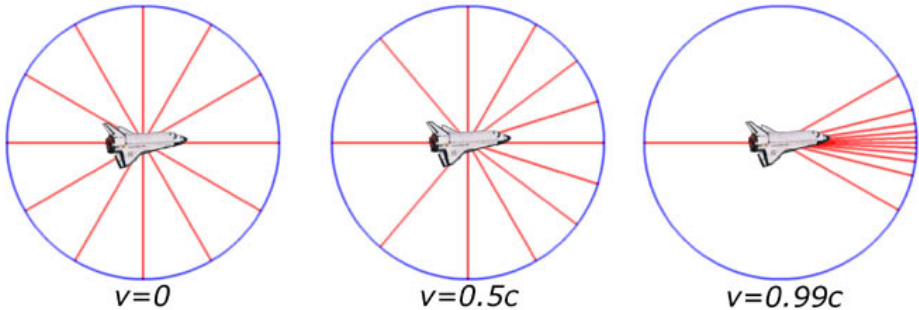


FIG. 1.8 – Beaming of the emission produced by a source moving at relativistic speeds. As the speed increases towards the speed of light, more and more radiation will be beamed in the direction in which the source is moving, rather than being isotropically emitted. Figure adapted from <https://math.ucr.edu/home/baez/physics/Relativity/SR/Spaceship/spaceship.html>

The effect of relativistic beaming will lead to a Doppler factor that is highly dependent on the viewing angle, as illustrated by Fig. 1.9. According to special relativity, the specific flux of an object  $F(\nu)$  (power emitted per unit frequency per unit area) at a given frequency transforms between frames as  $F(\nu) = \delta^3 F'(\nu)$ , and the bolometric flux (or luminosity)  $F$  will transform as  $F = \delta^4 F'$ . These relations can be derived from the fact that the emitted power (energy per unit time) is Lorentz invariant, but we do have to correct for the units of per frequency and per

unit area which leads to a factor  $\delta^3$  in the case of the specific flux (Rybicki & Lightman 1979). These relations show that relativistic beaming can have a significant effect on the observed luminosity of an astrophysical source. This effect is very important in understanding AGN jets. Going back to the AGN classification scheme by Urry & Padovani, we see that a jet which is very closely aligned with the line of sight will produce highly beamed emission. Looking straight into these AGN jets leads to the concept of blazars, and these sources have such a strong beaming effect that they can outshine entire galaxies and reach luminosities up to  $10^{50}$  erg/s (Ajello et al. 2009).

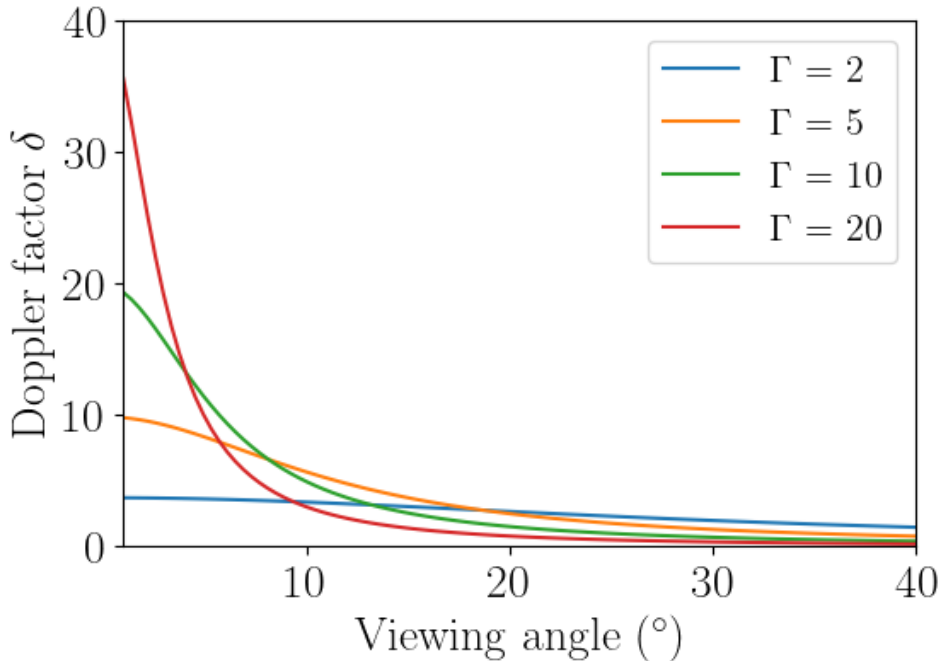


FIG. 1.9 – The Doppler/beaming factor of a source with different Lorentz factors as a function of viewing angle. Highly relativistic sources can have large beaming factors as they get more closely aligned with the line of sight. Image credit: M. Lucchini

Interestingly, relativistic beaming does not only apply to light but also to the relativistic particles that are being produced and accelerated by AGN jets. Observations show us that blazars produce very high fluxes of  $\gamma$ -rays because of the relativistic beaming effect. In turn, this means that if neutrinos are being co-produced with the  $\gamma$ -rays then there should also be a relatively high neutrino flux coming from these sources (e.g. Stecker & Salamon 1995; Atoyan & Dermer 2001; Suray & Troitsky 2023). Moreover, the large energy budget of AGN means that the jet could be able to accelerate protons and heavier nuclei such that they become UHECRs (Batista et al. 2021).

## Blazars

As discussed in the previous section, blazars are jetted AGN with their jets very closely aligned to our line of sight. Similar to the AGN classification scheme, blazars can also be divided into

different subcategories which is based on their Spectral Energy Distribution (SED). A typical blazar SED for the blazar Mrk 501 is illustrated in Fig. 1.10 where one clearly sees a double-humped structure without any substructure except for the black body component produced by the surrounding galaxy. Typically, the SED data of blazars is plotted in a logarithmic plot with the bolometric flux multiplied by the frequency as a function of frequency.

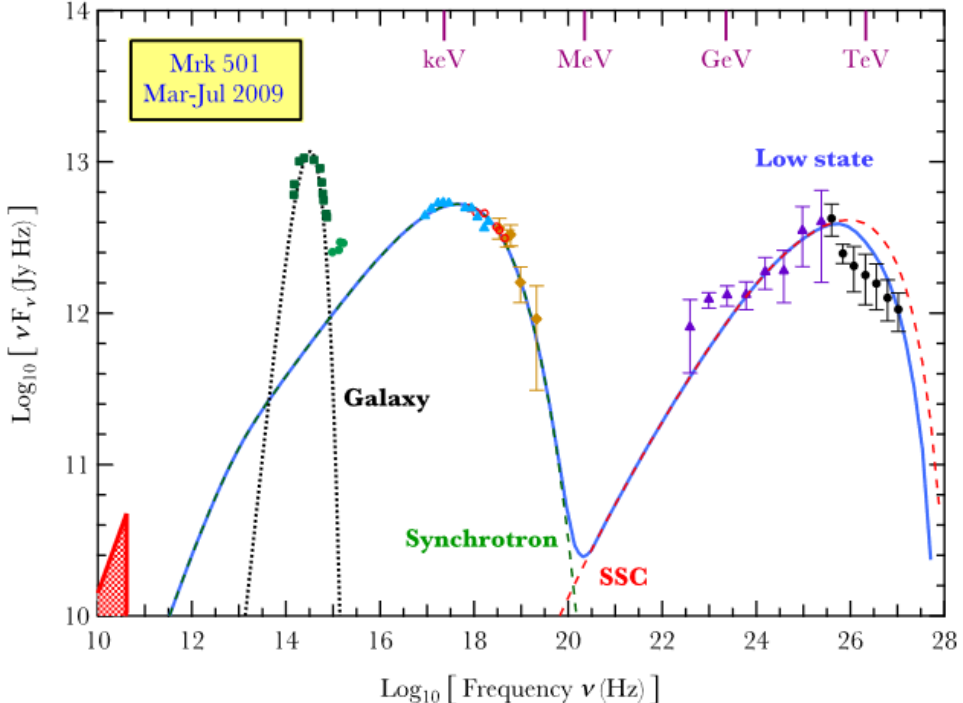


FIG. 1.10 – Example of a typical double-humped blazar SED with the multi-wavelength (MWL) data of the blazar Mrk 501 in 2009. One sees a fit to the data using a simple synchrotron self-Compton model and a black body contribution from the surrounding galaxy. Figure from [Baring et al. \(2017\)](#).

In 1995, Padovani & Giommi proposed to use the peak frequency of the synchrotron emission ([Padovani & Giommi 1995](#)) to classify blazars since this reflects the maximum energy of the emitting non-thermal particles. Later, this was extended by [Abdo et al. \(2010\)](#) to divide blazars into three categories:

1. Low synchrotron peaked blazars: Sources where the synchrotron power peaks at frequencies  $\nu_{\text{peak}} \leq 10^{14}$  Hz.
2. Intermediate synchrotron peaked blazars: Sources where the synchrotron power peaks at frequencies  $10^{14} \leq \nu_{\text{peak}} \leq 10^{15}$  Hz.
3. High synchrotron peaked blazars: Sources where the synchrotron power peaks at frequencies  $\nu_{\text{peak}} \geq 10^{15}$  Hz.

Using this classification scheme, we see that Mrk 501 can be classified as a high synchrotron peaked blazar since the synchrotron component peaks around  $10^{18}$  Hz for example.

Historically, blazars were also divided based on their optical spectra into the group of flat-spectrum radio quasars (FSRQs) or BL Lac objects, named after the discovery of the first BL Lac type source (e.g. Landt et al. 2004). FSRQs show strong, broad emission lines, and practically all of them belong to the low synchrotron peaked blazars. On the other hand, BL Lacs have a rather featureless optical spectrum and can belong to all three blazar classes (see Padovani et al. 2017 for a recent review). Recently, more progress has been made in blazar classification by incorporating the effects of radio jet kinematics (Hervet et al. 2016), accretion dynamics (Mondal & Mukhopadhyay 2019), and even utilizing machine learning techniques (Chiari et al. 2016; Kovačević et al. 2020).

#### 1.2.4 X-ray Binaries

On the other side of the BH mass scale, are the stellar mass BHs. One interesting type of system are the XRBs in which we see a stellar mass BH with a stellar companion. The companion is the source of matter for the accreting BH either by accreting the stellar wind, or by Roche lobe overflow (Done et al. 2007). The accretion can lead to the formation of relativistic jets such that XRBs produce prominent X-ray emission such that the first detection of an XRB, Cygnus X-1, was observed in the X-ray regime (Webster & Murdin 1972; Bolton 1972; Thorne & Price 1975), hence their name.

XRBs are interesting objects to study the dynamics and temporal evolution of accreting systems. As discussed in Section 1.2.2, many properties of accreting BHs are scale invariant and can be expressed in terms of  $R_g$  and  $L_{\text{Edd}}$ . The scale invariance can be used to find an associated typical timescale for every system. Many AGN have been observed in different states but it is very difficult to study the temporal evolution of these states. The fact that these massive objects evolve on timescales of  $10^3 - 10^6$  years far exceeds the human lifespan. On the other hand, stellar mass black holes have significantly shorter timescales ranging from days to a few years. These shorter timescales makes XRBs excellent laboratories to study the transition between different accretion states and how this can be linked to their spectral properties.

There are excellent reviews on how the different geometrical, spectral and timing properties of XRBs can be used to categorise these objects into different “states” by Remillard & McClintock (2006) and Belloni (2010). These states correspond remarkably well to the different AGN systems that we observe up to a few inherent differences that prevent a one-to-one comparison to XRBs. One major breakthrough in connecting XRBs to AGN was the discovery of the radio/X-ray correlation seen for XRBs that are in the ‘hard’ state (e.g. Hannikainen et al. 1998; Corbel et al. 2000; Corbel et al. 2003), where the correlation has the form of a powerlaw  $L_{\text{radio}} \propto L_{\text{X-ray}}^{0.7}$ . In the hard state, the X-ray emission is dominated by a hard powerlaw component after the accretion rate has increased. The source of this X-ray emission is thought to be in close proximity to the BH, but its exact origin is not yet well-constrained. On the other hand, the radio emission is believed to originate from the extended jet structure further from the central engine. Therefore, the correlation between radiation emitted close to the central object and that emitted further out, hints at a tight connection between the in-flowing and out-flowing material.

Shortly after the discovery of the radio/X-ray correlation, it was demonstrated that this correlation also applied to AGN by adding a mass term in the correlation relation (Merloni et al. 2003; Falcke et al. 2004). This correlation is known as the **Fundamental Plane (FP)** of

**Black Hole Activity** and is illustrated by Fig. 1.11. The universal nature of the FP implies that accreting black holes can be treated as scale-invariant objects, meaning that the physical processes are the same regardless of the mass of the system. The analysis of the FP by Plotkin et al. (2012) is the most advanced to date, in which they included a more curated AGN sample with dynamical mass measurements to reduce systematic errors (Gültekin et al. 2009) as well as to mitigate the effects of beaming and radiative cooling.

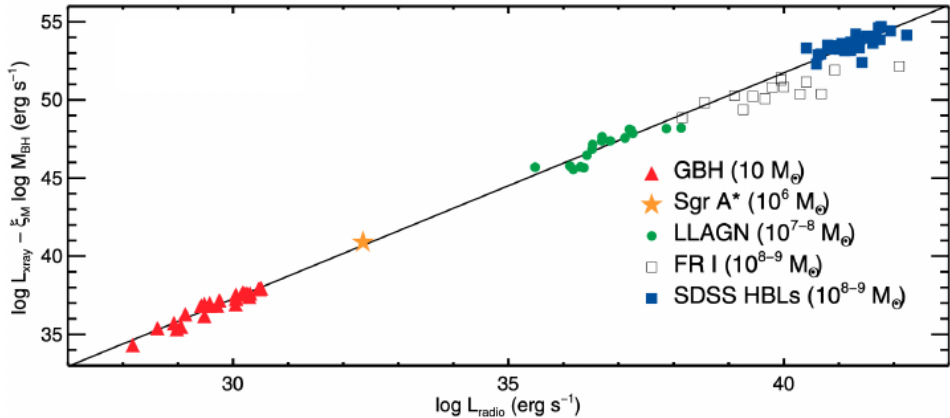


FIG. 1.11 – The Fundamental Plane of Black Hole activity, showing the correlation between radio and X-ray luminosities and black hole mass. Figure from Plotkin et al. (2012).

## 1.3 The Spectral Components of Accreting Black Holes

From discussing CRs and revealing their origin using multi-messenger astronomy to the promising candidacy of blazars to explain them, we now need to know how BHs produce their multi-wavelength (MWL) emission. For this, we need to consider the spectral components of an accreting BH and because of the fundamental plane of BH activity these principles apply to both stellar mass BHs and SMBHs. The most important components are the emitting accretion disk and the relativistic jet in which radiative, leptonic and hadronic processes play a role.

### 1.3.1 The Accretion Disk

As discussed in Section 1.2.1, the extraction of gravitational potential energy from material accreting onto a gravitating object is the principle source of power for the most luminous astrophysical objects. Especially the existence of compact objects provides us with a natural and powerful mechanism to produce high-energy radiation. In order to actually reach the surface of the compact object, it is crucial that the accreting matter loses angular momentum before it can be funneled onto the accreting object. Angular momentum is a conserved quantity in nature and accreting material typically has too much to be able to fall directly towards the central object. Luckily, nature has found a way to get rid of this excess angular momentum and this is most efficiently lost when the material forms an accretion disk around the compact object (e.g. Abramowicz & Fragile 2013).

The simplest description of an accretion disk is that of a geometrically thin, optically thick disk in which matter loses angular momentum through viscous forces. [Shakura & Sunyaev \(1973\)](#) laid the foundation for our understanding of these disks, and regardless of the dissipation mechanism, it can be shown that in a geometrically thin disk, the dissipation rate per unit area of a Shakura-Sunyaev disk is (e.g. [Frank et al. 2002](#))

$$D(R) = \frac{3GM_{\text{BH}}\dot{m}}{8\pi R^3} \left[ 1 - \left( \frac{R_{\text{ISCO}}}{R} \right)^{1/2} \right]. \quad (1.12)$$

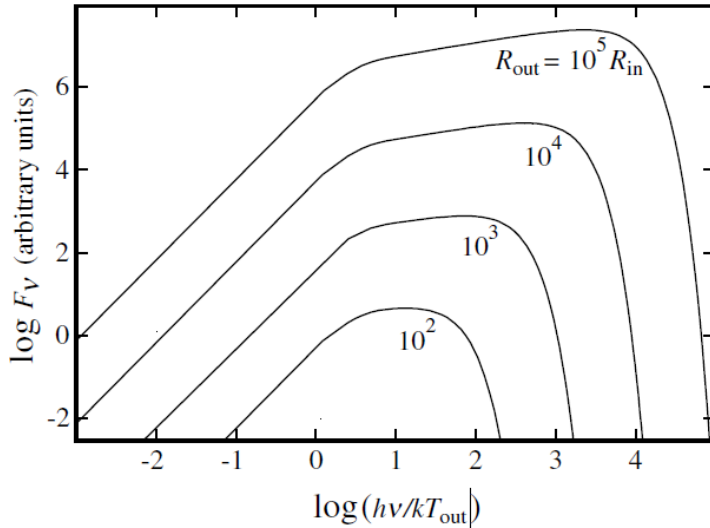


FIG. 1.12 – Spectra of a steady optically thick accretion disk radiating locally as a blackbody, for disks with different ratios of  $R_{\text{out}}/R_{\text{in}}$ . The frequency is normalized to  $k_b T_{\text{in}}/h$ . Figure from [Frank et al. \(2002\)](#).

If the material around the BH is optically thick, the radiation cannot escape the disk and it is heated such that the disk emits as a black body. From equation 1.12 we can see that as material moves closer to the BH, more gravitational binding energy and angular momentum have to be dissipated from a smaller surface area. This higher dissipation rate in an optically thick disk will lead to an increase in disk temperature. The resulting temperature profile increases as we move closer to the BH and is given by

$$T(R) = \left\{ \frac{3GM_{\text{BH}}\dot{m}}{8\pi R^3} \left[ 1 - \left( \frac{R_{\text{ISCO}}}{R} \right)^{1/2} \right] \right\}^{1/4}, \quad (1.13)$$

where the peak temperature of the profile is reached at the innermost radius of the disk  $R_{\text{in}}$  and is given by ([Frank et al. 2002](#))

$$k_b T_{\text{in}} = 2.34 \left( \frac{M_{\text{BH}}}{10 M_{\odot}} \right)^{-1/2} \left( \frac{\dot{m}}{10^{-8} M_{\odot} \text{ yr}^{-1}} \right)^{1/4} \left( \frac{R_{\text{in}}}{R_g} \right) \text{ keV}. \quad (1.14)$$

Note that the temperature of the disk in BHXBs peaks in the soft X-ray band at roughly one keV, while AGN disks peak at optical or UV frequencies. At every radius along the accretion

disk, there is a different peak temperature at which the black body emission peaks. When we look at the total emitted spectrum by the disk this results in a multi-color black body spectrum. Such a spectrum is illustrated in Fig. 1.12 for different ratios of  $R_{\text{out}}/R_{\text{in}}$ , where  $R_{\text{out}}$  is the outermost radius of the accretion disk. A multi-color black body spectrum is different from a regular black body spectrum as it has a almost flat part instead of only a peak in a logarithmic plot.

### 1.3.2 Jet Formation and Acceleration

The standard Shakura-Sunyaev disk is the simplest disk model in the literature, but there are many other models that were developed to explain a plethora of observational features (see e.g. the review by [Abramowicz & Fragile \(2013\)](#)). It is beyond the scope of this thesis to discuss all of them, but it is important to realize that there is a strong connection between accretion disks and the jets observed around BHs. As discussed earlier, jetted AGN need wind outflows of the disk in order to keep the jet collimated. These conditions are usually connected to lower accretion rates, higher temperatures and more puffed up disks.

Despite this phenomenological connection, the exact launching mechanism of relativistic jets is unknown, but it is thought that the immense rotational energy of the system is providing the required power. At the moment, there are two main explanations called the Blandford-Znajek (BZ) ([Blandford & Znajek 1977](#)) and the Blandford-Payne (BP) mechanism ([Blandford & Payne 1982](#)). Both mechanisms require strong magnetic fields to accelerate the jet and this is provided by the in-flowing material from the accretion disk. The BZ mechanism uses magnetic field lines that are anchored in the BH ergosphere and is sometimes compared to having beads on a string being flung out as you rotate the string. The BP mechanism exploits the magnetic field lines that are frozen into the disk and extract energy in the form of angular momentum from the disk to accelerate jets.

The underlying power source for both mechanisms determines the amount of power that is available for jet acceleration. The result is that BP jets are limited by the power provided by the accretion disk which means that their jet speeds are constrained to  $\Gamma \approx$  a few. On the other hand, BZ jets are less constrained by the in-flowing material which will lead to more available power and faster jets ( $\Gamma \leq 10$ ) ([Tchekhovskoy et al. 2011](#)). The development of General Relativistic Magneto-Hydrodynamic (GRMHD) simulations has led to more insight in the evolution of the bulk outflow for both mechanisms. Such simulations have shown that a Poynting flux dominated outflow can convert a significant amount of its initial magnetic energy into bulk kinetic energy ([McKinney 2006](#); [Komissarov et al. 2007, 2009](#); [Tchekhovskoy et al. 2008, 2009](#)). Interestingly, in GRMHD simulations one sees a light, fast, highly magnetized, BZ-type “spine” that is surrounded by a heavier, slower BP-type “sheath” (e.g. [McKinney 2006](#); [Chatterjee et al. 2019](#)). GRMHD simulations have thus made the picture more complex, and more development is needed to understand these mechanisms. For example, one problem is the simulations do not self-consistently include particle acceleration meaning that it is difficult to study the effect of different mechanisms on the spectral output.

From observations we know that highly relativistic jets produce non-thermal emission which requires them to be very efficient particle accelerators somewhere in the jet flow. However, the exact acceleration mechanism is also an open question in the field, and there is a large variety of possible explanations (e.g. [Matthews et al. 2020](#)). Currently, there are two mechanisms believed

to be the most promising which are called shock acceleration (e.g. Sironi & Spitkovsky 2011; Crumley et al. 2019) and magnetic reconnection (e.g. Sironi et al. 2013; Sironi & Spitkovsky 2014; Sironi et al. 2015; Petropoulou et al. 2019). Moreover, not only the exact mechanism is unknown, there is also the debate on where exactly the acceleration region in the jet is (e.g/ Romero et al. 2017).

The last major open question in jet physics is related to their matter composition. Intuitively, one would expect the jet plasma to have a neutral electric charge since the accretion flow is neutral and any particle creation will also demand charge conservation. A neutral electrical charge is also necessary to keep the jet stable. Taking this into account, we need to accelerate protons as well as electrons, but the former requires far more energy to be accelerated to relativistic speeds. If protons are indeed accelerated by the jet into non-thermal distributions, just like electrons, this implies that we should see signatures of hadronic interactions like  $\gamma$ -ray emission (Böttcher et al. 2013), and possibly also cosmic rays (e.g. Abraham et al. 2008; Cooper et al. 2020) and neutrinos (e.g. Kadler et al. 2016; IceCube Collaboration 2018a). We have no direct observational handle on the matter composition except for these signatures and sparse indirect estimates of the lepton-to-proton ratio. For example, if there would be no protons in the jet outflow, the radiation pressure of external photon fields around AGN would slow the jet down to sub-relativistic speeds (Ghisellini & Tavecchio 2010). This behavior is not observed in any source, from which an upper limit of  $\approx 10$  electron-positron pairs per proton is inferred.

### 1.3.3 Synchrotron Emission

After discussing the spectral component provided by the accretion disk and how the disk is tied to jet acceleration, we can focus on the non-thermal emission produced by the matter in the jet. The most dominant radiative mechanisms observed in accreting BHs are Inverse Compton (IC) scattering and synchrotron emission. Note that these mechanisms apply to any charged particle so the discussion below will be important for both electrons and protons. In this section, I will discuss the synchrotron emission mechanism, and IC emission will be discussed in Section 1.3.4.

Synchrotron emission occurs when a relativistic charged particle moves with a velocity  $\mathbf{v}$  through a region threaded by a magnetic field  $\mathbf{B}$ , where symbols in bold represent three-dimensional vectors. Within most astrophysical systems the mean electric field strength is very small ( $E = 0$ ) so the particle is subject to the Lorentz force as given by

$$F_{L,\perp} = |q(\mathbf{E} + \mathbf{v} \times \mathbf{B})| = q \frac{v_\perp}{c} B = \gamma m \frac{dv_\perp}{dt}, \quad (1.15)$$

where  $\gamma$  is the particle Lorentz factor,  $B = |\mathbf{B}|$  is the magnetic field strength, and  $v_\perp$  is the velocity component perpendicular to the direction of the magnetic field. The Lorentz force will lead to acceleration perpendicular to the direction in which the particle is moving such that the particle is forced to gyrate around the magnetic field lines leading to a helical motion. According to electrodynamics, the acceleration of a charged particle will lead to EM emission. For synchrotron radiation this will lead to continuous radiation losses such that the angle-averaged electromagnetic power emitted by a single relativistic particle moving in a magnetic field is (Rybicki & Lightman 1979; Ghisellini 2013)

$$\langle P_{\text{syn}} \rangle = - \left( \frac{dE}{dt} \right)_{\text{syn}} = \frac{4}{3} \sigma_T c U_B \gamma^2 \beta^2, \quad (1.16)$$

where  $E = \gamma mc^2$  is the particle energy, and  $U_B = B^2/8\pi$  is the magnetic field energy density. The emitted power can be used to derive a corresponding synchrotron loss timescale

$$t_{\text{syn}} = \frac{E}{-(dE/dt)_{\text{syn}}} = \frac{6\pi m^2 c^3}{\sigma_T B^2 E \beta^2}, \quad (1.17)$$

which is a measure of how efficient the particle can emit its energy through this process. We can derive similar loss timescales for the other radiative processes to determine which will be dominant under certain conditions or in different locations of the jet.

Considering that the relativistic particle is gyrating around the magnetic field lines, one can show that there is a typical frequency associated to the synchrotron emission. The single-particle spectrum spreads over a range of frequencies, but it will emit most of its power at this characteristic frequency given by:

$$\nu_c = \frac{3\gamma^2 qB \sin \alpha}{4\pi mc}, \quad (1.18)$$

where  $\alpha$  is the pitch angle defined as the angle between the velocity of the particle and the magnetic field. In reality, the particles in astrophysical systems do not have one single energy, but they follow a particle distribution that evolves as a function of energy. As discussed in Section 1.3.2, there are different acceleration mechanisms but they all accelerate particles into a non-thermal powerlaw which was also seen for CRs in Section 1.1.1. A powerlaw distribution is described by

$$N(\gamma) = A\gamma^{-p}; \quad \gamma_{\min} < \gamma < \gamma_{\max}, \quad (1.19)$$

where  $p$  is the powerlaw index and  $A$  is a normalization constant. Typical values of  $p$  in astrophysical systems range from 2 – 2.5. Alternatively, one can also express the particle distribution in terms of the particle energy  $E$  such that

$$N(E) = N(\gamma) \frac{dE}{d\gamma} = A'E^{-p}; \quad E_{\min} < E < E_{\max}, \quad (1.20)$$

where  $A'$  is a different normalization constant. In the case of a powerlaw, the specific emissivity  $j(\nu)$  at a given frequency  $\nu$  (power emitted per unit frequency, solid angle and volume), in an interval  $d\nu$ , is the result of the isotropic emission by electrons with the appropriate Lorentz factor  $\gamma$ , within an interval  $d\gamma$ :

$$j(\nu)d\nu = \frac{1}{4\pi} P_{\text{Syn}}(\gamma) N(\gamma) d\gamma = \frac{A}{4\pi} P_{\text{Syn}} \gamma^{-p} d\gamma. \quad (1.21)$$

Using equation 1.16, the specific emissivity is then proven to be proportional to (Ghisellini 2013):

$$j(\nu)d\nu \propto AB^2 \gamma^2 \gamma^{-p} \frac{d\gamma}{d\nu} \propto AB^{(p+1)/2} \nu^{-(p-1)/2}. \quad (1.22)$$

The emissivity is a useful quantity because it can directly be converted to a flux

$$F(\nu) = 4\pi j(\nu) \frac{V}{4\pi d_L^2}, \quad (1.23)$$

where  $V$  is the emitting volume and  $d_L$  is luminosity distance of the astrophysical source that we are looking at. The key feature of equation 1.22 is that a powerlaw distribution of particles produces a powerlaw spectrum of synchrotron emission where the spectral indices are related by  $\alpha \equiv \frac{p-1}{2}$ . Hence, the spectral index is a very powerful diagnostic when looking at observations allowing one to model the synchrotron spectrum, and infer information about the underlying particle distribution.

Critically, the derived relation above only holds true if the source of the synchrotron emission is optically thin. In order to quantify how optically thin the jet is, we can use the optical depth. The optical depth is defined as  $\tau(\nu) = \alpha(\nu)l$  for a homogeneous sources, where  $\alpha(\nu)$  is the absorption coefficient, and  $l$  the mean travelled path length. The optical depth is a frequency dependent quantity and being optically thin is written as  $\tau_\nu \ll 1$ . In an optically thin part of the jet, the produced radiation can escape the source without being absorbed. In contrast, if the source is optically thick, the shape of the observed spectrum changes as we enter the self-absorbed regime when  $\tau_\nu \gg 1$ . In that case, the intensity (power emitted per unit area) of the radiation is given by

$$I(\nu) \propto \nu^{5/2} B^{-1/2}, \quad (1.24)$$

and the transition between these two regimes will occur when  $\tau_\nu = 1$  at the SSA frequency  $\nu_{\text{SSA}}$ . As a result, the synchrotron spectrum emitted by a homogeneous source with a given magnetic field strength is a broken powerlaw. At low frequencies ( $\nu < \nu_{\text{SSA}}$ ), the source is optically thick with  $F(\nu) \propto \nu^{5/2}$ , and at higher frequencies ( $\nu > \nu_{\text{SSA}}$ ) the source is optically thin with  $F(\nu) \propto \nu^{-\alpha}$  with the slope determined by the underlying particle distribution. The resulting spectrum is shown in Fig. 1.13 where we see a clear spectral break between the optically thick and optically thin regime of the emission.

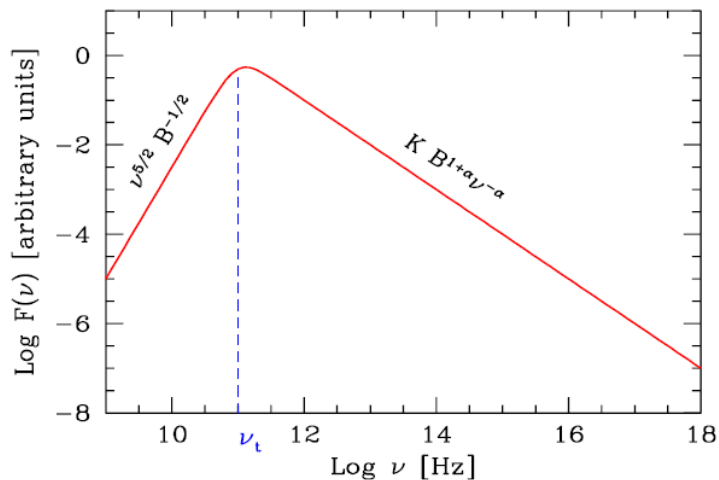


FIG. 1.13 – Emitted synchrotron spectrum by a powerlaw distribution of particles that transitions from the optically thick to optically thin regime at  $\nu = \nu_{\text{SSA}}$  ( $\nu_t = \nu_{\text{SSA}}$  in the figure). Figure from Ghisellini (2013).

The frequency where the break occurs, the SSA frequency, can be estimated using the radiative transfer equation. In the case of a one-dimensional slab of thickness  $z$ , the equation

for the intensity can be written as

$$I_\nu = zj(\nu) \frac{1 - e^{1-\tau(\nu)}}{\tau(\nu)}, \quad (1.25)$$

where  $j(\nu)$  is the emissivity defined in equation 1.22. In the optically thick regime, the radiative transfer equation simplifies to

$$I(\nu) = \frac{j(\nu)}{\alpha(\nu)}, \quad (1.26)$$

such that equations 1.22 and 1.24 give us an absorption coefficient

$$\alpha(\nu) = \frac{j(\nu)}{I(\nu)} \propto AB^{(p+2)/2} \nu^{-(p+4)/2}. \quad (1.27)$$

By definition,  $\nu_{SSA}$  occurs at the transition from the self-absorbed to optically thin regime which allows us to find the scaling of the SSA frequency with the other plasma parameters such that

$$\tau(\nu_{SSA}) = z\alpha(\nu_{SSA}) = 1 \rightarrow \nu_{SSA} \propto \left(zAB^{(p+2)/2}\right)^{2/(p+4)}. \quad (1.28)$$

Crucially, the only geometrical assumption that we made until now is that we are considering a one-dimensional slab. In reality an astrophysical system is never one-dimensional but equation 1.28 has a remarkable universal character. For instance, in the case of a relativistic jet, one can think of  $z$  as the distance from the BH when moving along the jet.

Obviously, a jet is not a one-dimensional object so let us be more specific about the geometry of a relativistic jet. In the case of a Blandford-Königl jet (Blandford et al. 1979), the jet is assumed to have a constant conical shape in combination with the conservation of magnetic energy and the number of particles implying  $B \propto z^{-1}$  and  $A \propto z^{-2}$ . On top of that, we assume that particles are constantly being re-accelerated along the jet axis such that for every  $z$  we have a powerlaw particle distribution with spectral index  $p = 2$ . It can be shown that for such a geometry, the SSA frequency in equation 1.28 scales as

$$\nu_{SSA} \propto \left(zAB^{(p+2)/2}\right)^{2/(p+4)} \propto \left(z^{1-2-((p+2)/2)}\right)^{2/(p+4)} \propto (z^{-3})^{1/3} \propto z^{-1}, \quad (1.29)$$

which means that the synchrotron radiation becomes optically thin at lower frequencies as we move away from the BH.

In order to derive the spectral shape of such a conical jet, one can think of it as many cylinders stacked on top of each other, each having a radius  $r = \tan(\theta)z$ , where  $\theta$  is the opening angle of the jet. Every cylindrical slice will have a volume  $V = \pi r^2 \Delta z$  such that  $V \propto z^3$ . Since the SSA process will cause each cylinder to emit mostly at its own frequency  $\nu_{SSA}(z)$ , we can simplify the calculation by assuming that each region of the jet emits only at the self-absorption frequency. Ultimately, combining the assumptions of  $p = 2$ ,  $B \propto z^{-1}$  and  $A \propto z^{-2}$ , together with equations 1.24 and 1.27, and the scaling relations for  $V$  and  $\nu_{SSA}$ , one finds

$$F(\nu) \propto \nu^{5/2} B^{-1/2} AB^2 \nu^{-3} z^3 \propto \nu^{5/2-1/2+2+2-3-3} = \nu^0. \quad (1.30)$$

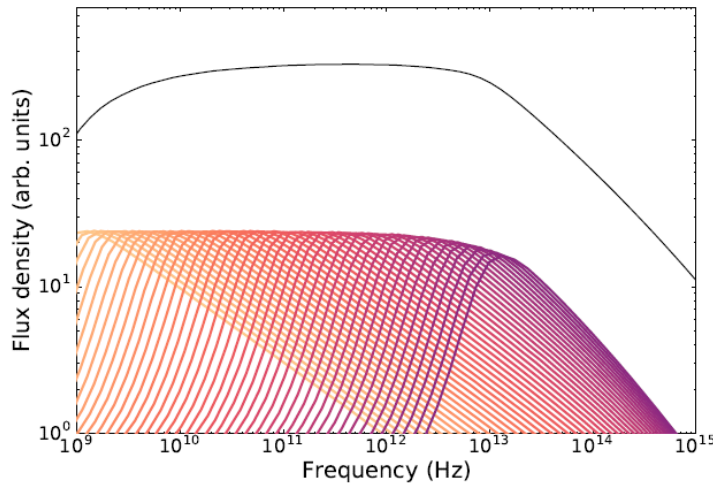


FIG. 1.14 – Flat radio spectrum from an isothermal jet. The colored lines indicate the spectrum from different cylindrical regions of the jet, with lighter colors indicating larger distances from the BH. The black line is the sum of all jet segments which results in the flat spectrum. Image credit: M. Lucchini.

The resulting spectrum is flat, showing no dependency on frequency whatsoever as illustrated by Fig. 1.14. The straight-forward argument presented above shows that the conditions required to obtain a flat synchrotron spectrum are very specific. Therefore, the detection of such a spectrum is considered to be solid evidence for a steady conical jet being launched by an accreting system ([van den Eijnden et al. 2018](#)).

### 1.3.4 Inverse Compton Scattering

Besides being accelerated by the magnetic field in the jet, charged particles can collide with photons in a process called *Compton scattering*. When the energy of the particle is lower than that of the photon, i.e.  $h\nu \gg mc^2$ , there is a transfer of energy from the photon to the particle. The opposite process is called *Inverse Compton Scattering* where the particle has an energy greater than that of the photon, i.e.  $h\nu \ll mc^2$ , and there is a transfer of energy to the particle as well. The discussion below will focus on the IC process for electrons but this applies to protons and any other charged particle. Before discussing the details of the IC interaction, it is important to note that the IC process can happen in two different regimes. Depending on the energy of the incoming photon, as observed in the rest frame of the electron, the cross section of the process will transition from a classical regime to one where quantum mechanical effects become important. For low photon energies,  $h\nu \ll m_e c^2$ , the

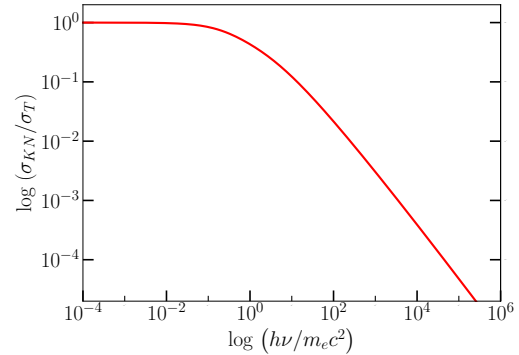


FIG. 1.15 – Ratio of the quantum mechanical Klein-Nishina to classical Thomson cross section. Figure from [Ghisellini \(2013\)](#).

scattering of radiation reduces to the classical case of Thomson scattering. As the incoming photon has a larger energy, quantum mechanical effects have to be taken into account and the *Klein-Nishina* (KN) formula from quantum electrodynamics is used (Klein & Nishina 1929). In Fig. 1.15 a comparison of the KN cross section and the classical Thomson cross section is shown. It is clear that using the classical version will significantly overestimate the interaction rate at higher photon energies.



FIG. 1.16 – The geometry of Inverse Compton scattering as observed in the observer frame on the left. The geometry as observed in the co-moving frame of the electron can be seen on the right. Figure from Rybicki & Lightman (1979).

For a mathematical description of IC scattering, the geometry in Fig. 1.16 can be used which shows the situation in both the lab frame and the rest frame of the scattered electron. The simplest way to do the calculations is by defining quantities in the frame of reference  $K'$ , co-moving with the electron. After doing the calculations, we can transform all quantities back to the observer frame  $K$  using a Lorentz transformation like the one shown in equation 1.10. Additionally, it is useful to express photon energies in units of the electron rest mass energy:  $x \equiv h\nu/m_e c^2$ . An incoming photon with energy  $x$  and an electron moving with velocity  $v$  in the lab frame, can be transformed to frame  $K'$  such that it has a photon energy

$$x' = x\gamma(1 - \beta \cos(\phi)), \quad (1.31)$$

where  $\phi$  is the angle between the electron velocity and the direction of the incoming photon as measured in frame  $K$ . If  $x' \ll 1$ , the scattering is elastic meaning that the photon will have the same energy before and after the scattering, i.e.  $x' = x'_1$ . The photon is scattered at an angle  $\phi'_1$  and converting back to frame  $K$  will give a final photon energy of

$$x_1 = x'_1\gamma(1 + \beta \cos(\phi'_1)), \quad (1.32)$$

where  $\phi'_1$  is the photon scattering angle with respect to the electron velocity in frame  $K'$ . After converting all the energies and angles back to the lab frame using equation 1.11, the resulting energy gain of the photon can be expressed as (Rybicki & Lightman 1979)

$$x_1 = x \frac{1 - \beta \cos(\phi)}{1 - \beta \cos(\phi_1)}. \quad (1.33)$$

Equation 1.33 is a general result for a single scattering event, but for astrophysical sources we do not see a single event. In order to quantify this result, let us assume an isotropic and monochromatic seed photon distribution meaning that the photons arrive in equal numbers

from all directions and they all have the same energy. Integrating over all possible incoming photon angles will lead to an average energy after scattering of  $\langle x_1 \rangle = (1 + \frac{1}{3}\beta^2) \gamma^2 x \approx \frac{4}{3}\gamma^2 x$  which scales with the electron Lorentz factor (Rybicki & Lightman 1979; Ghisellini 2013). Similar to synchrotron emission, there is a typical frequency associated to IC scattering in which the final frequency is on average a factor  $\gamma^2$  larger than the initial frequency. Therefore, in a typical double-humped SED, like the one shown in Fig. 1.10, one can use the distance between the first and the second peak as a rough estimate for the average Lorentz factor of the underlying particle distribution.

When a relativistic electron of energy  $E$  scatters off of a photon field with energy density  $U_{\text{phot}}$ , it will lose part of its energy due to IC scattering. The power radiated away is proportional to the energy of the electron and the energy density of the photon field, and can be remembered by using

$$\begin{aligned} P_{\text{IC}}(\gamma) &= -\left(\frac{dE}{dt}\right)_{\text{IC}} = \left(\text{Probability of scattering}\right) \times \left(\text{Average energy gain per scattering}\right) \\ &= \left(\sigma_t c \frac{U_{\text{phot}}}{\langle h\nu \rangle}\right) \left(\frac{4}{3}\langle h\nu \rangle \gamma^2\right) = \frac{4}{3}\sigma_t c U_{\text{phot}} \gamma^2 \beta^2. \end{aligned} \quad (1.34)$$

Compare this to equation 1.16 for the synchrotron power where the magnetic field energy density  $U_B$  is effectively replaced by photon field energy density  $U_{\text{phot}}$ . If the target photons are those produced by synchrotron radiation, the process is known as the *Synchrotron Self-Compton* (SSC) process and the emitted power is given by

$$P_{\text{SSC}} = P_{\text{Syn}} \frac{U_{\text{phot}}}{U_B}. \quad (1.35)$$

SSC emission is something we saw earlier when looking at a typical blazar SED in Fig. 1.10, and plays a crucial role in many BH jets. Particularly, this process is thought to be the dominant component that produces the high-energy bump in blazar SEDs. Again, a typical timescale associated to IC emission can be derived to estimate the time needed for an electron to lose a significant fraction of its energy through IC scattering:

$$t_{\text{IC}} = \frac{E}{-(dE/dt)_{\text{IC}}} = \frac{3m_e^2 c^3}{4\sigma_T U_{\text{phot}} E \beta^2} = t_{\text{syn}} \frac{U_B}{U_{\text{phot}}}. \quad (1.36)$$

Note that equations 1.34 - 1.36 are only valid in the Thomson regime. One needs to replace the Thomson cross section with the more general KN cross section for it be applicable when photons have a larger energy.

The fact that the energy gain of the photon is closely related to the Lorentz factor of the electrons, allows us to calculate the IC emission from a population of particles exactly like in the synchrotron case. Again, we consider a powerlaw distribution of particles as given by equation 1.19. Assuming that the seed photons are monochromatic, and that the Compton emissivity  $j(\nu)$  is given by equation 1.21 with  $P_{\text{Syn}}$  replaced by  $P_{\text{IC}}$ , yields an emissivity

$$j(\nu) = \frac{1}{4\pi} P_{\text{IC}}(\gamma) N(\gamma) d\gamma d\nu \propto \sigma_t A \frac{U_{\text{rad}}}{\nu_0} \left(\frac{\nu}{\nu_0}\right)^{-\alpha}, \quad (1.37)$$

where  $\nu_0$  is the frequency of the incoming photon, and  $\alpha = \frac{p-1}{2}$  similar to synchrotron emission. Once more, information about the underlying non-thermal particle distribution is encoded in the radiation emitted by the system.

## Thermal Comptonization

The expression for the specific emissivity only holds if the photons are involved in a single scattering event before they escape the system. In this case, the photons carry information about the electron distribution through the spectral index. The photons will experience a single scattering event only if Thomson optical depth is low, i.e.  $\tau = \sigma_T n_e R \ll 1$ , where  $n_e$  is the electron number density and  $R$  is the radius of the region in which the scattering occurs. However, photons can scatter multiple times if the Thomson optical depth is not small. In the very extreme case of  $\tau \rightarrow \infty$ , the photons will not be able to escape the emitting region entirely. Having multiple scattering events will significantly affect the spectral shape and the total energy of the photon distribution. In order to quantify this, let us define the  $y_{\text{IC}}$  parameter.  $y_{\text{IC}}$  is defined as the fractional energy gain for each scattering ( $\eta$ ), multiplied by the average number of scatterings that a photon experiences before escaping ( $N$ ). This parameter can be used to determine whether a photon will significantly change its energy when traversing the medium. If  $y_{\text{IC}} > 1$ , the Comptonization process is important and will alter the photon energy and spectrum significantly.

One such process where the effect of multiple scattering events has to be taken into account is thermal Comptonization. Thermal Comptonization is defined as the process of having multiple scatterings of seed photons by a thermal distribution of electrons. When considering relativistic electrons, such thermal distribution of electrons can be described by a relativistic Maxwellian of the form

$$N(\gamma) \propto \gamma^2 e^{-\gamma/\Theta_e}, \quad (1.38)$$

with  $\Theta_e \equiv \frac{k_B T_e}{m_e c^2}$  the dimensionless electron temperature where  $k_B$  is the Boltzmann constant, and  $T_e$  is the temperature of the thermal distribution in  $K$ . As the photons undergo many scatterings, they effectively lose all the information about the original photon and electron distributions. The average number of scatterings is  $\tau$  if the medium is optically thin or  $\tau^2$  if it is optically thick. Given a thermal distribution of electrons with temperature  $\Theta_e$  (or alternatively, with an average Lorenz factor  $\langle \gamma \rangle$  if the particle distribution is non-thermal), the fractional energy gain of the photons during each scattering is given by (Ghisellini 2013)

$$\frac{x_1 - x_0}{x_0} = \begin{cases} 16\Theta_e^2 & , \text{if } \Theta \geq 1 \text{ (relativistic electrons)} \\ 4\Theta_e - x & , \text{if } \Theta \leq 1 \text{ (non-relativistic electrons)} \end{cases} \quad (1.39)$$

The term  $-x$  accounts for the possibility of down-scattering, in which the photon loses some energy to an electron. Therefore, the general expression for  $y_{\text{IC}}$ , valid for all electron temperatures, is given by:

$$y_{\text{IC}} = (16\Theta_e^2 + 4\Theta_e - x) \times \text{Max} [\tau, \tau^2]. \quad (1.40)$$

Based on the value of  $y_{\text{IC}}$  we can distinguish between three different regimes for thermal Comptonization:

1. **Single scattering regime ( $y_{\text{IC}} \ll 1$ )**: This regime corresponds to a low optical depth in which we have only a single or maybe a few scattering event(s). In the spectrum we see the separated peaks of each scatter and no superposition or overlap between the peaks.

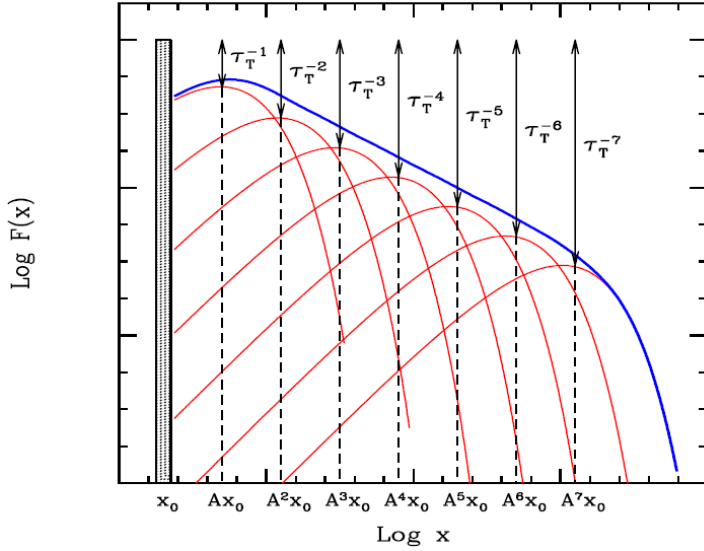


FIG. 1.17 – Thermal Comptonization spectrum in the saturated regime, in which the total spectrum (blue line) is the sum of multiple scattering orders (red lines). The slope of the spectrum is set by the energy gain and fraction of escaping photons. The cut-off at higher energies reflects the maximum attainable photon energy which is determined by the electron energy. Figure from Ghisellini (2013).

2. **Unsaturated regime ( $y_{\text{IC}} \lesssim 1$ ):** If  $\tau \approx 1$  and  $\Theta_e \leq 1$  the resulting spectrum, generated by the superposition of multiple scattering orders, is a powerlaw. The energy that the photons receive for each scattering (neglecting down-scattering) is:

$$C \equiv \frac{x_1}{x_0} = 16\Theta_e^2 + 4\Theta_e^2 + 1 \approx \frac{y}{\tau}. \quad (1.41)$$

Subsequently, a fraction  $\tau$  of photons from the previous scattering will undergo another interaction thereby gaining another fractional energy  $C$ . Summing all the scattering orders will lead to spectrum  $F(x) \propto x^{-\alpha}$  where the spectral index  $\alpha_{\text{IC}}$  of thermal Comptonization is defined to be:

$$\alpha_{\text{IC}} = -\frac{\log(\tau)}{\log(C)} \approx \frac{\log(\tau)}{\log(y) - \log(\tau)}, \quad (1.42)$$

where we used equation 1.41. The resulting spectrum is visualised in Fig. 1.17.

3. **Saturated regime ( $y_{\text{IC}} \gg 1$ ):** In this case the interactions of photons with electrons is so numerous that the system is driven towards equilibrium. The photons will interact so frequently that the photon distribution will have the same temperature as the electrons. The resulting spectrum has a Wien shape

$$I(x) \propto x^3 e^{-x/\Theta_e}, \quad (1.43)$$

which is similar to a black body spectrum, except that it is steeper at low frequencies.

### External Compton Scattering in Blazars

As discussed in Section 1.2.3, the effects of relativistic beaming are highly important when studying blazars. These effects become apparent when looking at blazar SEDs (see Fig. 1.10), especially for the IC bump in the spectrum. In the case of AGN, the low energy bump is practically always produced by synchrotron emission in the jet. For the second bump at higher energies, we need to consider IC emission but any photon field can act as the seed distribution for this process. SSC emission is often invoked since the synchrotron radiation is produced in the same region as the IC emission. However, the environments surrounding AGN host an accretion disk (see Section 1.3.1), a BLR and a DT which can all produce photon fields external to the jet. The high velocity of the jet relative to these photon fields will lead to relativistic boosting that enhances the energy density in the co-moving frame of the jet. This relativistic beaming makes External Compton (EC) scattering a crucial component in studying blazar emission (Finke 2016).

First of all, let us consider the radiation field produced by the accretion disk as seen in the co-moving frame of the jet. If we assume that all disk luminosity is emitted at the inner edge of the disk at radius  $R_{\text{in}}$  then

$$U_D(z) = \frac{\delta_D^2(z)L_D}{4\pi D(z, R_{\text{in}})^2}, \quad (1.44)$$

where  $L_D$  is the emitted disk luminosity,  $\delta_D$  is the (de-)boosting factor for the disk photons as seen in the co-moving frame of the jet, and  $D(z, R_{\text{in}})$  is the distance between the jet segment and the innermost radius of the disk.

For the BLR and DT, we have to account for the fact that they can absorb radiation emitted by the accretion disk, and will re-emit this as black body radiation with a characteristic temperature. In this thesis, we adopt the prescription by Ghisellini & Tavecchio (2009) in which we define all quantities in the co-moving frame of the jet as denoted by a prime. The radiation energy densities are heavily dependent on the distance of the emitting region with respect to the locations of the BLR and DT. It also depends on the temperature of the BLR/DT which are assumed to be  $T'_{\text{BLR}} = 13.6 \cdot \delta(z)$  eV equal to the (boosted) Lyman- $\alpha$  frequency, and  $T'_{\text{DT}} = 370 \cdot \delta(z)$  K with  $\delta(z)$  the Doppler factor in the emitting region of the jet at height  $z$ . In the case where the emitting region is within the BLR/DT, the radiation field energy densities are given by

$$U'_{\text{BLR}}(z) = \frac{17\delta(z)^2}{12} \frac{f_{\text{BLR}}L_D}{4\pi z_{\text{BLR}}^2} \quad z \leq z_{\text{BLR}}, \quad (1.45)$$

$$U'_{\text{DT}}(z) = \frac{17\delta(z)^2}{12} \frac{f_{\text{DT}}L_D}{4\pi z_{\text{DT}}^2} \quad z \leq z_{\text{DT}}, \quad (1.46)$$

where  $z_{\text{BLR}} = 10^{17} L_{D,45}^{1/2}$  cm,  $z_{\text{DT}} = 2.5 \times 10^{18} L_{D,45}^{1/2}$  cm,  $L_{D,45}$  is the disk luminosity in units of  $10^{45}$  ergs s $^{-1}$ , and  $f_{\text{BLR/DT}}$  is the reprocessed fraction of incoming disk photons by the BLR/DT. Note that these photon fields also contribute at large distance beyond the BLR/DT, i.e.  $z \gg z_{\text{BLR/DT}}$ , but the radiation will be strongly deboosted such that their contribution is subdominant. Nevertheless, these effects are also included and the expressions for the co-moving photon energy density can be found in Ghisellini & Tavecchio (2009).

The photon energy densities in equations 1.44, 1.45 and 1.46 add three additional photon fields that need be taken into account for the IC process. From these relations we can see that in the jet frame, the electrons will “see” the radiation fields boosted by  $\delta^2$ . In the case of blazars, we see Doppler factors of  $\delta \approx 20 - 30$  which means a boosting on the order of  $10^2 - 10^3$ . Therefore, the external photons fields can become more important than the synchrotron seed field and dominate the high-energy bump in the SED.

## 1.4 Hadronic Interactions

Section 1.1 discussed the apparent correlation between the origin of cosmic rays and the production mechanism(s) of  $\gamma$ -rays and neutrinos in the Universe. The processes responsible for this correlation are thought to be hadronic processes in astrophysical object with a larger power budget like BH jets. The need to explain certain astrophysical observations using hadronic processes was already recognised in the early stages of  $\gamma$ -ray astronomy and high-energy CR observations. Morrison (1958) and Ginzburg & Syrovatskii (1964) were the first to discuss the connection between  $\gamma$ -ray observations and the CR spectrum. Decades later, it is understood that hadronic interactions are absolutely necessary to explain  $\gamma$ -ray spectra of AGN (e.g. Böttcher et al. 2013) and high-energy astrophysical neutrinos (e.g. IceCube Collaboration 2018a). Moreover, hadronic interactions are also responsible for features in the CR spectrum like the Greisen-Zatsepin-Kuzmin (GZK) cutoff due to the interaction of CRs with the Cosmic Microwave Background (CMB) (Penzias & Wilson 1965; Greisen 1966; Zatsepin & Kuzmin 1966).

In the following, the two main channels of hadronic interactions that occur when accelerated protons interact with the ambient medium are described. The first process is referred to as proton-proton (pp) interactions, and the second process is named proton-photon ( $p\gamma$ ) interactions. We focus only on the accelerated protons and neglect heavier ions like helium, carbon, and iron. A description of hadronic interactions of heavier nuclei can be found in the review by Kotera & Olinto (2011). This description will be brief, and a more complete description can be found in Kantzas et al. (2020) and Kantzas et al. (2023a).

### 1.4.1 Proton-Proton Collisions

When accelerated protons carry enough kinetic energy to surpass the threshold for neutral pion production, they can interact with protons from the ambient medium in an inelastic pp interaction. The most dominant interaction channel will lead to the formation of charged and neutral pions through

$$p + p \rightarrow p + p + \alpha_{pp}\pi^0 + \beta_{pp}(\pi^+ + \pi^-), \quad (1.47)$$

where  $\alpha_{pp}$  and  $\beta_{pp}$  are the multiplicities of the related products. The multiplicity depends on the energy of the colliding protons, and its exact numerical value is derived from Monte Carlo simulations. In this work we use the semi-analytical expressions by Kelner et al. (2006). In reality there are other branching ratios possible in which charge exchange leads to neutron production for example, but these will not be considered in this thesis. Note that the production of a neutron require the production of a positively charged pion  $\pi^+$  to ensure charge conservation.

Subsequently, the charged pions decay into muons that further decay to secondary electrons, positrons, neutrinos and anti-neutrinos through the following processes

$$\begin{aligned}\pi^+ &\rightarrow \mu^+ + \nu_\mu \implies \mu^+ \rightarrow e^+ + \nu_e + \bar{\nu}_\mu, \\ \pi^- &\rightarrow \mu^- + \bar{\nu}_\mu \implies \mu^- \rightarrow e^- + \bar{\nu}_e + \nu_\mu,\end{aligned}\quad (1.48)$$

and the neutral pions decay into two  $\gamma$ -ray photons

$$\pi^0 \rightarrow \gamma + \gamma. \quad (1.49)$$

Note that all charged particles formed in these interactions will be emitting synchrotron radiation once they are produced, but since the electrons and positrons are the only stable decay product, they will emit the most radiation. We will refer to these positrons and electrons as secondaries in the rest of this thesis.

To estimate the contribution of pp interactions, the interaction cross section has to be determined. The fact that protons are hadrons made up of quarks, requiring the use of Quantum Chromo Dynamics (QCD), makes this a daunting task from a analytical point of view. Instead, one relies on the use of approximations and phenomenological models (Ulrich et al. 2011). Throughout the years, different approaches on the calculation of the cross section and the distributions of the products of pp-collisions have been developed (Dermer 1986; Berezinsky 1991; Mannheim 1993; Mannheim & Schlickeiser 1994; Aharonian 2000). The most up-to-date approximation for the cross section is (Kafexhiu et al. 2014)

$$\sigma_{\text{pp}}(T_p) = \left[ 30.7 - 0.96 \log\left(\frac{T_p}{T_{\text{thr}}}\right) + 0.18 \log^2\left(\frac{T_p}{T_{\text{thr}}}\right) \right] \times \left[ 1 - \left(\frac{T_{\text{thr}}}{T_p}\right)^{1.9} \right]^3 \text{ mb}, \quad (1.50)$$

where  $T_p$  is the proton kinetic energy in the lab frame,  $T_{\text{thr}} = 2 m_\pi + \frac{m_\pi^2}{2 m_p} \simeq 0.2797 \text{ GeV}$  is the threshold energy for this interaction, and  $1 \text{ mb} \equiv 10^{-27} \text{ cm}^2$  is the conventional unit to measure cross sections.

The severe complexity of these interactions and analytical developments, led to Monte Carlo algorithms, such as *Pythia* (Sjöstrand et al. 2006), *SIBYLL* (Fletcher et al. 1994), and *QGSJET* (Kalmykov et al. 1997; Ostapchenko 2011). These algorithms are widely used not only to reconstruct the initial conditions of CRs and  $\gamma$ -rays once they reach Earth's atmosphere, but also to examine the hadronic processes in astrophysical sources. At the moment, Monte Carlo simulations are the most accurate tools we have, but this enhanced precision comes at the cost of more computational time, slowing down the comparison to observational data. Kelner et al. (2006) were the first to parameterize the results of such simulations to reproduce accurate distributions of the products that can be calculated on reasonable timescales. They present derivations for the distributions of  $\gamma$ -rays, electrons, muon neutrinos, and muon anti-neutrinos resulting from the decay of charged pions and muons. In Fig. 1.18a, the distributions of the products from pp collisions as derived in Kelner et al. (2006) are plotted. Note that the produced distributions show a powerlaw with the same index as that of the initial accelerated protons. The typical distribution of the  $\gamma$ -rays is the so-called pion bump, and is a natural result of the acceleration of protons in the observed source.

Lastly, there is a typical timescale associated to the energy losses of protons through pp interactions similar to what was seen for the emission processes discussed in Sections 1.3.3 and

1.3.4. For this, we use the mean free path of the proton such that the timescale is given by:

$$t_{\text{pp}} = \frac{1}{K_{\text{pp}} \sigma_{\text{pp}} n_H c}, \quad (1.51)$$

where  $K_{\text{pp}}$  corresponds to the average number of secondary particles produced and  $n_H$  is the number density of target protons. The timescale is almost independent of the proton energy as the pp cross section has a relatively small dependence on the proton energy (Workman et al. 2022). In fact, increasing the proton energy by 7 orders of magnitude will only double the pp cross section.

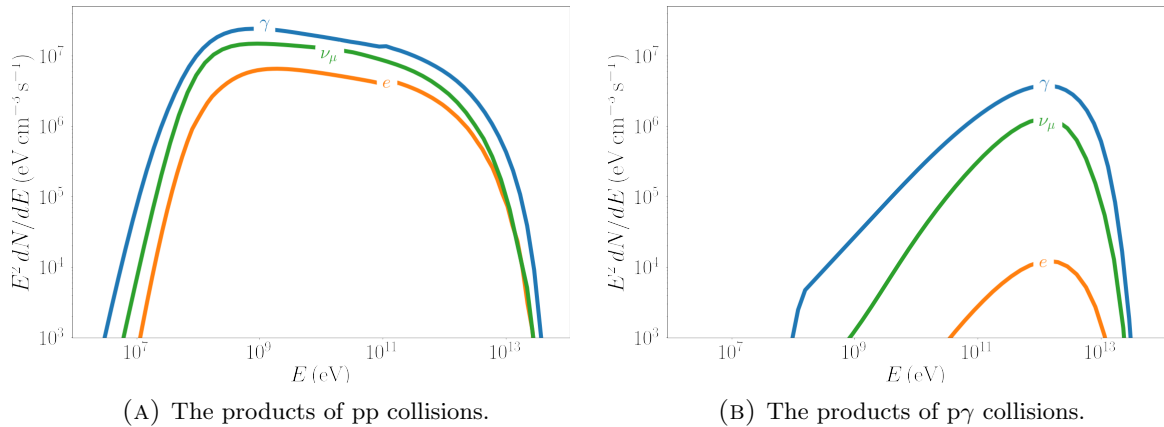


FIG. 1.18 – The particle distributions for the products of pp/p $\gamma$  collisions between accelerated protons and cold protons/photons. The protons follow a powerlaw with a spectral index  $p = 2.2$  that ranges from 1 GeV to 60 TeV. The distributions of  $\gamma$ -rays ( $\gamma$ ), muon neutrinos ( $\nu_\mu$ ) and secondary electrons ( $e$ ) cut off at the maximum energy of the accelerated protons. Image credit: D. Kantzas.

#### 1.4.2 Proton-Photon Collisions

While IC scattering is the main channel for interactions between electrons and photons, the inelastic collisions between protons and photons will dominate to particle cascades similar to the pp interactions. Nonetheless, Protons can undergo IC scattering, but the cross section for that process is simply lower compared to other interactions. The p $\gamma$  interactions also allow for another channel in which electron-positron pairs are directly produced. This process is known as the Bethe-Heitler process (Bethe & Heitler 1934), and only occurs if the available energy is larger than is the combined rest mass of an electron and a positron, approximately 1 MeV. The produced pairs carry away only a small fraction of the incident proton energy which is why it is often neglected in the literature (e.g. Petropoulou et al. 2015). In this thesis, we will consider its effect but we will not expand on the Bethe-Heitler process in the rest of this Section.

The main channel of p $\gamma$  interactions is known as the *photomeson* interaction. This interaction of an accelerated proton and a target photon field is very similar to the pp interactions and it initiates particle cascades in two main channels. The first one is



and leads to a proton together with pions, whereas the second one



will produce a neutron together with pions. Here  $\alpha_{p\gamma}$  and  $\beta_{p\gamma}$  are again the multiplicities but they are different compared to the pp interactions. For  $p\gamma$  interactions to occur, the energy of the accelerated proton must exceed the threshold of

$$E_{p, \text{thr}} \simeq 70 \left( \frac{\epsilon_\gamma}{1 \text{ eV}} \right)^{-1} \text{PeV}, \quad (1.54)$$

where  $\epsilon_\gamma$  is the energy of the target photon, such that the threshold energy is typically higher than for the pp interactions. After the initial  $p\gamma$  interaction, the produced pions further decay following equations 1.48 and 1.49.

Again, these interactions are challenging to describe theoretically and Monte Carlo simulations are used to calculate the resulting particle distributions. [Kelner & Aharonian \(2008\)](#) were the first to produce semi-analytical expressions to approximate the distributions of the secondary particles produced in  $p\gamma$  interactions. These relations are similar to those for pp interactions and Fig. 1.18b shows the produced distributions of  $\gamma$ -rays, muon neutrinos and electrons. Once more, there is a timescale associated to photomeson losses which is calculated by using the mean free path of the relativistic proton as given by

$$t_{p\gamma} = \frac{1}{K_{p\gamma}\sigma_{p\gamma}f_{\text{ph}}c}, \quad (1.55)$$

where  $f_{\text{ph}}$  is the distribution of the target photon field,  $\sigma_{p\gamma}$  is the cross section with a value on the order of 0.2 mb, and  $K_{p\gamma}$  is the multiplicity ([Mannheim & Schlickeiser 1994](#)). The full analytical expression for the cross section is shown in [Blumenthal \(1970\)](#) and [Chodorowski et al. \(1992\)](#).

#### 1.4.3 Synchrotron and IC Emission by Protons and Secondary Particles

As stated in Section 1.3.3, the synchrotron and IC processes apply to all charged particles moving through a magnetic field. Therefore, it is important to estimate how large the contribution of electrons will be relative to protons and the secondaries produced in hadronic interactions. This estimate can be made using the loss timescales for each energy loss process as defined in equations 1.17 and 1.36. For synchrotron and IC scattering, we see that the losses of protons are suppressed by a factor of  $(m_e/m_p)^3$  and  $(m_e/m_p)^4$ , respectively. Since the proton mass is significantly larger than the electrons mass, i.e.  $m_p \approx 1800m_e$ , this leads to a severe suppression of these processes for protons. In this thesis, we will take both proton synchrotron and IC into account but their contribution will be negligible most of the time. Moreover, the pp and  $p\gamma$  collision timescales in equations 1.51 and 1.55, are relatively energy independent such that they quickly become the dominant channel as the proton energy decreases.

Nevertheless, synchrotron losses for the secondaries produced in hadronic interactions could be important to consider. The secondary electrons and positrons do not suffer from this suppression factor and they are constantly being injected because of the relatively energy independent cross section for hadronic collisions. On top of that, the produced pions and muons can emit synchrotron radiation themselves in the presence of a strong magnetic field even though

they have extremely short lifetimes of 26 ns for charged pions, and 2.2  $\mu$ s for muons in their rest frame ([The Particle Data Group 2020](#)). The extremely short lifetimes mean that the synchrotron losses are only important when the following criteria are satisfied:

$$\left(\frac{B}{1 \text{ G}}\right) \left(\frac{E_p}{1 \text{ GeV}}\right) \ll \begin{cases} 7.8 \times 10^{11} & \text{for pions} \\ 5.6 \times 10^{10} & \text{for muons} \end{cases} \quad (1.56)$$

These conditions imply that the synchrotron emission from pions and muons is insignificant in most astrophysical sources. Hence, [Kelner et al. \(2006\)](#) and [Kelner & Aharonian \(2008\)](#) made the approximation that the charged pions and muons decay quick enough such that they do not lose any energy due to synchrotron radiation. It is very difficult to determine the exact value of the magnetic field and/or the maximum energy of the accelerated protons in astrophysical sites such that it is not (yet) clear whether this process plays an important role. Even in the extreme case where these processes have a shorter loss timescale than the lifetime, we need the spectra of the other produced particles to explain observations (e.g. [Rachen & Mészáros 1998](#); [Mücke et al. 2003](#); [Kashti & Waxman 2005](#); [Hümmer et al. 2010](#)).

## 1.5 Standard Modelling Techniques for Blazars

After having discussed the relativistic jets in blazars together with their spectral components, let us now focus on how to actually model such a system. The main method to obtain information about blazars, and BH jets in general, is to look at their SED. Different types of telescopes are used to observe the broadband radiation they emit ranging from radio to  $\gamma$ -ray frequencies. Subsequently, we can design a model of the system to try and explain the observations and extract physical information. Nowadays, state-of-the-art GRMHD simulations (see [The Event Horizon Telescope Collaboration 2019a](#) for a comparison of nine GRMHD codes) can give us insight into the fluid dynamics by studying the interplay between the accretion disk, the wind outflows and the jet. However, these simulations are not yet able to explain broadband emission coming from BH jets. Predictions of spectra and VLBI images are being developed (e.g. [Mościbrodzka et al. 2016](#); [Ball et al. 2018](#); [The Event Horizon Telescope Collaboration 2019b](#)) as well as MWL lightcurves ([Chatterjee et al. 2019](#)), but these are not yet able to self-consistently explain entire broadband SEDs. Therefore, semi-analytical jet models are needed to reproduce the MWL emission of these sources.

The technique of semi-analytic modelling means that various physical processes are treated using approximate, analytic techniques supported by computational methods. A specific example for BH jets is that in order to calculate the spectrum resulting from IC scattering one would have to integrate over the non-thermal electron distribution as well as the target photon distribution. One can write this integral down but only for relatively simple electron and photon distributions this integral can be solved analytically. Generally, in the astrophysical systems that are studied there is no analytic solution possible, and it requires the use of computational methods like numerical integration or interpolation.

### 1.5.1 Single-Zone Jet Models

Semi-analytical BH jet models are able to predict broadband SEDs, which can be fitted to SED data in order to find the model that matches the data best. Typically, blazar jet models

take a single-zone approach (e.g. [Tavecchio et al. 1998](#); [Böttcher et al. 2013](#); [Gao et al. 2017](#)). Such models only consider a single, homogeneous spherical region of the jet in which a non-thermal particle distribution is injected. These non-thermal particle distributions can be only electrons, for leptonic models, or one can include protons as well for a lepto-hadronic model. The confined nature of these models makes it computationally feasible to have detailed particle interactions and a time-dependent character, making this the dominant approach in the blazar SED modelling community.

A typical geometry of a single-zone jet model and its emission components is shown in Fig. 1.19. In such models, we assume the presence of a BH with a certain mass that is surrounded by an accretion disk. The BH produces a relativistic jet that expands with a fixed opening angle  $\phi$  starting from the BH. However, this jet is not modelled explicitly and one only considers the emission coming from a spherical ‘blob’ of plasma inside the jet which is traditionally referred to as the *blazar zone*. This blob moves away from the BH with a Lorentz factor  $\Gamma$  and has a homogeneous particle number density and magnetic field strength.

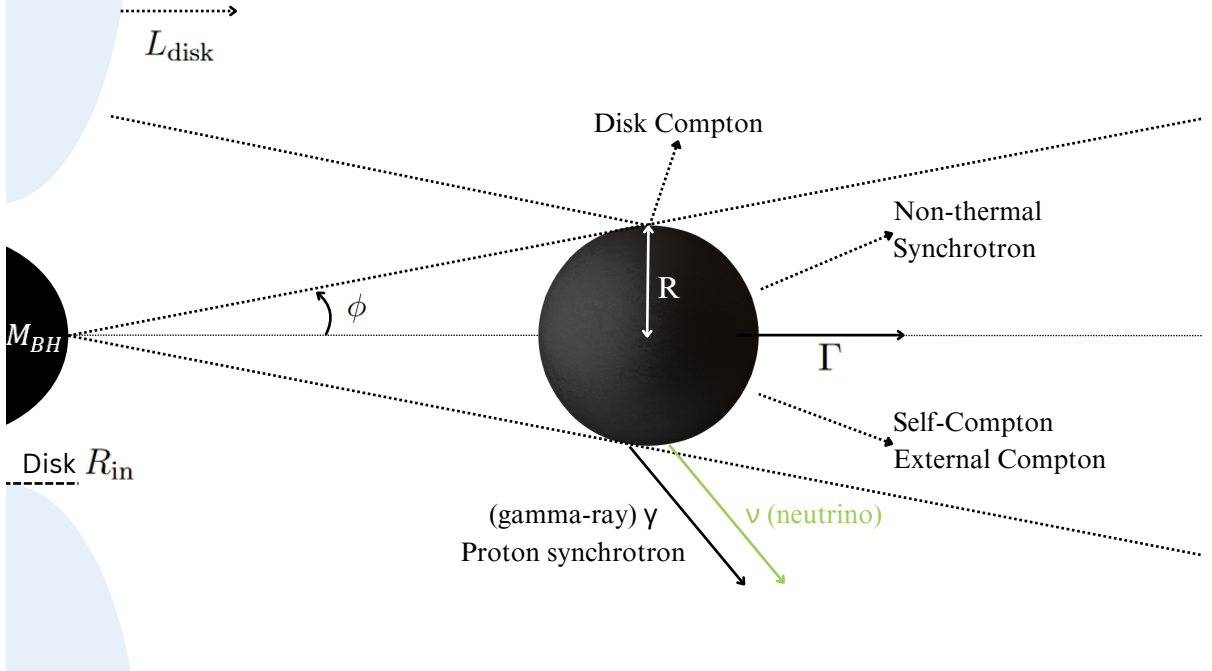


FIG. 1.19 – Geometry of a single-zone jet model.

One of the most important reasons to use single-zone models is that the variability timescales observed in AGN can reach down to the order of minutes. The source variability can be studied using X-ray or  $\gamma$ -ray timing, and these short timescales require relatively small production regions for the emission (e.g. [Tavecchio et al. 2010](#); [MAGIC Collaboration 2011](#)). The radius of the emission region can be related to the variability timescale  $t_v$  by using the fact that the blob size scales as:

$$R' \approx \delta c t_v (1 + z_{\text{red}})^{-1}, \quad (1.57)$$

in the co-moving frame of the jet. This relation calculates the distance that light can travel in

a time  $t_v$ , and then applies a relativistic and cosmological correction since blazars are extra-galactic. By assuming that the blob covers the full cross sectional area of the conical jet, the distance of the blob from the BH,  $z$ , is given by

$$z = \tan^{-1}(\phi)R' \approx \phi^{-1}R' \approx \Gamma R' \approx \frac{\delta^2 ct_v}{1 + z_{\text{red}}}. \quad (1.58)$$

Note that this relation assumes a very small opening angle of the jet, i.e.  $\phi \ll 1$ , such that  $\tan^{-1}(\phi) \approx \phi^{-1} \approx \Gamma \approx \delta$ . Using this relation and a variability timescale of a day ( $1 \text{ d} \approx 10^5 \text{ s}$ ), we see that the blob typically has a radius  $R' \approx 7.5 \times 10^{16}(1 + z_{\text{red}})^{-1}(\delta/25)(t_v/10^5 \text{ s}) \text{ cm}$ . Similarly, the distance to the BH will typically be  $z \approx 1.875 \times 10^{18}(1 + z_{\text{red}})^{-1}(\delta/25)^2(t_v/10^5 \text{ s}) \text{ cm}$ . These distances seem large, but they can also be expressed in terms of the gravitational radius,  $R_g$ , to see how they scale with respect to the BH mass. For a SMBH with a mass of  $10^8 M_\odot$ , the gravitational radius is given by  $R_g = GM_{\text{BH}}/c^2 \approx 1.5 \times 10^5(M_{\text{BH}}/M_\odot) \approx 1.5 \times 10^{13} \text{ cm}$ . Expressing  $R'$  and  $z$  in units of  $R_g$  shows that variability on even shorter timescales such as minutes will lead to very confined emission regions that are relatively close to the BH. These arguments show that the bulk of the high energy emission in blazar jets can be described by a single confined region in the jet.

In the past, single-zone models have been studied extensively, and they are able to explain most of the SED data for all kinds of sources very well. Their relatively constrained structure of a single region allows to add detailed time-dependent calculations of all possible particle interactions. Therefore, these models are tailored to closely probe the location of the acceleration region as well as the particle dynamics and the possibility of producing CRs and neutrinos (e.g. Tavecchio et al. 1998; Ghisellini & Tavecchio 2010; Böttcher et al. 2013; Reimer et al. 2019). Their success has led to the majority of the field using this type of models, and there are many examples of single-zone codes in the literature. For example, ATHE $\nu$ A (Mastichiadis & Kirk 1995), Böttcher2013 (Böttcher et al. 2013), LeHa-Paris (Cerruti et al. 2015) and AM<sup>3</sup> (Klinger et al. 2023) are all well known single-zone codes. Nevertheless, single-zone models do have fundamental shortcomings which severely limits the study of the large scale plasma dynamics observed in relativistic jets.

### Disadvantages of Single-Zone Modelling

First of all, single-zone models can explain the optically thin, high-energy fraction of the jet emission, but they are not able to explain the lower energy (radio) emission coming from the extended structure of relativistic jets. As explained in Section 1.3.3, synchrotron self-absorption effects will lead to a spectral break where the emission becomes optically thick in the synchrotron spectrum. In the case of a conical jet, the spectral slope below this break is nearly flat, i.e.  $F(\nu) \propto \nu^{-\alpha}$  with  $\alpha \lesssim 0$ , whereas the non-thermal synchrotron emission from a single region is predicted to be  $F(\nu) \propto \nu^{5/2}$  (Blandford & Ostriker 1978). Exactly this flat spectrum is observed practically all jetted AGN, thus for blazars as well (e.g. Marscher 1980; Hardcastle & Croston 2020). This spectral feature poses a problem for single-zone models and more recent works have tried to take a multi-zone approach by using two single-zone regions at different locations (e.g. Baring et al. 2016; Böttcher & Baring 2019; Xue et al. 2019). Yet, conceptually this is the same as one is looking at a relatively localised parts of the jet flow.

Secondly, the very detailed calculations and time-dependent behavior of single-zone models can also be a disadvantage. This type of calculations make the models computationally

expensive. For this reason, a majority of the field fits SED data using a ‘fit by eye’ approach as doing a more thorough statistical analysis, using MCMC for example, is simply too time consuming. Moreover, the fact that single-zone models are fundamentally not able to fit radio data in combination with sometimes sparse and non-simultaneous observational data even prevents people from using a more simple  $\chi^2$  statistic (Sol & Zech 2022).

Theoretically, the behavior of leptonic, single-zone models, and their fundamental limits and degeneracies are well understood (e.g. Böttcher & Reimer 2004; Ahnen et al. 2017; Sol & Zech 2022). There is a clear one-to-one correspondence between spectral features and what this implies for the parameters of the single-zone model. However, the dominance of leptonic emission processes and the additional parameters for lepto-hadronic models make it theoretically challenging to do the same for lepto-hadronic models. Extending this even further to multi-zone models will lead to a multitude of possibilities and we can only study the behavior and model degeneracies in a numerical sense as shown in Chapters 3 and 4.

### 1.5.2 BHJet: A Leptonic, Multi-Zone Jet Model

As discussed in the previous section,, the more confined nature of single-zone models allows the user to include very detailed, time-dependent particle physics that is important to study the transitions between different state of any source. While this can provide very rich results provide there are enough constraints, there are a number of problems associated to using single-zone models (see e.g. Böttcher et al. 2013; Cerruti et al. 2015; EHT MWL Science Working Group 2021; Li et al. 2022). There are some fundamental problems with single-zone jet models and the complexity of lepto-hadronic models lead to computationally expensive models than can show degeneracy between the model parameters. Alternatively, one can take the step towards more self-consistent, multi-zone jet models that describe the jet from start to end. Multi-zone models are designed to couple the accretion flow surrounding the BH to the production of relativistic jets and the large scale outflow (e.g. Falcke & Biermann 1995; Falcke et al. 1995). The majority of AGN jet models take a single-zone approach but there are a few noticeable exceptions (Potter & Cotter 2012, 2013; Potter 2017; Zacharias et al. 2022). In this thesis, we will use the `BHJet` model where the most recent version is described by Lucchini et al. (2022). This paper accompanied the public release of the code<sup>3</sup> and gives an extensive description description of the model, including its assumptions and caveats.

Let us first focus on how this multi-zone jet model was developed and what it actually calculates to reproduce an SED. The foundation of the `BHJet` model was developed by Falcke & Biermann (1995), who extended the first semi-analytical model of a coupled disk-jet system developed by Blandford et al. (1979). This first iteration of the model was especially focused on the overall dynamics of a disk-jet system and did not include any particle physics yet. Subsequently, the model was further developed by Markoff et al. (2001) to a full bipolar, multi-zone, and MWL model incorporating particle distributions, synchrotron emission and single-scattering IC radiation called `agnjet`. This first test of the model was to apply it to the SMBH in the Galactic centre, Sgr A\* (Falcke & Markoff 2000; Markoff et al. 2001), and was successful. With the improved version of the model, the results showed that the X-ray emitting corona, practically always observed in BH accretion, may be located in the innermost regions of the jet. Further investigation confirmed that this same spectral component can reproduce the

---

<sup>3</sup><https://github.com/matteolucchini1/BHJet>

X-ray emission of BHXBs as well (Markoff et al. 2001, 2003; Markoff et al. 2005). Since then the overall structure of the jet model has remained similar, but modifications have been made to include an irradiated accretion disk and its importance for the IC scattering (Maitra et al. 2009). Another modification was made in response to criticism from Zdziarski (2016), to ensure the conservation of energy in the jet by accounting for the lepton acceleration (Crumley et al. 2017). Recently, the model has undergone several major changes as discussed in Lucchini et al. (2019b), who introduced an improved dynamical model version, called `b1jet`, which considers a magnetically driven jet. This code was released publicly and is described in Lucchini et al. (2022). For convenience, a full list of all model parameters can be found in Appendix B.1.

## Jet Geometry and Evolution

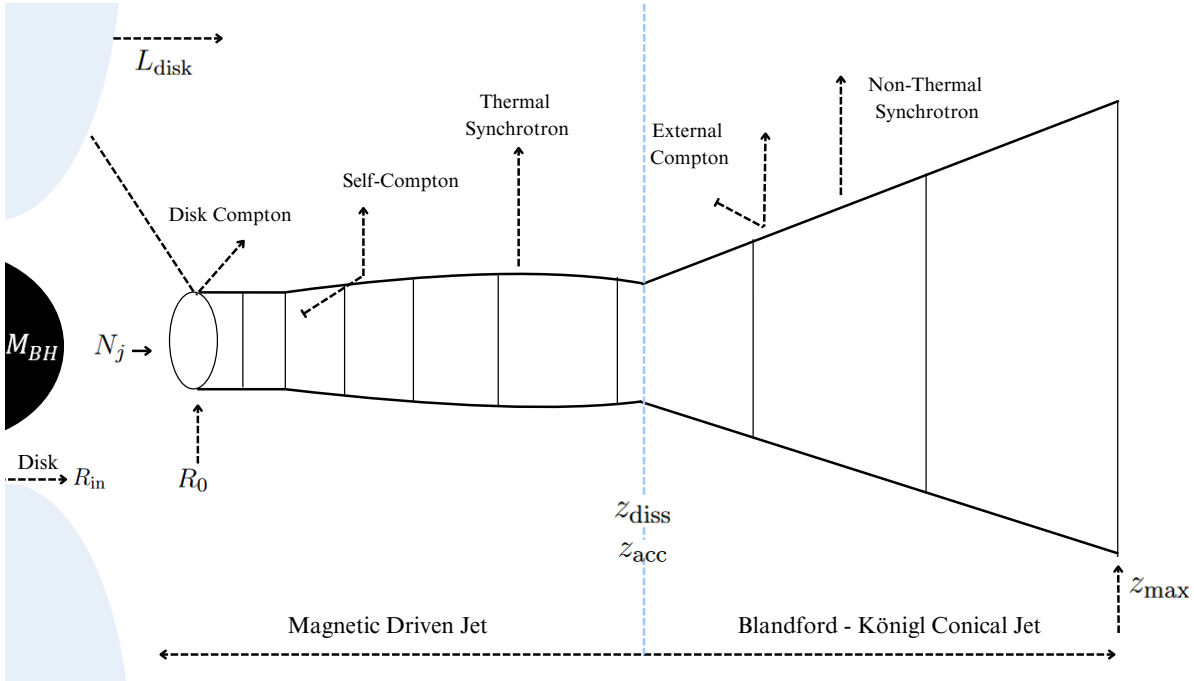


FIG. 1.20 – Geometry of the `BHJet` model.

In order to understand the model and its dynamics better, Fig. 1.20 presents a schematic overview of the geometry consider in `BHJet`. In this thesis, we only use the model ‘flavor’ called `b1jet` (Lucchini et al. 2022) that describes a magnetically driven jet. In this version, the jet starts with a cylindrical jet base that has an aspect ratio of  $h = z_0/r_0 = 2$ , where the subscript 0 means that we consider quantities at the base of the jet. The initial speed of the jet is fixed to  $\beta_0 \equiv v/c \approx 0.43$  which is the sound speed for a relativistic gas with adiabatic index 4/3 (Crumley et al. 2017). The jet nozzle is assumed to be highly magnetized and the magnetic energy is converted into bulk kinetic energy as the jet evolves which is designed to be in agreement with global GRMHD simulations (Komissarov et al. 2007; Tchekhovskoy et al. 2009). The acceleration of the jet follows a parabolic expansion, in agreement with VLBI observations of several AGN (Hada et al. 2013; Mertens et al. 2016; Nakamura et al. 2018).

The jet keeps accelerating until we reach a maximum Lorentz factor  $\gamma_{\text{acc}}$  at the distance  $z_{\text{acc}}$  from the BH. The resulting acceleration profile is thus given by

$$\gamma(z) = \gamma_0 + (\gamma_{\text{acc}} - \gamma_0) \frac{z^{1/2} - z_0^{1/2}}{z_{\text{acc}}^{1/2} - z_0^{1/2}}. \quad (1.59)$$

At the base of the jet, the power injected in the co-moving frame of the jet is given by

$$L_{\text{jet}} = 2\beta_0\Gamma_0 c\pi r_0^2\omega_0, \quad (1.60)$$

where  $\Gamma_0$  is the Lorentz factor at the base of the jet, and the factor of 2 accounts for the fact that we consider a bipolar jet. Until we reach the distance  $z_{\text{acc}}$ , the particles are assumed to be thermal and the jet is collimated by the interplay between the magnetic field and the gas pressure from the surrounding wind outflows. Throughout the jet bulk acceleration up to a distance  $z = z_{\text{diss}}$ , energy conservation is imposed by solving the Bernoulli equation (Konigl 1980)

$$\gamma(z) \frac{\omega(z)}{n(z)} = \text{const.}, \quad (1.61)$$

where  $\omega(z) = U_p(z) + U_e(z) + P_e(z) + U_B(z) + P_B(z)$  is the total enthalpy in the jet and we have several energy density ( $U_i$ ) and pressure ( $P_i$ ) terms for cold protons (p), electrons (e) and the magnetic field (B).

As the jet base is highly magnetized, it is useful to use the magnetization of the jet which we define as the ratio of magnetic to particle energy:

$$\sigma(z) = \frac{U_b(z) + P_b(z)}{U_p(z) + U_e(z) + P_e(z)}. \quad (1.62)$$

In the `b1jet` flavor, it is always assumed that most of the energy budget is in the cold protons which means that the contribution of electrons to the total energy budget is negligible such that  $U_e(z)$  and  $P_e(z)$  can be removed from equation 1.62. This simplification will give us the *cold* magnetization defined by  $\sigma = B^2/4\pi nm_p c^2$ , where  $n$  is the particle number density. An important feature of the model is that as long as the electron component of the enthalpy remains negligible, the model conserves energy throughout the jet. From this definition of the magnetization, we can derive the initial value of the magnetization as

$$\sigma_0 = (1 + \sigma_{\text{acc}}) \frac{\gamma_{\text{acc}}}{\gamma_0} - 1. \quad (1.63)$$

As the model needs to convert magnetic energy into the high Lorentz factors we observe in nature,  $\sigma_{\text{acc}}$  and  $z_{\text{acc}}$  are left as free parameters to give the model more freedom. Similarly, we can use equation 1.63 to determine the evolution of the magnetization along the jet:

$$\sigma(z) = \frac{\gamma_0}{\gamma(z)} (1 + \sigma_0) - 1. \quad (1.64)$$

## Jet Matter Content

At the acceleration region, magnetic energy is converted into particle kinetic energy, and one can think of this location as a region of energy dissipation caused by instabilities. In the acceleration region, a fraction of the thermal particles from the base of the jet are accelerated into a non-thermal powerlaw which then leads to non-thermal emission from the jet slices with  $z > z_{\text{acc}}$ . After this acceleration region, the jet switches from a magnetically driven jet to the standard Blandford-Königl jet as described in Section 1.3.3 which is collimated by gas pressure from the surrounding medium. The magnetic energy has been converted so what remains is a pressure driven jet with a constant Lorentz factor  $\gamma_{\text{acc}}$  and a fixed opening angle  $\theta_{\text{acc}} = \rho/\gamma_{\text{acc}}$  with  $\rho = 0.15$  inferred from VLBI surveys. In every slice after the acceleration region, there will be continuous particle re-acceleration such that non-thermal particle distributions is identical in every slice. Technically, the continuous re-acceleration breaks the conservation of energy, but the re-acceleration of electrons requires only a small fraction of the total energy budget. Therefore, energy is conserved for a leptonic model such as BHJet, but if the acceleration of protons is included the re-acceleration does have a significant effect on the energy conservation and the subsequent jet evolution (Kantzas et al. 2023b). The re-acceleration and the resulting emission continues to be calculated until we reach the end of the jet at  $z_{\text{max}}$ .

The advantage of this type of model is that we can follow the plasma dynamics, and the slicing of the jet allows the user to map the contribution of each emission process in every slice of the jet. In order to capture the evolution of the accelerated particle population in the jet, the continuity equation or Fokker-Planck equation is used (Fokker 1914; Planck 1917). In its full form this is given by

$$\frac{\partial N}{\partial t} + \frac{\partial(\Gamma v_j N)}{\partial z} + \frac{\partial}{\partial E} \left( \frac{dE}{dt} N \right) - \frac{N}{t_{\text{esc}}} = Q, \quad (1.65)$$

where  $N$  is the number of particles that evolve with time  $t$ ,  $\Gamma v_j$  is the bulk velocity of the jet,  $dE/dt$  describes the energy losses as a function of time,  $t_{\text{esc}}$  is the characteristic escape timescale, and  $Q$  is called a source term that can act as an injection rate of particles. It is important to note that all quantities depend implicitly on the particle energy  $E$ , the time  $t$  and the height  $z$  even though this is not explicitly shown. This equation connects the radiative processes through which the particles lose energy to their acceleration, escape and advection all along the jet.

Earlier in Sections 1.3 and 1.4 we showed that all radiative processes have their own characteristic timescale (see equations 1.17, 1.36, 1.51 and 1.55). In principle, all radiative mechanisms need to be taken into account when solving the continuity equation but this is computationally challenging to solve. Therefore, approximations are often made such that the calculations are more efficient and tractable. In the case of a steady-state jet, all time dependencies disappear and the first term in equation 1.65 can be dropped. The injection term is specified by assuming that the injected particles follow a powerlaw resulting from some particle acceleration mechanism. Lastly, when considering the emission from a single slice in the jet (see Fig. 1.20), we can simplify equation 1.65 by assuming that the advection happens on longer timescales than the radiative losses such that we can drop the advection (second) term. To illustrate, taking all of these assumptions into account for a distribution of electrons

in a magnetic field of strength  $B$ , equation 1.65 will simplify to

$$\sum_i \frac{N_e}{t_i} - \frac{N_e}{t_{\text{esc}}} \simeq \dot{N}_0 E_e^{-p}, \quad (1.66)$$

where the sum runs over the radiative losses through synchrotron and IC emission. Equation 1.66 shows a time-independent injection term that is balanced by the losses through either escape or radiation.

While the continuity equation is not explicitly solved by `BHJet`, it does enforce the conservation of the number of particles when going from one slice to the other. The evolution of the particle population along the jet can be described once the initial conditions are known, such that

$$n_{e/p}(z) = n_{e/p,0} \left( \frac{\gamma_0 \beta_0}{\gamma(z) \beta(z)} \right) \left( \frac{r_0}{r(z)} \right)^2, \quad (1.67)$$

where  $n_{e/p,0}$  is the initial number density of either electrons or protons. In order to determine the initial lepton number density, we define the equipartition factor:

$$f_{\text{eq}}(\beta_p, \eta, \langle \gamma_e \rangle) \equiv \frac{U_{e,0} + U_{b,0} + U_{p,0}}{n_e} = \langle \gamma_e \rangle m_e c^2 \left( 1 + \frac{1}{\beta_p} + \frac{m_p}{\eta \langle \gamma_e \rangle m_e} \right), \quad (1.68)$$

where  $U_{p,0} = n_{p,0} m_p c^2$  is the energy density of the injected protons, which we always assume to be cold. The parameter  $\beta_p$  is defined as  $\beta_p \equiv U_{e,0}/U_{b,0}$ , and  $\eta = n_e/n_p$  is the lepton-to-proton ratio that quantifies the jet matter content.  $\beta_p$  is in analogy with the standard plasma- $\beta$  parameter in plasma physics, but it is different as the pressure terms are not being incorporated in the definition. Nevertheless, it is a useful tool to probe whether a plasma is more magnetically dominated or more dominated by the internal energy of the particles. If there is an equilibrium  $\beta_p = 1$ , but generally the equipartition parameter varies between  $\beta_p = 0.01 - 100$  for astrophysical systems (e.g. [Burbidge 1956](#); [Zdziarski 2014](#)). Using the equipartition factor and defining an injected power as  $N_j = q_j \dot{M}_{\text{acc}} c^2$  allows us to write the injected lepton number density as

$$n_{e,0} = \frac{N_j}{2\pi r_0^2 \gamma_0 \beta_0 c f_{\text{eq}}(\beta, \eta, \langle \gamma_e \rangle)}, \quad (1.69)$$

Ultimately, by using the velocity and collimation profiles for the `b1jet` flavor, we have a fully specified evolution of the particle number density. The particle number density is used to derive the Thomson optical depth of the jet as a function of  $z$ :

$$\tau(z) = n_e(z) r(z) \sigma_T, \quad (1.70)$$

such that for every slice it can be determined whether its optically thick or optically thin. Combining equations 1.69 and 1.70, leads to a dependence of the optical depth on the jet radius of the form  $\tau(z) \propto r(z)^{-1}$ . Therefore, the optical depth depth will drop quickly as the jet expands such that we have a tool to estimate the importance of thermal Comptonization in the corona as compared to the X-ray emission produced by non-thermal emission processes.

## 1.6 Thesis Outline

This chapter has introduced important concepts to understand what blazars are, what kind of emission they produce and how they could be connected to the observed diffuse backgrounds of  $\gamma$ -rays, neutrinos and CRs. AGN are numerous objects in the Universe and depending on their orientation, these can be classified as blazars when their relativistic jet is closely aligned with our line of sight. Blazars all host a strong relativistic jets which can outshine their host galaxy due to relativistic beaming effects. The formation and evolution of these jets are crucial to understand, since they accelerate particles to relativistic velocities leading to non-thermal synchrotron and IC emission, and an SED with typical spectral features than can be related to the underlying particle distribution. Blazar SEDs are dominated by the emission produced by non-thermal electron distribution. However, proton acceleration is also expected in these jets, such that hadronic processes will start to play a role leading to the production of  $\gamma$ -rays and neutrinos.

These extreme astrophysical environments are very interesting objects to study, but some major open questions surrounding BH jets remain. There is yet much to be learned about the launching mechanism(s) of these jets and how they accelerate matter in the first place. Following on this, the matter content of the jet is uncertain and it is not clear whether matter from the surrounding medium can enter the jet as it propagates ([Kantzas et al. 2023b](#)). Moreover, when the matter in the jet has been accelerated, where do certain emission processes dominate in the jet and how do these transitions work? Lastly, could these jets even be the sources of astrophysical neutrinos that we observe? These are all complex questions, and only accurate BH jet models to reproduce blazar SEDs will help us further in this.

The majority of jet models in the literature take a single-zone approach while it is known that jets are extended structures. Alternatively, one can use multi-zone jet models that do follow the entire evolution of the jet. Multi-zone models do appear to be more self-consistent, but they do not (yet) include the same detailed and time-dependent calculations that single-zone models have. Nevertheless, it could be a significant step forward to transition to multi-zone models. To understand the differences between different models, code comparisons have been done before to see whether different codes predict the same results (see e.g. [Böttcher et al. 2013](#)).

More specifically, [Cerruti et al. \(2022\)](#) have undertaken the first ever comprehensive comparison of four lepto-hadronic codes designed to reproduce blazar emission. These code comparisons are crucial to reach consensus on fundamental aspects of the models while leaving enough room for everyone to vary and experiment. However, these comparisons tend to only focus on comparing single-zone models. Comparing models is challenging as every code uses its own parameters and the input differs for time-dependent versus time-independent codes requiring numerous conversions and assumption to be made. Moreover, when one does not use fit statistics, but a ‘fit by eye’ approach it is hard to say whether one model actually performs better than another. In order to really transition from single-zone models to multi-zone models, we have to bridge the gap between both types of models.

In this MSc thesis, a self-consistent, systematic comparison between single- and multi-zone models, and leptonic versus lepto-hadronic models is done by using statistical techniques such as  $\chi^2$  and Markov Chain Monte Carlo (MCMC). The goal is to uncover any systematic differences between using these types of models, allowing the community to take a step forward

in SED modelling of blazars and BH jets in general. To this end, I will discuss the blazar sources TXS 0506+056 and PKS 1424-418 together with their SEDs in Chapter 2. Here I will also discuss the method of fitting their SEDs and how we have to account for the fact that blazars are extra-galactic objects. Chapter 3 will discuss the SED fits done with the multi-zone, leptonic jet model called **BHJet**. As this model version was the most reliable, this is also used to investigate the degeneracies of the model as well as the statistical reliability of the MCMC fitting. After having established a baseline, we will continue to do SED fits with the other jet models. Chapter 4 will discuss the SED fits done with the lepto-hadronic, multi-zone jet model **HadJet** and how adding hadronic interactions leads to differences in the modelling. Lastly, single-zone fitting of blazar SEDs is discussed in Chapter 5. It discusses how leptonic and lepto-hadronic single-zone jet models are derived from **BHJet** and **HadJet**, respectively. This chapter will discuss the SED fits done with the single-zone versions of the model and how the results are different for single-zone modelling compared to multi-zone modelling of blazars. Interestingly, neither of the blazar sources have been modelled with any multi-zone jet model before which makes this the first time that a comparison with the results from single-zone models can be done.

# Chapter 2

## Multi-Wavelength SED Modelling of Blazars

As discussed in Chapter 1, there are different methods of modelling and simulating BH jets, and one method is to try to reproduce the MWL emission using semi-analytical jet models. For semi-analytical jet models it is very important to study sources that have a good MWL coverage together with (quasi-) simultaneous SED data. By looking at simultaneous emission ranging from radio to  $\gamma$ -rays we can constrain the source parameters and obtain reliable results in our modelling. The lack of simultaneous MWL data for the SED of an AGN usually means that we have to rely on quasi-simultaneous data under the assumption that the emission does not change significantly. Admittedly, the variability timescales of AGN are appreciably longer than for XRBs, but having simultaneous data would be best to understand emission mechanisms in a single state of the source.

For AGN it can be a problem that the AGN spectrum is contaminated by contributions from the surrounding galaxy or very bright star populations. However, the fact that blazars have a large bolometric flux means that they outshine their galaxy and the observations only see the blazar itself. This aspect has made blazars interesting objects to study, but the first detection of a neutrino coinciding with a  $\gamma$ -ray flare in the blazar TXS 0506+056 ([IceCube Collaboration 2018a](#)) led to an increased interest in blazars. Many research groups started modelling SEDs of blazars with lepto-hadronic models in order to explain observed neutrino fluxes (e.g. [Keivani et al. 2018](#); [Sahakyan et al. 2023](#); [Kun et al. 2023](#)). However, there are only a few blazars that actually have a statistical connection to a neutrino event. The advantage of this increased interest is that it led to better MWL coverage and more simultaneous SEDs for these sources.

Throughout this Chapter, I will describe the blazar sources that are used in this thesis in Section 2.1 together with the observational data. Secondly, Section 2.2 discusses the addition of Extra-galactic Background Attenuation (EBL) attenuation to the models to account for the fact that the  $\gamma$ -ray emission of extra-galactic sources is attenuated.

### 2.1 Blazar Sources

The enormous luminosity of blazars in combination with their recent connection to neutrino emission has led to good MWL coverage through MWL observational campaigns. In 2017, the detection of the neutrino event IceCube-170922A coinciding with a  $\gamma$ -ray flare for the blazar TXS 0506+056 led to a huge coordinated MWL observational campaign in the two weeks after the event ([IceCube Collaboration 2018b](#)). Afterwards, other blazars have also been associated to neutrino events such as PKS 1424-418 ([Kadler et al. 2016](#)), PKS 1741-038 ([Plavin et al.](#)

2021) and PKS 0735+168 (Plavin et al. 2021; Acharyya et al. 2023). In this thesis, we will focus on the blazars TXS 0506+056 and PKS 1424-418 because of their good MWL coverage with (quasi-)simultaneous SED data that was readily available from the literature. In the rest of this section, we will discuss the intrinsic source parameters and show the SED(s) of both sources.

Let us start with summarizing a few of the source characteristics of both PKS 1424-418 and TXS 0506+056. An overview of their parameters such as their location on the sky, redshift, distance to Earth, BH mass, Hydrogen column depth, disk luminosity and the number of SEDs per source were obtained from the literature and are given in Table 2.1. The position in the sky is not directly important for modelling their SEDs, but it does affect the specific earth-based telescopes than can be used to study these sources. While PKS 1424-418 is located in the southern sky, as indicated by the negative declination angle, can TXS 0506+056 be found in the northern sky close to the celestial equator<sup>1</sup>. The other source parameters such as the redshift, distance to Earth, BH mass and Hydrogen column depth can all be used as intrinsic source properties which are parameters in the BH jet models (see Appendix B.1 and B.2). In order to convert the redshift to a distance, the standard cosmological model, i.e. the  $\Lambda$  Cold Dark Matter ( $\Lambda$ CDM) model, with  $\Omega_m = 0.315$ ,  $\Omega_\Lambda = 0.685$ , and  $H_0 = 67.4 \text{ km s}^{-1} \text{ Mpc}^{-1}$  is used (Planck Collaboration 2020). Lastly, there is the disk luminosity as derived in the literature. This quantity will be used as a free parameter in the modelling, but it will be useful to compare the results to.

Source	PKS 1424-418	TXS 0506+056
Right ascension (J2000, °)	216.98 <sup>a</sup>	77.36 <sup>b</sup>
Declination (J2000, °)	-42.11 <sup>a</sup>	+5.69 <sup>b</sup>
Redshift	1.5220 <sup>c</sup>	0.3365 <sup>d</sup>
Distance (kpc)	$1.155 \times 10^7$	$1.488 \times 10^6$
BH mass ( $M_\odot$ )	$4.5 \times 10^9$ <sup>e</sup>	$3 \times 10^8$ <sup>d</sup>
Column depth $N_H$ (cm <sup>-2</sup> )	$7.71 \times 10^{-20}$ <sup>f</sup>	$1.20 \times 10^{-21}$ <sup>g</sup>
L <sub>Disk</sub> (L <sub>Edd</sub> )	0.15 <sup>h</sup>	0.18 <sup>i</sup>
# SEDs	4	1

TABLE 2.1 Source parameters of the blazars PKS 1424-418 and TXS 0506+056 obtained from the literature.

**References:** <sup>(a)</sup>Johnston et al. (1995), <sup>(b)</sup>Lanyi et al. (2010), <sup>(c)</sup>White et al. (1988), <sup>(d)</sup>Paiano et al. (2018), <sup>(e)</sup>Fan & Cao (2004), <sup>(f)</sup>Krauß et al. (2016), <sup>(g)</sup>Keivani et al. (2018), <sup>(h)</sup>Abhir et al. (2021), <sup>(i)</sup>Padovani et al. (2019).

### 2.1.1 TXS 0506+056

Discovered as a bright radio source in 1983 (Lawrence et al. 1983), TXS 0506+056 can be found in the sky close to the left shoulder of the constellation Orion. Initially, TXS 0506+056 was thought to be a BL Lac type blazar (Massaro et al. 2009), but recent work has argued that it is in fact a *masquerading* BL Lac (Padovani et al. 2019). The term masquerading BL Lac means refers to a FSRQ type blazar, but its broad-lined spectrum is heavily diluted by other spectral components such that it appears to be a BL Lac. Nevertheless, TXS 0506+056 is among the top 0.3% of the brightest radio sources in the sky as well as among the top 4% of the brightest

<sup>1</sup><https://science.nasa.gov/learn/basics-of-space-flight/chapter2-2/>

$\gamma$ -ray sources despite its highly variable  $\gamma$ -ray flux (Padovani et al. 2018). Its luminosity places TXS 0506+056 among the most powerful (masquerading) BL Lacs known, particularly in the  $\gamma$ -ray regime.

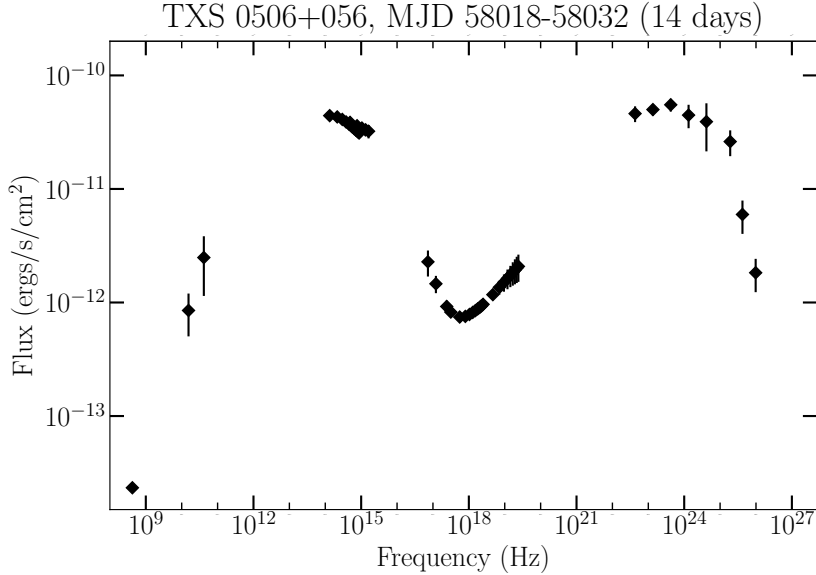


FIG. 2.1 – SED of TXS 0506+056 collected in the two weeks after the detection of neutrino event IceCube-170922A coinciding with a  $\gamma$ -ray flare. Data was retrieved from Keivani et al. (2018).

The existence of this object has been known for several decades such that there are many observations in different wavelength regimes spread out over decades. This non-simultaneous character of all SED data, makes it impossible to study a single state of the source for most of its observational history. However, there is one short period in time during which a simultaneous SED of TXS 0506+056 was obtained, and this was during the MWL campaign in 2017 (IceCube Collaboration 2018a). This MWL campaign was initiated because of the temporal coincidence of a  $\gamma$ -ray flare detected by *Fermi*/LAT and the neutrino event IceCube-170922A (IceCube Collaboration 2018b) on September 22, 2017. For this thesis, a slightly modified dataset from this campaign was obtained from Keivani et al. (2018) who used part of the data collected slightly before and in the two weeks after the neutrino event. The follow-up observations made use of *Fermi*/LAT<sup>2</sup> (Atwood et al. 2009), *Swift*<sup>3</sup> (UVOT and XRT; Roming et al. 2005), X-shooter<sup>4</sup> (Vernet et al. 2011), and NuSTAR<sup>5</sup> (Harrison et al. 2013) data. We refer to the papers by IceCube Collaboration (2018a) and Keivani et al. (2018) for more details on the MWL observations and data analysis to obtain the SED presented in Fig. 2.1. Tables with all the data points can be found in Appendix A.1.

<sup>2</sup><https://fermi.gsfc.nasa.gov/>

<sup>3</sup><https://swift.gsfc.nasa.gov/>

<sup>4</sup><https://www.eso.org/sci/facilities/paranal/instruments/xshooter.html>

<sup>5</sup><https://www.nustar.caltech.edu/>

### 2.1.2 PKS 1424-418

PKS 1424-418 was discovered in 1981 (Glass 1981), and is an FSRQ which means that its  $\gamma$ -ray luminosity dominates its radiative power. The large redshift of 1.522 makes the source somewhat difficult to observe, but similar to TXS 0506+056 there are numerous observations of PKS 1424-418 in different wavelengths. The source has shown recent periods of flaring/active behavior from 2008 to 2011 (Buson et al. 2014) and from 2012 to 2013 (Dirirsa et al. 2015) making it an interesting object for the possible neutrino- $\gamma$ -ray correlation. Moreover, PKS 1424-418 has been modelled by Celotti & Ghisellini (2008) and Paliya et al. (2017) in the past presenting us with reference material.

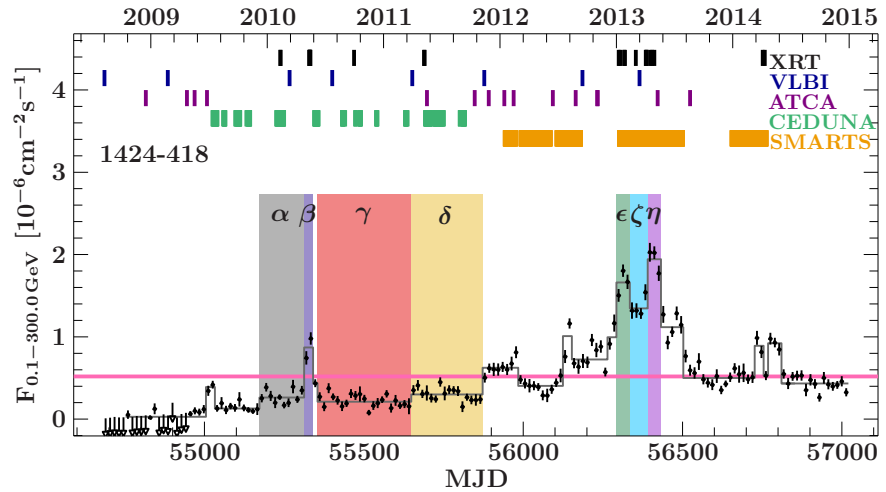


FIG. 2.2 – *Fermi*/LAT light curve for PKS 1424-418 from August 4, 2008 to January 1, 2015. A Bayesian block analysis was performed on the data by Krauß et al. (2016) and is shown in dark gray. The horizontal pink line shows the average flux over the full light curve. Blocks with sufficient data for a broadband SED are shown in color and are labeled with Greek letters. Figure from Krauß et al. (2016).

The data for PKS 1424-418 used in this thesis was obtained from Krauß et al. (2016) who collected the data during the TANAMI MWL campaign. We will refer to this paper for a detailed description of the different instruments that were used, and how the data was prepared for analysis. In short, the Tracking Active Galactic Nuclei with Austral Milliarcsecond Interferometry (TANAMI<sup>6</sup>; Ojha et al. 2010) program covers southern flat spectrum sources with flux densities above 1 Jy at 5 GHz, as well as *Fermi* detected  $\gamma$ -ray loud blazars. With high resolution Very Long Baseline Interferometry (VLBI), the TANAMI program has confirmed that most of the emission of PKS 1424-418 comes from a compact central region, and it has a low surface brightness, compact jet with a rather wide opening angle.

A considerable number of different instruments were involved to obtain the MWL SED data for PKS 1424-418. The (quasi-)simultaneous radio data was collected using TANAMI with VLBI at 8.4 GHz and 22 GHz, single dish observations with ATCA<sup>7</sup> (Stevens et al. 2012)

<sup>6</sup><https://pulsar.sternwarte.uni-erlangen.de/tanami/>

<sup>7</sup><https://www.narrabri.atnf.csiro.au/>

and Ceduna<sup>8</sup> (McCulloch et al. 2005). These observations were complemented using SMARTS<sup>9</sup> (Bonning et al. 2012), *Swift* (UVOT and XRT), and *Fermi*/LAT. Specifically for PKS 1424-418, archival data was added using the 2MASS point source catalog (Skrutskie et al. 2006), the ALLWISE catalog (Wright et al. 2010), and aperture photometry values from the *Planck* Catalog of Compact Sources (Planck Collaboration et al. 2014).

A very important milestone for studying AGN was the launch of *Fermi* in 2008 which led to the availability of continuous  $\gamma$ -ray light curves for the entire sky. Krauß et al. (2016) extracted *Fermi*/LAT light curves for multiple sources from the 3FGL catalog for the time period August 4, 2008 to January 1, 2015. The light curve for PKS 1424-418 is shown in Fig. 2.2, where different periods of flaring and quiescent behavior can clearly be distinguished. Based on the light curve, these epochs can divided into two groups either corresponding to a quiescent state ( $\alpha$ ,  $\gamma$ ,  $\delta$ ) or a flaring state ( $\beta$ ,  $\epsilon$ ,  $\zeta$ ,  $\eta$ ) of the source. The light curve clearly reflects the continuous transitioning from somewhat longer quiescent states to epochs where the source is showing  $\gamma$ -ray flares that last several days.

Combining the observational data of the different instruments within each epoch will lead to one SED per epoch. For this thesis, we are interested in what changes in the source parameters when a blazar transitions from a quiescent state into a flaring state and how this could affect possible  $\gamma$ -ray and neutrino production. Nevertheless, the models that will be used are steady-state models such that they cannot recover fluctuations on very short timescales. Therefore, we select epochs  $\alpha$ ,  $\gamma$  and  $\delta$  to represent the quiescent state of PKS 1424-418, and we select epoch  $\eta$  to represent the flaring state. The SEDs of these four epochs are shown in Fig. 2.3 where we also included the archival data for the quiescent states. Tables with all the data points can be found in Appendix A.2.

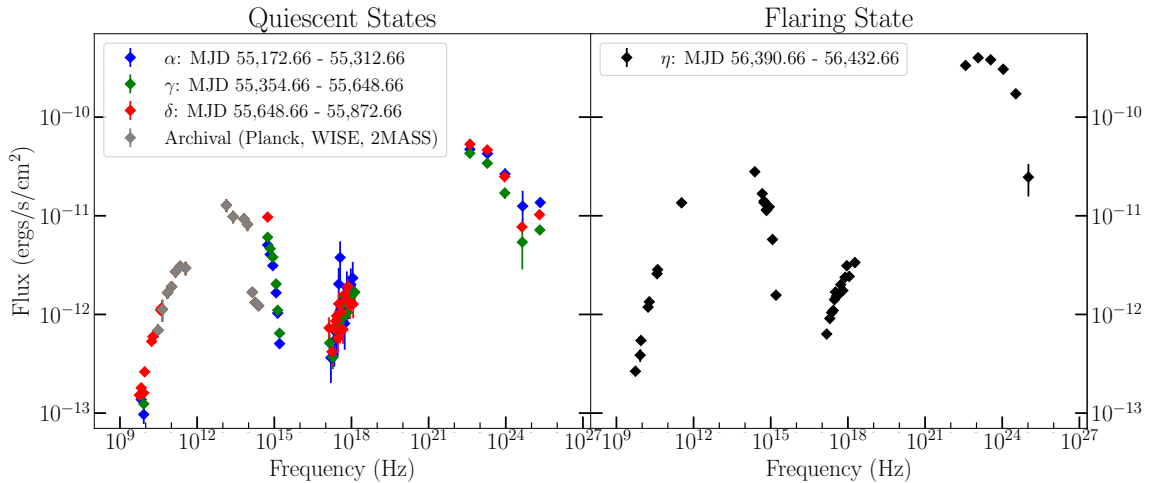


FIG. 2.3 – MWL SEDs of PKS 1424-418 with the logarithmic flux as a function of logarithmic frequency. The left panel shows SEDs of the epochs  $\alpha$ ,  $\gamma$  and  $\delta$  where PKS 1424-418 is in a quiescent state. The right panel shows the epoch  $\eta$  during which the source is in a flaring state. The data was retrieved from Krauß et al. (2016).

Something to note is that the four SEDs of PKS 1424-418 span roughly 1100 days which

<sup>8</sup><https://www.utas.edu.au/natural-sciences/physics/ceduna-observatory>

<sup>9</sup><http://www.astro.yale.edu/smarts/>

is approximately 3 years. On this timescale, the source is not expected to change its overall behavior drastically as AGN have rather long variability timescales. Whereas XRBs can show transitions in timescales on the order of days, AGN have variability timescales on the order of years. Nevertheless, there can be variability on shorter time-scales, but as the model represents a steady-state jet we cannot expect it to be able to capture this type of behavior. This is the reason that we chose to use the SED of the  $\eta$  epoch to represent the flaring state of the source. This epoch lasted roughly from 56250-56450 MJD spanning half a year which is sufficiently long to be confident that the steady-state nature of the models remains reliable. Another reason to use the  $\eta$  epoch is that its time range matches with the observation of a PeV neutrino event called ‘Big Bird’ in 2013 (IC35; [Kadler et al. 2016](#)).

Looking at the SEDs in Fig. 2.3, one can see in the left panel that the 2MASS archival data does not match the rest of the data for the quiescent states. This mismatch is probably caused by non-simultaneity which is the reason that we will not make use of these three data points in our fitting. Another thing to notice, is that the overall flux during the flaring state is significantly higher than for the quiescent state. This effect is the strongest for the high-energy bump, which is the reason for the flaring behavior in the  $\gamma$ -ray light curve presented in Fig. 2.2.

## 2.2 Extra-Galactic Background Light Attenuation

We have seen for the typical blazar SED in Fig. 1.10, that the emission can reach up to frequencies of  $10^{26}$  Hz and above because of relativistic beaming. Thus, blazars are capable of producing a considerable amount of highly energetic  $\gamma$ -rays. A very important aspect to consider when looking at high-energy emission from extra-galactic objects is that of *Extra-galactic Background Light (EBL) attenuation*. In this process, a very high-energy (VHE) photon will interact with an EBL photon according to

$$\gamma_{\text{VHE}} + \gamma_{\text{EBL}} \rightarrow e^+ + e^-, \quad (2.1)$$

leading to photon-photon pair production as they travel towards Earth. This interaction will reduce the observed flux of  $\gamma$ -rays for an extra-galactic source making it more difficult to study the intrinsic  $\gamma$ -ray flux at the source.

The collective term *Extra-galactic Background Light* refers to all the radiation that accumulated during the evolution of the Universe. Stars and other astrophysical objects at all epochs have emitted light throughout their lifetime. The redshifting and dilution due to the expansion of the Universe, then led to the EBL with wavelengths ranging from the UV to the far IR. Therefore, there is an intimate connection between the EBL and the history of the Universe ([Robertson et al. 2010](#)), and makes it an interesting component of the Universe on itself. However, a full discussion of all potential science in the EBL is beyond the scope of this thesis. For this thesis, a model is needed to describe the EBL spectrum such that the attenuation of the  $\gamma$ -ray flux produced by blazars can be quantified. Below, I will present a brief overview of this effect, but [Singh & Meintjes \(2020\)](#) present a more extensive review on different EBL models and what implications these have for observing blazars.

Mathematically the EBL attenuation of the intrinsic source flux can be accounted for by

correcting the emitted flux with an attenuation factor as described by

$$F_{\text{obs}} = F_{\text{em}} \times e^{-\tau(E, z_{\text{red}})}$$

$$\text{with } \tau(E, z_{\text{red}}) = \int_0^{z_{\text{em}}} \left( \frac{dl}{dz_{\text{red}}} \right) dz_{\text{red}} \int_0^2 \frac{\mu}{2} d\mu \int_{\varepsilon_{\text{th}}}^{\infty} n_{\text{EBL}}(\varepsilon, z_{\text{red}}) \sigma_{\gamma\gamma}(E, \varepsilon, \mu) d\varepsilon, \quad (2.2)$$

where we have the optical depth  $\tau(E, z_{\text{red}})$  as a function of the incoming photon energy  $E$  and redshift  $z_{\text{red}}$ ,  $\mu \equiv 1 - \cos(\theta)$  is the angle between the momenta of the two photons in the lab frame,  $\varepsilon$  is the energy of the EBL photon, and  $n_{\text{EBL}}(\varepsilon, z_{\text{red}})$  is the EBL photon number density in  $\text{cm}^{-3}$ . A cosmological correction comes in through the use of the line element for a  $\gamma$ -ray photon in the standard  $\Lambda$ CDM cosmology given by

$$\frac{dl}{dz_{\text{red}}} = \frac{c}{H_0(1 + z_{\text{red}})} \frac{1}{\sqrt{\Omega_{\Lambda} + \Omega_m(1 + z_{\text{red}})^3}}. \quad (2.3)$$

In order for the process in equation 2.1 to happen, the combined energy of the two photons needs to be larger than the combined rest mass of the electron-positron pair which is around 1.22 MeV. This threshold energy for the interaction mostly depends on the energy of the incoming VHE photon, and is given by

$$\varepsilon_{\text{th}}(E, \mu, z_{\text{red}}) = \frac{2m_e^2 c^4}{E\mu(1 + z_{\text{red}})^2}. \quad (2.4)$$

Lastly, there is the pair production cross section defined as ([Gould & Schréder 1967](#))

$$\sigma_{\gamma\gamma}(E, \varepsilon, \mu) = \frac{\pi q^4}{2m_e^2 c^4} (1 - \beta^2) \times \left[ (3 - \beta^4) \ln \left( \frac{1 + \beta}{1 - \beta} \right) - 2\beta (2 - \beta^2) \right], \quad (2.5)$$

where

$$\beta = \sqrt{1 - \frac{2m_e^2 c^4}{E\varepsilon\mu}}, \quad (2.6)$$

which does depend on the energies of both photons, and quantifies the probability for the process to actually occur.

With these relations, there is a mathematical framework to implement the effects of EBL attenuation. The last component that is left unspecified, is the photon number density of the EBL as a function of energy and redshift  $n_{\text{EBL}}(\varepsilon, z_{\text{red}})$ . As an analytical expression cannot be derived from first principles, we have to rely on observations, but there are some intricacies here. Directly measuring the EBL is difficult due to strong foreground emission by objects in our Solar system and the Milky way ([Hauser et al. 1998](#); [Chary & Pope 2010](#)). Therefore, researchers often rely on semi-analytical modelling of the EBL photon number density. They do this by considering the key processes for the production of radiation as a result of galaxy formation and evolution throughout the history of the Universe ([Primack et al. 1999](#)). The fact that this is an evolving scientific field, has led to different underlying assumptions of current EBL models. Consequently, uncertainties in the star formation rate, initial mass function, dust

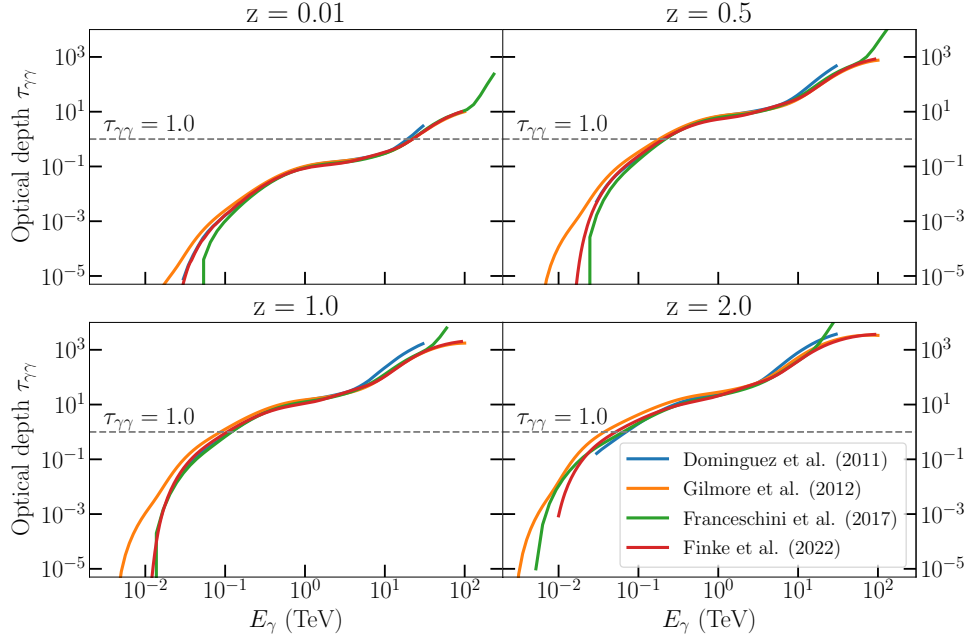


FIG. 2.4 – The optical depth for photon-photon pair production as a function of the incoming photon energy (in TeV) for four different EBL models. The figure shows the optical depth for redshifts ( $z_{\text{red}}$ ) 0.01, 0.5, 1.0 and 2.0. The gray dashed line represents  $\tau_{\gamma\gamma} = 1.0$  where the flux is attenuated by a factor  $1/e$ . The optical depth data was retrieved from Domínguez et al. (2011), Gilmore et al. (2012), Franceschini & Rodighiero (2017) and Finke et al. (2022).

extinction, and galaxy evolution with redshift have resulted in discrepancies between different EBL models.

Currently, there are a few prominent EBL models in the literature which were developed by Domínguez et al. (2011), Gilmore et al. (2012), Franceschini & Rodighiero (2017) and Finke et al. (2022). The optical depth derived from these four models is plotted in Fig. 2.4 for different redshift values, and they all agree well in the majority of the energy range from approximately 0.1 - 100 TeV for different redshifts. At the moment, the EBL attenuation models mentioned above are equally likely and there is no reason to believe that one is more correct than the others. In this thesis, we chose to use the fiducial EBL model by Gilmore et al. (2012) as this has been tested against observational data for low redshifts ( $z \leq 0.5$ ), and the authors implemented a cosmological evolution correction factor for higher redshifts based on *Wilkinson Microwave Anisotropy Probe* 5-year (WMAP5<sup>10</sup>; Komatsu et al. 2009) cosmology data and other empirical evidence. The relatively large uncertainties on the observational flux data in the TeV range make it very difficult to distinguish between different EBL models anyway. Another reason to choose the EBL model by Gilmore et al. (2012) is that it typically has the highest optical depth at lower photon energies. By using the model by Gilmore et al. (2012) we choose the most attenuating model such that this will put an upper limit on the intrinsic  $\gamma$ -ray flux that we obtain during the SED modelling.

The most recent versions of the multi-zone jet models, BHJet and HadJet, do not take the

<sup>10</sup>[https://wmap.gsfc.nasa.gov/news/5yr\\_release.html](https://wmap.gsfc.nasa.gov/news/5yr_release.html)

effect of EBL attenuation into account, but it is important for the distant blazars considered in this work. Until now, the mentioned models have mostly been used to fit the SED data of low luminosity AGN (LLAGN) and XRBs for which the MWL emission does not extend beyond X-rays around frequencies of  $10^{20}$  Hz (e.g. [Markoff et al. 2001](#); [Markoff et al. 2005](#); [Maitra et al. 2009](#); [Plotkin et al. 2014](#); [Markoff et al. 2015](#); [Connors et al. 2016](#)). In practice, EBL attenuation will only affect the flux at photon energies larger than 1 GeV which corresponds to a frequency of  $\nu \sim 2.4 \times 10^{23}$  Hz making it a crucial feature in blazar SEDs. This effect is shown in Fig. 2.5 where a fit from Section 4.3 is shown with and without EBL attenuation. There are more emission components that lead to this fit, but the ones that are affected by EBL attenuation are the non-thermal IC emission and the  $\gamma$ -rays produced in hadronic interactions. Fig. 2.4 shows that the EBL attenuation can constrain the  $\gamma$ -ray flux significantly, and the redshift of the source can play a crucial role. Since the redshift of PKS 1424-418 is relatively large, the EBL attenuation is strong and there is no observable emission above  $10^{26}$  Hz. Nevertheless, for PKS 1424-418 there is no SED data above  $10^{25}$  Hz so accounting for the EBL attenuation does not affect the fitting substantially, but it is more realistic to apply the correction for all fits in the rest of this thesis.

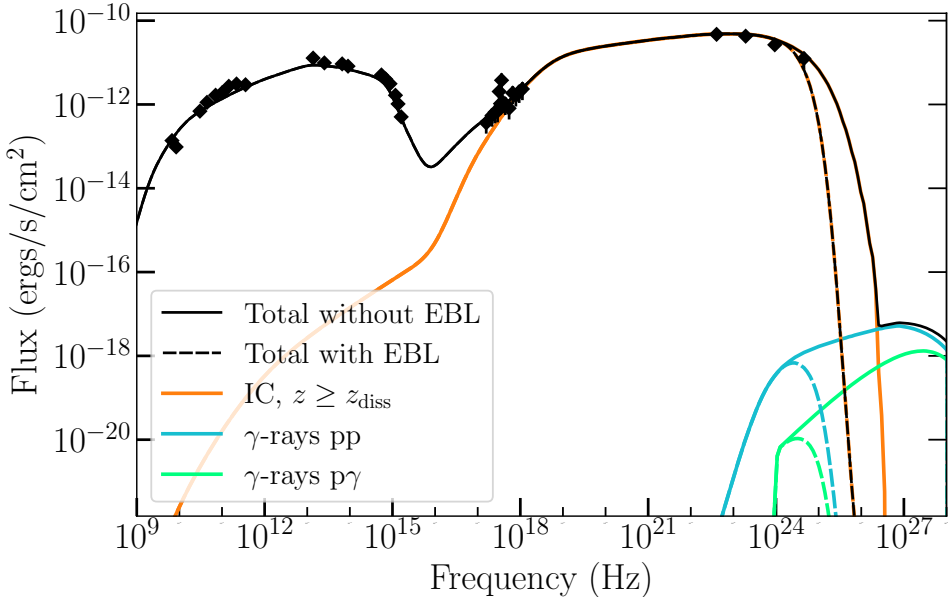


FIG. 2.5 – The fit for the  $\alpha$  epoch of PKS 1424-418 as obtained for the joint fit in Section 4.3. The full lines represent the model without accounting for EBL attenuation and the dashed lines represent the case where EBL attenuation is taken into account. The spectral components that are affected by EBL attenuation are also shown.

# Chapter 3

## Multi-Zone Modeling of Blazar SEDs with BHJet

In order to do SED modelling of blazar jets, we need a numerical model designed to reproduce the emission components seen in the SED. All models used in this thesis, are or will be derived from a semi-analytical, steady-state, multi-zone jet model. This Chapter will only consider the leptonic version called `BHJet` whereas Chapter 4 will make use of the lepto-hadronic version called `HadJet`. As `BHJet` is the most tested model, this Chapter will be the baseline for the rest of the results in following Chapters. In Section 1.5.2 the general structure of the multi-zone jet model has been discussed together with its evolution and particle properties. In this chapter, Section 3.2 will highlight potential degeneracy in the model for the electron temperature in. Before showing the actual fits of the data, some boundary conditions of the model and fixed parameters are specified in Section 3.1. Lastly, the SED fits of TXS 0506+056 and PKS 1424-418 are presented in Sections 3.4 and 3.5, respectively.

### 3.1 Fixing Model Parameters for Blazar Sources

In Section 1.5.2, several important features of the leptonic, multi-zone jet model `BHJet` were discussed such as the jet geometry, its evolution and the way particle distributions are treated as we move away from the BH. Naturally, one needs enough model parameters to specify all features and a full list for the multi-zone models `BHJet` and `HadJet` is shown in Appendix B.1. When fitting an SED, we cannot fit for all these parameters so we make use of constraints inferred from observations. These constraints are used to fix parameters of the model and limit the number of degrees of freedom. Section 2.1 already discussed a number of intrinsic source parameters like the redshift, distance to Earth, BH mass and Hydrogen column depth that can be fixed from the start. Moreover, other model parameters can be fixed or constrained by using sensible parameter values when compared to the literature or simply because there is a theoretical limit. The parameters that are always fixed to the same value for both PKS 1424-418 and TXS 0506+056 are given in table 3.1 together with a description as to why.

First of all, relativistic beaming of blazar emission will lead to most of the observed emission coming from regions  $z \geq z_{\text{diss}}$  in the jet once the particles have been accelerated. The jet nozzle in blazars is therefore mostly unconstrained such that we need to make assumptions on the initial conditions of the jet. The height of the jet nozzle,  $h$ , cannot be constrained without data that probes the innermost regions. For example, this can be done using reflection signatures in the X-ray spectrum (Lightman & White 1988; Ross & Fabian 1993). Due to the lack of constraints the aspect ratio of the jet nozzle, defined as  $h/r_0$ , is fixed to 2.0. Moreover, recent work has found jet base radii on the order of  $\sim 10R_g$  for the BL Lac PKS 2155–304, but they

also showed that radius of the jet base can show degeneracy together with other bulk source parameters (Lucchini et al. 2019b). Therefore, we fix the jet base radius to  $R_0 = 20 R_g$  for all our SED fits.

The second aspect of modelling blazars is that the fraction of electrons that is accelerated into the non-thermal powerlaw tail,  $f_{\text{nth}, e}$ , needs to be specified. Recent works have used BHJet to study the SEDs of XRBs and LLAGN which used  $f_{\text{nth}, e} \approx 1$  in combination with  $f_{\text{heat}} \approx 1$  (Connors et al. 2016, 2019; Lucchini et al. 2019a; Kantzas et al. 2020; Lucchini et al. 2020). As discussed by Lucchini et al. (2022), a larger non-thermal fraction is necessary to ensure smooth non-thermal emission bumps as seen in blazar observations (e.g. Ballo et al. 2002). Therefore, we fix the non-thermal fraction of electrons to 0.5 leading to a quasi-Maxwellian electron distribution where half the electrons are accelerated into a powerlaw.

One more parameter that remained fixed while fitting is  $z_{\max}$  which specifies the length over which the model calculates the jet emission. From Section 1.3.3 we know that a conical jet will produce a flat radio spectrum because of the SSA process. The flat spectrum is also observed in blazars as seen in Fig. 2.1 and 2.3 for example. In order to obtain such a flat spectrum with the multi-zone jet models,  $z_{\max}$  needs to have a large value of  $z_{\max} \gtrsim 10^6 R_g$  such that the jet does not end too close to the acceleration region. Using a larger value of  $z_{\max}$  will lead to a broader frequency range over which we see a flat spectrum, so  $z_{\max}$  effectively determines the cutoff at lower frequencies. After some trial and error, the optimal values were found to be  $z_{\max} = 10^6 R_g$  for PKS 1424-418 and  $z_{\max} = 5 \times 10^7 R_g$  for TXS 0506+056. These values are not necessarily the exact physical extent of the jets, but they are large enough to fit the data without showing numerical artefacts that arise when truncating the jet too early.

Lastly, the fractions of disk photons that are reprocessed by the BLR and DT need to be discussed. In the case of TXS 0506+056, the SED fitting showed that these were needed as free parameters to be able to get a good fit of the  $\gamma$ -rays through the EC process. Thus,  $f_{\text{BLR}}$  and  $f_{\text{DT}}$  are free to vary between 0.05 – 0.4 for TXS 0506+056. On the other hand, the SED fitting of PKS 1424-418 showed that these fractions remained relatively constant. Therefore,  $f_{\text{BLR}}$  and  $f_{\text{DT}}$  are fixed to the values 0.05 and 0.2 for PKS 1424-418, respectively.

Parameter	Value	Description
$R_0 (R_g)$	20.0	Radius of the jet base. Since the base of the jet is hard to observe in blazars, this value is fixed.
$z_{\text{diss}} (R_g)$	$z_{\text{acc}}$	$z_{\text{diss}}$ is tied to $z_{\text{acc}}$ as it is unknown whether the acceleration region is the same as the dissipation region. Observations do suggest that they are the same (Marscher et al. 2008), although this might not be the only viable choice (Russell et al. 2014).
$R_{\text{out}} (R_g)$	$10^4$	The outer radius of the accretion disk needs to be large enough to produce a full multi-color black body spectrum, but it does not influence the fits significantly.
Compsw	2	Compsw=2 will activate external photon fields emitted by the BLR and DT for EC scattering as expected in AGN, and are especially important for blazars.
EBLsw	1	EBLsw=1 activates EBL attenuation which is needed blazars are extra-galactic objects as discussed in Section 2.2.

**Table 3.1 continued from previous page**

Parameter	Value	Description
$p_\beta$	0	The model is designed such that a value of $p_\beta = 0$ together with $\Gamma \geq 1$ (by setting $\text{velsw} > 1$ ) leads to a matter content of one proton per electron throughout the jet. Physically, one expects the jet to be neutrally charged which requires an equal number of protons and electrons. In a leptonic model, this assumption leads to the highest possible jet power for a given observed jet luminosity and to a reasonable energy budget for canonical blazars (e.g. <a href="#">Ghisellini et al. 2014</a> ).
$f_{\text{nth},e}$	0.5	Fraction of thermal electrons that is being accelerated into a non-thermal powerlaw tail.
$f_{\text{pl}}$	0	Reduces the particle temperature and percentage of accelerated particles along the jet after $z_{\text{diss}}$ , resulting in an inverted radio spectrum. Setting it to 0 will lead to a standard flat spectrum which is the case for both PKS 1424-418 and TXS 0506+056.
$f_b$	0.1	Factor to increase/decrease the adiabatic cooling timescale defined as $t_{\text{ad}} \equiv r/f_b c$ . There is no cooling break in the SEDs so the default value of 0.1 is kept.

TABLE 3.1 Model parameters that are fixed in the SED fits for both PKS 1424-418 and TXS 0506+056.

## 3.2 Degenerate Thermal Electron Temperature for Blazars

Before we look at the fits done with `BHJet` for the SEDs discussed in Chapter 2, there is an important issue to address for blazars. The multi-zone models `BHJet` and `HadJet` have a parameter  $T_e$  which determines the temperature of the thermal electrons at the base of the jet. However, due to the alignment of the jet, blazar SEDs hardly contain any information about the base of the jet since it is obscured by the non-thermal emission from the rest of the jet. From observations, we know that accreting BHs have a hot corona close to the BH ([Padovani et al. 2017](#); [Gallo 2018](#); [Alston et al. 2020](#)), and measurements of the coronal temperature for the SMBH M87\* have shown that this temperature can be relatively high on the order of  $10^{11}$  K ([EHT Collaboration 2021](#)). Such a temperature translates to a thermal electron energy of  $E = \frac{3}{2}k_B T_e \approx 8.6 \times 10^3$  keV. While the jet model does not explicitly contain a feature that is directly reflecting a corona, the SED contains coronal emission such that the physical conditions at the base of the jet are influenced by its presence. In order for the jet model to be able to fit coronal emission and the corresponding conditions, we expect that the model needs rather extreme parameters at the jet base. It needs a high electron temperature in order to fit the coronal emission, but in the case of the blazars it also needs a high magnetization providing the energy necessary to accelerate the jet to the extreme Lorentz factors we observe.

In order to study the behavior of  $T_e$ , we do fits of the quiescent  $\alpha$  epoch of PKS 1424-418 with `BHJet`. We test different electron temperatures in three fits, where we set  $T_e = 200$  keV,  $T_e = 1000$  keV and one in which we use  $T_e$  as a free parameter within a range  $100 \leq T_e \leq 1000$

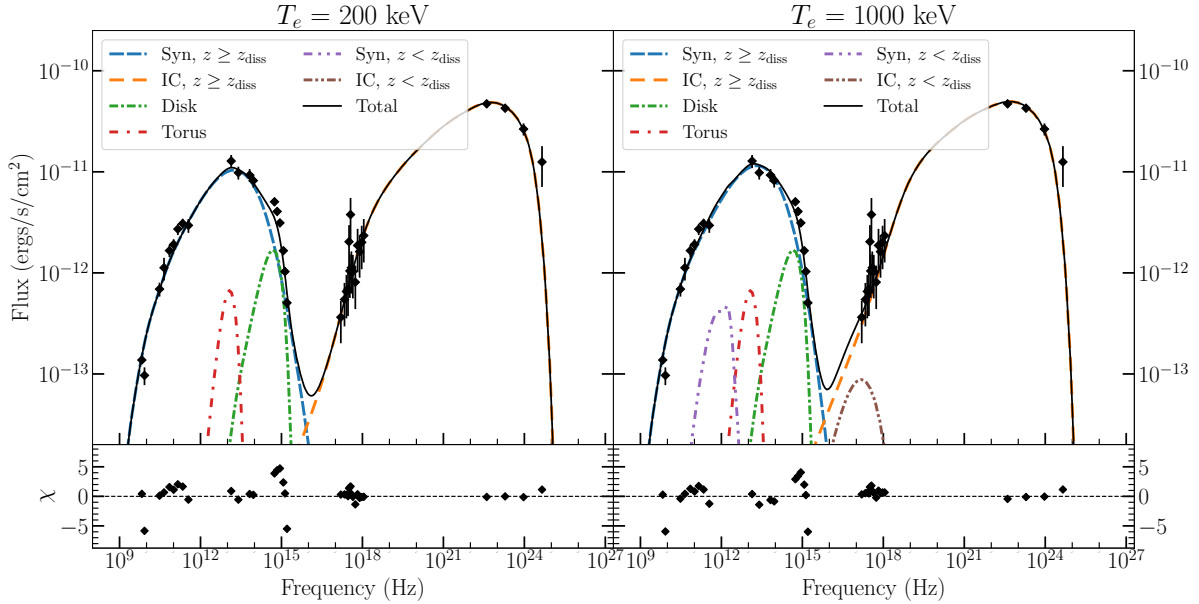


FIG. 3.1 – Fits with BHJet for the  $\alpha$  epoch of PKS 1424-418 for two different electron temperatures. The left panel shows a fit with  $T_e = 200$  keV and the panel on the right uses  $T_e = 1000$  keV. The full black line shows the sum of all components which are shown as: non-thermal synchrotron in blue, non-thermal IC in orange, black body spectra from the disk (green) and torus (red), thermal synchrotron in purple and the thermal IC component in brown.

keV. The fits for the fixed electron temperatures can be seen in Fig. 3.1 which give a good idea of the dominant contributions to a blazar SED. The SED is dominated by the non-thermal ( $z \geq z_{\text{diss}}$ ) synchrotron and IC emission, while the thermal ( $z \leq z_{\text{diss}}$ ) and black body components are sub-dominant. Both fits are very similar since the non-thermal emission dominates, but there are some differences due to the different thermal electron temperature. The most important difference between the two fits is that we see the thermal ( $z < z_{\text{diss}}$ ) synchrotron and IC emission components become more prominent for  $T_e = 1000$  keV. An important aspect of blazar SEDs, i.e. Fig. 1.10, 2.1 or 2.3, is that we never actually see the thermal synchrotron component in observations. Therefore, this component cannot be noticeable in our fits such that an electron temperature of 1000 keV is the maximum value we can use before we start to see a bump around  $10^{12}$  Hz.

Since the electron temperature is important for the conditions at the base of the jet, we monitor these to see which temperature is most physical. Values for the magnetization,  $\beta_p$ , the average electron Lorentz factor and the optical depth at the base of the jet are shown in Table 3.2. The table also shows the value for the  $f_{\text{heat}}$  parameter that introduces artificial heating in the acceleration region. In BHJet,  $f_{\text{heat}}$  is used to mimic shock heating by increasing  $T_e$  with a factor  $f_{\text{heat}}$  at  $z = z_{\text{diss}}$ . This shock heating is seen in observations and also in Particle In Cell simulations (e.g. Sironi & Spitkovsky 2011; Tran & Sironi 2019), but it is poorly understood so that is why the model uses this alternative parameter. Because the exact physical mechanism responsible for shock heating is unknown we would like to keep the effects of  $f_{\text{heat}}$  reasonably low with values 1-15. Despite the fact that this parameter has no direct effect on the base of

the jet, it remains a measure of how much extra energy we need in the electron distribution to reproduce the spectrum. A higher electron temperature at the base of the jet will inject more power from the start, reducing the need for artificial heating.

Property	$T_e = 200 \text{ keV}$	$T_e = 1000 \text{ keV}$
$\sigma_0$	29.731	30.796
$\beta_p$	$6.370 \times 10^{-5}$	$2.135 \times 10^{-4}$
$\langle \gamma \rangle$	1.741	6.062
$\tau_0$	$1.544 \times 10^{-3}$	$1.666 \times 10^{-3}$
$f_{\text{heat}}$	22.509	4.465

TABLE 3.2 Parameters to determine the physical conditions at the base of the jet for different electron temperatures  $T_e$ . These values were obtained from the fits shown in Fig. 3.1.

For  $T_e = 1000 \text{ keV}$  we see that the base of the jet is more strongly magnetized, it requires a lower value of  $f_{\text{heat}}$  and it has a slightly higher optical depth. Based on the value of  $f_{\text{heat}}$ , the temperature  $T_e = 1000 \text{ keV}$  is clearly favoured. Secondly,  $\beta_p$  is typically observed to lie in the range  $f_{\text{eq}} = 0.01 - 100$ . In Table 3.2, both fits lie outside this range, but as the fit with  $T_e = 1000 \text{ keV}$  requires a less extreme value this seems more reliable. Lastly, the stronger magnetization for the fit with  $T_e = 1000 \text{ keV}$  will lead to more available power for the system which we need in order to accelerate the jet and produce the large luminosity observed in blazars. Therefore, fitting blazar SEDs with a higher electron temperature appears to produce more reliable and more physical results. The higher temperature also matches observations better even though we can never reach that exact range of temperatures with the model.

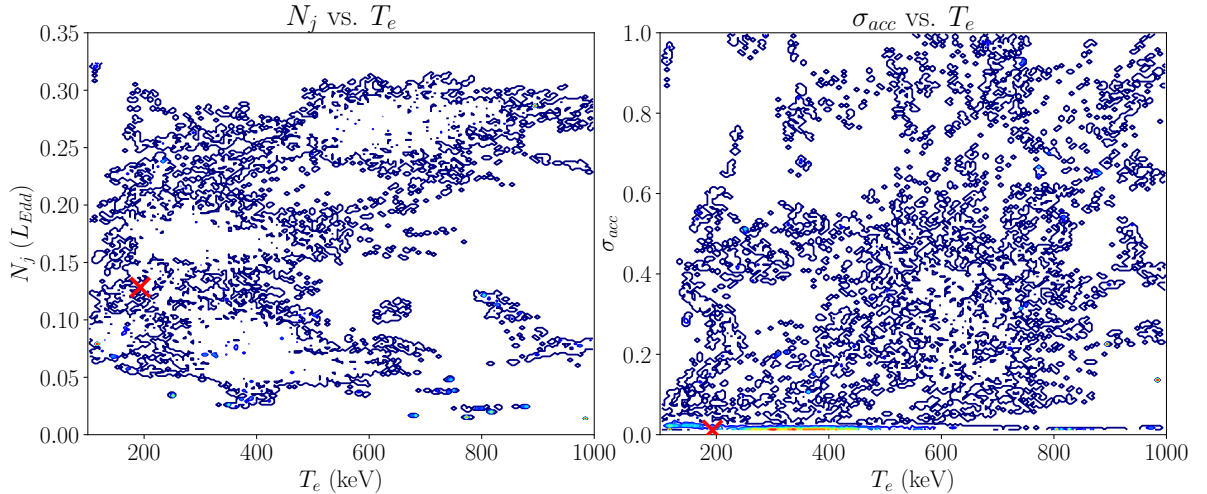


FIG. 3.2 – We show the 2D-posterior distributions with the electron temperature  $T_e$  on the x-axis and the parameters for the jet power ( $N_j$ ) and the magnetization at the acceleration region ( $\sigma_{\text{acc}}$ ) on the y-axis from left to right, respectively. The best-fit values are marked by a red cross.

In order to judge whether  $T_e$  can be used as a free parameter in our fits, we can look at the MCMC results of a fit where the electron temperature is free to vary within a range

$100 \leq T_e \leq 1000$  keV. In Fig. 3.2 we see that using  $T_e$  as a free parameter in our modelling will lead to a large amount of degeneracy with respect to other parameters. Especially, the parameters that directly influence the power budget of the jet are affected by this degeneracy. In this case, we used the jet power ( $N_j$ ), which is connected to the accretion rate, and the magnetization of the jet in the acceleration region ( $\sigma_{\text{acc}}$ ) which is the leftover magnetization after particles have been accelerated. This degeneracy is understandable because a larger electron temperature will lead to more energy in the accelerated particles such that lower values for other parameters that put power in the jet system like the jet power and the magnetization are favored. This degenerate behavior will negatively affect how well the other parameters can be constrained if the electron temperature is left free. Considering that there is no way to infer the electron temperature in blazars, we will fix the electron temperature to  $T_e = 1000$  keV in every fit presented in this thesis as this is the most physically reliable explanation possible while continuing to agree with observations.

### 3.3 SED Fitting Strategy

As discussed in Section 1.5, in order to extract physical information from blazar SEDs we fit the SED with a semi-analytical BH jet model. In general, semi-analytical jet models are complex models with a large number of degrees of freedom if they cannot be constrained enough. Even if the model can be constrained, there can be degeneracies in our parameter space for `BHJet` as shown in Section 3.2 (e.g. [Markoff et al. 2005, 2015; Lucchini et al. 2019b](#)). Therefore, we do not limit ourselves to the typical ‘fit-by-eye’ approach often used in blazar modelling.

In this thesis, the fitting strategy revolves around using the software referred to as the Interactive Spectral Imaging System (ISIS<sup>1</sup>; [Houck & Denicola 2000](#)). ISIS will allow us to perform least- $\chi^2$  fits while every model is folded through an instrument’s response function when available which is especially important when using X-ray data (see [Nowak et al. 2005](#) for more details). On top of that, we also include an absorption model (`tbabs`; [Wilms et al. 2000](#)) and a reddening model (`redden`; [Cardelli et al. 1989](#)) to account for absorption and extinction in the interstellar medium. Both of these models use the Hydrogen column depth reported for PKS 1424-418 and TXS 0506+056 in Table 2.1. Lastly, we adopt the elemental abundances of [Wilms et al. \(2000\)](#) and the photo-ionization cross-sections of the different elements of [Verner et al. \(1996\)](#). The final ISIS-syntax of the model will be of the form

$$N_{\text{ph}}(E) = \text{redden} \times \text{tbabs} \times \text{Own Model}, \quad (3.1)$$

where  $N_{\text{ph}}$  is the photon flux and `Own Model` refers to any other model that we import into ISIS ourselves. For this thesis, multiple types of jet models will be used in order to compare their results. Therefore, `Own Model` can be the multi-zone models `BHJet` and `HadJet` or their corresponding single-zone versions `OneZone_lep` and `OneZone_lephad` (see Chapter 5).

After loading the SED data into ISIS and specifying the fitting model, the “subplex”  $\chi^2$  minimization scheme is used to find a good fit. Subsequently, a further exploration of the parameter space is done using the `emcee` function. This function is a MCMC method ([Foreman-Mackey et al. 2013](#)) in which we apply 20 walkers for each free parameter where each walker performs 10.000 steps in the parameter space. The MCMC run is initialized with the

---

<sup>1</sup><https://space.mit.edu/cxc/isis/>

parameter values found with the least- $\chi^2$  fit, and will randomly move through the parameter space in order to find the statistically most optimal fit. The MCMC method has a so-called ‘burn-in’ phase in order to become statistically reliable which means that we reject the first 50% of the steps. The other 50% can be used to not only find the best fit, but also obtain confidence intervals on the parameters and allows to study any degeneracies present in the models. The results of such an MCMC run were already shown in Fig. 3.2 when the degeneracy of  $T_e$  was discussed.

### 3.4 Leptonic Multi-Zone SED Fit for TXS 0506+056

After having discussed the details of the model together with some inherent degeneracies and how we constrain it, we can look at the first SED fit with BHJet for TXS 0506+056. Again, this source gained attention after the temporal coincidence of a neutrino event and a  $\gamma$ -ray flare in 2017. The SED data spans about two weeks and is one of the most simultaneous blazar SEDs found in the literature. In Fig. 3.3 one sees the fit which shows excellent agreement with the data up to the  $\gamma$ -rays. As before in Section 3.2, similar components can be seen with the synchrotron and IC components from the thermal ( $z < z_{\text{diss}}$ ) and non-thermal ( $z \geq z_{\text{diss}}$ ) regions of the jet as well as the disk and DT black body contribution.

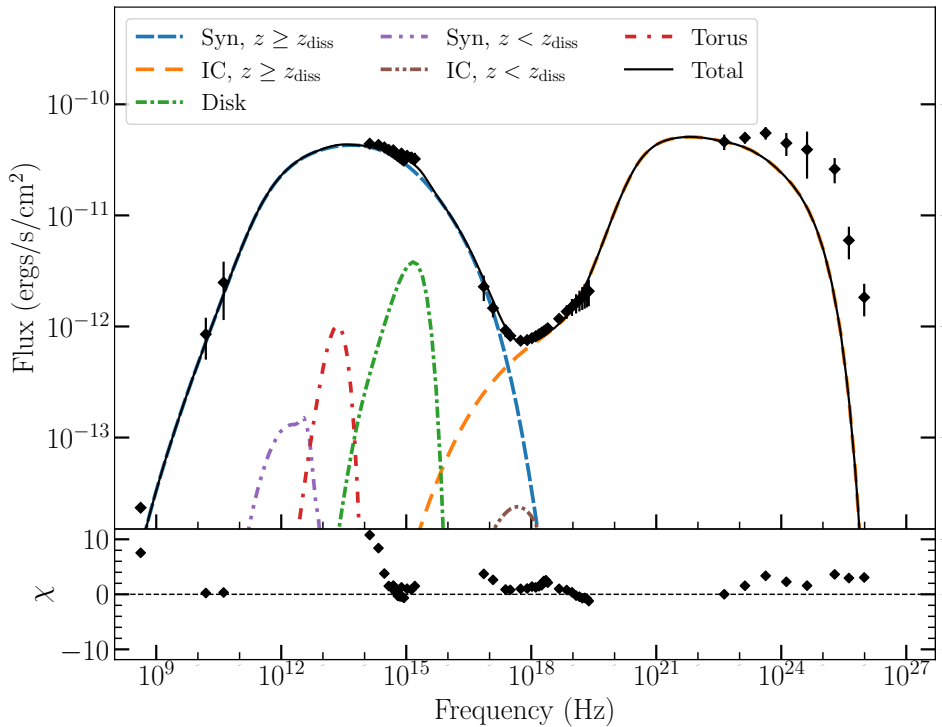


FIG. 3.3 – Fit of the flaring state of TXS 0506+056 in 2017 with BHJet together with the residuals in the lower panel. All components of the SED are shown as well as the sum of them which fits the SED data.

The emission is dominated by the non-thermal components as is expected for blazars.

However, the fit clearly falls below the data in the  $\gamma$ -ray regime. While *Fermi*/LAT has proven to be a very useful telescope, the relatively large error bars on the  $\gamma$ -ray data causes these problems. The model in combination with the statistical fitting favours a good fit of the other data points, especially in the optical and the X-rays, over a good fit of the  $\gamma$ -rays. The reasonable statistics become clear when one compares the residuals in the  $\gamma$ -ray regime to those in the optical regime, where the latter are significantly larger even though the fit seems to be closer to the data. Intuitively, one would say that this fit is wrong, but statistically this is really the best possible fit. The statistical fitting simply does not lend enough priority to the  $\gamma$ -ray data to force the model more towards those points.

In an attempt to improve on this, we tried to artificially reduce the error bars on the  $\gamma$ -ray data. The reduced error bars led to an improved fit for the  $\gamma$ -rays, but this meant that the fit was not able to explain the observed data in the X-ray regime. The data around  $10^{16}$  Hz limits the maximum Lorentz factor of the non-thermal electron distribution meaning that the most energetic electrons do not have energy to produce the high energy  $\gamma$ -rays. Artificially reducing the error bars on the  $\gamma$ -ray data will shift priority to higher Lorentz factors, which led to the synchrotron emission falling above the X-ray data. Another method to fit the  $\gamma$ -ray data better could be to change the EC calculation. In Section 1.3.4 the importance of EC scattering in blazars due to relativistic beaming was discussed together with the mathematical description. This EC model assumes that the BLR and DT emit black body radiation only at specific frequencies, but more detailed prescriptions are also available which include photon distributions that are anisotropic or span a wider energy range (Finke 2016).

$\theta$ ( $^{\circ}$ )	$N_j$ ( $L_{\text{Edd}}$ ) $10^{-2}$	$z_{\text{diss}}$ ( $R_g$ ) $10^4$	p	$f_{\text{heat}}$	$f_{\text{sc}}$ $10^4$	$\sigma_{\text{acc}}$
$1.63^{+2.51}_{-0.29}$	$2.16^{+26.0}_{-0.66}$	$1.84^{+0.13}_{-1.13}$	$2.13^{+0.11}_{-0.46}$	$14.9^{+3.17}_{-13.1}$	$1.25^{+0.28}_{-0.60}$	$0.55^{+0.32}_{-0.22}$
$L_{\text{Disk}}$ ( $L_{\text{Edd}}$ ) $10^{-2}$	$R_{\text{in}}$ ( $R_g$ )	$f_{\text{BLR}}$	$f_{\text{DT}}$	$\Gamma$	$\chi^2/\text{d.o.f.}$	
$8.77^{+4.64}_{-6.29}$	$74.5^{+19.1}_{-32.3}$	$0.26^{+0.11}_{-0.14}$	$0.12^{+0.08}_{-0.05}$	$24.0^{+5.91}_{-5.19}$	377.76/36	

TABLE 3.3 Best fit parameters for the SED data of TXS 0506+056 using BHJet together with their confidence intervals. We also report the reduced  $\chi^2$  value for the fit.

The best-fit parameters of the fit shown in Fig. 3.3 are given in Table 3.3 together with their confidence intervals obtained with MCMC. The overall reduced  $\chi^2$  value of the fit is reasonably good with  $377.76/36 = 10.49$ . Normally, when using the least- $\chi^2$  statistic a value close of 1 means that the fit exactly matches every data point. For SED fitting of blazars this is simply impossible as there are too many unknown factors in the modelling. The reasons for this are our incomplete knowledge of the exact acceleration mechanism for both the jet and the particles, combined with necessary assumptions and simplifications in any jet model. Therefore, a very good fit typically has a reduced  $\chi^2$  value of 2-3. The fit for TXS 0506+056 has a higher reduced  $\chi^2$  value, but at least we have a quantitative result of how good the fit is instead of using a ‘fit-by-eye’ approach.

Despite the reasonable reduced  $\chi^2$  value, the uncertainties on our best-fit parameters derived from the MCMC method are not as good with some being as large as or even larger than the best-fit value. Regardless of the fact that the SED is simultaneous, it is a difficult task to obtain well constrained parameters. The imperfect fit proves that we have to deal with a difficult parameter space and existing methods are not able to deal with the data very well. This kind of behavior has been seen for other sources as well, see for example [Lucchini et al.](#)

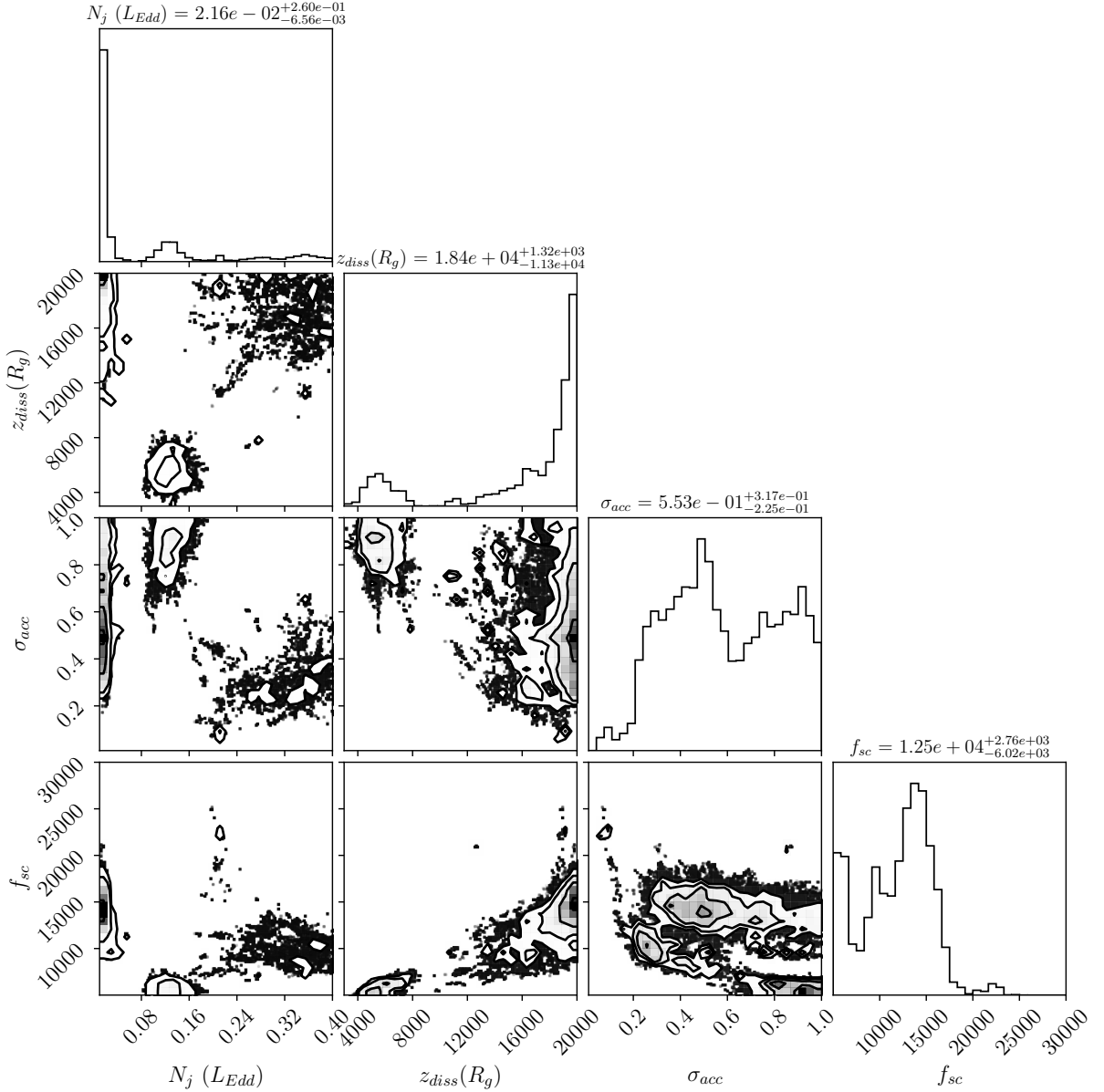


FIG. 3.4 – Corner plot with posterior distributions for the fit of the TXS 0506+056 SED with BHJet. In the plot, the model parameters for the jet power  $N_j$ , the dissipation region  $z_{diss}$ , the magnetization at the dissipation region  $\sigma_{acc}$  and  $f_{sc}$  are shown.

(2019b). Therefore, in the next section we will make use of a joint fit for the multiple epochs of PKS 1424-418 to try and obtain more reliable fit statistics.

The main advantage of using ISIS and its *emcee* function is that we can obtain posterior distributions for all the free parameters of the fit. An example of how to use this was already shown in Section 3.2, and it has proven to allow for a thorough exploration of the parameter space and the identification of model degeneracies (see e.g. Markoff et al. 2005; Lucchini et al. 2019b; Kantzas et al. 2020). These posteriors can help us identify degeneracies, both intrinsic to the model and fundamental, allowing us to obtain confidence intervals on our best-fit parameters as shown in Table 3.3. Fig. 3.4 shows a corner plot for the fit of the TXS 0506+056 SED. In this case, the corner plot is focused on the model parameters  $N_j$ ,  $z_{\text{diss}}$ ,  $\sigma_{\text{acc}}$  and  $f_{\text{sc}}$  which are intimately related to the power budget of the jet and the particle acceleration. The one-dimensional posteriors on the right-hand side show that all four of these parameters are not well constrained. Their posterior distribution are very wide, peaks are too close to the boundary or there are multiple peaks visible. This behavior is reflected by the relatively large confidence intervals that we already saw in Table 3.3. Nevertheless, the two-dimensional posteriors do show that there are some regions in the parameter space that are more favorable than others. Overall, we can conclude that the model can reproduce blazar SED data accurately, but we need additional constraints to obtain statistically well constrained parameters.

### 3.5 Leptonic Multi-Zone SED Fits for PKS 1424-418

Similar to TXS 0506+056, let us fit the SEDs of PKS 1424-418 for the epochs  $\alpha$ ,  $\gamma$ ,  $\delta$  and  $\eta$  which were discussed in Section 2.1.2. These fits can be seen in Fig. 3.5 where the quiescent states are grouped in the panel on the left. Visually, these fits worked out very well, but also the reduced  $\chi^2$  values in Table 3.4 and the residuals panels show that the fits are in excellent agreement with the data. Clearly the model is able to fit the  $\gamma$ -rays here which was not the case for TXS 0506+056. One thing to note in Fig. 3.5 is that the accretion disk component is relatively prominent and similar for all epochs of PKS 1424-418.

Table 3.4 reports the best-fit parameters for the fits shown in Fig. 3.5. As we saw before for the fit of TXS 0506+056, the uncertainties of the parameters for separate SED fits can be considerably large. Similar behavior can also be seen for the fits of the PKS 1424-418 epochs in Table 3.4, especially for the  $\delta$  epoch fit. For the  $\delta$  epoch SED, the MCMC routine was not able to find an acceptable fit with the setup discussed in Section 3.3. Using the median values of the parameter distributions, reported in Table 3.4, leads to a fit that it is not fully able to explain the  $\gamma$ -rays. Surprisingly, the fit with the lowest reduced  $\chi^2$  value that the MCMC routine found has a reduced  $\chi^2$  value of  $54.15/29 \approx 1.87$  which is extremely close to 1. This value is the lowest reduced  $\chi^2$  value found for all fits of PKS 1424-418, but apparently the MCMC algorithm diverges to quickly from this local minimum and favours other regions of the parameter space. This result again proves the intricacies of the parameter space that the model is exploring to fit these blazar SEDs.

From Table 3.4 it can also be deduced that the MCMC results show large confidence intervals on the same parameters for different epochs and comparing the median of the posterior for each parameter leads to varying results. There are large differences in the parameter values for the inclination angle,  $f_{\text{heat}}$ , the magnetization, the inner disk radius and the Lorentz factor of the jet. The jumps in the parameter values mostly occur when comparing the  $\delta$  epoch to

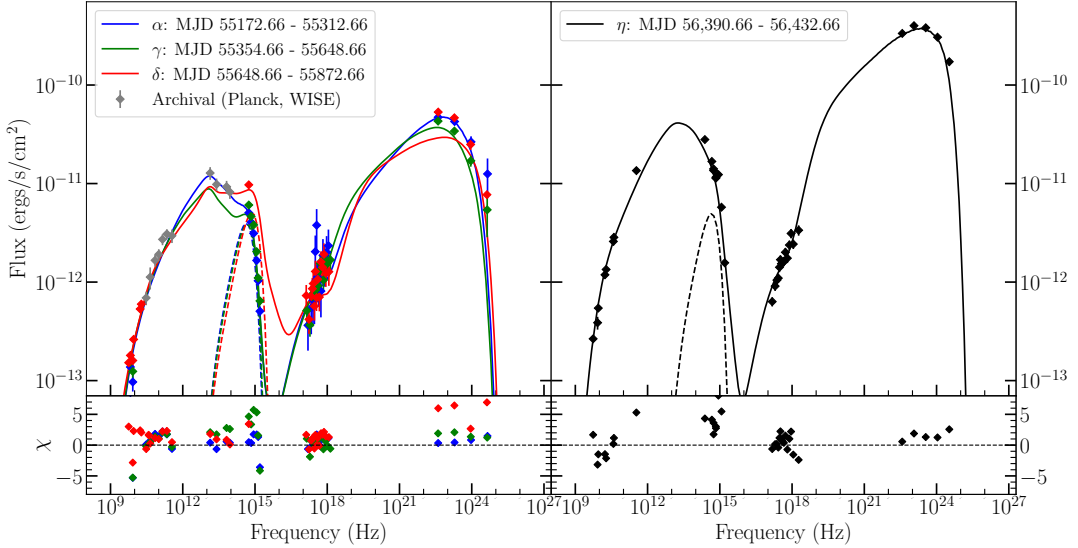


FIG. 3.5 – Fits with BHJet for all epochs of PKS 1424-418 together with their residuals in the lower panels. Left: the  $\alpha$  epoch in blue,  $\gamma$  in green and  $\delta$  in red. Right: the  $\eta$  (flaring) epoch in black. The contribution of the accretion disk for each epoch is shown by the dashed lines.

Epoch	$\theta$ ( $^{\circ}$ )	$N_j$ ( $L_{\text{Edd}}$ ) $10^{-2}$	$z_{\text{diss}}$ ( $R_g$ ) $10^4$	p	$f_{\text{heat}}$	$f_{\text{sc}}$ $10^3$	$\sigma_{\text{acc}}$ $10^{-2}$	$L_{\text{Disk}}$ ( $L_{\text{Edd}}$ ) $10^{-1}$	$R_{\text{in}}$ ( $R_g$ )	$\Gamma$	$\chi^2/\text{d.o.f.}$
$\alpha$	$1.76^{+0.48}_{-0.32}$	$5.33^{+2.23}_{-1.19}$	$3.17^{+0.53}_{-0.65}$	$1.36^{+0.08}_{-0.04}$	$2.30^{+3.61}_{-0.99}$	$3.68^{+0.89}_{-0.57}$	$9.11^{+5.91}_{-4.82}$	$3.00^{+0.15}_{-0.24}$	$115.89^{+7.42}_{-9.71}$	$35.28^{+3.25}_{-4.06}$	150.16/27
$\gamma$	$1.71^{+0.33}_{-0.17}$	$6.03^{+2.09}_{-1.18}$	$1.93^{+0.05}_{-0.11}$	$1.52^{+0.05}_{-0.02}$	$2.09^{+1.65}_{-0.42}$	$3.70^{+0.83}_{-0.38}$	$9.77^{+4.62}_{-3.28}$	$2.97^{+0.91}_{-1.29}$	$98.97^{+0.77}_{-1.68}$	$31.16^{+3.18}_{-2.90}$	379.23/28
$\delta$	$3.12^{+0.97}_{-0.63}$	$3.25^{+15.79}_{-0.77}$	$1.86^{+0.88}_{-0.61}$	$1.68^{+0.10}_{-0.07}$	$8.29^{+10.88}_{-3.89}$	$15.49^{+0.62}_{-0.33}$	$14.92^{+13.46}_{-0.57}$	$3.88^{+0.59}_{-1.11}$	$45.51^{+15.95}_{-13.43}$	$17.13^{+9.10}_{-1.68}$	1418.92/29
$\eta$	$0.14^{+0.03}_{-0.02}$	$2.23^{+0.14}_{-0.10}$	$3.87^{+0.09}_{-0.21}$	$1.503^{+0.005}_{-0.002}$	$2.02^{+0.15}_{-0.13}$	$4.95^{+0.27}_{-0.23}$	$3.32^{+0.78}_{-0.67}$	$3.76^{+0.08}_{-0.13}$	$121.66^{+3.57}_{-3.48}$	$33.29^{+1.21}_{-1.37}$	340.04/27

TABLE 3.4 Best fit parameters for the quiescent epochs  $\alpha$ ,  $\gamma$  and  $\delta$  and the flaring epoch  $\eta$  of PKS 1424-418. We also report the reduced  $\chi^2$  value for each fit and the confidence intervals for all parameters.

the other epochs, but also when we compare the flaring state to the quiescent  $\alpha$  and  $\gamma$  epochs. Overall, we see that the source parameters do not change drastically when looking at a different epoch, but the uncertainties for all parameters make it difficult to actually verify this.

To give more insight into whether the parameters are actually well constrained, we make a corner plot for the same parameters as was done for TXS 0506+056. The corner plot for the  $\alpha$  epoch of PKS 1424-418 is shown in Fig. 3.6. When we compare this corner plot to Fig. 3.4, we do see an improvement in the posteriors. The posteriors are less scattered around the parameter space and there really appears to be one favoured region. Nevertheless, the one-dimensional posteriors can be rather broad such that the confidence intervals are relatively large. Interestingly, we see clear signs of degeneracies in the fitting. The ‘banana’ shaped two-dimensional posteriors for  $N_j$  and  $\sigma_{\text{acc}}$  and for  $f_{\text{sc}}$  and  $\sigma_{\text{acc}}$  is a sign of the existence of a degeneracy between these parameters. Intuitively, for the first case this makes sense as both the magnetization and the jet power are ways to give energy to the system and lead to more emission. For the second case, it is less intuitive, but a possible explanation might be that

converting more magnetic energy into particle acceleration will lead to particles with a higher overall Lorentz factor. Nevertheless, it would be better if the parameters could be constrained even better.

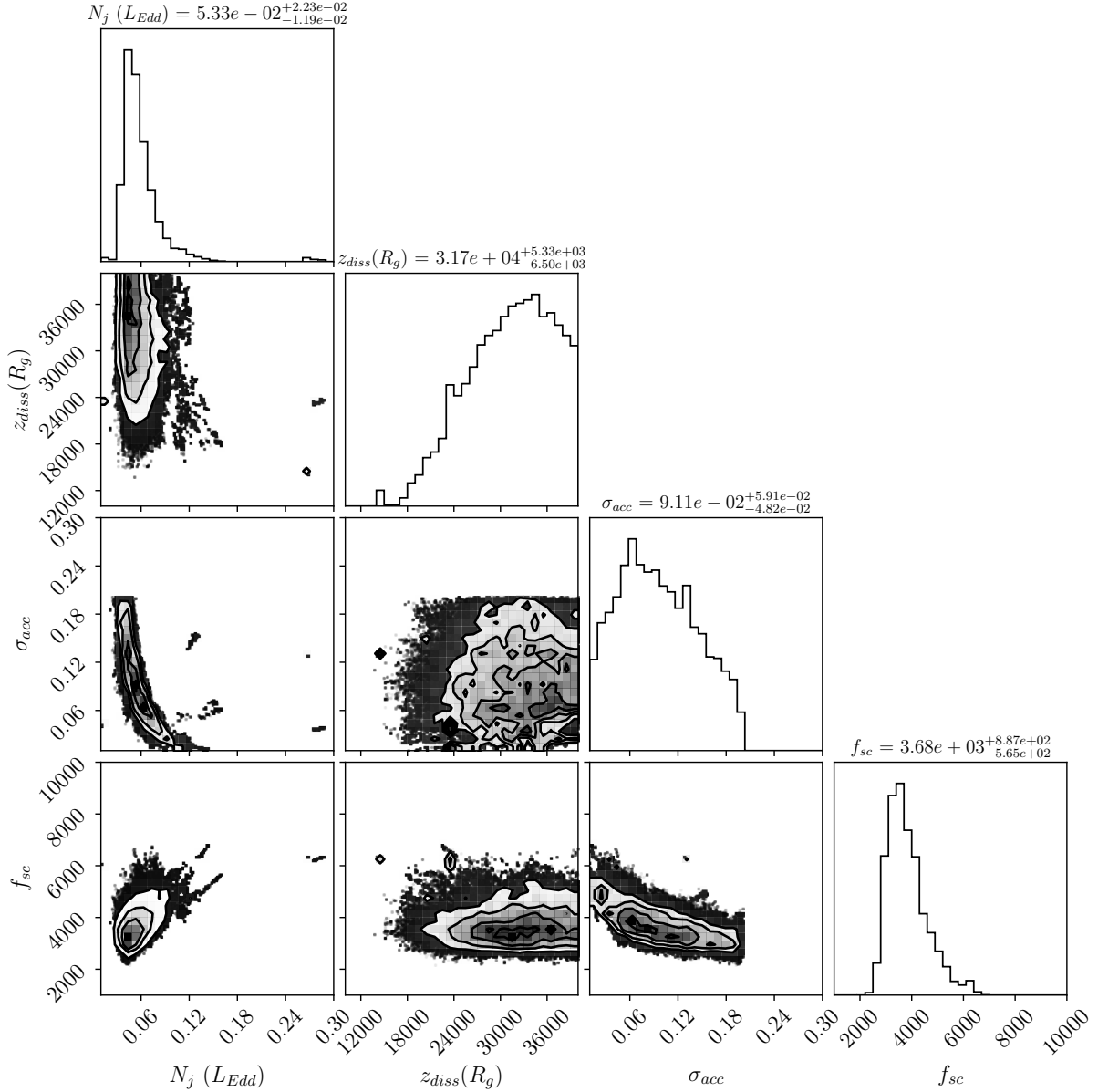


FIG. 3.6 – Corner plot with posterior distributions for the fit of the  $\alpha$  epoch of PKS 1424-418 with BHJet. In the plot, the model parameters for the jet power  $N_j$ , the dissipation region  $z_{diss}$ , the magnetization at the dissipation region  $\sigma_{acc}$  and  $f_{sc}$  are shown.

### 3.5.1 Joint Fit of the Quiescent and Flaring State of PKS 1424-418

After having seen the fits with `BHJet` for TXS 0506+056 and all epochs of PKS 1424-418, the goal of this section is to improve the statistics obtained during fitting by using *joint* SED fitting. The availability of SEDs for multiple epochs of PKS 1424-418 make this a very useful source for this purpose. First of all, what is a joint fit? A joint fit means that we fit multiple datasets simultaneously with the same model where we tie certain parameters for both. There are components like the jet length or the accretion disk luminosity of which we know that they cannot change drastically in the time span between two data sets. The consistent behavior of blazars thus allows us to constrain the available parameter space more. In the past, joint SED fitting has been used successfully to study individual SEDs of LLAGN and BH binaries simultaneously (Markoff et al. 2015; Connors et al. 2016). Subsequently, joint SED fitting was applied to different MWL data sets of the same source by Connors et al. (2019) for the BH binary GX 339-4 and by Lucchini et al. (2019b) for the BL Lac PKS 2155–304. In this section, we will use the latter approach where we fit the SEDs of the multiple epochs of PKS 1424-418.

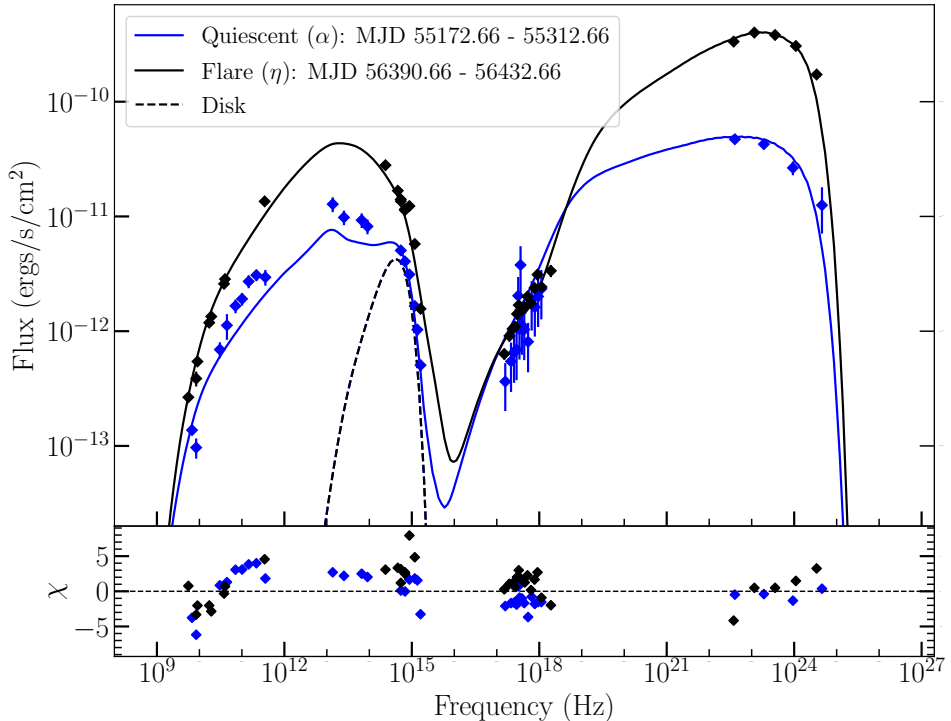


FIG. 3.7 – Joint fit with `BHJet` for the epochs  $\alpha$  and  $\eta$  of PKS 1424-418 which represent a quiescent and a flaring state of the source respectively. The contribution of the accretion disk for each epoch is shown by the dashed lines. The residuals for the fits of both epochs are shown in the lower panel.

For such a joint fit we use the SEDs corresponding to the  $\alpha$  and  $\eta$  epochs which represent a quiescent and a flaring state, respectively. Since we do not expect the properties of the bulk jet flow to change drastically, we will tie parameters such as the inclination angle, the jet power, the location of the acceleration region and the magnetization. Additionally, the

accretion disk parameters will be tied between both epochs. [Lucchini et al. \(2019b\)](#) found that the differences between epochs of the BL Lac PKS 2155-304 could be explained by only changing the parameters that determine the non-thermal particle distribution. Therefore, we will let the spectral index,  $f_{\text{heat}}$  and  $f_{\text{sc}}$  vary independently for both epochs. The resulting joint fit of these SEDs can be seen in Fig. 3.7 where we see excellent agreement between the fits and the SED data. We also found that we could not tie the jet Lorentz factor since the quiescent and flaring state required different Doppler factors to fit the data.

Epoch	$\theta$ (°)	$N_j$ ( $L_{\text{Edd}}$ ) $10^{-2}$	$z_{\text{diss}}$ ( $R_g$ ) $10^4$	p	$f_{\text{heat}}$	$f_{\text{sc}}$ $10^3$	$\sigma_{\text{acc}}$ $10^{-2}$	$L_{\text{Disk}}$ ( $L_{\text{Edd}}$ ) $10^{-1}$	$R_{\text{in}}$ ( $R_g$ )	$\Gamma$	$\chi^2/\text{d.o.f.}$
Joint	$0.27^{+0.04}_{-0.01}$	$2.80^{+0.17}_{-0.32}$	$3.88^{+0.08}_{-0.06}$				$3.61^{+1.50}_{-0.68}$	$3.27^{+0.18}_{-0.04}$	$129.20^{+0.60}_{-1.36}$		589.37/60
$\alpha$				$1.77^{+0.04}_{-0.04}$	$1.11^{+0.13}_{-0.08}$	$5.17^{+0.40}_{-0.55}$					$33.94^{+1.36}_{-1.36}$
$\eta$				$1.502^{+0.002}_{-0.001}$	$2.49^{+0.24}_{-0.15}$	$5.05^{+0.33}_{-0.29}$					$29.43^{+1.34}_{-1.59}$

TABLE 3.5 Best fit parameters for the joint fit of the quiescent epoch  $\alpha$  and the flaring epoch  $\eta$  of PKS 1424-418 together with their confidence intervals. We also report the reduced  $\chi^2$  value for the fit.

The best-fit parameters for the joint fit together with their confidence intervals can be found in Table 3.5. Despite the fact that the joint fit is more constrained, it is able to find fits which are in good agreement with the data. Moreover, it immediately becomes clear from the confidence intervals that the joint fitting has helped to obtain best-fit parameters that are better constrained than before. The value of some parameters like the dissipation region, the accretion disk luminosity and the Lorentz factor of the jet remains rather similar to the separate fits in Table 3.4. However, there is an obvious change in the joint fit where we find a significantly lower inclination angle than before. The same change was seen for the separate fit of the flaring epoch, but for none of the quiescent states in Table 3.4. A lower inclination angle leads to more relativistic beaming and decreases the values of the jet power and magnetization that determine the power budget in the system. Interestingly, the change from the quiescent state into the flaring state of PKS 1424-418 can be described by only changing the details of the particle distribution with the spectral index (p), the heating of the electrons ( $f_{\text{heat}}$ ) and the maximum Lorentz factor ( $f_{\text{sc}}$ ) while we need a slightly lower bulk jet Lorentz factor ( $\Gamma$ ). Moreover, the flaring state favours a non-thermal spectral index of 1.5 which is lower than one would expect for known acceleration mechanism like Fermi acceleration of magnetic reconnection.

Once more, let us use a corner plot of the same model parameters to judge whether the fit is statistically more constrained than what we found before. This corner plot is shown in Fig. 3.8 where we clearly see an improvement in the posteriors of the used parameters. Not only are all posteriors single peaked, their width has also shrunk down to a level where we can actually be certain of the best-fit value. Looking at the two-dimensional posteriors, there remains some scatter but compared to previous fits this is an improvement. To confirm this, note the plot ranges used in Fig. 3.8 and compare these to Fig. 3.4 and 3.6. These corner plots confirm that using joint fits allows us to be more confident about the best-fit parameters.

As the joint fit is the best constrained fit we have with well defined posteriors, we can use these to study the transition from a quiescent to a flaring state more closely. The best-fit values showed that the transition can be explained by just changing the jet velocity and the details

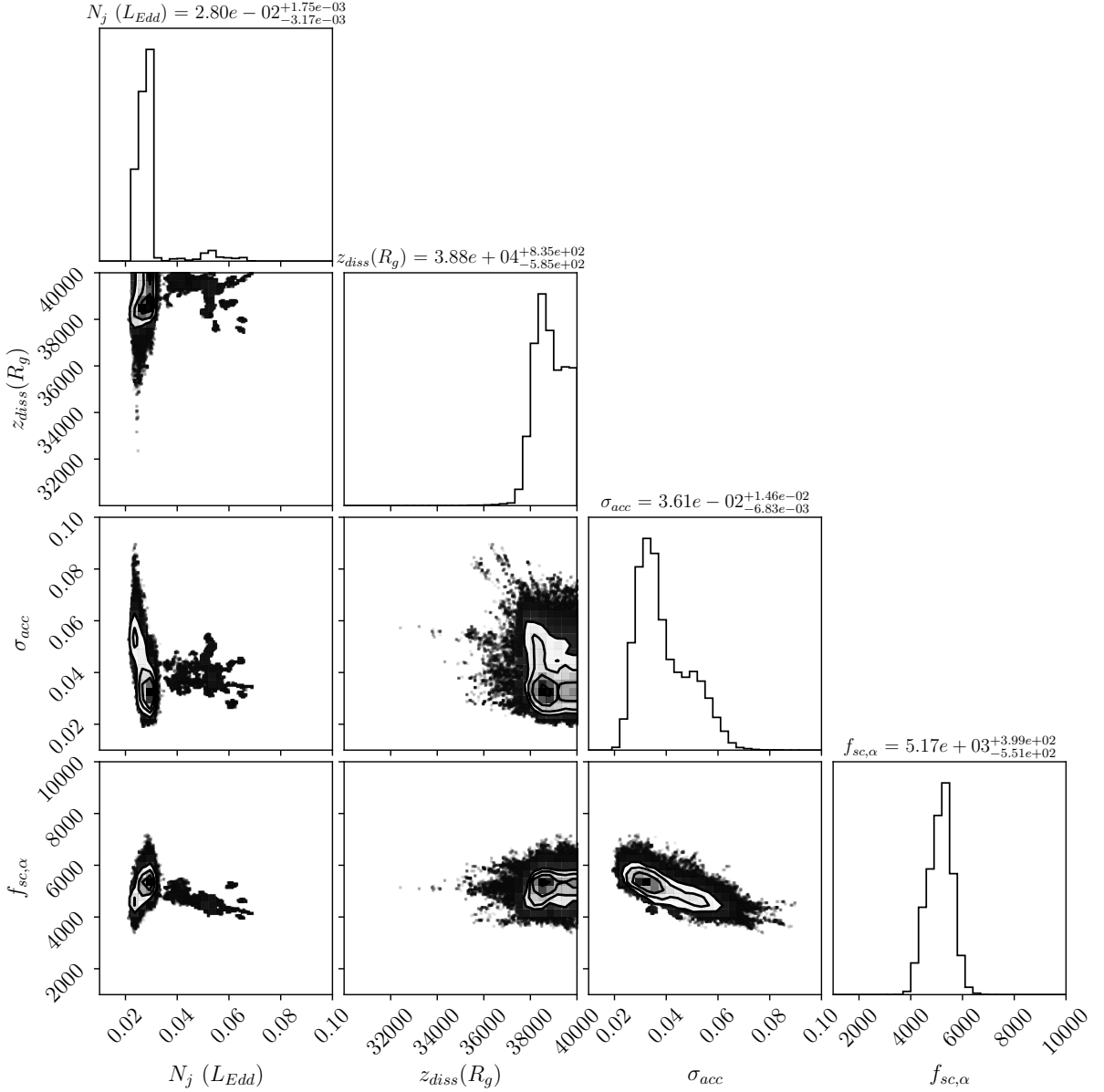


FIG. 3.8 – Corner plot with posterior distributions for the joint fit of  $\alpha$  and  $\eta$  epochs of PKS 1424-418 with BHJet. In the plot, the model parameters for the jet power  $N_j$ , the dissipation region  $z_{diss}$ , the magnetization at the dissipation region  $\sigma_{acc}$  and  $f_{sc}$  are shown.

of the emitting particle distribution. Similar to what we did in Section 3.2, we can compare the conditions in the jet by using some physical quantities at the base and the acceleration region as can be seen in Table 3.6. The table shows that the jet base for the flaring state is less strongly magnetized, slightly more magnetically dominated and has a higher optical depth. As the jet evolved towards the acceleration region, their magnetization is the same because of the joint fit but we do see some important differences. While the flaring state demands slightly

Jet Base	$\alpha$	$\eta$	Acceleration Region	$\alpha$	$\eta$
$\sigma_0$	30.509	26.346	$\sigma_{\text{acc}}$	$3.548 \times 10^{-2}$	$3.548 \times 10^{-2}$
	$2.155 \times 10^{-4}$	$2.495 \times 10^{-4}$	$\beta_p$	0.423	1.075
	$3.443 \times 10^{-4}$	$3.948 \times 10^{-4}$	$f_{\text{heat}}$	1.095	2.450
			$P_{\text{jet}}$ (erg/s)	$4.840 \times 10^{44}$	$5.614 \times 10^{44}$
			$P_B$ (erg/s)	$8.306 \times 10^{42}$	$9.642 \times 10^{42}$
			$P_e$ (erg/s)	$3.515 \times 10^{42}$	$1.037 \times 10^{43}$
			$P_p$ (erg/s)	$4.722 \times 10^{44}$	$5.414 \times 10^{44}$

TABLE 3.6 Parameters to determine the physical conditions at the base of the jet and the acceleration region for the joint fit of PKS 1424-418 with BHjet. These values were obtained from the fits shown in Fig. 3.7.

more power in the acceleration region, it does accelerate the electrons to a lower maximum Lorentz factor (see Table 3.5). Even more power is injected by the larger value of  $f_{\text{heat}}$ , and is reflected by a more particle dominated equipartition parameter. These physical conditions support the idea that the structural parameters of the jet remain the same, and that a flaring state can be explained by altering the emitting lepton distribution.

# Chapter 4

## Multi-Zone Modelling of Blazar SEDs with HadJet

After having discussed the fits with the leptonic multi-zone model `BHJet` in Chapter 3, we can now focus on the lepto-hadronic version called `HadJet`. This version contains the same leptonic processes as `BHJet` which have been discussed in [Lucchini et al. \(2022\)](#) or Section 1.3. The difference between the codes is that `HadJet` takes the emission of accelerated protons into account. The addition of non-thermal protons leads to proton synchrotron emission and the hadronic processes discussed in Section 1.4. In this thesis, we will use the most recent version by [Kantzas et al. \(2020\)](#). This paper together with the one by [Kantzas et al. \(2023a\)](#), give a very detailed description of `HadJet`, including its assumptions and caveats while highlighting the differences with `BHJet`. In this Chapter, Section 4.1 discusses the `HadJet` code to highlight its differences with `BHJet`, and the modifications that were made to both make it more compatible with results produced by `BHJet` and also to make the model more realistic. This section will be followed by the fits for TXS 0506+056 and PKS 1424-418 in Sections 4.2 and 4.3, respectively.

### 4.1 HadJet: A Lepto-Hadronic Multi-Zone Jet Model

The history of `HadJet` is very similar to that of `BHJet` in terms of its development. The first version of the model was developed by [Falcke & Biermann \(1995\)](#) after which [Markoff et al. \(2001\)](#) extended it to a full bipolar, multi-zone jet model. At the time, the model only considered radiation produced by leptons, but protons were present as a cold, non-interacting component. Taking the development and improvements described in [Lucchini et al. \(2019b\)](#) into account, `HadJet` was developed in tandem with `BHJet` such that both codes have the same structure and underlying libraries. The assumed jet geometry is the same as presented in Fig. 1.20 as well as the underlying assumptions for the jet evolution and the jet matter content described in Section 1.5.2.

The main difference with `BHJet` is that a fraction  $f_{\text{nth, p}}$  of the cold protons are now accelerated into a powerlaw once they reach the acceleration region at  $z = z_{\text{diss}}$ . In Section 1.2.2, we discussed that the exact mechanism for particle acceleration is unknown so this also applies to both electrons as well as protons. Therefore, we make the simplest assumption of the protons being accelerated into a non-thermal powerlaw. In order to specify this extra feature, one needs four new parameters (in bold) including  $f_{\text{nth, p}}$ . The hadronic particle distribution is a powerlaw, with a spectral index  $\mathbf{p_p}$  ranging between the Lorentz factors determined by the parameters `hadsw` (minimum value) and the maximum set by  $f_{\text{sc}}$ . The powerlaw is normalized by setting the lepton-to-proton ratio  $\eta_e$  such that electron and proton number density are tied together. The fact that protons are only accelerated after we reach  $z = z_{\text{diss}}$  means that the

emission resulting from hadronic processes will only be produced in the slices of the jet after this region. As discussed in Section 1.5.2, there is continuous re-acceleration of the particles in this part of the jet. In theory, the parameter  $\mathbf{z}_{\text{diss, max}}$  allows us to set the maximum value of  $z$  up to which we consider this continuous re-acceleration for the non-thermal protons. However, this feature of the model is not used in this thesis and protons keep being accelerated until  $z = z_{\text{max}}$  is reached.

It is important to note that the acceleration mechanisms of both electrons and protons in these relativistic jets are uncertain, but we would like to keep the number of free parameters limited. Therefore, we need to make assumptions for the non-thermal particle distributions that are used in the SED fitting. Assuming that most of the emission is leptonic, spectral features like the slope of the flat synchrotron emission and maximum frequency can be translated into details of the non-thermal electron distribution. However, as the hadronic emission is sub-dominant, this cannot be done for the non-thermal proton distribution. Therefore, we assume that there is a common acceleration mechanism of both protons and electrons such that the spectral index ( $p_p$ ) and the maximum Lorentz factor of the non-thermal protons is the same as for the non-thermal electron distribution. Initially, we also tried an identical fraction of non-thermal protons ( $f_{\text{nth, p}}$ ) and electrons ( $f_{\text{nth, e}}$ ), but the modelling required smaller hadronic fractions.

#### 4.1.1 Modifications to the HadJet Code

As `HadJet` is a rather new code, it is being improved and expanded to make it a more realistic jet model. For this thesis, I implemented a number of improvements making it somewhat different than the model presented in [Kantzias et al. \(2020\)](#). Firstly, the process of the EBL attenuation described in Section 2.2 was implemented in `HadJet` just as for all the other jet models used in this thesis. For a lepto-hadronic model, EBL attenuation can have a significant effect on the SED by attenuating the  $\gamma$ -ray flux produced in the hadronic interactions. An example of this effect is shown in Fig. 2.5.

Secondly, in Appendix B.1 one can see that the  $f_{\text{sc}}$  parameter can be set to values  $f_{\text{sc}} < 0.1$  and to values  $f_{\text{sc}} > 10$  for `BHJet`. For values  $f_{\text{sc}} < 0.1$  this parameterizes the acceleration timescale, and in turn determines the acceleration efficiency by using the timescale of each process in the jet. For values  $f_{\text{sc}} > 10$  this parameter directly sets the maximum Lorentz factor of the accelerated electrons without using the characteristic timescales. Intuitively, the first case is more realistic, but the extreme environments of blazar jets are difficult to explain with such a numerical setup and require values of  $f_{\text{sc}} \sim 10^{-7} - 10^{-9}$ . Such extreme acceleration efficiencies lead to numerical instability of the models, requiring us to use values  $f_{\text{sc}} > 10$  instead. Therefore, we directly set the maximum Lorentz factor of the accelerated electrons for the fits done with `BHJet` (see Chapter 3). For `HadJet` it was known that the code was not compatible with values below  $f_{\text{sc}} \sim 10^{-4}$  which again confirmed the problem at hand. Therefore, for `HadJet` I adopted the same implementation of  $f_{\text{sc}}$  as done in `BHJet` where one can directly set the maximum Lorentz factor of the accelerated electrons and protons. Due to uncertainties on the exact acceleration mechanisms of protons and electrons,  $f_{\text{sc}} > 10$  also directly sets the maximum Lorentz factor of the accelerated protons to the same value as for the electrons.

Lastly, the effects of proton synchrotron emission were neglected in previous versions of

the `HadJet` code. Previous research has shown that proton synchrotron emission can become a dominant component in blazars because of the strong magnetic fields present (Mannheim 1993; Mücke et al. 2003; Böttcher et al. 2013; Liidakis & Petropoulou 2020). Indirectly, the synchrotron photons emitted by the protons will also be available for IC scattering. Although these interactions might be suppressed compared to electrons (see Section 1.4.3), they need to be taken into account. To estimate the significance of these interactions, we again come back to the acceleration of protons and the conservation of energy. Previous work has shown that proton synchrotron models can work when fitting blazar SEDs, but these models do require relatively extreme conditions (Böttcher et al. 2013). Previously proposed jet launching mechanisms that consider hadronic processes have struggled with the large amount of energy required to accelerate protons. The power demand is far larger than when just accelerating electrons and can surpass the energy budget of the jets or even the Eddington luminosity of the source. This problem is called the *blazar energy crisis* (Cao & Wang 2014; Liidakis & Petropoulou 2020), and it is an open question in the field.

There has been intense debate on how to solve the blazar energy crisis, and some have even proposed that hadronic models are not applicable to blazars and that we need a change of the accretion paradigm (Zdziarski & Böttcher 2015). One potential solution for the proton energy crisis is to consider a conserved mass loading jet model in which mass entrainment into the jet is considered (Kantzas et al. 2023b). Magnetic pinch instabilities at the boundary between the jet and the surrounding wind outflows lead to the formation of eddies that trap matter from the wind and drive it into the jet (Begelman 1998; Mignone et al. 2013; Gourgouliatos & Komissarov 2018; Bodo et al. 2021). This mass entrainment has been seen in GRMHD simulations (Chatterjee et al. 2019), and the region in the jet where the effects of mass loading become important have been suggested to be connected to the region where the non-thermal particle acceleration occurs (Markoff et al. 2005; Polko et al. 2014). The first results for this novel approach seem promising but there is no definitive answer yet.

## 4.2 Lepto-Hadronic Multi-Zone SED Fit for TXS 0506+056

Similar to Chapter 3, we first look at a fit of the SED data for the flare of TXS 0506+056 in 2017. This fit can be seen in Fig. 4.1 where we see a similar fit as before with the same components, but now there are also hadronic components as expected. Generally, the contribution of proton synchrotron and proton IC is small as explained in Section 1.4.3. The components for proton synchrotron (pink dashed line) and the synchrotron emission produced by secondaries from proton-proton interactions (gray dashed line) are rather weak. Normally, they would fall below the lower limit of Fig. 4.1 so we multiply their flux by a constant to give an idea of their shape and strength. More noticeable is the component for secondary synchrotron emission produced by secondaries from the p $\gamma$  interactions (yellow dashed line). The fact that this component is stronger was to be expected since proton synchrotron emission is significantly suppressed and the relatively low proton number density will severely inhibit pp interactions. Alternatively, the p $\gamma$  interactions occur more often as there is a strong radiation field due to the electron synchrotron emission and the external photon fields in AGN.

The best-fit parameters for the fit with `HadJet` are reported in Table 4.1, where we report confidence intervals for the parameters as well as the reduced  $\chi^2$  value of the fit. When we compare these parameters to the ones for the leptonic model in Table 3.3, we see that the results

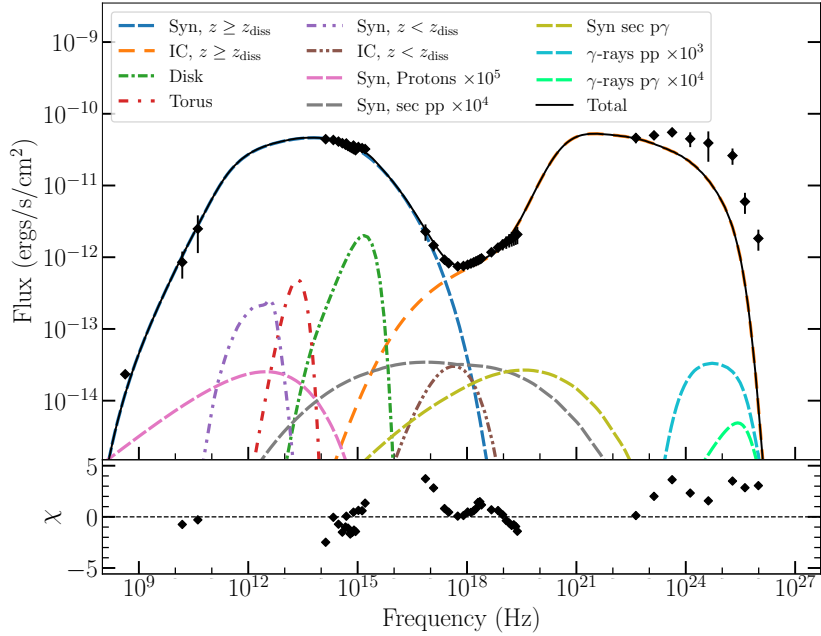


FIG. 4.1 – Fit of the flaring state of TXS 0506+056 in 2017 with `HadJet` together with the residuals in the lower panel. All components of the SED are shown as well as the sum of them which fits the SED data.

$\theta$ (°)	$N_j$ ( $L_{\text{Edd}}$ ) $10^{-2}$	$z_{\text{diss}}$ ( $R_g$ ) $10^4$	$p$ ( $= p_p$ )	$f_{\text{heat}}$	$f_{\text{sc}}$ $10^4$	$\sigma_{\text{acc}}$
$1.41^{+1.69}_{-0.22}$	$2.65^{+10.40}_{-0.58}$	$2.59^{+0.31}_{-0.42}$	$2.22^{+0.08}_{-0.34}$	$14.12^{+2.22}_{-11.28}$	$1.71^{+0.19}_{-0.29}$	$0.34^{+0.10}_{-0.10}$
$L_{\text{Disk}}$ ( $L_{\text{Edd}}$ ) $10^{-2}$	$R_{\text{in}}$ ( $R_g$ )	$f_{\text{BLR}}$	$f_{\text{DT}}$	$\Gamma$	$f_{\text{nth, p}}$	$\chi^2/\text{d.o.f.}$
$13.63^{+7.05}_{-6.79}$	$50.48^{+31.00}_{-26.53}$	$0.23^{+0.11}_{-0.12}$	$0.11^{+0.11}_{-0.04}$	$25.43^{+5.89}_{-4.15}$	$0.35^{+0.36}_{-0.26}$	151.91/35

TABLE 4.1 Best fit parameters for the SED data after the 2017 flare of TXS 0506+056 using `HadJet`. We also report the reduced  $\chi^2$  value for the fit.

for `HadJet` are slightly different but they agree with each other considering the corresponding confidence intervals. First of all, `HadJet` is able to find a fit with a lower reduced  $\chi^2$  value, but based on the residuals panel this can mostly be attributed to a better fit in the optical/UV regime. The uncertainties on the data are very small there such that a small difference in the fit can lead to a relatively large improvement in the reduced  $\chi^2$  value.

The most obvious differences are that the fit with `HadJet` requires more jet power, a lower magnetization and particles with a higher maximum Lorentz factor. There are also some minor differences in the best-fit values for  $z_{\text{diss}}$  and the disk parameters  $L_{\text{Disk}}$  and  $R_{\text{in}}$ . The fact that protons need to be accelerated requires more power such that the initial jet power needs to be

increased. However, the acceleration of protons will reduce the energy available to accelerate electrons, but these still provide the dominant contribution to the SED fit. In order to have enough power in the electrons, we see that the relativistic beaming is stronger through a higher jet Lorentz factor and a smaller inclination angle. We also see that the accretion disk is more luminous and closer to the BH for the hadronic fit. While the accretion disk component is similar to the one found in Section 3.4, it does provide denser photon fields with more energy per photon for the EC scattering.

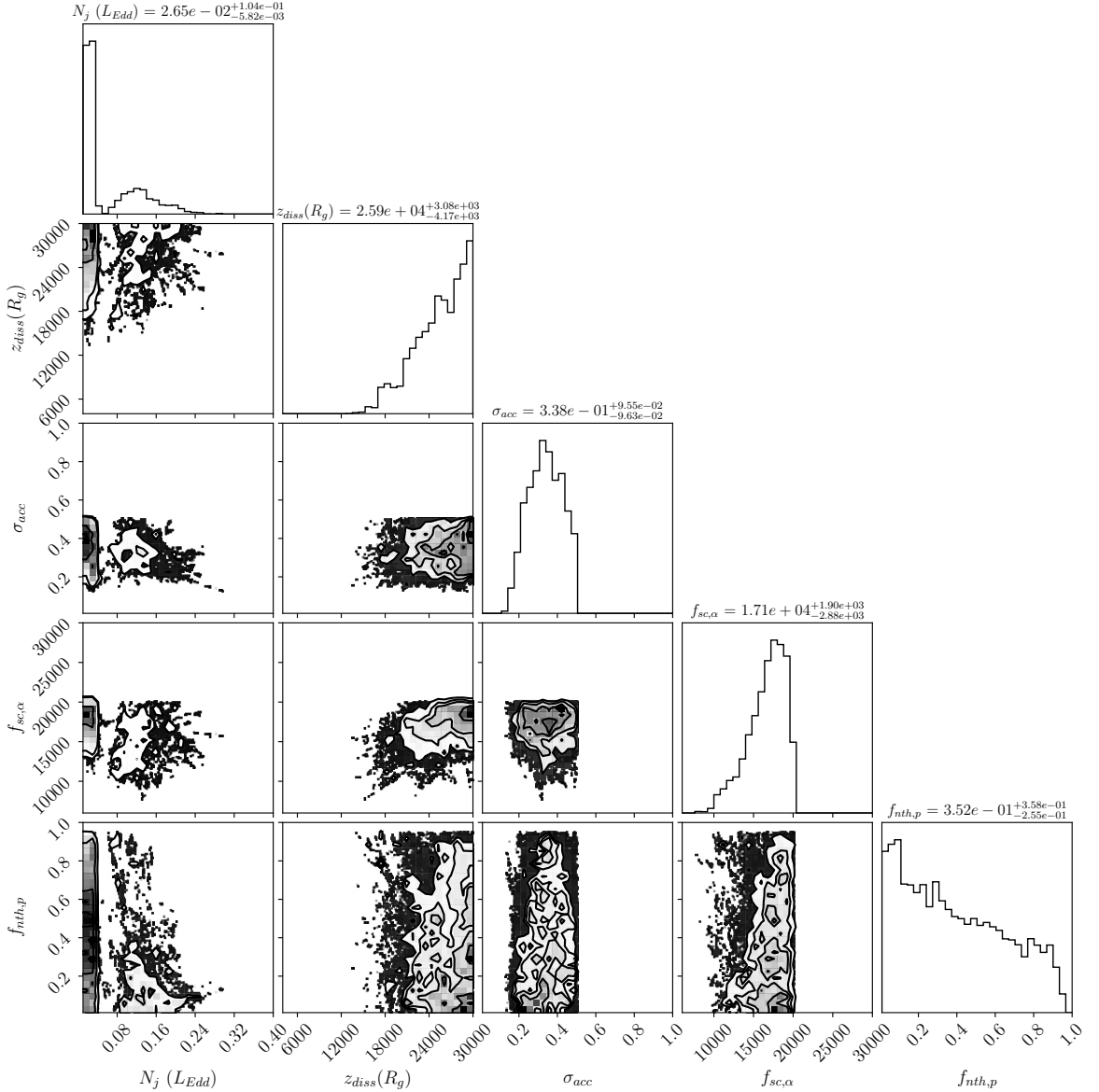


FIG. 4.2 – Corner plot with posterior distributions for the fit with `HadJet` of the TXS 0506+056 SED. In the plot, the model parameters for the jet power  $N_j$ , the dissipation region  $z_{diss}$ , the magnetization at the dissipation region  $\sigma_{acc}$ ,  $f_{sc}$  and the non-thermal proton fraction  $f_{nth, p}$  are shown.

Despite the addition of non-thermal protons and the corresponding hadronic interactions, the fit is dominated by leptonic emission. Looking at Table 4.1, we see that  $f_{\text{nth}, p} = 0.35^{+0.36}_{-0.26}$ , which is very close to the non-thermal fraction of electrons which we fixed to  $f_{\text{nth}, e} = 0.5$ . However, the large confidence intervals make it difficult to judge whether this is the case. When comparing the hadronic components to the leptonic components, we see that it would be challenging to fit the same SED with a model where the hadronic components are dominating. The dominance of the leptonic emission is the reason that leptonic jet models, either single- or multi-zone, work so well in explaining most of the blazar SEDs available. Looking at any SED fit, it is difficult to judge what the relative contribution of protons compared to leptons should be. The only firm constraint on the non-thermal proton fraction is that the secondary emission cannot overshoot the X-ray emission that is observed around  $10^{18} - 10^{20}$  Hz. Nevertheless, Fig. 4.1 shows that the secondary synchrotron emission is orders of magnitude below the X-ray data. For the fit we could allow more protons than electrons in the jet, i.e.  $\eta_e < 1$ , but this contradicts the current understanding of the jet matter content. When we look at the posteriors of the fit in Fig. 4.2, we also see that the non-thermal proton fraction is badly constrained. The probability for lower values tends to be a bit higher, but one could ask whether that is really true since not accelerating protons will simply lead to the complete leptonic fit again.

Looking at the corner plot in Fig. 4.2, we see that the parameters are badly constrained. They are even less constrained than for the fit with BHJet in Section 3.4. There is simply too much scatter in the posteriors which is reflected by the confidence intervals in Table 4.1. Some parameters like  $z_{\text{diss}}$ ,  $p$ ,  $f_{\text{sc}}$  and  $\Gamma$  do show well constrained behavior, and the magnetization is better constrained than for the fit with BHJet. Overall, these separate fits of the TXS 0506+056 SED seem to be unable to explain the data well enough while also being constrained.

In order to study the conditions in the jet, we can again look at some physical quantities at the base and the acceleration region of the jet just as we did in Sections 3.2 and 3.5. Table 4.2 shows the initial conditions for the magnetization, the equipartition parameter and the optical depth at the base of the jet. At the base the conditions are very similar in both the leptonic and the lepto-hadronic case. The leptonic fit has a slightly higher magnetization, but is not more magnetically dominated. The only difference is a slightly higher optical depth for the lepto-hadronic model caused by the injection of more electrons due to the higher jet power  $N_j$ .

Moving on to the acceleration region, Table 4.2 also shows the shock heating of the electrons as well as the power budget of the jet that is composed of the power in the magnetic field, protons and electrons, i.e.  $P_{\text{jet}} = P_B + P_e + P_p$ . For the acceleration region we see that the conditions are different for both models. Although the magnetization for the lepto-hadronic fit is lower, it is more magnetically dominated than the leptonic version. A more magnetically dominated lepton distribution means that power is taken away from the electrons to fuel the proton power. The electron power in the fit with HadJet is almost an order of magnitude lower than for the BHJet fit. Therefore, we see that adding non-thermal protons to the model does not necessarily change the predicted SED significantly, but it does affect the power balance. The protons require a large fraction of the total power budget, leaving less power for the other components which has to be compensated with more relativistic beaming or stronger external photon fields.

Lastly, we can compare the power components to the theoretical Eddington luminosity. Considering that TXS 0506+056 has a BH mass of  $3 \times 10^8 M_{\odot}$ , this source has an Eddington luminosity of  $L_{\text{Edd}} \approx 1.3 \times 10^{38} \left( \frac{M_{\text{BH}}}{M_{\odot}} \right) \text{ erg s}^{-1} = 3.9 \times 10^{46} \text{ erg s}^{-1}$ . Comparing this power

to the values in Table 4.2 shows that both multi-zone jet models require roughly 0.1% of the Eddington luminosity to fit the SED of TXS 0506+056. Although the acceleration of protons requires more power, `HadJet` does not require super Eddington luminosities in order to explain the SED data as was discussed in Section 4.1.1. In fact, comparing the leptonic and lepto-hadronic cases shows that accelerating protons does not require excessively more power than when considering only cold protons.

Jet Base	BHJet	HadJet	Acceleration Region	BHJet	HadJet
$\sigma_0$	32.189	29.442	$\sigma_{\text{acc}}$	0.539	0.338
$\beta_p$	$2.330 \times 10^{-4}$	$2.233 \times 10^{-4}$	$\beta_p$	0.294	0.048
$\tau_0$	$2.330 \times 10^{-4}$	$3.162 \times 10^{-4}$	$f_{\text{heat}}$	14.711	14.036
			$P_{\text{jet}}$ (erg/s)	$2.855 \times 10^{43}$	$5.310 \times 10^{43}$
			$P_B$ (erg/s)	$5.740 \times 10^{42}$	$4.866 \times 10^{42}$
			$P_e$ (erg/s)	$1.688 \times 10^{42}$	$2.312 \times 10^{41}$
			$P_p$ (erg/s)	$2.130 \times 10^{43}$	$4.800 \times 10^{43}$

TABLE 4.2 Parameters to determine the physical conditions at the base and the acceleration region of the jet for the fits of TXS 0506+056 with `BHJet` and `HadJet`. These values were obtained from the fits shown in Fig. 3.3 and 4.1.

### 4.3 Lepto-Hadronic Multi-Zone SED Fits for PKS 1424-418

As shown in last section, it is difficult to obtain a good fit for TXS 0506+056 that also has reliable statistics using current methods regardless of whether we use a leptonic or a lepto-hadronic jet model. Nevertheless, the fits done with `BHJet` and `HadJet` did show similar results for the same MWL data of TXS 0506+056. In addition, Section 3.5 showed that doing a joint fit with multiple epochs of data for the same source can help constrain the parameter space. Therefore, we will again do a joint fit for the  $\alpha$  and  $\eta$  epochs of PKS 1424-418, but now using `HadJet`. We will not show the fits done for each epoch separately as the statistics do not really help us in understanding the behavior of this blazar and the models. Instead, we will only consider the joint fit which can be seen in Fig. 4.3, where we again see excellent agreement with the data and a fit that is very similar to the joint fit with `BHJet` in Section 3.5. For the joint fit, we do not plot all the emission components as was done for TXS 0506+056. Instead, we focus on the contributions by the accretion disk, the secondary synchrotron and the  $\gamma$ -ray emission.

Looking at the joint fit, we clearly see that the flux of the hadronic components for the flaring state is stronger than those in the quiescent state. One would say that this makes sense as the flux data of the flaring epoch is higher, but it really seems that the relative contribution of hadronic processes increases as well. Another aspect to point out, is that the  $\gamma$ -rays resulting from pp-interactions dominate over the flux produced in p $\gamma$ -interactions. Similar behavior was seen for the `HadJet` fit of the TXS 0506+056 data. Despite the presence of the synchrotron photon field and the fact that the external photon fields are relatively strong in blazars, the

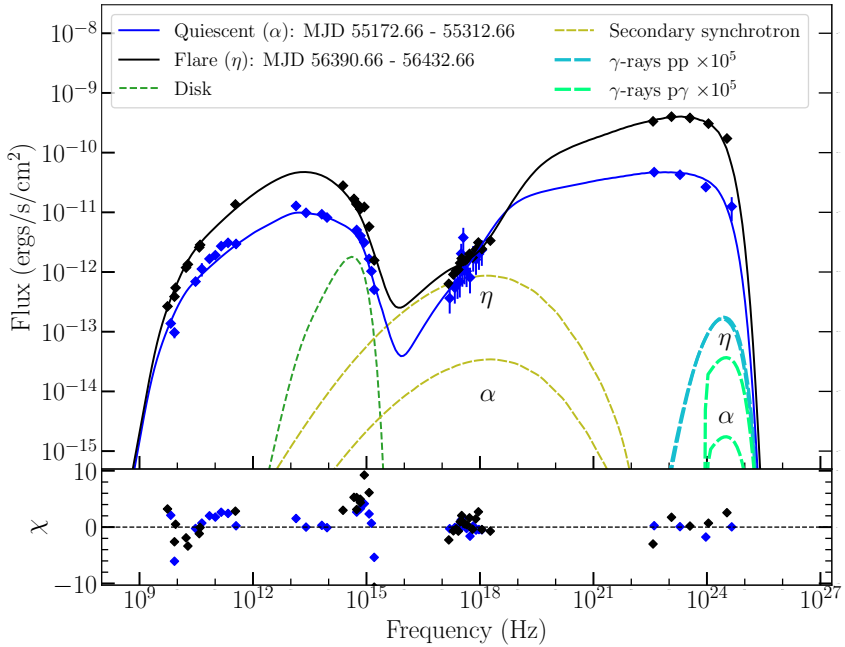


FIG. 4.3 – Joint fit with `HadJet` for the epochs  $\alpha$  and  $\eta$  of PKS 1424-418 which represent a quiescent and a flaring state of the source respectively. The contribution of the accretion disk, secondary synchrotron emission and pion decay for each epoch is shown by the dark green, yellow, and blue/green dashed lines, respectively. The residuals for the fits of both epochs are shown in the lower panel..

non-thermal protons encounter more cold protons in the jet. This result is good to remember and interesting to compare to the case where we only have a single emitting region in Section 5.3.

The best-fit parameters for the joint fit are reported in Table 4.3. These parameters again show that the transition from the quiescent to the flaring state can be explained by changing the details of the non-thermal particle distribution. A harder, more heated electron distribution in combination with a slightly lower jet velocity is able change to reproduce the flaring state SED. Remarkably, the maximum Lorentz factor is lower for the flaring state which we also saw for the leptonic fit. It is unclear as to why this happens, but it might be the combination of the constant electron power budget and a harder particle distribution such that there is not enough energy to extend the particles to higher energies.

Epoch	$\theta$ (°)	$N_j$ ( $L_{\text{Edd}}$ ) $10^{-2}$	$z_{\text{diss}}$ ( $R_g$ ) $10^4$	P	$f_{\text{nth, p}}$ $10^{-3}$	$f_{\text{heat}}$	$f_{\text{sc}}$ $10^3$	$\sigma_{\text{acc}}$ $10^{-2}$	$L_{\text{Disk}}$ ( $L_{\text{Edd}}$ ) $10^{-1}$	$R_{\text{in}}$ ( $R_g$ )	$\Gamma$	$\chi^2/\text{d.o.f.}$
Joint	$0.19^{+0.03}_{-0.03}$	$3.44^{+0.37}_{-0.38}$	$3.70^{+0.18}_{-0.29}$		$8.05^{+1.49}_{-1.17}$			$1.12^{+0.19}_{-0.09}$	$4.31^{+0.07}_{-0.07}$	$85.00^{+5.02}_{-4.91}$		$585.42/59$
$\alpha$					$1.73^{+0.02}_{-0.02}$	$1.05^{+0.08}_{-0.04}$	$5.31^{+0.24}_{-0.24}$				$39.34^{+0.47}_{-0.87}$	
$\eta$					$1.502^{+0.003}_{-0.001}$	$2.77^{+0.23}_{-0.18}$	$4.55^{+0.15}_{-0.14}$				$35.57^{+0.87}_{-1.03}$	

TABLE 4.3 Best fit parameters for the joint fit of the quiescent epoch  $\alpha$  and the flaring epoch  $\eta$  of PKS 1424-418 together with their confidence intervals. We also report the reduced  $\chi^2$  value for the fit.

We can compare the best-fit values to the ones reported in Table 3.5 to see the differences between fitting the same SED with BHJet and HadJet. The parameters for the HadJet joint fit show a similar jet but adding protons has led to a jet that is faster, less magnetised, and requires more power as signified by a lower inclination angle and a higher jet power. Moreover, the disk luminosity is higher and the jet has to be accelerated to higher bulk Lorentz factors. These are all trends that were seen for the fits of TXS 0506+056 as well. Overall, the confidence intervals have a similar size for both models meaning that the parameters remain well constrained.

Remarkably, the accretion disk contribution is stronger for the fit with the lepto-hadronic model than it was for the leptonic model. The same behavior was also seen in the fits for TXS 0506+056. The suspected reason for this, is the fact that the presence of non-thermal protons will lead to interactions between protons and the external photon fields. Presumably, this will reduce the number of external photons available for the non-thermal electrons which we need to fit the high-energy bump in the spectrum. By supplying a stronger disk photon field, the flux resulting from the external IC interactions of the electrons is maintained.

A trend that is different from the fits of TXS 0506+056 is that we saw an increase of almost 40% in the maximum Lorentz factor for TXS 0506+056, while PKS 1424-418 only shows a slight increase for the quiescent state and even a decrease for the flaring state. It is not exactly clear why this is the case, but it probably has to do with the very sharp cutoff in the SED for the lower energy bump around  $10^{15}$  Hz. The sharp cutoff enforces a maximum Lorentz factor such that  $f_{sc}$  is very sensitive to any changes in the other parameters.

Jet Base	$\alpha$	$\eta$	Acceleration Region	$\alpha$	$\eta$
$\sigma_0$	34.768	31.308	$\sigma_{\text{acc}}$	$1.086 \times 10^{-2}$	$1.086 \times 10^{-2}$
$\beta_p$	$1.891 \times 10^{-4}$	$2.100 \times 10^{-4}$	$\beta_p$	0.981	1.228
$\tau_0$	$3.806 \times 10^{-4}$	$4.201 \times 10^{-4}$	$f_{\text{heat}}$	1.044	2.737
			$P_{\text{jet}}$ (erg/s)	$9.546 \times 10^{43}$	$2.810 \times 10^{44}$
			$P_B$ (erg/s)	$2.842 \times 10^{42}$	$3.073 \times 10^{42}$
			$P_e$ (erg/s)	$2.784 \times 10^{42}$	$9.657 \times 10^{42}$
			$P_p$ (erg/s)	$8.984 \times 10^{43}$	$2.683 \times 10^{44}$

TABLE 4.4 Parameters to determine the physical conditions at the base and the acceleration region of the jet for the joint fit of PKS 1424-418 with HadJet. These values were obtained from the fits shown in Fig. 3.7.

Similar to what was done in Section 3.5, we can compare the physical conditions at the base and the acceleration region of the jet for the quiescent and flaring state. These values are reported in Table 4.4 and show very similar behavior to that observed for the joint fit with BHJet. The most significant change compared to the leptonic parameters is that the total power budget in the acceleration region is less, and it is divided differently among the leptonic, hadronic and magnetic components. Firstly, the protons make up around  $\sim 95\%$  of the total power budget just as they did for the leptonic case. Considering that PKS 1424-418 has a BH mass of  $4.5 \times 10^9 M_\odot$ , this source has an Eddington luminosity of  $L_{\text{Edd}} \approx 1.3 \times 10^{38} (M_{\text{BH}}/M_\odot)$  erg s $^{-1}$  =  $5.85 \times 10^{47}$  erg s $^{-1}$ . Although the larger mass of protons does require more power to accelerate them, our multi-zone jet model does not require super Eddington luminosities

in order to explain the SED data. Again, comparing the leptonic and lepto-hadronic cases shows that accelerating protons does not require more power than when considering only cold protons.

Secondly, the fits with `HadJet` start with a higher magnetization at the base, but the larger jet speed demands that more of the magnetic energy is converted into bulk kinetic energy such that the magnetization at the acceleration region is lower for the lepto-hadronic fits. The lower

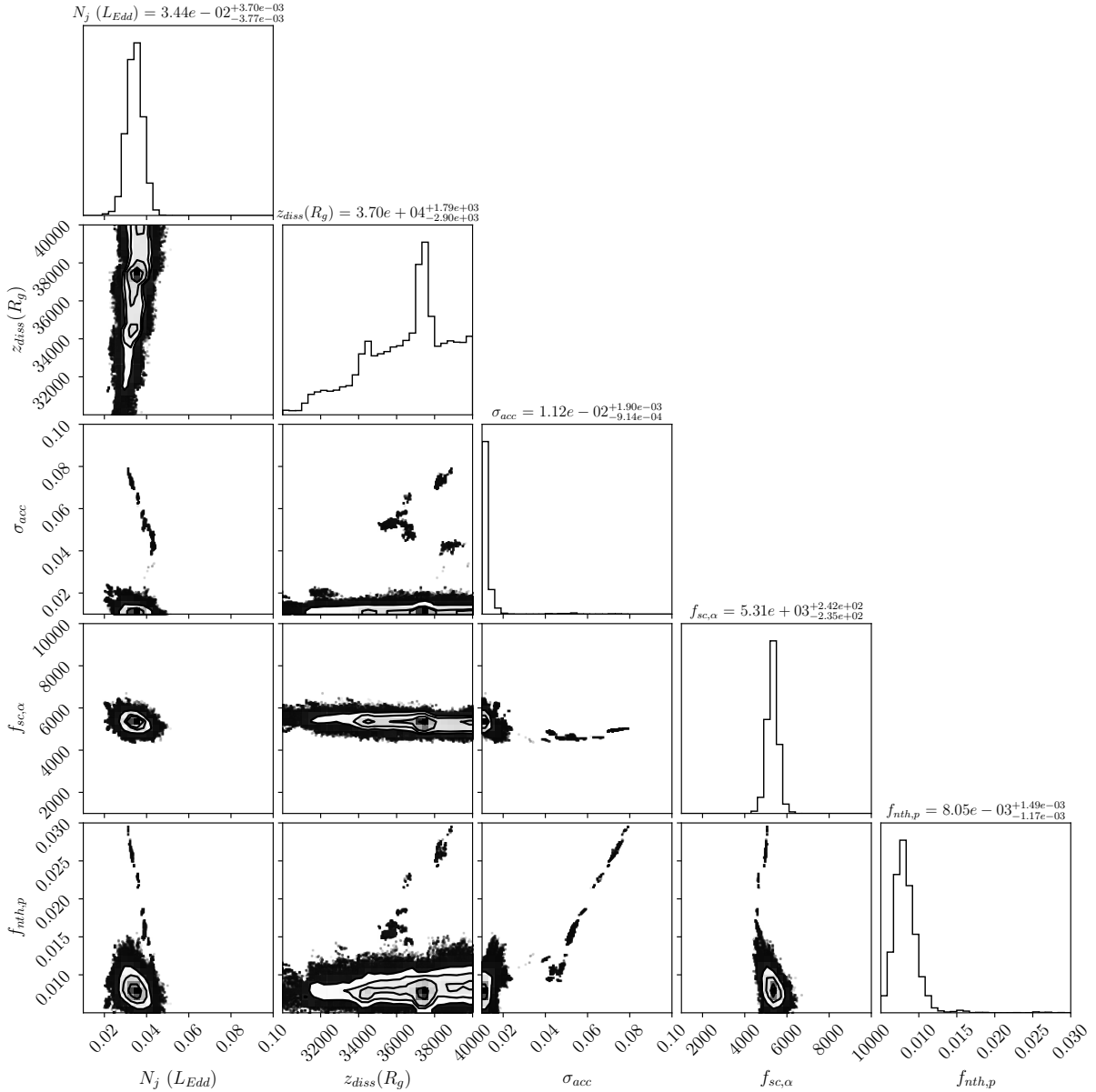


FIG. 4.4 – Corner plot with posterior distributions for the joint fit of  $\alpha$  and  $\eta$  epochs of PKS 1424-418 with `HadJet`. In the plot, the model parameters for the jet power  $N_j$ , the dissipation region  $z_{diss}$ , the magnetization at the dissipation region  $\sigma_{acc}$ ,  $f_{sc}$  and the non-thermal fraction of protons  $f_{nth,p}$  are shown.

magnetic power in both the quiescent and flaring state confirm this.

Another thing to notice, is that the reduced  $\chi^2$  value of the joint fits with BHJet and HadJet are almost identical. In the leptonic case this value is  $589.37/60 = 9.823$ , whereas in the lepto-hadronic case this value is  $585.42/59 = 9.922$ . From a *statistical* point of view, both of these models fit the data equally well and one cannot say that one is better than the other. Looking at the confidence intervals of the model parameters, we see that these are also very similar as signified by the corner plot in Fig. 4.4. The peaks in the one-dimensional posteriors are a bit wider for HadJet, and only the posterior  $z_{\text{diss}}$  is ill constrained. The posterior distribution of  $\sigma_{\text{acc}}$  is close to the edge of the parameter space making it difficult to judge whether this is well constrained or not. Generally, such posteriors are unwanted but several fitting attempts have shown that adding protons will complicate the parameter space leading to this type of posteriors.

Looking more closely at the posterior distributions, the degeneracy between the maximum Lorentz factor  $f_{\text{sc}}$  and the magnetization in the acceleration region  $\sigma_{\text{acc}}$  is observed, but adding protons seems to have broken the degeneracy between the jet power  $N_j$  and the magnetization. The non-thermal fraction of protons being accelerated is also well constrained for PKS 1424-418, and this suggests that adding protons to the model helps to lift any degeneracies or ambiguity. However, the hadronic fraction does have a value  $f_{\text{nth, p}} = 8.05^{+1.49}_{-1.17} \times 10^{-3}$  which is far lower than the leptonic equivalent with a value of 0.5. The fit in Fig. 4.3 shows that this is really the maximum fraction of protons before the secondary synchrotron emission overproduces the X-ray emission under these conditions. The posterior distributions show that the MCMC is confident about this value, but it is very different from the results for TXS 0506+056. Therefore, the non-thermal hadronic fraction can be very source specific, thereby affecting whether adding protons will actually help in fitting an SED.

# Chapter 5

## Single-Zone vs Multi-Zone Modelling of Blazar SEDs

In Chapters 3 and 4 the SEDs of the blazars TXS 0506+056 and PKS 1424-418 were modelled using the multi-zone jet models `BHJet` and `HadJet`. This multi-zone approach for BH jets aims to connect the geometrical evolution of the jet to the launching conditions at the base of the jet in a coupled disk-jet system. This evolution is studied by simulating the plasma dynamics and accelerating particles from a thermal to a non-thermal regime such that they produce MWL emission. However, blazar jet models typically take a single-zone approach (Tavecchio et al. 1998; Böttcher et al. 2013; Gao et al. 2017). In such models, only a single, homogeneous spherical region is considered in which a non-thermal particle distribution is injected. Similar to the multi-zone models, these single-zone models can be both leptonic and lepto-hadronic. The more confined nature of these models makes it computationally more feasible to have more detailed particle interactions and a time-dependent character, making this the dominant approach in the blazar SED modelling community.

Section 1.5 discussed that making the transition to multi-zone jet models could help to overcome fundamental limitations of single-zone models. However, in order to make this transition it is important to bridge the gap between both types of models. To this end, this section will be focused on self-consistently comparing the single-zone versions of `BHJet` and `HadJet` to their multi-zone equivalent. From the multi-zone models we extracted the physics for the radiative processes and used this for a leptonic and a lepto-hadronic single-zone model. By using the same libraries, we ensure consistency between the single- and multi-zone versions of the model in order to be able to do a more reliable comparison. These single-zone versions of the multi-zone models will be referred to as `OneZone_1ep` and `OneZone_1ephad` for the leptonic and lepto-hadronic version, respectively. In Section 1.5.1, a more detailed description of single-zone jet models was given. The new single-zone models will be tested against the Astrophysical Multi-Messenger Modeling (AM<sup>3</sup>)<sup>1</sup> single-zone code in Section 5.1. Subsequently, the single-zone models derived from `BHJet` and `HadJet` will be used to fit the SEDs of TXS 0506+056 and PKS 1424-418 in Sections 5.2 and 5.3. Lastly, we will discuss the general outcomes of this comparison and how this fits into the field of modelling blazar SEDs in Section 5.4.

### 5.1 Comparing the Single-Zone Version of `BHJet` to AM3

As discussed before, single-zone versions of the multi-zone jet models `BHJet` and `HadJet` were developed using the same libraries that describe the radiative mechanisms and particle dis-

---

<sup>1</sup><https://am3.readthedocs.io/en/latest/>

tributions. The main difference is that instead of considering a full multi-zone jet, only a single spherical emission region is considered as shown in Fig. 1.19. The full list of parameters for both `OneZone_lep` and `OneZone_lephad` can be found in Appendix B.2 together with a description of each parameter.

The fact that only a single blob of plasma is considered, does not allow for a self-consistent evolution of the jet starting from the base. The multi-zone models use initial conditions for the power and magnetization to evolve the jet according to the Bernoulli equation (see equation 1.61). Alternatively, the single-zone models do not have such a self-consistent evolution which forces the user to directly specify the conditions for the emission region. We need to define the magnetic field strength ( $B$ ), the size of the emission region ( $R$ ) and the emitting particle distribution. The source specific parameters as well as the setup for the accretion disk and external photon fields remain the same as seen before for the multi-zone models.

In order to verify that the single-zone models work, we test `OneZone_lep` in a simple SSC scenario. This test is the same as was done in the blazar code comparison project by Cerruti et al. (2022). Instead of comparing the results of `OneZone_lep` to all the models used in Cerruti et al. (2022), we only compare them to the AM<sup>3</sup> code. The simple SSC test considers a system where the BH has a mass of  $10^8 M_\odot$  at a redshift of  $z_{\text{red}} = 0.01$  such that the distance is  $4.421 \times 10^4$  kpc. There is no accretion disk present and the blob has an assumed Doppler factor of  $\delta = 30$ , a size of  $R = 10^{15}$  cm, and is threaded by a homogeneous magnetic field with strength  $B = 0.1$  G. These conditions ensure that the IC scattering occurs exclusively in the Thomson regime which is useful because the implementation of IC scattering in the Klein-Nishina regime can differ between different codes and complicate the comparison.

The emitting electron distribution is assumed to be a powerlaw with spectral index  $p_e = 1.9$  that extends between  $\gamma_{\min, e} = 10$  and  $\gamma_{\max, e} = 10^4$ , and has an exponential cutoff at  $\gamma = \gamma_{\max, e}$ . Note that  $\gamma_{\min, e}$  is slightly higher than was used by Cerruti et al. (2022). The reason for this is that our models use the dimensionless momentum of the particles to track the energy of the particle. This dimensionless momentum is defined as  $\zeta = p/m_e c$  such that the particle Lorentz factor is given by  $\gamma(\zeta) = \sqrt{\zeta^2 + 1}$  (Lucchini et al. 2022). In the relativistic limit we have  $\zeta \approx \gamma$ , but for energies close to  $\gamma = 1$  this will lead to a non-relativistic bump in the particle distribution. Since we only want to consider a simple powerlaw distribution for this comparison, we chose to set the minimum Lorentz factor slightly higher to avoid this bump.

Cerruti et al. (2022) normalize the powerlaw of electrons by using an injection compactness of  $l_{e, \text{inj}} \equiv \frac{L_{\text{inj}}}{R} \frac{\sigma_T}{4\pi m_e c^3} = 10^{-4.47}$ . The reason being that AM<sup>3</sup> (as well as ATHE $\nu$ A) is a time-dependent code for which one needs the injection rate of particles per unit volume per unit time,  $Q_{\text{inj}}(\gamma, t)$ , as input. In contrast, the time-independent nature of `OneZone_lep` takes the particle number density as input, so we need to calculate this from the injection compactness. The particle injection rate can be converted to a bolometric injection luminosity,  $L_{\text{inj}}$ , by using

$$L_{\text{inj}} = \frac{4}{3}\pi R^3 m_e c^2 \int_1^\infty d\gamma (\gamma - 1) Q_{\text{inj}}(\gamma). \quad (5.1)$$

The injection compactness is then related to the injection rate by

$$l_{\text{inj}} \equiv \frac{\sigma_T L_{\text{inj}}}{4\pi R m_e c^3} = \frac{\sigma_T R^2}{3c} \int_1^\infty d\gamma (\gamma - 1) Q_{\text{inj}}(\gamma) \quad (5.2)$$

In the absence of cooling, the particle number density is related to the injection rate through  $Q_{\text{inj}}(\gamma) = n_e(\gamma)/t_{\text{esc}}$ , where  $t_{\text{esc}} = R/c$  is the typical timescale to cross the emitting region and escape the source. Ultimately, the electron number density is related to the injection compactness by

$$l_{\text{inj}} = \frac{\sigma_T R^2}{3ct_{\text{esc}}} \int_{\gamma_{e,\min}}^{\gamma_{e,\max}} d\gamma (\gamma - 1) n_e(\gamma). \quad (5.3)$$

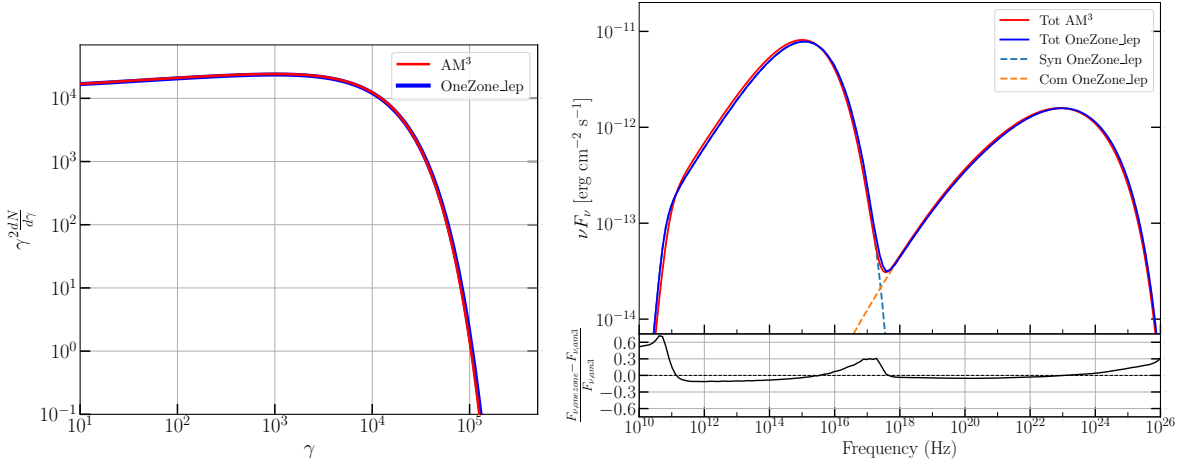
With these relations, the powerlaw can be normalized by fixing the number density at  $\gamma = \gamma_{\min, e}$ , i.e.  $n_e|_{\gamma=\gamma_{\min, e}}$ . For a powerlaw distribution with a spectral index  $p$ , between  $\gamma_{\min, e}$  and  $\gamma_{\max, e}$ , we can integrate the relation in equation 5.3 to obtain

$$n_e|_{\gamma=\gamma_{\min, e}} = \frac{3ct_{\text{esc}} l_{\text{inj}}}{\sigma_T R^2} \begin{cases} \frac{2-p}{\gamma_{\max, e}^{2-p} - \gamma_{\min, e}^{2-p}} & p \neq 2 \\ \ln^{-1} \left( \frac{\gamma_{\max, e}}{\gamma_{\min, e}} \right) & p = 2 \end{cases} \quad (5.4)$$

The powerlaw distribution in the simple SSC scenario described above, has a spectral index  $p = 1.9$  and extends between  $\gamma_{\min, e} = 10$  and  $\gamma_{\max, e} = 10^4$  such that we obtain  $n_e|_{\gamma=10} = 1.159 \times 10^4 \text{ cm}^{-3}$  as normalization factor.

There is one difference between `OneZone_1ep` and `AM3` left to point out. When using single-zone models, it is custom in the community to specify the Doppler factor of the spherical blob instead of using an inclination angle and the Lorentz factor of the jet. These can be related to each other by the relations derived in Section 1.2.3. Assuming that the velocity of the jet is very close to the speed of light, i.e.  $\beta \equiv v/c \approx 1$ , we have a Doppler factor  $\delta = (\Gamma(1 - \cos(\theta)))^{-1}$  such that it is related to the bulk Lorentz factor and the inclination angle of the jet. Instead of only using the Doppler factor, `OneZone_1ep` uses the inclination angle as a parameter because the inclination angle does not only affect the Doppler factor of the jet, but is also important in the relativistic beaming of the external photon fields (if present). For the SSC scenario a combination of  $\Gamma = 27$  and  $\theta = 1.9$  was chosen in `OneZone_1ep` to reproduce the Doppler factor  $\delta = 30$  used in [Cerruti et al. \(2022\)](#).

The first verification is to compare the non-thermal electron distributions of `OneZone_1ep` and `AM3`. Ensuring that the injected electron distributions are the same allows us to see potential differences in how the codes treat the synchrotron and IC processes. In Fig. 5.1a we see the comparison of both electron distributions, and they are in excellent agreement. After having verified that the emitting electron distributions are the same, we continue with the resulting simulated SEDs for the simple SSC scenario in Fig. 5.1b. Again, we see excellent agreement between the two codes and the normalized deviation shows that they differ only a few % in most of the frequency range. Only at the edges and at the transition from the first to the second bump we see larger deviations up to 50% which are due to numerical errors. Note that in Fig. 1 of [Cerruti et al. \(2022\)](#) the deviation panel shows the difference of every model with respect to the mean of all models. The averaging will suppress any normalized deviations which is why the deviations in [Cerruti et al. \(2022\)](#) seem to be less than in Fig. 5.1b. The figures here show that both codes agree well and can reproduce the same result for a simple leptonic SSC scenario.



(A) Simulated relativistic electron distributions.

(B) Simulated SEDs where the upper panel shows the actual SEDs together with the synchrotron and IC components of `OneZone_lep`. The lower panel shows the normalized deviation of the two codes.FIG. 5.1 – Comparison of the results with  $\text{AM}^3$  and `OneZone_lep` for a simple SSC scenario.

## 5.2 Leptonic Single-Zone SED Modelling of Blazar SEDs

In the previous section, we have verified that the leptonic, time-independent, single-zone version of `BHJet` can reproduce the results of the  $\text{AM}^3$  code for a simple SSC scenario. This test case is useful for verification, but it will not teach us about the results for real sources. Therefore, this section will be focused on fitting the SEDs of TXS 0506+056 and PKS 1424-418 with `OneZone_lep`. The resulting fit parameters can then be compared to those of the fits with `BHJet` to see if there are any systematic differences. As usual, we will start with the SED of TXS 0506+056 followed by joint fit of two epochs of PKS 1424-418.

As discussed in Section 1.5, there are some differences between single- and multi-zone models. Similar to what we did for the multi-zone models, we need to make certain assumptions on the model to keep the number of free parameters limited. The parameters that we fixed for `BHJet` and `HadJet` were discussed in Sections 3.1 and 4.1, but the model parameters for the single-zone model are different (see Appendix B.2). For the non-thermal electron distribution we assume a regular powerlaw without a break, i.e. `brksw=0`, where  $\gamma_{\min, e} = 1.1$  and  $\gamma_{\max, e}$  is free to vary. Other parameters like  $\theta$ ,  $R$ ,  $B$ ,  $\Gamma$ ,  $n_e$ , and  $p_{1, e}$  are also free to vary. Similar to the multi-zone models, the EC emission cannot be neglected and the parameters are set in the same way as described in Section 3.1. Therefore,  $R_{\text{in}}$  and  $L_{\text{disk}}$  are free whereas  $R_{\text{out}} = 10^4 R_g$  is again fixed. The external photon fields from the BLR and DT are included by setting `compsw=2`, and  $f_{\text{BLR}}$  and  $f_{\text{DT}}$  are free to vary between 0.05 – 0.4 for TXS 0506+056. For PKS 1424-418  $f_{\text{BLR}}$  and  $f_{\text{DT}}$  are fixed to the values 0.05 and 0.2, respectively. Adding up the number of free parameters yields a total of 11 which is bit high, but previous experience has shown that it is difficult to fit the SEDs when using a less flexible model.

### 5.2.1 Leptonic Single-Zone SED Fit for TXS 0506+056

In this section, the fit of the SED for TXS 0506+056 collected during the two weeks after the neutrino event using `OneZone_1ep` is shown. As discussed in Section 2.1.1, this is not the first time that the SED data of TXS 0506+056 has been fitted with a single-zone jet model. The neutrino event in 2017 sparked an increased interest in this source leading to multiple attempts to fit the flaring data (see e.g. Keivani et al. 2018; Cerruti et al. 2019; Xue et al. 2019). The temporal correlation of a neutrino event and a  $\gamma$ -ray flare initiated a search for other flares in the past. One other flare was found in 2014–2015, and this was also extensively studied in retrospect (Murase et al. 2018; Reimer et al. 2019; Rodrigues et al. 2019). Visually, all fits in these papers seem to explain the SED data very well, but there is significant variation between all the models that were used. Moreover, everyone is focused on having the most accurate prediction of the neutrino flux produced during these flares. While this is important to study the correlation between neutrinos and  $\gamma$ -rays, this creates a bias towards enhancing hadronic interactions and none of these papers report confidence intervals on their jet model parameters. The absence of any statistics complicates the search for the model that explains the flaring data best.

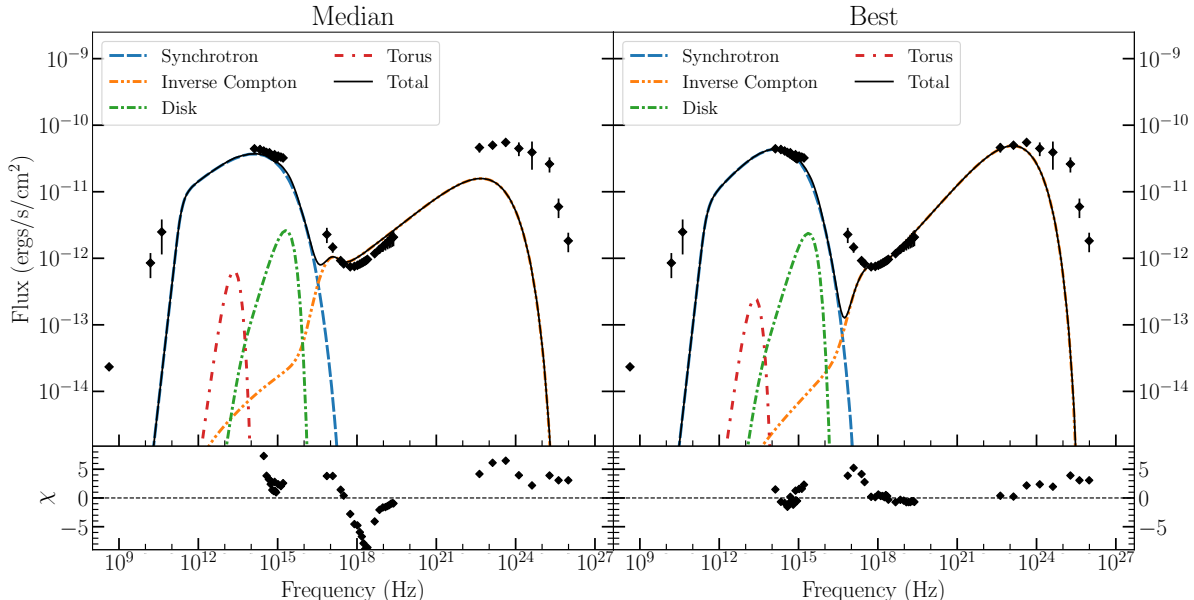


FIG. 5.2 – Fits of the flaring state of TXS 0506+056 in 2017 with `OneZone_1ep` together with the residuals in the lower panel. All components of the SED are shown as well as the sum of them which fits the SED data. The left-hand panel shows the fit with the parameters obtained from the median of all parameter posteriors. The right-hand panel shows the fit using the parameters that result in the lowest reduced  $\chi^2$ .

In order to improve, the next step is to look at a fit of the SED for TXS 0506+056 with `OneZone_1ep` and see what the best-fit parameters are using statistics. First of all, the fit of the SED data is shown in Fig. 5.2. The left-hand panel shows the fit produced by taking the median of all parameter posteriors produced with MCMC. The right-hand panel shows the fit with the parameters that produce the lowest reduced  $\chi^2$  value. We immediately notice that the

fits cannot explain the radio data below  $10^{11}$  Hz, but this is something that we would expect from a single-zone model. Before, we saw that it was difficult to fit the data of TXS 0506+056 with the multi-zone jet models. With `OneZone_1ep` this proves even more challenging, and we see that especially the optical/UV and  $\gamma$ -ray regimes are not well explained by the fits. The ‘median’ fit shows that the tight uncertainties on the data in the optical to X-ray range make it a daunting task to obtain a statistically favoured fit that also seems to fit all the data points well. Nevertheless, even the ‘best’ fit seems to not be able to accelerate particles to a Lorentz factor that is large enough to bring the high-energy end of both bumps closer to the data. Looking a bit more closely at Fig. 5.2, we see that the IC emission is used to fit the UV data to compensate for the lack of synchrotron emission at  $10^{17}$  Hz. Moreover, the ‘median’ fit is far from the  $\gamma$ -ray data since it inhibits the maximum Lorentz factor of the electrons, making it unable to reach the energies required to fit the  $\gamma$ -rays.

In order to get a better idea of the resulting fit, let us look at the values of the fit parameters in Table 5.1. Most of all, these values show that the ‘median’ and ‘best’ fits are not close to each other in the parameter space. Nevertheless, the parameter values of the ‘best’ fit are roughly within one standard deviation of the median values of the parameter posteriors. This difference is not terribly large, and the model is most likely stuck in a local minimum. For any comparison of the fit with `OneZone_1ep` to what we found earlier with `BHJet` in Section 3.4, the ‘median’ will be used as these enables the use of the confidence intervals on the parameters.

Fit	$\theta$ (°)	R $10^{16}$	B $10^{-1}$	$n_e$ $10^3$	$\gamma_{\max, e}$ $10^3$	$p_e$	$L_{\text{disk}}$ ( $L_{\text{Edd}}$ ) $10^{-1}$	$R_{\text{in}}$ ( $R_g$ )	$f_{\text{BLR}}$ $10^{-1}$	$f_{\text{DT}}$ $10^{-1}$	$\Gamma$	$\chi^2/\text{d.o.f.}$
Best	0.81	1.21	8.23	1.73	1.09	2.03	1.45	21.12	2.21	0.52	49.50	150.75/38
Median	$1.60^{+1.06}_{-0.59}$	$3.45^{+17.78}_{-1.97}$	$10.85^{+4.50}_{-7.11}$	$2.52^{+2.09}_{-1.97}$	$1.80^{+2.09}_{-0.56}$	$2.32^{+0.14}_{-0.24}$	$1.72^{+0.64}_{-0.80}$	$31.13^{+19.75}_{-16.78}$	$2.11^{+0.99}_{-0.69}$	$1.15^{+1.62}_{-0.57}$	$42.87^{+6.05}_{-22.00}$	1728.62/38

TABLE 5.1 Fit parameters for the SED data after the 2017 flare of TXS 0506+056 using `OneZone_1ep`. The upper row are the fit parameters for the best fit and the parameters in the lower row are the median values obtained with MCMC. We also report the reduced  $\chi^2$  value for the fit.

For other parameters like the size of the emission region and the magnetic field strength, one needs to convert these first in order to compare them to the results found with `BHJet`. An important quantity for this comparison is the Doppler factor, for which a simple calculation shows that the ‘median’ fit has a Doppler factor  $\delta = (\Gamma(1 - \beta \cos(\theta)))^{-1} \approx 35.61$ . With the Doppler factor we can derive an upper limit on the size of the emission region using observational constraints and equation 1.57. Observations have shown that the X-ray variability timescale of TXS 0506+056 is roughly equal to 1 day (Keivani et al. 2018). For a Doppler factor of  $\delta \approx 35.61$  and a redshift of  $z_{\text{red}} = 0.3365$  this yields  $R' \approx 7.99 \times 10^{16}$  cm. The region size is somewhat smaller in the fits, which is good as this calculated region size is an upper limit. Another check is to see how far the emission zone is from the BH. For this, we can use equation 1.58 which yields  $z \approx 2.85 \times 10^{18}$  cm. The distance to the BH can be expressed in units of gravitational radii using the mass of the BH in TXS 0506+056. This mass is  $3 \times 10^8 M_\odot$  resulting in a gravitational radius of  $R_g \approx 4.5 \times 10^{13}$  cm. Therefore, the distance to the BH is roughly equal to  $z \approx 2.85 \times 10^{18}$  cm  $\approx 6.33 \times 10^4 R_g$ . Looking at the fit with `BHJet` this is larger than the best-fit value found for  $z_{\text{diss}}$ . Nevertheless, considering all the assumptions in this calculation, the location of the acceleration region is very similar for both the single- and multi-zone model.

Another parameter that we can compare for `OneZone_1ep` and `BHJet` is the magnetization

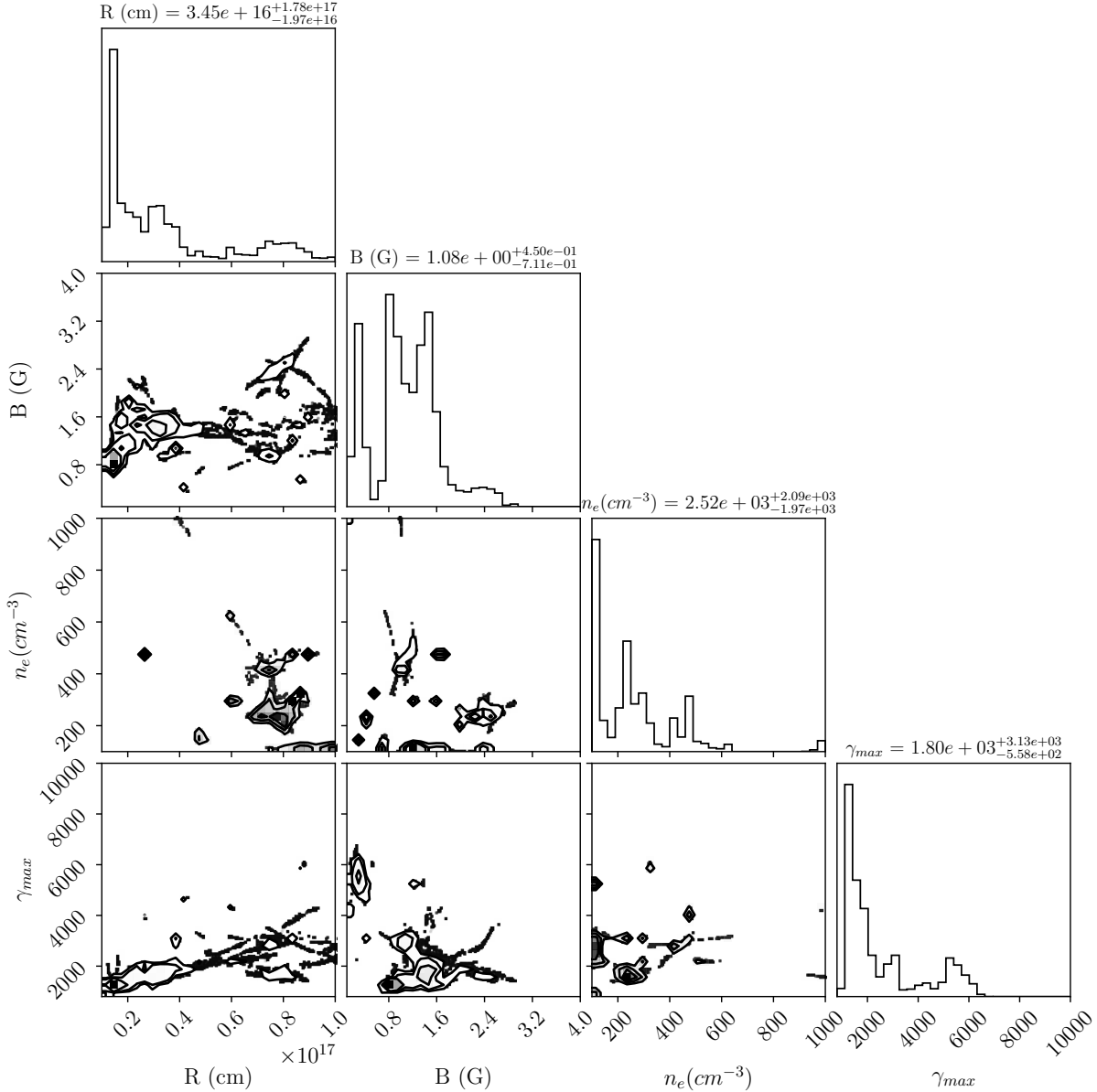


FIG. 5.3 – Corner plot with posterior distributions for the fit of the TXS 0506+056 SED with `OneZone_lep`. In the plot, the model parameters for the radius of the emission region  $R$ , the magnetic field strength  $B$ , the electron number density  $n_e$  and the maximum Lorentz factor  $\gamma_{max}$  are shown.

which can be derived from the magnetic field strength. In Section 1.5.2, we showed that the magnetization in BHJet is related to the magnetic field by

$$\sigma = \frac{B^2}{4\pi nm_p c^2}, \quad (5.5)$$

under the assumption that electrons do not contribute significantly to the total energy budget of

the jet. Using the values for  $B$  and  $n_e$  from Table 5.1, yields  $\sigma \approx 2.47 \times 10^{-2}$ . The magnetization is more than an order of magnitude smaller than what was found in the acceleration region for the fit with `BHJet` meaning that there is less magnetic energy available in the single-zone model to produce synchrotron emission.

The parameter values in Table 5.1 show that the best fit with `OneZone_lep` is not that different from the best fit with `BHJet`. The inclination angle, location and size of the emission region, the spectral index, and the external Compton parameters are all close to each other and certainly fall within each others confidence intervals. However, the comparison also shows that there are some significant differences. First of all, the fits with `OneZone_lep` have a maximum Lorentz factor for the electron distribution that is almost an order of magnitude lower. The lower maximum Lorentz factor is compensated by having a significantly higher jet Lorentz factor and a more luminous accretion disk that has a smaller truncation radius.

In addition, the statistics of the fit with `OneZone_lep` are somewhat different as shown by the corner plot in Fig. 5.3. This figure shows different quantities than we saw before for the multi-zone models. In Fig. 5.3, we see the posterior distributions for the size of the blob  $R$ , the magnetic field strength  $B$ , the electron number density  $n_e$ , and the maximum Lorentz factor of the electron powerlaw  $\gamma_{\max, e}$ . The first three quantities can be converted into the power budget, the location of the acceleration region and the magnetization of the blob, and the maximum Lorentz factor obviously has the same meaning as for the multi-zone models.

The corner plot shows the same scattered behavior as seen before for `BHJet`, but there are some differences. The two-dimensional posteriors show that there are some favourable regions in the parameter space, but there are multiple of these regions for almost every plot. Some of these regions lie relatively far from the median values that are shown in Table 5.1, and seem to be equally probable. Again, this confirms that the SED of TXS 0506+056 is difficult to deal with in a statistical sense. While the multi-zone model had the radio data as an additional constraint, the single-zone model seems to have more difficulty without any additional constraints. The next step will be to do a joint fit of two epochs of PKS 1424-418 in Section 5.2.2.

### 5.2.2 Leptonic Single-Zone SED Fits for PKS 1424-418

In Section 2.1.2, it was shown that PKS 1424-418 has had some interesting transitions in its behavior over time. Therefore, this source has been modelled during several time windows (see e.g. Buson et al. 2014; Gao et al. 2017; Abhir et al. 2021), and it was present in the TANAMI MWL program (Krauß et al. 2016). These different epochs of the source have led to an abundance of single-zone fits of the source and they all seem to differ from one another. Moreover, most of these groups have not attempted to estimate the confidence intervals of the model parameters, except for Gao et al. (2017), such that this will be first time this is ever done for this source.

In previous sections, obtaining well constrained parameter values for the separate fits of the SED of TXS 0506+056 has proven to be a challenge using current methods. The separate fits for PKS 1424-418 with `BHJet` were slightly better constrained, but not extremely accurate. The use of a joint fit for the multiple epochs of PKS 1424-418 has shown to lead to more constrained statistics which is why it could help in constraining the `OneZone_lep` model as well. The joint fit of PKS 1424-418 using the `OneZone_lep` model is shown in Fig. 5.4. This fit does not look as good as for the multi-zone jet models, but for the quiescent state there is a good

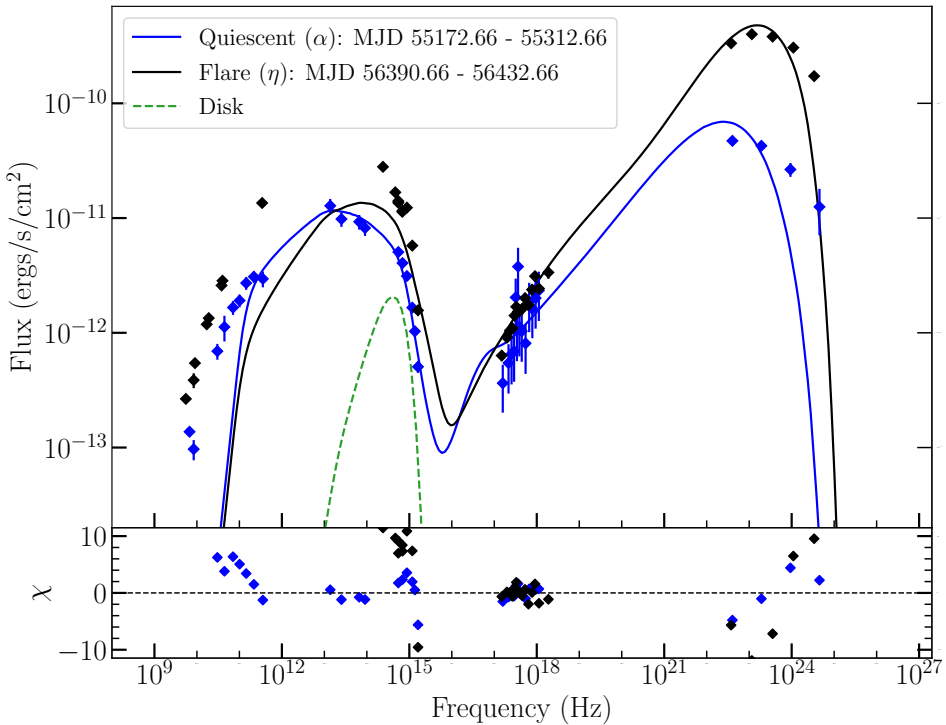


FIG. 5.4 – Joint fit with `OneZone_1ep` for the epochs  $\alpha$  and  $\eta$  of PKS 1424-418 which represent a quiescent and a flaring state of the source respectively. The contribution of the accretion disk for each epoch is shown by the dashed lines. The residuals for the fits of both epochs are shown in the lower panel.

agreement with the data. For the flaring state, the model has difficulty explaining the lower energy emission while also being able to fit the rest of the SED data. Below a frequency of  $10^{11}$  Hz single-zone models are not expected to fit the data, but for the flaring state the fit is too far off and is not able to explain the SED data at higher frequencies as well. A problematic part of the SED data for PKS 1424-418 is the very sharp cutoff of the lower energy bump around  $10^{15}$  Hz. For both the quiescent and flaring data, the synchrotron emission drops almost vertically making it very difficult to fit the data using a electron distribution with a simple exponential cutoff. Others have tried manipulated versions of cutoffs like a ‘super’ exponential cutoff or even a step function (Buson et al. 2014). While this might work to fit the SED, Buson et al. (2014) do admit that this choice was purely made to fit the SEDs, and not to reflect any type of particle acceleration or cooling mechanism.

The parameter values for the joint fit of PKS 1424-148 with `OneZone_1ep` are reported in Table 5.2. The set of parameters for the flaring state seem to be different from that for the quiescent state. The emission region in the flaring state is smaller, it has a weaker magnetic field, a higher maximum Lorentz factor and a lower spectral index. Therefore, the available power budget is lower which needs to be compensated with a slightly larger Lorentz factor of the blob resulting in a higher Doppler factor.

Before diving into a comparison of the results for `OneZone_1ep` and those for `BHJet`, let us first take a look at the posterior distributions for the fit with the `OneZone_1ep` model.

Epoch	$\theta$ (°)	R $10^{16}$	B $10^{-1}$	$n_e$ $10^3$	$\gamma_{\max, e}$ $10^3$	$p_e$	L <sub>disk</sub> (L <sub>Edd</sub> ) $10^{-1}$	R <sub>in</sub> (R <sub>g</sub> )	$\Gamma$	$\chi^2/\text{d.o.f.}$
Joint	$1.07^{+0.15}_{-0.14}$						$4.95^{+0.04}_{-0.55}$	$95.46^{+8.82}_{-9.63}$		1681.83/50
$\alpha$		$7.82^{+0.14}_{-2.57}$	$4.31^{+0.62}_{-0.46}$	$1.93^{+0.07}_{-0.09}$	$0.98^{+0.32}_{-0.09}$	$2.06^{+0.07}_{-0.05}$			$23.38^{+3.73}_{-3.11}$	
$\eta$		$4.00^{+0.70}_{-0.54}$	$1.98^{+0.15}_{-0.17}$	$1.96^{+2.29}_{-0.31}$	$1.69^{+0.52}_{-0.11}$	$1.52^{+0.17}_{-0.02}$			$26.57^{+2.00}_{-2.20}$	

TABLE 5.2 Best fit parameters for the joint fit with `OneZone_1ep` of the quiescent epoch  $\alpha$  and the flaring epoch  $\eta$  of PKS 1424-418 together with their confidence intervals. We also report the reduced  $\chi^2$  value for the fit.

The corner plot in Fig. 5.5, shows that there is always a clear peak in the one-dimensional posteriors. Based on these one-dimensional posteriors, the joint fit does seem to be able to find well constrained parameters similar to what was found in Section 3.5. However, the two-dimensional posteriors show that there is a significant amount of scatter. Being limited by the maximum region size (see equation 1.57) and only having a single region to reproduce the SED data has led the model to explore a large part of the parameter space. Similar behavior was seen for the single-zone fit for TXS 0506+056, so this suggests that single-zone models are not as well constrained as multi-zone models. This is confirmed by the reduced  $\chi^2$  value in Table 5.2 which is significantly higher for the single-zone fit and was to be expected by looking at the fits.

The parameter values in Table 5.2 can be compared to the best-fit values found for the joint fit with `BHJet` in Section 3.5 to show that the inclination angle and the accretion disk luminosity are larger for the `OneZone_1ep` fit. Moreover, the upper limit on the size of the emitting region can be estimated using the fitting results and the observed variability of the source. The variability timescale of PKS 1424-418 based on UV, X-ray and  $\gamma$ -ray observations has been estimated to be on the order of a few days (Fan & Cao 2004; Abhir et al. 2021), and we adopt a value of  $t_v = 2.50$  d =  $2.16 \times 10^5$  s. Note that this variability timescale was obtained for a flaring state of the source, so the quiescent state could theoretically have a different timescale. Using the parameter values from Table 5.2, we see slightly different Doppler factors for the quiescent state,  $\delta_q = 39.23$ , and the flaring state,  $\delta_f = 42.75$ . The subscripts denote whether quantities belong to the quiescent state (q) or the flaring state (f). These Doppler factors lead to an upper limit on the region size of  $R'_q \approx 9.07 \times 10^{16}$  cm and  $R'_f \approx 1.10 \times 10^{17}$  cm for the quiescent and flaring state, respectively. Based on the region size in the table, the found value for  $R$  does not violate this upper limit. However, looking at the corner plot of the fit parameters in Fig. 5.5, one sees that there is tendency towards a larger region size than  $R = 8 \times 10^{16}$  cm. The inferred size is not that far from the upper limit, and it shows that more power is required to explain the SEDs than what the variability timescale allows.

The region sizes calculated above can be used to calculate the distance between the blob and the BH. This calculation yields distances of  $z_q \approx 3.56 \times 10^{18}$  cm and  $z_f \approx 4.70 \times 10^{18}$  cm. The BH in PKS 1424-418 has an estimated mass of  $4.5 \times 10^9 M_\odot$  such that the gravitational radius is  $R_g \approx 6.75 \times 10^{14}$  cm. Expressing the distances of the blob in units of  $R_g$  yields  $z_q \approx 5.27 \times 10^3 R_g$  and  $z_f \approx 6.96 \times 10^3 R_g$ . Whereas `OneZone_1ep` predicted a blob that was farther away from the BH than what `BHJet` predicted for TXS 0506+056, it is now the other way around. The values are roughly one order of magnitude smaller, but this proves that distance estimates can be source dependent and the predictions from single- and multi-

zone models will be different. The last quantity to study is the magnetization in the blob compared to the magnetization in the acceleration region found with the multi-zone model. Using equation 1.62 and the values for  $B$  and  $n_e$  in Table 5.2, the magnetization is predicted to be  $\sigma_q = 5.088 \times 10^{-3}$  and  $\sigma_f = 1.057 \times 10^{-3}$  for both states. These values are both about an order of magnitude lower than what was found with BHJet. The same trend was seen for TXS 0506+056 and seems to be a systematic difference between single- and multi-zone fits.

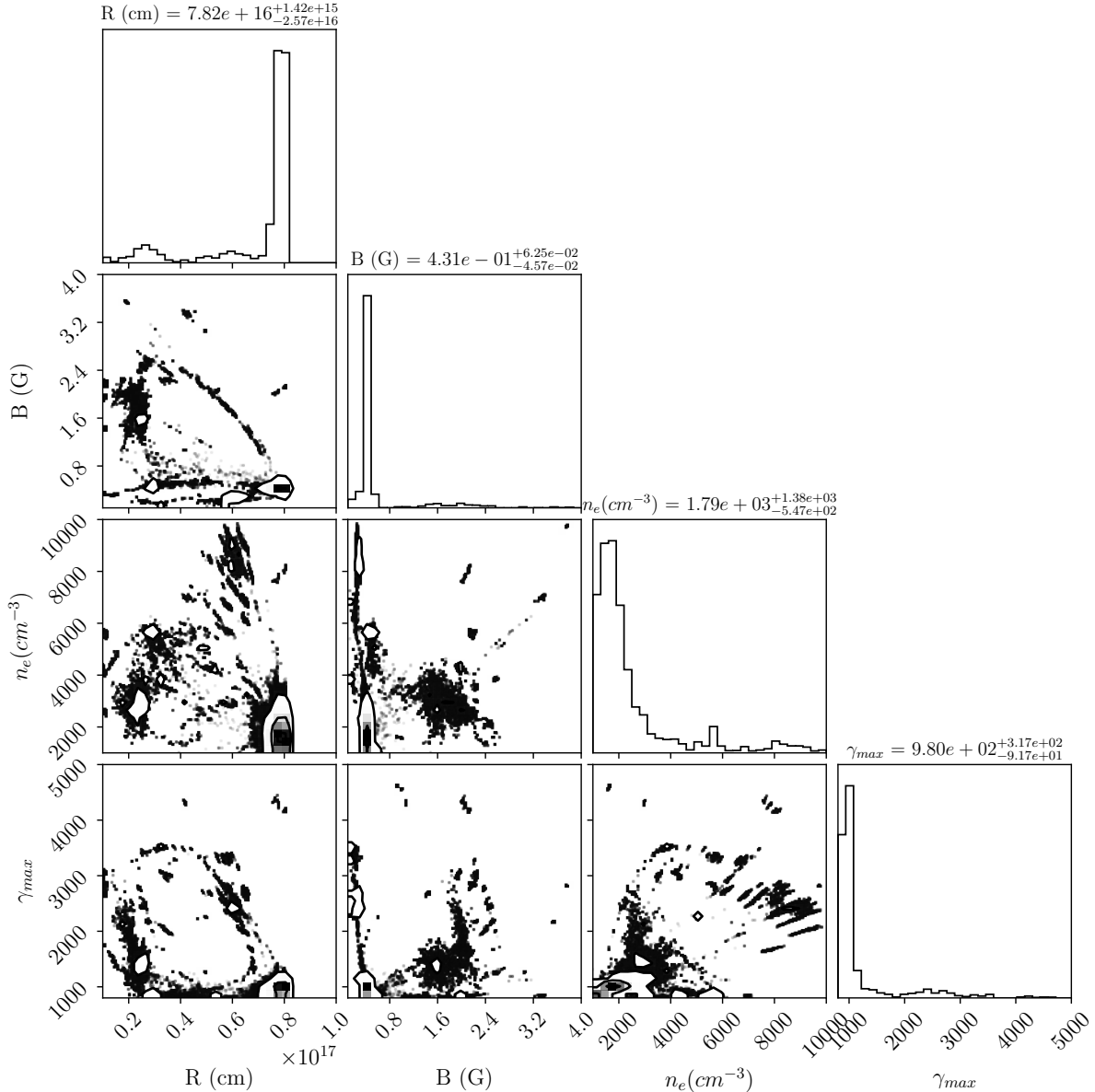


FIG. 5.5 – Corner plot with posterior distributions for the joint fit of  $\alpha$  and  $\eta$  epochs of PKS 1424-418 with `OneZone_lep`. The model parameters for the radius of the emission region  $R$ , the magnetic field strength  $B$ , the electron number density  $n_e$  and the maximum Lorentz factor  $\gamma_{max}$  are shown.

In order to compare the conditions found with both jet models more thoroughly, the values of several physical quantities are reported in Table 5.3. Since the single-zone model can be found with both models are clearly different, where the large difference in required jet power is the most noticeable. Table 5.3 shows that the magnetization is roughly an order of magnitude smaller leading to a more particle dominated plasma. Another difference is that the fit with `OneZone_lep` has significantly less high energy particles as signified by the larger spectral index and a lower maximum Lorentz factor. Combined with a lower Doppler factors, it becomes very difficult to produce enough  $\gamma$ -ray emission which was seen in Fig. 5.4.

The most important result of the comparison is that the single-zone model requires roughly three orders of magnitude more power to explain the SED data than the multi-zone model for both the quiescent and the flaring state. This result might seem counter-intuitive as a multi-zone model considers the emission coming from an entire extended jet. However, the power in a specific slice of the multi-zone jet is conserved and we practically follow that zone as it evolves along with the jet. Hence, the total jet emission will represent the integration of a single zone in the jet over its entire evolution. The conservation of energy in that zone means that the acceleration region will dominate the non-thermal synchrotron and IC emission, so regions further out in the jet will contribute less and less as the particle number density decreases. Even naively assuming that the jet region contributes the same amount of power in all slices, yields a total jet power that is an order of magnitude lower than that found for `OneZone_lep`. For comparison, the Eddington luminosity of PKS 1424-418 can be calculated using equation 1.9 to find that  $L_{\text{Edd}} \approx 5.85 \times 10^{47} \text{ erg s}^{-1}$ . The power requirements of the single-zone model are clearly too large and this result lies at the heart of the *blazar energy crisis*. Usually this solely applies to lepto-hadronic models, but here it is shown that the power demand of single-zone models is generally high and close to the Eddington limit as well.

Quiescent	BHJet	OneZone_lep	Flare	BHJet	OneZone_lep
$\sigma$	$3.548 \times 10^{-2}$	$5.088 \times 10^{-3}$	$\sigma$	$3.548 \times 10^{-2}$	$1.057 \times 10^{-3}$
$\delta$	66.036	39.23	$\delta$	57.64	42.75
$z (R_g)$	$3.88 \times 10^4$	$5.27 \times 10^3$	$z (R_g)$	$3.88 \times 10^4$	$6.96 \times 10^3$
$\beta_p$	0.423	0.889	$\beta_p$	1.075	27.516
$p$	1.77	2.06	$p$	1.50	1.52
$\gamma_{\text{max}}$	$5.17 \times 10^3$	$0.98 \times 10^3$	$\gamma_{\text{max}}$	$5.05 \times 10^3$	$1.69 \times 10^3$
$P_{\text{jet}}$ (erg/s)	$4.840 \times 10^{44}$	$8.107 \times 10^{47}$	$P_{\text{jet}}$ (erg/s)	$5.614 \times 10^{44}$	$3.004 \times 10^{47}$
$P_B$ (erg/s)	$8.306 \times 10^{42}$	$2.065 \times 10^{45}$	$P_B$ (erg/s)	$9.642 \times 10^{42}$	$3.695 \times 10^{45}$
$P_e$ (erg/s)	$3.515 \times 10^{42}$	$1.836 \times 10^{45}$	$P_e$ (erg/s)	$1.037 \times 10^{43}$	$1.343 \times 10^{45}$
$P_p$ (erg/s)	$4.722 \times 10^{44}$	$8.068 \times 10^{47}$	$P_p$ (erg/s)	$5.414 \times 10^{44}$	$2.966 \times 10^{47}$

TABLE 5.3 Parameters to determine the physical conditions in the acceleration region for the joint fit of PKS 1424-418 with `BHJet` and `OneZone_lep`. These values were obtained from the fits shown in Fig. 3.7 and 5.4.

## 5.3 Lepto-Hadronic Single-Zone Modelling of Blazar SEDs

After having fitted the SEDs of TXS 0506+056 and PKS 1424-418 with `BHJet` in Chapter 3), `HadJet` in Chapter 4 and `OneZone_lep` in Section 5.2, there is only the lepto-hadronic single-zone model left to study. This discussion will complete the comparison of the different choices one has when modelling blazar SEDs. The multi-zone fits with `HadJet` turned out to be slightly better constrained than the leptonic multi-zone joint fit for PKS 1424-418. The addition of non-thermal protons even lifted some of the degeneracies seen in the fits done with `BHJet`. For the single SED of TXS 0506+056 it turned out to be difficult to judge whether the lepto-hadronic model was better constrained. This section will study whether this trend is the same for the lepto-hadronic single-zone model referred to as `OneZone_lephad`.

Before showing any fits, the differences between `OneZone_lep` and `OneZone_lephad` need to be pointed out. Similarly to the difference between `BHJet` and `HadJet`, there are now non-thermal protons that produce emission as well. In order to describe the powerlaw distribution for the protons, new parameters were introduced (in bold). The non-thermal proton distribution is fully described by specifying a spectral index  $\mathbf{p}_p$ , a minimum ( $\gamma_{\min, p}$ ) and a maximum Lorentz factor ( $\gamma_{\max, p}$ ), and a proton number density  $\mathbf{n}_p$  as can be seen in Appendix B.2. Before, we saw that the fraction of non-thermal protons is only constrained by the fact that the secondary synchrotron emission cannot overshoot the X-ray data. Because of the lack of constraints, the proton number density was set equal to the electron number density which enforces a lepton-to-proton ratio of 1 just as for the fits with `HadJet`. Another similarity with the multi-zone fits is that the maximum Lorentz factor of the protons is equivalent to that of the electron distribution.

### 5.3.1 Lepto-Hadronic Single-Zone SED Fit for TXS 0506+056

Sections 3.4, 4.2 and 5.2.1 have all shown that the statistically most probable fit parameters have difficulties explaining the SED data of TXS 0506+056 visually. While the fits with the multi-zone models led to a visually acceptable fit, the `OneZone_lep` model clearly had more difficulty. For `OneZone_lephad` this was not any different as the median values of the parameter posteriors led to the fit presented in the left panel in Fig. 5.6.

This fits shows that both bumps in the SED do not extend to high enough frequencies similar to the fit with `OneZone_lep`. As discussed before, imposing a modified cutoff on the particle distribution could fix this type of problem. Sometimes, a sharper cutoff is required as the SED drops very quickly or a slower cutoff could help in the situation for TXS 0506+056. However, the acceleration mechanism(s) in relativistic jets are poorly understood as is the exact shape of the cutoff. Therefore, imposing a cutoff other than a simple exponential cutoff would only be convenient for the user while not motivated by physics. Another possible explanation would be that this steady state model is simply not able to explain the flaring periods of blazars. A time-dependent injection of non-thermal particles, such as that used in AM<sup>3</sup> for example (Klinger et al. 2023), could help alleviate the issues with reaching the highest energies in the SEDs. Yet again, these flaring epochs are to be better understood and the conditions could vary significantly from source to source before any drastic changes are implemented in the model.

For comparison, the fit with the lowest reduced  $\chi^2$  value found in the MCMC run is shown in

the right-hand panel of Fig. 5.6. This fit shows better agreement with the SED data, but again the optical data is being fitted with IC emission which is generally not expected to be the case for blazars. The fit parameters of both fits are presented in Table 5.4. An interesting feature of the fits shown in Fig. 5.6 is the contribution of the  $p\gamma$ -interactions compared to that of the pp-interactions. For the fit with `HadJet` of the same data in Fig. 4.1, the pp-interactions were the dominant hadronic channel to produce  $\gamma$ -rays. For that fit, the  $p\gamma$ -interactions produced less  $\gamma$ -rays, but this was on a similar level as the the pp-interactions. For the fit with `OneZone_lephad` this is not the case, and the  $p\gamma$ -interactions are dominant while the pp-interactions have a very low flux. Even multiplying the flux due to pp-interactions by a factor of  $10^3$  does not make that component visible. Therefore, we conclude that this component is negligible for this fit. Interestingly, the resulting  $\gamma$ -ray flux from the  $p\gamma$ -interactions is also larger than that found with `HadJet`. Having a multi-zone jet model allows for more proton-proton interactions as the jet has multiple slices in which the protons can interact. However, the same photon fields in the relatively confined region of a single-zone model lead to more  $p\gamma$  interactions.

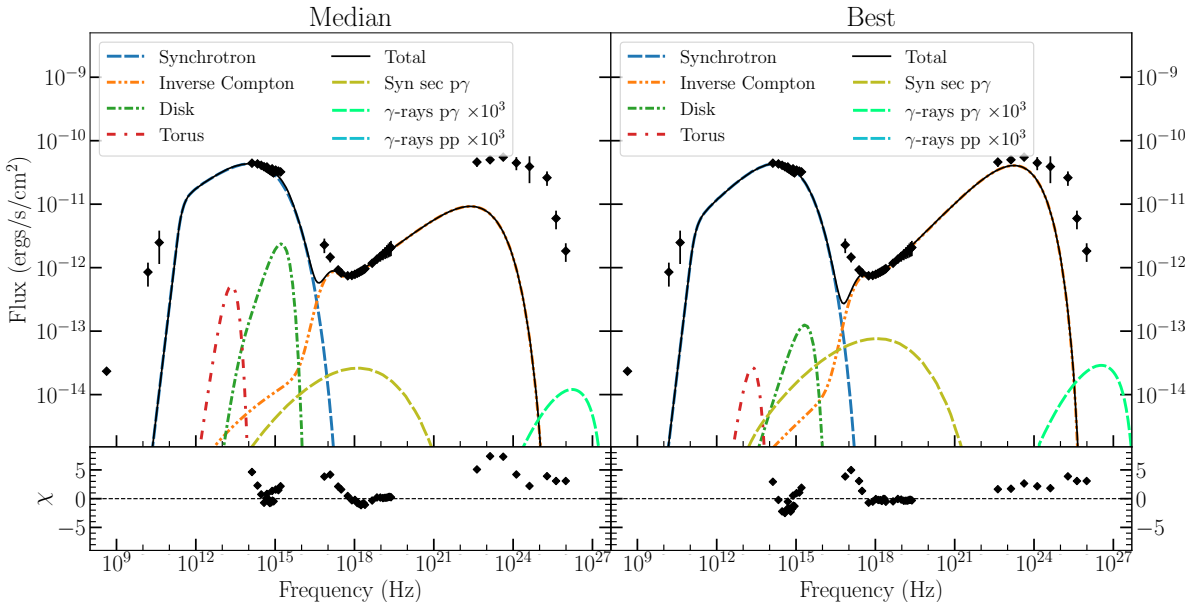


FIG. 5.6 – Fits of the flaring state of TXS 0506+056 in 2017 with `OneZone_lephad` together with the residuals in the lower panel. All components of the SED are shown as well as the sum of them which fits the SED data. The left-hand panel shows the fit with the parameters obtained from the median of all parameter posteriors. The right-hand panel shows the fit using the parameters that result in the lowest reduced  $\chi^2$ .

As expected, the fit parameters for the ‘best’ and ‘median’ fit are very different in analogy to the fits in Section 5.2.1. Interestingly, the confidence intervals on the median values are better constrained than they were for the leptonic single-zone model. Comparing the best-fit values for `OneZone_lep` and `OneZone_lephad` shows that the lepto-hadronic fit requires a stronger magnetic field, a higher particle number density, a lower maximum electron Lorentz factor and a slower jet than the fit with the `OneZone_lep` model. All the other fit parameters are very similar considering their confidence intervals.

Looking back at Section 4.2, where the differences between the `BHJet` and `HadJet` fits of

Fit	$\theta$ (°)	R $10^{16}$	B $10^{-1}$	$n_e$ $10^2$	$\gamma_{\max, e}$ $10^3$	$p_e$	$L_{\text{disk}}$ $10^{-1}$	$R_{\text{in}}$ $R_g$	$f_{\text{BLR}}$ $10^{-1}$	$f_{\text{DT}}$ $10^{-1}$	$\Gamma$	$\chi^2/\text{d.o.f.}$
Best	0.80	5.87	6.44	0.93	1.59	2.12	0.11	7.00	39.99	0.76	39.25	160.27/38
Median	$1.44^{+0.12}_{-0.13}$	$4.41^{+0.80}_{-0.53}$	$22.28^{+5.10}_{-4.08}$	$5.46^{+1.70}_{-1.12}$	$1.16^{+0.15}_{-0.10}$	$2.33^{+0.07}_{-0.19}$	$1.64^{+0.87}_{-1.05}$	$44.46^{+47.55}_{-31.14}$	$2.58^{+1.04}_{-1.29}$	$0.97^{+0.63}_{-0.31}$	$35.43^{+3.91}_{-4.27}$	285.64/38

TABLE 5.4 Fit parameters for the SED data after the 2017 flare of TXS 0506+056 using `OneZone_lephad`. The upper row are the fit parameters for the best fit and the parameters in the lower row are the median values obtained with MCMC. We also report the reduced  $\chi^2$  value for the fit.

TXS 0506+056 were discussed, the trends between parameters are a bit different. For the multi-zone models, there was a decrease in the magnetization and the jet power together with an increase in the jet Lorentz factor when using a lepto-hadronic model, while the opposite is seen here. A drop in the maximum Lorentz factor of the particles was seen in the fits with both single- and multi-zone models. Moreover, the increase in the disk luminosity as well as a lower inclination angle was observed in the multi-zone models.

The next step is to directly compare to the results found using `HadJet` in Table 4.1. These show a remarkable similarity with the parameters found using the `OneZone_lephad` model. Parameters like the inclination angle, the spectral index, the disk luminosity and its truncation radius,  $f_{\text{BLR}}$ , and  $f_{\text{DT}}$  are all very close to each other. In order to compare the other parameters, they can again be converted to see if they match those found with the multi-zone model. The Doppler factor for the fit with `OneZone_lephad` is determined to be  $\delta \approx 39.79$  which is somewhat higher than for the leptonic single-zone fit. Assuming that the variability timescale of TXS 0506+056 is about a day, the upper limit on the size of the emitting region is  $R' \approx 8.93 \times 10^{16}$  cm. This size is in agreement with both the results found in Table 5.4 and those found with `OneZone_lep`. The region size will yield an approximate distance to the BH of  $z \approx 3.55 \times 10^{18}$  cm  $\approx 7.90 \times 10^4 R_g$  which is again similar, but further away than the location of the acceleration region found with `HadJet`.

The last quantity left to compare between the fits with the single- and multi-zone model is the magnetization. Using equation 1.62 and the magnetic field strength and particle number density in Table 5.4, this yields  $\sigma = 5.04 \times 10^{-1}$ . Note that this is close to the value found with `HadJet`, and is in fact slightly higher which is opposite to what was found with the `OneZone_lep` model. Nevertheless, this means that the conditions in the acceleration region as well as most of the model parameters found with `HadJet` and `OneZone_lephad` are very similar. Our statistical approach of fitting the SED data does seem to lead to certain conditions in the jet which are reflected by the median values of the parameter posteriors. The results suggest that the jet conditions producing a good fit for a multi-zone model will not directly lead to a single-zone fit that fits the data well visually. Apparently we have to explore a different of the parameter space for lepto-hadronic, single-zone models in order to that. Alternatively, one could resort to extra modifications like broken powerlaws, different forms for the cutoff of the particle distribution or different external photon fields.

Lastly, we can look at the posterior distributions resulting from the fit with `OneZone_lephad` shown in Fig. 5.7. As `OneZone_lephad` does not have a parameter like  $f_{\text{nth}, p}$  seen in `HadJet`, Fig. 5.7 shows the distributions for the same four parameter shown for `OneZone_lep`. These posteriors are actually well constrained and we see clear favoured regions in the two-dimensional posteriors. Once again, the statistics show that the statistically most probable fit parameters do

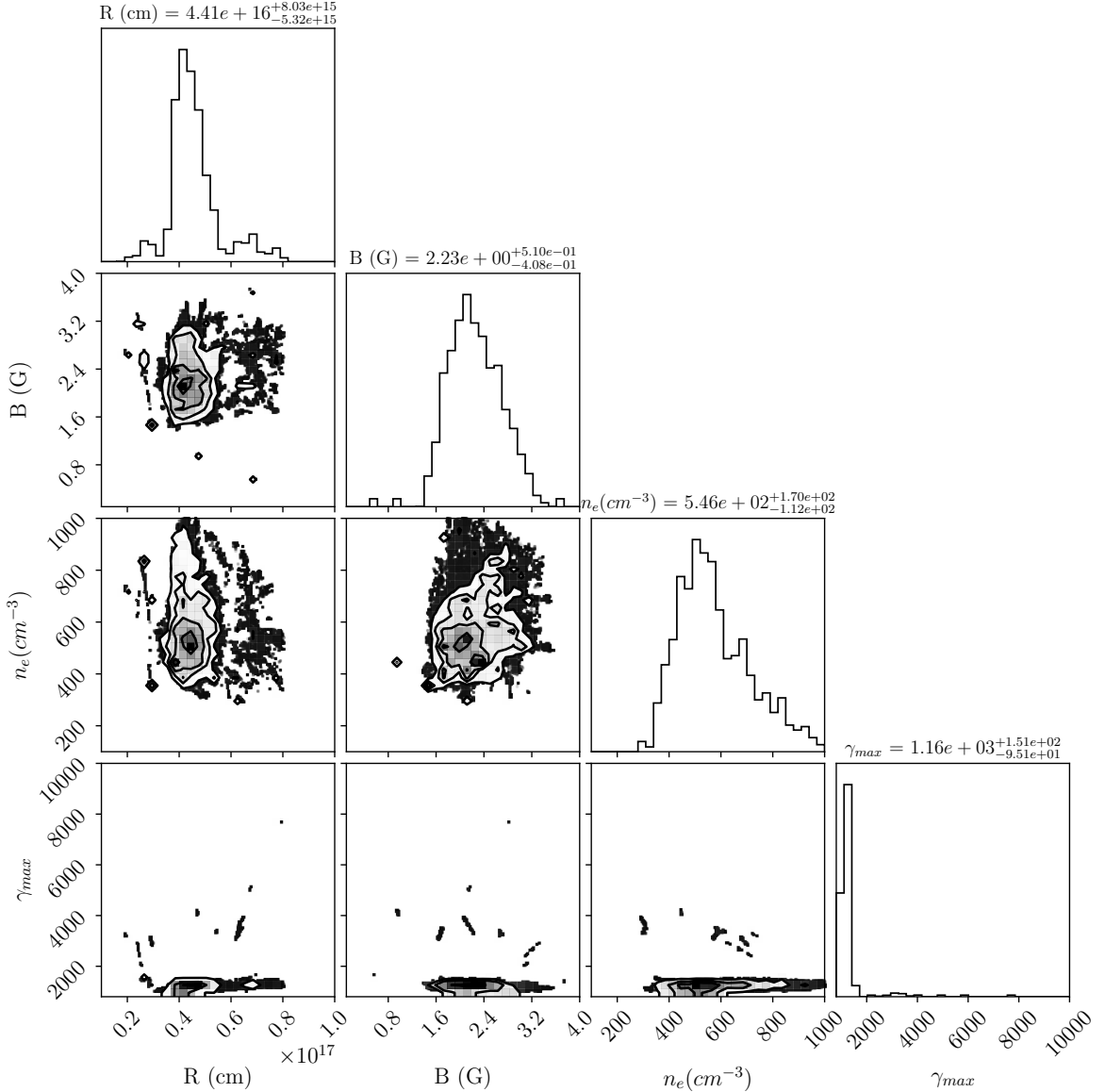


FIG. 5.7 – Corner plot with posterior distributions for the fit of the TXS 0506+056 SED with `OneZone_lephad`. In the plot, the model parameters for the radius of the emission region  $R$ , the magnetic field strength  $B$ , the electron number density  $n_e$  and the maximum Lorentz factor  $\gamma_{max}$  are shown.

not always produce a visually acceptable fit. Current statistical methods have difficulty finding the most optimal parameters and new methods need to be developed in order to compare models more accurately in a statistical sense. It is interesting to see that the addition of hadronic interactions leads to a more well defined set of best-fit parameters when compared to the corner plot in Fig. 5.3. The fits with single-zone models do have more scattered posteriors than the fits with multi-zone models making it hard to identify any degeneracies, but Fig. 5.3 does not seem to show any degeneracies at all.

### 5.3.2 Lepto-Hadronic Single-Zone SED Fits for PKS 1424-418

The last fit to consider, is the joint fit of the  $\alpha$  and  $\eta$  epochs for PKS 1424-418 with `OneZone_lephad`. The fits with the other models have shown that the joint fit does help in constraining the fit parameters, but for `OneZone_lep` this remained a difficult task. For the fit with the leptonic, single-zone model we encountered problems for the flaring state of PKS 1424-418, and its power requirements were very close to the Eddington luminosity. On top of that, the multi-zone models are more constrained by the full MWL dataset even though the resulting conditions in the jet can be comparable between the single- and multi-zone models. Adding hadronic interactions has led to narrower confidence intervals for the fit with `OneZone_lephad` of the TXS 0506+056 SED, and it also led to less degenerate results for the multi-zone jet model `HadJet`.

The joint fit for PKS 1424-418 with the `OneZone_lephad` model is shown in Fig. 5.8. This fit shows similar behavior as the joint fit with the `OneZone_lep` model. Fitting the  $\gamma$ -rays as well as possible, leads to a worse fit in the synchrotron regime, and there are again problems with the sharp drop of the lower energy bump. Another thing to notice, is that the secondary synchrotron emission is practically maximized. It cannot be any stronger since it would start to overpredict the X-ray data. Clear the powerlaw shape of the X-ray data cannot be described solely by the secondary emission as this peaks around the same frequency as the X-ray data. The relative strength of the secondary synchrotron component is different from that found for

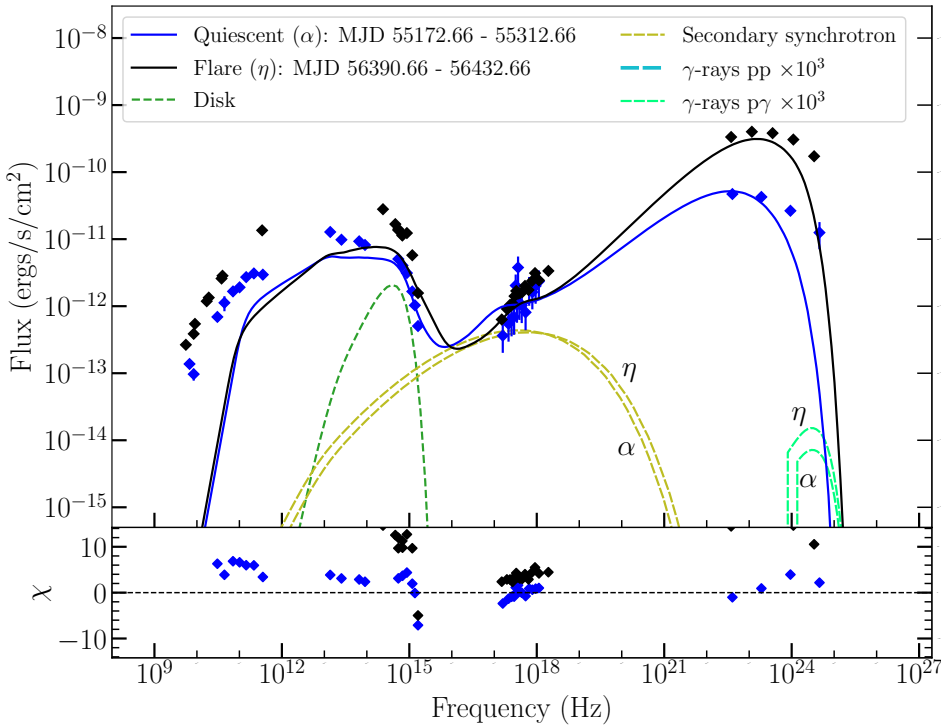


FIG. 5.8 – Joint fit with `OneZone_lephad` for the epochs  $\alpha$  and  $\eta$  of PKS 1424-418 which represent a quiescent and a flaring state of the source respectively. The contribution of the accretion disk for each epoch is shown by the dashed lines. The residuals for the fits of both epochs are shown in the lower panel.

TXS 0506+056, where the fits with both `HadJet` and `OneZone_lephad` predicted a smaller contribution. Additionally, the joint fit for PKS 1424-418 with `HadJet` showed a larger secondary synchrotron component for the flare relative to the quiescent state, but Fig. 5.8 shows very similar contributions in both states.

While the contribution of the pp-interactions to the  $\gamma$ -rays was weaker than that of the  $p\gamma$ -interactions for the fit of TXS 0506+056, it is the more dominant contribution for this fit which agrees with the results for the fits of TXS 0506+056 and PKS 1424-418 with `HadJet`. Therefore, the resulting conditions found for TXS 0506+056 in last section, occupy a very specific part in parameter space that we normally do not see for blazars. The background population of cold protons is expected to lead to more pp- than  $p\gamma$ -interactions in both single- and multi-zone lepto-hadronic jet models.

The best fit parameters for the fit in Fig. 5.8 are reported in Table 5.5. First of all, let us compare these parameters to the ones found with `OneZone_lep` in Section 5.2.2. The tables show that the fit with `OneZone_lephad` has a significantly higher reduced  $\chi^2$  value than the leptonic single-zone fit. The confidence intervals of the parameters are slightly wider and the values themselves differ from those found with `OneZone_lep`. The fact that the fit with the lepto-hadronic model requires an extremely low inclination angle of 0.13 suggests that there is not enough power available in the blob such that relativistic beaming is enhanced in order to compensate. Indirectly, this will affect the other parameters making it difficult to compare the two fits. Nevertheless, the main differences between the leptonic and lepto-hadronic fits are that the lepto-hadronic fit predicts a stronger magnetic field for both epochs, and especially the parameters in the flaring state are very different. This epoch has very different best-fit values for the particle number density, the maximum particle Lorentz factor, the spectral index and the Lorentz factor of the blob.

Epoch	$\theta$ (°)	R $10^{16}$	B $10^{-1}$	$n_e$ ( $= n_p$ ) $10^2$	$\gamma_{\max, e}$ ( $= \gamma_{\max, p}$ ) $10^2$	$p_e$ ( $= p_p$ )	L <sub>disk</sub> (L <sub>Edd</sub> ) $10^{-1}$	R <sub>in</sub> (R <sub>g</sub> )	$\Gamma$	$\chi^2/\text{d.o.f.}$
Joint	$0.13^{+0.09}_{-0.20}$						$4.97^{+0.03}_{-0.10}$	$99.09^{+5.80}_{-3.71}$		3174.35/50
$\alpha$		$7.89^{+0.08}_{-2.88}$	$6.88^{+0.39}_{-0.36}$	$1.84^{+3.21}_{-0.34}$	$8.07^{+4.21}_{-0.05}$	$1.96^{+0.13}_{-0.05}$			$29.48^{+1.72}_{-1.44}$	
$\eta$		$7.79^{+0.16}_{-3.61}$	$5.30^{+0.16}_{-0.29}$	$0.15^{+1.68}_{-0.91}$	$8.72^{+2.59}_{-0.30}$	$1.73^{+0.02}_{-0.02}$			$49.65^{+0.28}_{-2.48}$	

TABLE 5.5 Best fit parameters for the joint fit with `OneZone_lephad` of the quiescent epoch  $\alpha$  and the flaring epoch  $\eta$  of PKS 1424-418 together with their confidence intervals. We also report the reduced  $\chi^2$  value for the fit.

Despite the fact that the fits in Fig. 5.8 do not seem to fit the data very well, we can extract important physical quantities like the Doppler factor, the upper limit on the region size, the distance to the BH and the magnetization for both the quiescent and the flaring state. These values are reported in Table 5.6 where the conditions are compared to those found in the acceleration region of the fits done with `HadJet`. The upper limit on the region sizes is calculated to be  $R'_q \approx 1.50 \times 10^{17}$  cm and  $R'_f \approx 2.52 \times 10^{17}$  cm for the quiescent and flaring state, respectively. Once again, the region sizes found in the fit do not violate the upper limit, but looking at the corner plot in Fig. 5.9 shows that we probably need larger values of  $R$ . Using these values to calculate the distance from the BH shows that the emission region is actually very close to the BH. The calculated distance is slightly less than that of the acceleration region,

which was also found for the fits with `OneZone_lep`.

Interestingly, the fit with the lepto-hadronic model does not predict a large value of  $\beta_p$  as was seen for the fit with `OneZone_lep`, meaning that it is more magnetically dominated. In fact, the fit with `OneZone_lephad` requires very low values of  $\beta_p$  that are almost beyond the normally observed range for astrophysical systems. These low values are mostly caused by the relatively small particle number densities which were not seen for the fits with `OneZone_lep`. This dominant magnetic field is also reflected by the higher magnetization and there is even less power required to fit the SED. However, the power demand is far larger than that of the acceleration region in `HadJet`. The power demand for the lepto-hadronic single-zone model is slightly lower than for the leptonic version, but it is too close to the Eddington limit to be physically possible. From that point of view, one would favour a multi-zone jet model. It must be noted that the fits with `OneZone_lephad` show very large Doppler factors, especially for the flaring state because the inclination angle had a very low value. While high Doppler factors can be seen in other blazar SED fits, it always remains a question whether Doppler factors on the order of  $\delta \sim 100$  are actually physical or just required to be able to fit the data.

Quiescent	HadJet	OneZone_lephad	Flare	HadJet	OneZone_lephad
$\sigma$	$1.086 \times 10^{-2}$	$1.361 \times 10^{-2}$	$\sigma$	$1.086 \times 10^{-2}$	$9.900 \times 10^{-2}$
$\delta$	77.37	58.493	$\delta$	70.09	97.960
$z (R_g)$	$3.70 \times 10^4$	$1.302 \times 10^4$	$z (R_g)$	$3.70 \times 10^4$	$3.653 \times 10^4$
$\beta_p$	0.981	0.030	$\beta_p$	1.228	$6.540 \times 10^{-3}$
$p$	1.73	1.96	$p$	1.50	1.73
$\gamma_{\max}$	$5.31 \times 10^3$	$0.81 \times 10^3$	$\gamma_{\max}$	$4.55 \times 10^3$	$0.87 \times 10^3$
$P_{\text{jet}} (\text{erg/s})$	$9.546 \times 10^{43}$	$1.451 \times 10^{47}$	$P_{\text{jet}} (\text{erg/s})$	$2.810 \times 10^{44}$	$3.862 \times 10^{46}$
$P_B (\text{erg/s})$	$2.842 \times 10^{42}$	$8.978 \times 10^{45}$	$P_B (\text{erg/s})$	$3.073 \times 10^{42}$	$1.496 \times 10^{46}$
$P_e (\text{erg/s})$	$2.784 \times 10^{42}$	$2.725 \times 10^{44}$	$P_e (\text{erg/s})$	$9.657 \times 10^{42}$	$9.786 \times 10^{43}$
$P_p (\text{erg/s})$	$8.984 \times 10^{43}$	$1.358 \times 10^{47}$	$P_p (\text{erg/s})$	$2.683 \times 10^{44}$	$2.356 \times 10^{46}$

TABLE 5.6 Parameters to determine the physical conditions in the acceleration region for the joint fit of PKS 1424-418 with `HadJet` and `OneZone_lephad`. These values were obtained from the fits shown in Fig. 4.3 and 5.8.

Lastly, the corner plot in Fig. 5.9 shows that the model parameters are well constrained with single-peaked posterior distributions. There is again a significant amount of scatter just as observed for the fit with `OneZone_lep`. Nevertheless, the lepto-hadronic fits are better constrained than their leptonic equivalent which is something that was seen for all the fits in this thesis. While the addition of extra components and interactions might seem to lead to more ambiguity or even degeneracy in the models, the acceleration of protons actually helps to constrain the parameter space.

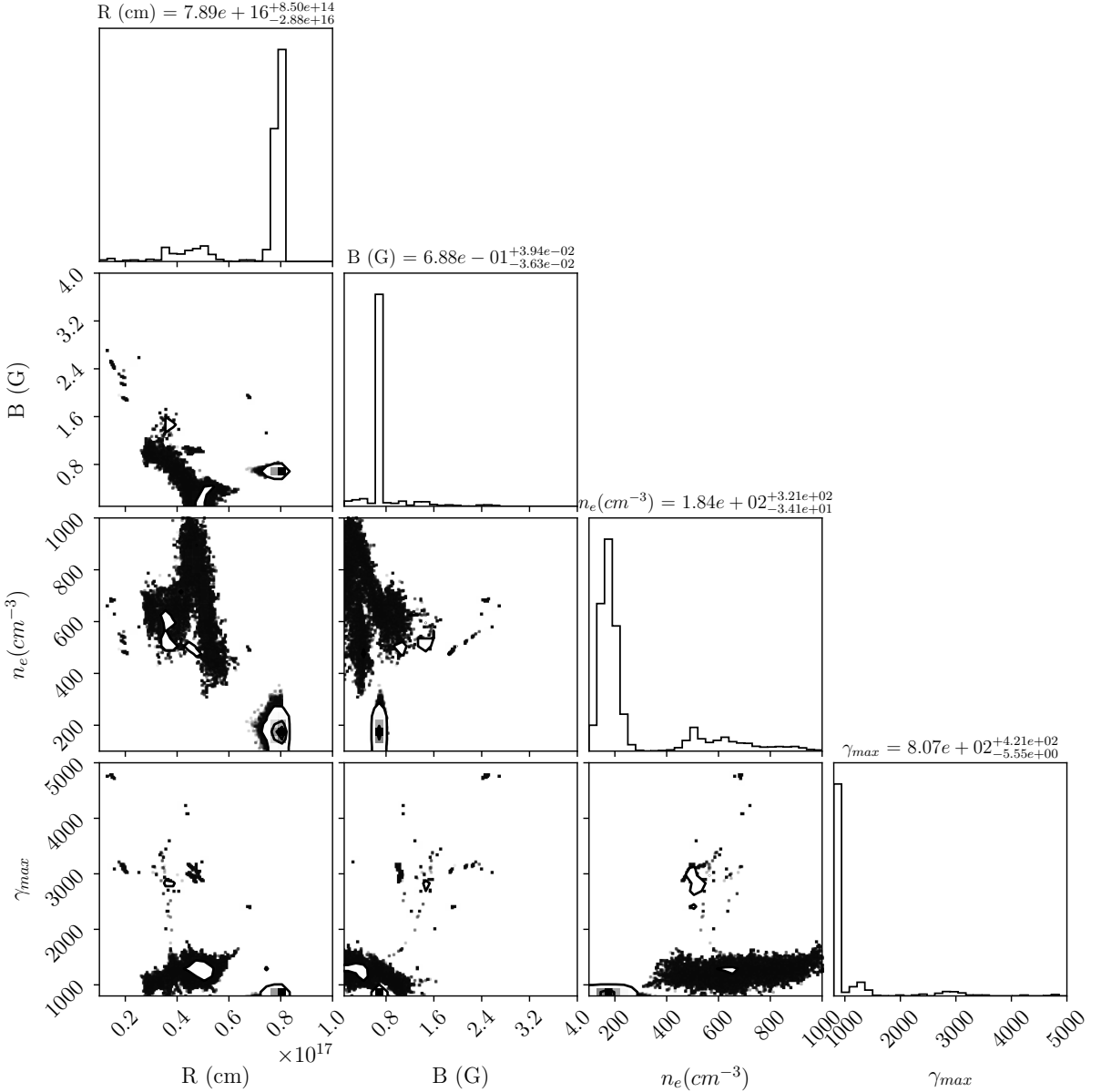


FIG. 5.9 – Corner plot with posterior distributions for the joint fit of  $\alpha$  and  $\eta$  epochs of PKS 1424-418 with `OneZone_lephad`. The model parameters for the radius of the emission region  $R$ , the magnetic field strength  $B$ , the electron number density  $n_e$  and the maximum Lorentz factor  $\gamma_{\max}$  are shown.

## 5.4 Reflective Analysis and Broader Implications

With the fits presented in the previous section, we have concluded this comparison project. This thesis represents one of the first instances where the multi-zone models `BHJet` and `HadJet` have been used to fit the SEDs of blazars. Previously, the multi-zone model has mostly been used to study XRBs and LLAGN, with some recent exceptions ([Lucchini et al. 2019a,b](#)). The short variability timescales of blazars, combined with the more confined nature of single-zone models, have led to the majority of the blazar SED modelling community to use single-zone models (e.g. [Tavecchio et al. 1998](#); [Ghisellini & Tavecchio 2010](#); [Böttcher et al. 2013](#); [Gao et al. 2017](#); [Reimer et al. 2019](#)). The increase in computing power, along with a better understanding of leptonic and hadronic processes, has led to significant progress in understanding blazar jets. Despite this progress, there is no consensus on which particle interactions are most important, and only recently have researchers begun to compare models and consider whether single-zone models are the most appropriate to use. The lepto-hadronic blazar code comparison paper by [Cerruti et al. \(2022\)](#) was the first collaborative attempt to self-consistently study different models. Despite its importance in understanding the different models, [Cerruti et al. \(2022\)](#) focused only on hypothetical situations and did not include an SED of a real source.

While there is no agreement on the exact particle interactions that should be used, blazars are still being studied with the available models. In this thesis, we considered two different blazar sources: TXS 0506+056 and PKS 1424-418. Remarkably, a significant effort resulted in the modelling of 324 blazars with the lepto-hadronic AM<sup>3</sup> model ([Rodrigues et al. 2023](#)). Lepto-hadronic studies of blazar samples have been conducted before (e.g. [Tavecchio et al. 2010](#); [Böttcher et al. 2013](#); [Petropoulou et al. 2015](#); [Oikonomou et al. 2019](#); [Lioudakis & Petropoulou 2020](#)), but this study is the largest to date. Regardless of which particle interactions should be included, studying such a large collection of sources allows to find correlations within the blazar population. [Rodrigues et al. \(2023\)](#) aimed to systematically model the effect of CR protons on the MWL data to learn about the multi-messenger nature of the blazar population. They concluded that the optical and GeV  $\gamma$ -ray broadband spectrum of blazars is well described by leptonic emission, but for a third of their blazar population, the modelling of the X-rays benefited from an additional hadronic component. In particular, blazars that are brighter in the GeV  $\gamma$ -rays were found to favor a higher neutrino production efficiency and a lower baryonic loading factor, i.e. a higher lepton-to-proton ratio. However, it should be noted that [Rodrigues et al. \(2023\)](#) used all available data from the literature for each source in their catalogue, resulting completely non-simultaneous SEDs.

In this thesis, a similar comparison to that of [Rodrigues et al. \(2023\)](#) can be made. In Chapter 3 and Section 5.2 fits for TXS 0506+056 and PKS 1424-418 were performed using a leptonic single- and multi-zone model, respectively. In contrast to the results found by [Rodrigues et al. \(2023\)](#), the leptonic fits did not have any trouble to fit the X-ray data for either source. For the SED fit for TXS 0506+056 with `HadJet`, a significant fraction of non-thermal protons was found, but this did not significantly contribute to fitting the X-rays. In the case of PKS 1424-418, the secondary synchrotron component was significant, but the best-fit hadronic fraction was roughly two orders of magnitude smaller than the leptonic fraction. Nevertheless, for PKS 1424-418 the secondary emission did help fit the X-ray data, as the leptonic component was too steep. Therefore, our results agree with the conclusion of [Rodrigues et al. \(2023\)](#) that some sources benefit from adding a hadronic component, while others are

perfectly well explained by leptonic emission only. However, considering that this thesis only examined two blazars, we cannot generalize these findings to the entire blazar population.

Secondly, from a statistical perspective, the addition of non-thermal protons helped to lift degeneracies seen in the leptonic model. This applied to the MCMC results for both single- and multi-zone modelling. The requirement that protons must be accelerated places additional constraints on the magnetization and the jet power. Even when the hadronic components did not directly affect the SED fit, the parameter posteriors benefited from the inclusion of protons in the model.

Lastly, another important aspect discussed in this thesis is that single-zone models require a large fraction of the Eddington luminosity to fit blazar SED data. This is a known problem in the field, referred to as the blazar energy crisis ([Cao & Wang 2014](#); [Liodakis & Petropoulou 2020](#)). Admittedly, the Eddington luminosity is the maximum luminosity for a steady, spherically symmetric accreting system such that it is not a fundamental limit. However, practically every single-zone fit of a blazar SED requires jet powers that exceed this quantity (see e.g. figure 5 in [Rodrigues et al. \(2023\)](#)). During flaring states, blazars can temporally exceed the Eddington luminosity, but this luminosity cannot be maintained during quiescent states. The need for excessive jet powers in single-zone models was also demonstrated in Chapter [1.5.1](#). In contrast, the fits with the multi-zone models, either leptonic or lepto-hadronic, in Chapters [3](#) and [4](#) found more conservative jet powers. This clearly indicates the advantage of using multi-zone jet models over the fundamentally limited single-zone models.

# Chapter 6

## Summary and Conclusions

Black holes provide one of the most extreme astrophysical environments known from observations. Ranging from the smaller stellar mass black holes to the supermassive ones at the center of galaxies, they all power the production of emission spanning the entire EM spectrum through accretion. Accretion of the surrounding matter not only leads to growth of the BH, but also to relativistic outflows in the form of either winds or jets. Relativistic jets are collimated, highly relativistic outflows of matter capable of emitting highly energetic non-thermal radiation. In the case of an actively accreting SMBH, called an AGN, the orientation of this relativistic jet is crucial for the characteristics of the system. The inclination angle with respect to the line of sight for these jetted AGN can determine whether one is looking at a LLAGN or an extremely powerful blazar that can outshine its host galaxy by over a million times. Such blazars are observed when the relativistic jet has a small inclination angle, leading to strong relativistic beaming effects.

The temporal coincidence of a  $\gamma$ -ray flare of the blazar TXS 0506+056 with the neutrino event IC-170922A in 2017 ([IceCube Collaboration 2018b](#)), has led to an increased interest in blazars. This detection suggested that blazars could be major contributors to the astrophysical backgrounds of  $\gamma$ -rays, neutrinos and CRs for which the sources remain unknown. In order to understand the mechanisms responsible for the formation of relativistic jets as well as blazars specifically, BH jet models are used to reproduce the MWL emission of these sources and extract physical information. This SED modelling has led to a zoo of different jet models, with different geometries, particle interactions and temporal evolution. Most models make use of a single-zone approach in which the emission region is a single, spherical, homogeneous region in the jet responsible for all high-energy, optically thin emission. Increased computational power and a better understanding of hadronic interactions in these jets, has led to the development of leptohadronic, single-zone models. Hadronic interactions are necessary if one wants to explain the production of  $\gamma$ -rays, neutrinos and CRs in blazars. However, single-zone models are unable to explain the plasma dynamics involved in jet launching and its subsequent evolution. Moreover, the large amount of detail in single-zone models makes them computationally expensive such that a majority of the community uses a ‘fit-by-eye’ approach to do SED fits. In such an approach no statistical tools like least- $\chi^2$  or MCMC are used to extract information about the reliability of the fit parameters, and how these compare to different models.

Instead, one can use extended, multi-zone jet models that do make use of statistical tools when fitting an SED. Before this step forward can be taken, it is important to understand the fundamental differences between single- and multi-zone models, and if these could change when going from a leptonic to a leptohadronic model. To achieve this, this thesis aimed to do a self-consistent comparison of these types of jet models by using models with the same underlying structure and fitting the same sources. In practice, this meant that the SEDs of the blazars TXS 0506+056 and PKS 1424-418 were fitted using four different jet models. By

comparing the fit parameters, their confidence intervals, their posterior distributions, and the resulting physical conditions in the jet a complete picture of the differences and similarities between all types of models was obtained.

The first fits of TXS 0506+056 and PKS 1424-418 were done with the leptonic, multi-zone jet model **BHJet** in Chapter 3. This model was the most tested of all models used in this thesis, therefore providing a baseline to compare all results to. The SEDs of these blazars have been modelled before (see [Celotti & Ghisellini 2008](#); [Buson et al. 2014](#); [Paliya et al. 2017](#); [Keivani et al. 2018](#); [IceCube Collaboration 2018a](#)), but this thesis presents the first ever fits using a multi-zone jet model. The low inclination angle of blazars jets, leads to SEDs being dominated by non-thermal emission such that we are unable to constrain the base of the jet without introducing degeneracy in the model. An exploration of these degeneracies was done, providing important insights for future modelling in multi-zone jets.

The first fit considered the most simultaneous blazar SED in the literature of TXS 0506+056 collected in the two weeks after the aforementioned neutrino event in 2017. This fit showed excellent agreement with the data, but also the challenge to accelerate particles in the jet up to high enough Lorentz factors to explain  $\gamma$ -ray data of blazars. The fit also showed that using statistical methods to find the best fit is helpful, but large uncertainties can lead to a visually unsatisfying SED fit with a considerable amount of scatter in the parameter distributions. The lack of constraints can make it difficult to obtain well constrained parameters.

In order to improve on this, the blazar PKS 1424-418 was used for which multiple epochs with MWL data have been identified ([Krauß et al. 2016](#)). The fits for all these epochs agreed with the data, but the fits differed significantly from epoch to epoch while this is the same source. By doing a joint fit of a quiescent and flaring epoch of PKS 1424-418, the fits showed more agreement with significantly better constrained parameters. It was shown that the transition from a quiescent to a flaring state of this blazar can be explained by only changing the details of the emitting particle distribution. Although the joint fit showed better constrained parameters, there was a degeneracy of the jet power and the maximum Lorentz factor connected to the magnetization of the jet.

After the fits with **BHJet**, the next fits were done with the lepto-hadronic, multi-zone jet model **HadJet** in Chapter 4. This model contains the same physics, but now the injection of non-thermal protons and their corresponding hadronic interactions are considered. The fits with **HadJet** showed that the SED fits remain dominated by leptonic emission, as the hadronic components are inhibited by the upper limit imposed by the X-ray emission. The synchrotron emission produced by secondary leptons from the hadronic interactions peaks in the X-rays, and is relatively strong because of the strong magnetic field in blazars jets. For TXS 0506+056 the non-thermal proton fraction was found to be on the same order of the non-thermal electron fraction. On the other hand, for PKS 1424-418 the non-thermal proton fraction was found to be relatively small, but it did have a well constraint best-fit value. Importantly, the addition of hadronic interactions led to the degeneracies from the leptonic fits being lifted. A more thorough comparison of the two types of models showed that the overall behavior is similar, but the lepto-hadronic seemed to require a larger total power budget in which more magnetic energy is converted into kinetic energy. Moreover, the fits with **HadJet** favoured stronger external photon fields to enhance the EC emission needed to explain the  $\gamma$ -ray data.

Lastly, new single-zone versions of **BHJet** and **HadJet** were developed using the same libraries to ensure a self-consistent comparison with the multi-zone modelling results. In Section

5.1, these models were tested against the AM<sup>3</sup> single-zone code (Klinger et al. 2023) which confirmed that they reproduce the same results in steady-stay conditions for a simple SSC scenario (Cerruti et al. 2022). Subsequently, the single-zone models were used to fit the SEDs of TXS 0506+056 and PKS 1424-418 in Sections 5.2 and 5.3. These fits showed that it can be challenging to fit blazar SEDs with single-zone models. Especially for TXS 0506+056, the statistical methods were not able to converge on a visually acceptable fit, and even the fit with the lowest reduced  $\chi^2$  value seemed to be lacking the flexibility to fit the data perfectly. Nevertheless, the conditions that were found in the single-zone regions were comparable to those found in the acceleration region of the multi-zone models which applied to both the leptonic and lepto-hadronic codes.

A very important problem found during the fitting with the single-zone models was that these models require powers that are close to or even exceed the Eddington luminosity, whereas the multi-zone models required roughly 0.1% of Eddington luminosity in the acceleration region. The larger power demand is a known problem for single-zone models, and it has been seen in other studies of blazar samples (e.g. Tavecchio et al. 2010; Böttcher et al. 2013; Rodrigues et al. 2023). This consistent result for single-zone modelling of blazars confirmed that multi-zone models are more realistic in terms of energy budget and its evolution along the jet.

Interestingly, there were also some differences between the leptonic and lepto-hadronic single-zone models. The fits with the leptonic version required a lower magnetization than seen in the multi-zone model, but for the lepto-hadronic version a stronger magnetization than seen in the multi-zone model was required. The fits with the multi-zone models showed that the addition of protons requires more magnetic energy to power their acceleration, and the same behavior was seen for the single-zone models. For a single-zone geometry it impossible to consider the conversion the initial magnetization at the base of the jet into kinetic energy, such that a stronger magnetization in the emission region itself is needed. Therefore, single-zone models will consistently favour an emission region that it is more magnetically dominated.

In conclusion, the self-consistent comparison of different types of BH jet models presented here has shown that multi-zone models can lead to statistically better constrained models. These models can exploit all MWL emission of the source to put constraints on the launching, evolution and acceleration of the relativistic jet. The use of simultaneous data is important, but it will not automatically lead to a good fit, and other constraints like multiple epochs of the same source can help to constrain the model. Nevertheless, the leptonic multi-zone model showed degeneracies for the blazar SEDs, leading to ambiguity in the interpretation of the results. It was shown that the addition of non-thermal protons in a lepto-hadronic, multi-zone model could lift these degeneracies while preserving the overall conditions in the jet. The same behavior was shown for the single-zone equivalents of these models, where lepto-hadronic fits were better constrained and showed no degeneracies. The fits with the single-zone models did have difficulty fitting the SEDs without imposing any additional constraints or assumptions. They also required very strong magnetically dominated emission regions, with high Doppler factors that exceeded the Eddington luminosity for some fits. While blazars are extreme astrophysical objects, this showed that multi-zone models can explain these objects requiring less extreme conditions than the single-zone models while providing better fits.

# Bibliography

- Abbasi, R., Ackermann, M., Adams, J., et al. 2023, ApJ, 954, 75
- Abbasi, R. et al. 2013, Astroparticle Physics, 44, 40
- Abdo, A. A., Ackermann, M., Agudo, I., et al. 2010, The Astrophysical Journal, 716, 30
- Abhir, J., Joseph, J., Patel, S. R., & Bose, D. 2021, Monthly Notices of the Royal Astronomical Society, 501, 2504
- Abraham, J., Abreu, P., Aglietta, M., et al. 2008, Astroparticle Physics, 29, 188
- Abramowicz, M. A. & Fragile, P. C. 2013, Living Reviews in Relativity, 16, 1
- Abramowicz, M. A. & Fragile, P. C. 2013, Living Rev. Rel., 16, 1
- Acharyya, A., Adams, C. B., Archer, A., et al. 2023, Astrophysical Journal, 954, 70
- Ackermann, M., Bustamante, M., Lu, L., et al. 2022, Journal of High Energy Astrophysics, 36, 55
- Adamo, M., Pietroni, S., & Spurio, M. 2022, PoS, CORFU2021, 318
- Aguilar, M., Ali Cavasonza, L., Alpat, B., et al. 2019a, Phys. Rev. Lett., 122, 101101
- Aguilar, M., Ali Cavasonza, L., Ambrosi, G., et al. 2019b, Phys. Rev. Lett., 122, 041102
- Aguilar, M. et al. 2014a, Phys. Rev. Lett., 113, 121102
- Aguilar, M. et al. 2014b, Phys. Rev. Lett., 113, 221102
- Aguilar, M. et al. 2015a, Phys. Rev. Lett., 115, 211101
- Aguilar, M. et al. 2015b, Phys. Rev. Lett., 114, 171103
- Aguilar, M. et al. 2016, Phys. Rev. Lett., 117, 091103
- Aharonian, F. A. 2000, New Astronomy, 5, 377
- Ahnen, M. L., Ansoldi, S., Antonelli, L. A., Antoranz, P., et al. 2017, Astronomy and Astrophysics, 603, A31
- Ajello, M., Costamante, L., Sambruna, R. M., et al. 2009, The Astrophysical Journal, 699, 603
- Alston, W. N., Fabian, A. C., Kara, E., et al. 2020, Nature Astronomy, 4, 597
- Apel, W. et al. 2013, Astroparticle Physics, 47, 54
- Atoyan, A. & Dermer, C. D. 2001, Physical Review Letters, 87, 221102

## Bibliography

---

- Atwood, W. B., Abdo, A. A., Ackermann, M., et al. 2009, *Astrophysical Journal*, 697, 1071
- Ball, D., Sironi, L., & Özel, F. 2018, *The Astrophysical Journal*, 862, 80
- Ballo, L., Maraschi, L., Tavecchio, F., et al. 2002, *The Astrophysical Journal*, 567, 50
- Band, D., Matteson, J., Ford, L., et al. 1993, *The Astrophysical Journal*, 413, 281
- Bardeen, J. M. 1973, in *Black Holes (Les Astres Occlus)*, 215–239
- Baring, M. G., Böttcher, M., & Summerlin, E. J. 2017, *Monthly Notices of the RAS*, 464, 4875
- Baring, M. G., Böttcher, M., & Summerlin, E. J. 2016, *Monthly Notices of the Royal Astronomical Society*, 464, 4875
- Batista, R. A., Amin, M. A., Barenboim, G., et al. 2021, *Arxiv*, 46, 124
- Begelman, M. C. 1998, *The Astrophysical Journal*, 493, 291
- Belloni, T. 2010, *The Jet Paradigm*, Vol. 794 (Springer Berlin, Heidelberg)
- Berezinsky, V. 1991, *Nuclear Physics B - Proceedings Supplements*, 19, 375
- Bethe, H. & Heitler, W. 1934, *Proceedings of the Royal Society of London Series A*, 146, 83
- Biehl, D., Boncioli, D., Lunardini, C., & Winter, W. 2018, *Scientific Reports*, 8
- Bird, D. J., Corbató, S. C., Dai, H. Y., et al. 1993, *Phys. Rev. Lett.*, 71, 3401
- Blandford, R., Meier, D., & Readhead, A. 2019, *Annual Review of Astron and Astrophysics*, 57, 467
- Blandford, R., Simeon, P., & Yuan, Y. 2014, *Nuclear Physics B - Proceedings Supplements*, 256-257, 9, cosmic Ray Origin – Beyond the Standard Models
- Blandford, R. D., Königl, A., & Kellogg, W. K. 1979, *Relativistic Jets as Compact Radio Sources*
- Blandford, R. D. & Ostriker, J. P. 1978, *ApJL*, 221, L29
- Blandford, R. D. & Payne, D. G. 1982, *Monthly Notices of the Royal Astronomical Society*, 199, 883
- Blandford, R. D. & Znajek, R. L. 1977, *Monthly Notices of the Royal Astronomical Society*, 179, 433
- Blumenthal, G. R. 1970, *Phys. Rev. D*, 1, 1596
- Bodo, G., Mamatsashvili, G., Rossi, P., & Mignone, A. 2021, *Monthly Notices of the Royal Astronomical Society*, 510, 2391
- Bööttcher, M. & Reimer, A. 2004, *The Astrophysical Journal*, Volume 609, Issue 2, pp. 576-588., 609, 576

- Bolton, C. T. 1972, *Nature*, 235, 271
- Bonning, E., Urry, C. M., Bailyn, C., et al. 2012, *Astrophysical Journal*, 756, 13
- Böttcher, M. & Baring, M. G. 2019, *The Astrophysical Journal*, 887, 133
- Böttcher, M., Reimer, A., Sweeney, K., & Prakash, A. 2013, *Astrophysical Journal*, 768, 54
- Branchesi, M. 2016, *J. Phys. Conf. Ser.*, 718, 022004
- Brüggen, M. & Kaiser, C. R. 2002, *Nature*, 418, 301
- Burbidge, G. R. 1956, *The Astrophysical Journal*, 124, 416
- Buson, S., Longo, F., Larsson, S., et al. 2014, *Astronomy and Astrophysics*, 569, A40
- Cao, G. & Wang, J. 2014, *The Astrophysical Journal*, 783, 108
- Cardelli, J. A., Clayton, G. C., & Mathis, J. S. 1989, *Astrophysical Journal*, 345, 245
- Celotti, A. & Ghisellini, G. 2008, *Monthly Notices of the Royal Astronomical Society*, 385, 283
- Cendes, Y., Eftekhari, T., Berger, E., & Polisensky, E. 2021, *The Astrophysical Journal*, 908, 125
- Cerruti, M., Kreter, M., Petropoulou, M., et al. 2022, in 37th International Cosmic Ray Conference, 979
- Cerruti, M., Zech, A., Boisson, C., et al. 2019, *Monthly Notices of the Royal Astronomical Society*, 483, L12
- Cerruti, M., Zech, A., Boisson, C., & Inoue, S. 2015, *Monthly Notices of the Royal Astronomy Society*, 448, 910
- Chary, R.-R. & Pope, A. 2010, arXiv e-prints, arXiv:1003.1731
- Chatterjee, K., Liska, M., Tchekhovskoy, A., & Markoff, S. B. 2019, *Monthly Notices of the Royal Astronomical Society*, 490, 2200
- Chiaro, G., Salvetti, D., La Mura, G., et al. 2016, *Monthly Notices of the Royal Astronomical Society*, 462, 3180
- Chodorowski, M. J., Zdziarski, A. A., & Sikora, M. 1992, *The Astrophysical Journal*, 400, 181
- Coleman, A., Eser, J., Mayotte, E., et al. 2023, *Astroparticle Physics*, 149, 102819
- Connors, R. M. T., Markoff, S., Nowak, M. A., et al. 2016, *Monthly Notices of the Royal Astronomical Society*, 466, 4121
- Connors, R. M. T., van Eijnatten, D., Markoff, S., et al. 2019, *Monthly Notices of the Royal Astronomical Society*, 485, 3696

## Bibliography

---

- Cooper, A. J., Gaggero, D., Markoff, S., & Zhang, S. 2020, Monthly Notices of the Royal Astronomical Society, 493, 3212
- Corbel, S., Fender, R. P., Tzioumis, A. K., et al. 2000, Astronomy and Astrophysics, 359, 251
- Corbel, S., Nowak, M. A., Fender, R. P., Tzioumis, A. K., & Markoff, S. 2003, Astronomy and Astrophysics, 400, 1007
- Crumley, P., Caprioli, D., Markoff, S., & Spitkovsky, A. 2019, Monthly Notices of the Royal Astronomical Society, 485, 5105
- Crumley, P., Ceccobello, C., Connors, R. M. T., & Cavecchi, Y. 2017, Astronomy and Astrophysics, 601, A87
- Curtis, H. D. 1918, Publications of Lick Observatory, 13, 9
- Dermer, C. D. 1986, Astronomy and Astrophysics, 157, 223
- Di Matteo, T., Springel, V., & Hernquist, L. 2005, Nature, 433, 604
- Dirirsa, F. F., Britto, R. J., & Razzaque, S. 2015, in 60th Annual Conference of the South African Institute of Physics, 284–289
- Domínguez, A., Primack, J. R., Rosario, D. J., et al. 2011, Monthly Notices of the Royal Astronomical Society, 410, 2556
- Done, C., Gierliński, M., & Kubota, A. 2007, The Astronomy and Astrophysics Review, 15, 1
- Dubois, Y., Peirani, S., Pichon, C., et al. 2016, Monthly Notices of the Royal Astronomical Society, 463, 3948
- Eckart, A. & Genzel, R. 1996, Nature, 383, 415
- EHT Collaboration. 2021, The Astrophysical Journal Letters, 910, L13
- EHT MWL Science Working Group. 2021, The Astrophysical Journal, 911, L11
- Evoli, C. 2023, The Cosmic-Ray Energy Spectrum
- Falcke, H. & Biermann, P. L. 1995, Astronomy and Astrophysics, 293, 665
- Falcke, H., Körding, E., & Markoff, S. 2004, Astronomy & Astrophysics, 414, 895
- Falcke, H., Malkan, M. A., & Biermann, P. L. 1995, Astronomy and Astrophysics, 298, 375
- Falcke, H. & Markoff, S. 2000, Astronomy & Astrophysics, 362, 113
- Fan, Z.-H. & Cao, X. 2004, The Astrophysical Journal, 602, 103
- Farrell, S., Webb, N., Barret, D., Godet, O., & Rodrigues, J. 2009, Nature, 460, 73
- Fender, R. 2003, Jets from X-ray binaries

- Fender, R. & Belloni, T. 2012, *Science*, 337, 540–544
- Fender, R. & Gallo, E. 2014, *Space Science Reviews*, 183, 323–337
- Fender, R. P., Pooley, G. G., Brocksopp, C., & Newell, S. J. 1997, *Monthly Notices of the Royal Astronomical Society*, 290, L65
- Finke, J. D. 2016, *The Astrophysical Journal*, 830, 94
- Finke, J. D., Ajello, M., Domínguez, A., et al. 2022, *The Astrophysical Journal*, 941, 33
- Fiorito, R. & Titarchuk, L. 2004, *The Astrophysical Journal*, 614, L113
- Fletcher, R. S., Gaisser, T. K., Lipari, P., & Stanev, T. 1994, *Phys. Rev. D*, 50, 5710
- Fokker, A. D. 1914, *Annalen der Physik*, 348, 810
- Forbush, S. E. 1938, *Phys. Rev.*, 54, 975
- Foreman-Mackey, D., Hogg, D. W., Lang, D., & Goodman, J. 2013, *Publications of the Astronomical Society of the Pacific*, 125, 306
- Formaggio, J. A. & Zeller, G. P. 2012, *Reviews of Modern Physics*, 84, 1307
- Fornasa, M. & Sánchez-Conde, M. A. 2015, *Physics Reports*, 598, 1, the nature of the Diffuse Gamma-Ray Background
- Franceschini, A. & Rodighiero, G. 2017, *Astronomy and Astrophysics*, 603, A34
- Frank, J., King, A., & Raine, D. J. 2002, *Accretion Power in Astrophysics*: Third Edition (Cambridge University Press)
- Gabici, S., Evoli, C., Gaggero, D., et al. 2019, *International Journal of Modern Physics D*, 28, 1930022
- Gallo, L. 2018, in Revisiting Narrow-Line Seyfert 1 Galaxies and their Place in the Universe, 34
- Gao, S., Pohl, M., & Winter, W. 2017, *The Astrophysical Journal*, 843, 109
- Ghez, A. M., Klein, B. L., Morris, M., & Becklin, E. E. 1998, *The Astrophysical Journal*, 509, 678
- Ghisellini, G. 2013, *Radiative Processes in High Energy Astrophysics*, Vol. 873 (Springer Cham)
- Ghisellini, G. & Tavecchio, F. 2009, *Monthly Notices of the Royal Astronomical Society*, 397, 985
- Ghisellini, G. & Tavecchio, F. 2010, *Monthly Notices of the Royal Astronomical Society: Letters*, 409, L79
- Ghisellini, G., Tavecchio, F., Maraschi, L., Celotti, A., & Sbarato, T. 2014, *Nature*, 515, 376

## Bibliography

---

- Gilmore, R. C., Somerville, R. S., Primack, J. R., & Domínguez, A. 2012, Monthly Notices of the Royal Astronomical Society, 422, 3189
- Ginzburg, V. & Syrovatskii, S. 1964, The Origin of Cosmic Rays (Elsevier Science)
- Glass, I. S. 1981, Monthly Notices of the Royal Astronomical Society, 194, 795
- Goodwin, S. P., Gribbin, J., & Hendry, M. A. 1998, The Observatory, 118, 201
- Gould, R. J. & Schréder, G. P. 1967, Phys. Rev., 155, 1408
- Gourgouliatos, K. N. & Komissarov, S. S. 2018, Nature Astronomy, 2, 167
- Greisen, K. 1966, Phys. Rev. Lett., 16, 748
- Guépin, C., Kotera, K., & Oikonomou, F. 2022, Nature Reviews Physics, 4, 697
- Gültekin, K., Cackett, E. M., Miller, J. M., et al. 2009, The Astrophysical Journal, 706, 404
- Hada, K., Kino, M., Doi, A., et al. 2013, The Astrophysical Journal, 775, 70
- Halzen, F. & Kheirandish, A. 2020, Nature Physics, 16, 498
- Halzen, F., Kheirandish, A., Weisgarber, T., & Wakely, S. P. 2019, The Astrophysical Journal Letters, 874, L9
- Hannikainen, D. C., Hunstead, R. W., Campbell-Wilson, D., & Sood, R. K. 1998, Astronomy and Astrophysics, 337, 460
- Hardcastle, M. J. & Croston, J. H. 2020, New Astronomy Reviews, 88, 101539
- Harrison, F. A., Craig, W. W., Christensen, F. E., et al. 2013, Astrophysical Journal, 770, 103
- Hauser, M. G., Arendt, R. G., Kelsall, T., et al. 1998, The Astrophysical Journal, 508, 25
- Hawking, S. W. & Ellis, G. F. R. 1973, The Large Scale Structure of Space-Time, Cambridge Monographs on Mathematical Physics (Cambridge University Press)
- Heckman, T. M. & Best, P. N. 2014, Annual Review of Astronomy and Astrophysics, 52, 589
- Heinz, S. & Sunyaev, R. A. 2003, Monthly Notices of the Royal Astronomical Society, 343, L59
- Hervet, O., Boisson, C., & Sol, H. 2016, Astronomy and Astrophysics, 592, A22
- Hess, V. 1912, On the Observations of the Penetrating Radiation during Seven Balloon Flights
- Hillas, A. M. 1984, Annual Review of Astronomy and Astrophysics, 22, 425
- Houck, J. C. & Denicola, L. A. 2000, in Astronomical Society of the Pacific Conference Series, Vol. 216, Astronomical Data Analysis Software and Systems IX, ed. N. Manset, C. Veillet, & D. Crabtree, 591

- Huber, M. 2019, Searches for steady neutrino emission from 3FHLblazars using eight years of IceCube data from the Northern hemisphere
- Hümmer, S., Rüger, M., Spanier, F., & Winter, W. 2010, *The Astrophysical Journal*, 721, 630
- IceCube Collaboration. 2016, *The Astrophysical Journal*, 824, 115
- IceCube Collaboration. 2018a, *Science*, 361
- IceCube Collaboration. 2018b, *Science*, 361, 147
- IceCube collaboration. 2022, *Science*, 378, 538–543
- Israel, W. 1967, *Phys. Rev.*, 164, 1776
- Jansky, K. G. 1933, *Nature*, 132, 66
- Johnston, K. J., Fey, A. L., Zacharias, N., et al. 1995, *Astronomical Journal*, 110, 880
- Kadler, M., Krauß, F., Mannheim, K., et al. 2016, *Nature Physics*, 12, 807
- Kafexhiu, E., Aharonian, F., Taylor, A. M., & Vila, G. S. 2014, *Phys. Rev. D*, 90, 123014
- Kalmykov, N., Ostapchenko, S., & Pavlov, A. 1997, *Nuclear Physics B - Proceedings Supplements*, 52, 17
- Kang, D. & Haungs, A. 2024, *Advances in Space Research*
- Kantzas, D., Markoff, S., Beuchert, T., et al. 2020, *Monthly Notices of the Royal Astronomical Society*, 500, 2112
- Kantzas, D., Markoff, S., Cooper, A. J., et al. 2023a, *Monthly Notices of the Royal Astronomical Society*, 524, 1326
- Kantzas, D., Markoff, S., Lucchini, M., Ceccobello, C., & Chatterjee, K. 2023b, *Monthly Notices of the Royal Astronomical Society*, 520, 6017
- Kashti, T. & Waxman, E. 2005, *Phys. Rev. Lett.*, 95, 181101
- Kazanas, D. & Ellison, D. C. 1986, *The Astrophysical Journal*, 17, 178
- Keivani, A., Murase, K., Petropoulou, M., et al. 2018, *Astrophysical Journal*, 864, 84
- Kelner, S. R. & Aharonian, F. A. 2008, *Physical Review D - Particles, Fields, Gravitation and Cosmology*, 78, 034013
- Kelner, S. R., Aharonian, F. A., & Bugayov, V. V. 2006, *Physical Review D - Particles, Fields, Gravitation and Cosmology*, 74, 034018
- Kerr, R. P. 1963, *Phys. Rev. Lett.*, 11, 237
- Kimura, S. S., Murase, K., & Zhang, B. T. 2018, *Physical Review D*, 97

## Bibliography

---

- King, A. & Pounds, K. 2015, Annual Review of Astronomy and Astrophysics, 53, 115
- Klein, O. & Nishina, T. 1929, Zeitschrift fur Physik, 52, 853
- Klinger, M., Rudolph, A., Rodrigues, X., et al. 2023, arXiv e-prints, arXiv:2312.13371
- Komatsu, E., Dunkley, J., Nolta, M. R., et al. 2009, The Astrophysical Journal Supplement, 180, 330
- Komissarov, S. S., Barkov, M. V., Vlahakis, N., & Königl, A. 2007, Monthly Notices of the Royal Astronomical Society, 380, 51
- Komissarov, S. S., Vlahakis, N., Königl, A., & Barkov, M. V. 2009, Monthly Notices of the Royal Astronomical Society, 394, 1182
- Königl, A. 1980, Physics of Fluids, 23, 1083
- Königl, A. 2006, Mem. Societa Astronomica Italiana, 77, 598
- Kormendy, J. & Ho, L. C. 2013, Annual Review of Astronomy and Astrophysics, 51, 511
- Kotera, K. & Olinto, A. V. 2011, Annual Review of Astronomy and Astrophysics, 49, 119
- Kovačević, M., Chiaro, G., Cutini, S., & Tosti, G. 2020, Monthly Notices of the Royal Astronomical Society, 493, 1926
- Krauß, F., Wilms, J., Kadler, M., et al. 2016, Astronomy and Astrophysics, 591, A130
- Kulikov, G. V. & Khristiansen, G. B. 1959, Sov. Phys. JETP, 35(8), 635
- Kumar, P. & Zhang, B. 2015, Physics Reports, 561, 1
- Kun, E., Bartos, I., Tjus, J. B., et al. 2022, The Astrophysical Journal, 934, 180
- Kun, E., Bartos, I., Tjus, J. B., et al. 2023, arXiv, arXiv:2305.06729
- Landt, H., Padovani, P., Perlman, E. S., & Giommi, P. 2004, Monthly Notices of the Royal Astronomical Society, 351, 83
- Lanyi, G. E., Boboltz, D. A., Charlot, P., et al. 2010, The Astronomical Journal, 139, 1695
- Lawrence, C. R., Bennett, C. L., Garcia-Barreto, J. A., Greenfield, P. E., & Burke, B. F. 1983, The Astrophysical Journal Supplement, 51, 67
- Lazarian, A., Xu, S., & Hu, Y. 2023, Frontiers in Astronomy and Space Sciences, 10, 1154760
- Levinson, A. & Eichler, D. 1993, The Astrophysical Journal, 418, 386
- Li, W.-J., Xue, R., Long, G.-B., et al. 2022, Astronomy and Astrophysics, 659, A184
- Lightman, A. P. & White, T. R. 1988, Astrophysical Journal, 335, 57
- LIGO Scientific Collaboration and Virgo Collaboration. 2016, Phys. Rev. Lett., 116, 061102

- Liodakis, I. & Petropoulou, M. 2020, *The Astrophysical Journal*, 893, L20
- Lucchini, M., Ceccobello, C., Markoff, S., et al. 2022, *Monthly Notices of the Royal Astronomical Society*, 517, 5853
- Lucchini, M., Krauß, F., & Markoff, S. 2019a, *Monthly Notices of the Royal Astronomical Society*, 489, 1633
- Lucchini, M., Markoff, S., Crumley, P., Kraub, F., & Connors, R. M. 2019b, *Monthly Notices of the Royal Astronomical Society*, 482, 4798
- Lucchini, M., Russell, T. D., Markoff, S. B., et al. 2020, *Monthly Notices of the Royal Astronomical Society*, 501, 5910
- MAGIC Collaboration. 2011, *The Astrophysical Journal*, 730, L8
- Maitra, D., Markoff, S., Brocksopp, C., et al. 2009, *Monthly Notices of the Royal Astronomical Society*, 398, 1638
- Mannheim, K. 1993, *Astronomy and Astrophysics*
- Mannheim, K. & Schlickeiser, R. 1994, *Astronomy and Astrophysics*, 286, 983
- Marchant, P. & Bodensteiner, J. 2023, *The Evolution of Massive Binary Stars*
- Markoff, S., Falcke, H., & Fender, R. 2001, *A&A*, 372, 25
- Markoff, S., Falcke, H., Yuan, F., & Biermann, P. L. 2001, *Astronomy and Astrophysics*, 379, L13
- Markoff, S., Nowak, M., Corbel, S., Fender, R., & Falcke, H. 2003, *New Astronomy Reviews*, 47, 491–493
- Markoff, S., Nowak, M. A., Gallo, E., et al. 2015, *The Astrophysical Journal*, 812, L25
- Markoff, S., Nowak, M. A., & Wilms, J. 2005, *The Astrophysical Journal*, 635, 1203
- Marscher, A. P. 1980, *The Astrophysical Journal*, 235, 386
- Marscher, A. P., Jorstad, S. G., D'Arcangelo, F. D., et al. 2008, *Nature*, 452, 966
- Massaro, E., Giommi, P., Leto, C., et al. 2009, *Astronomy and Astrophysics*, 495, 691
- Mastichiadis, A. & Kirk, J. G. 1995, *Astronomy and Astrophysics*, 295, 613
- Matthews, J. H., Bell, A. R., & Blundell, K. M. 2020, *New Astronomy Reviews*, 89, 101543
- McClintock, J. E. & Remillard, R. A. 2004, *Black Hole Binaries*
- McCulloch, P. M., Ellingsen, S. P., Jauncey, D. L., et al. 2005, *Astronomical Journal*, 129, 2034
- McKinney, J. C. 2006, *Monthly Notices of the Royal Astronomical Society*, 368, 1561

## Bibliography

---

- Merloni, A., Heinz, S., & Matteo, T. D. 2003, Monthly Notices of the Royal Astronomical Society, 345, 1057
- Mertens, F., Lobanov, A. P., Walker, R. C., & Hardee, P. E. 2016, Astronomy and Astrophysics, 595, A54
- Mészáros, P. 2002, Annual Review of Astronomy and Astrophysics, 40, 137
- Mészáros, P., Fox, D. B., Hanna, C., & Murase, K. 2019, Nature Reviews Physics, 1, 585
- Mignone, A., Striani, E., Tavani, M., & Ferrari, A. 2013, Monthly Notices of the Royal Astronomical Society, 436, 1102
- Mirabel, I. F. & Rodríguez, L. F. 1994, Nature, 371, 46
- Mondal, T. & Mukhopadhyay, B. 2019, Monthly Notices of the Royal Astronomical Society, 486, 3465
- Morrison, P. 1958, Il Nuovo Cimento, 7, 858
- Mościbrodzka, M., Falcke, H., & Shiokawa, H. 2016, Astronomy and Astrophysics, 586, A38
- Mummery, A., Ingram, A., Davis, S., & Fabian, A. 2024, Monthly Notices of the Royal Astronomical Society, 531, 366
- Murase, K., Dermer, C. D., Takami, H., & Migliori, G. 2012, The Astrophysical Journal, 749, 63
- Murase, K., Oikonomou, F., & Petropoulou, M. 2018, The Astrophysical Journal, 865, 124
- Mészáros, P. 2006, Reports on Progress in Physics, 69, 2259
- Mücke, A., Protheroe, R. J., Engel, R., Rachen, J. P., & Stanev, T. 2003, Astroparticle Physics, 18, 593
- Naab, T. & Ostriker, J. P. 2017, Annual Review of Astronomy and Astrophysics, 55, 59
- Nakamura, M., Asada, K., Hada, K., et al. 2018, Astrophysical Journal, 868, 146
- Narayan, R. & Quataert, E. 2005, Science, 307, 77
- Newman, E. T., Couch, R., Chinnapared, K., et al. 1965, J. Math. Phys., 6, 918
- Nowak, M. A., Wilms, J., Heinz, S., et al. 2005, The Astrophysical Journal, 626, 1006
- Oikonomou, F., Murase, K., Padovani, P., Resconi, E., & Mészáros, P. 2019, Monthly Notices of the Royal Astronomical Society, 489, 4347
- Ojha, R., Kadler, M., Böck, M., et al. 2010, Astronomy and Astrophysics, 519, A45
- Ostapchenko, S. 2011, Phys. Rev. D, 83, 014018
- Padovani, P. 2017, Nature Astronomy, 1

- Padovani, P. & Giommi, P. 1995, *The Astrophysical Journal*, 444, 567
- Padovani, P., Giommi, P., Resconi, E., et al. 2018, *Monthly Notices of the Royal Astronomical Society*, 480, 192
- Padovani, P., Oikonomou, F., Petropoulou, M., Giommi, P., & Resconi, E. 2019, *Monthly Notices of the Royal Astronomical Society*, 484, L104
- Padovani, P. et al. 2017, *Astron. Astrophys. Rev.*, 25, 2
- Paiano, S., Falomo, R., Treves, A., & Scarpa, R. 2018, *Astrophysical Journal, Letters*, 854, L32
- Paliya, V. S., Marcotulli, L., Ajello, M., et al. 2017, *The Astrophysical Journal*, 851, 33
- Palladino, A. & Winter, W. 2018, *Astronomy & Astrophysics*, 615, A168
- Parker, E. 1967, *Planetary and Space Science*, 15, 1723
- Pelletier, G., Lemoine, M., & Marcowith, A. 2009, *Monthly Notices of the Royal Astronomical Society*, 393, 587
- Penzias, A. A. & Wilson, R. W. 1965, *Astrophysical Journal*, 142, 419
- Petropoulou, M., Dimitrakoudis, S., Padovani, P., Mastichiadis, A., & Resconi, E. 2015, *Monthly Notices of the Royal Astronomical Society*, 448, 2412
- Petropoulou, M., Sironi, L., Spitkovsky, A., & Giannios, D. 2019, *The Astrophysical Journal*, 880, 37
- Pierre Auger Collaboration. 2017, *Science*, 357, 1266
- Planck, M. 1917, *Annalen der Physik*, Jan-Dec 1917, 323
- Planck Collaboration. 2020, *Astronomy and Astrophysics*, 641, A6
- Planck Collaboration, Ade, P. A. R., Aghanim, N., et al. 2014, *Astronomy and Astrophysics*, 571, A28
- Plavin, A. V., Kovalev, Y. Y., Kovalev, Y. A., & Troitsky, S. V. 2021, *The Astrophysical Journal*, 908, 157
- Plotkin, R. M., Gallo, E., Markoff, S., et al. 2014, *Monthly Notices of the Royal Astronomical Society*, 446, 4098
- Plotkin, R. M., Markoff, S., Kelly, B. C., Körding, E., & Anderson, S. F. 2012, *Monthly Notices of the Royal Astronomical Society*, 419, 267
- Polko, P., Meier, D. L., & Markoff, S. 2014, *Monthly Notices of the Royal Astronomical Society*, 438, 959
- Potter, W. J. 2017, *Monthly Notices of the Royal Astronomical Society*, 473, 4107

## Bibliography

---

- Potter, W. J. & Cotter, G. 2012, Monthly Notices of the Royal Astronomical Society, 423, 756
- Potter, W. J. & Cotter, G. 2013, Monthly Notices of the Royal Astronomical Society, 436, 304
- Primack, J. R., Bullock, J. S., Somerville, R. S., & MacMinn, D. 1999, Astroparticle Physics, 11, 93
- Rachen, J. P. & Mészáros, P. 1998, Physical Review D, 58, 123005
- Reichherzer, P., Merten, L., Dörner, J., et al. 2022, SN Applied Sciences, 4, 15
- Reimer, A., Böttcher, M., & Buson, S. 2019, The Astrophysical Journal, 881, 46
- Remillard, R. A. & McClintock, J. E. 2006, Annual Review of Astron and Astrophys, 44, 49
- Robertson, B. E., Ellis, R. S., Dunlop, J. S., McLure, R. J., & Stark, D. P. 2010, Nature, 468, 49
- Rodrigues, X., Fedynitch, A., Gao, S., Boncioli, D., & Winter, W. 2018, The Astrophysical Journal, 854, 54
- Rodrigues, X., Gao, S., Fedynitch, A., Palladino, A., & Winter, W. 2019, The Astrophysical Journal Letters, 874, L29
- Rodrigues, X., Heinze, J., Palladino, A., van Vliet, A., & Winter, W. 2021, Phys. Rev. Lett., 126, 191101
- Rodrigues, X., Paliya, V. S., Garrappa, S., et al. 2023, arXiv, arXiv:2307.13024
- Romero, G. E., Böttcher, M., Markoff, S., & Tavecchio, F. 2017, Space Science Reviews, 207, 5
- Roming, P. W. A., Kennedy, T. E., Mason, K. O., et al. 2005, Space Science Reviews, 120, 95
- Ross, R. R. & Fabian, A. C. 1993, Monthly Notices of the Royal Astronomical Society, 261, 74
- Russell, T. D., Soria, R., Miller-Jones, J. C. A., et al. 2014, Monthly Notices of the Royal Astronomical Society, 439, 1390
- Rybicki, G. B. & Lightman, A. P. 1979, Radiative processes in astrophysics (Wiley Vch Verlag)
- Sahakyan, N., Giommi, P., Padovani, P., et al. 2023, Monthly Notices of the Astronomical Royal Society, 519, 1396
- Satyapal, S., Secrest, N. J., Ricci, C., et al. 2017, The Astrophysical Journal, 848, 126
- Schaye, J., Crain, R. A., Bower, R. G., et al. 2014, Monthly Notices of the Royal Astronomical Society, 446, 521
- Schmidt, M. 1963, Nature, 197, 1040
- Schwarzschild, K. 1916, Sitzungsber. Preuss. Akad. Wiss. Berlin (Math. Phys. ), 1916, 189
- Seyfert, C. K. 1943, The Astrophysical Journal, 97, 28

- Shakura, N. I. & Sunyaev, R. A. 1973, *A&A*, 24, 337
- Simpson, J. A. 1954, *Phys. Rev.*, 94, 426
- Singh, K. K. & Meintjes, P. J. 2020, *NRIAG Journal of Astronomy and Geophysics*, 9, 309
- Sironi, L., Petropoulou, M., & Giannios, D. 2015, *Monthly Notices of the Royal Astronomical Society*, 450, 183
- Sironi, L. & Spitkovsky, A. 2011, *The Astrophysical Journal*, 726, 75
- Sironi, L. & Spitkovsky, A. 2014, *The Astrophysical Journal Letters*, 783, L21
- Sironi, L., Spitkovsky, A., & Arons, J. 2013, *The Astrophysical Journal*, 771, 54
- Sjöstrand, T., Mrenna, S., & Skands, P. 2006, *Journal of High Energy Physics*, 2006, 026
- Skrutskie, M. F., Cutri, R. M., Stiening, R., et al. 2006, *Astronomical Journal*, 131, 1163
- Sol, H. & Zech, A. 2022, *Galaxies*, 10, 105
- Spitkovsky, A. 2008, *The Astrophysical Journal*, 682, L5
- Stecker, F. W. & Salamon, M. H. 1995, *SSRv*, 75, 341
- Stevens, J., Edwards, P. G., Ojha, R., et al. 2012, arXiv e-prints, arXiv:1205.2403
- Suray, A. & Troitsky, S. 2023, *Monthly Notices of the Royal Astronomical Society: Letters*, 527, L26
- Takekawa, S., Oka, T., Iwata, Y., Tsujimoto, S., & Nomura, M. 2019, *The Astrophysical Journal Letters*, 871, L1
- Tamborra, I. & Ando, S. 2015, *Journal of Cosmology and Astroparticle Physics*, 2015, 036
- Tavecchio, F., Ghisellini, G., Bonnoli, G., & Ghirlanda, G. 2010, *Monthly Notices of the Royal Astronomical Society: Letters*, 405, L94
- Tavecchio, F., Maraschi, L., & Ghisellini, G. 1998, *The Astrophysical Journal*, 509, 608
- Tchekhovskoy, A., McKinney, J. C., & Narayan, R. 2008, *Monthly Notices of the Royal Astronomical Society*, 388, 551
- Tchekhovskoy, A., McKinney, J. C., & Narayan, R. 2009, *The Astrophysical Journal*, 699, 1789
- Tchekhovskoy, A., Narayan, R., & McKinney, J. C. 2011, *Monthly Notices of the Royal Astronomical Society: Letters*, 418, L79
- Telescope Array Collaboration. 2020, *The Astrophysical Journal Letters*, 898, L28
- Tetarenko, A. J., Russell, T. D., Miller-Jones, J. C. A., Sivakoff, G. R., & Jacpot Xrb Collaboration. 2017, *The Astronomer's Telegram*, 10745, 1

## Bibliography

---

- The Event Horizon Telescope Collaboration. 2019a, *The Astrophysical Journal Supplement Series*, 243, 26
- The Event Horizon Telescope Collaboration. 2019b, *The Astrophysical Journal*, 875, L5
- The Event Horizon Telescope Collaboration. 2022, *The Astrophysical Journal*, 930, L12
- The Event Horizon Telescope Collaboration. 2024, *A&A*, 681, A79
- The Particle Data Group. 2020, *Progress of Theoretical and Experimental Physics*, 2020, 083C01
- Thorne, K. S. & Price, R. H. 1975, *The Astrophysical Journal*, 195, L101
- Thoudam, S., Rachen, J. P., van Vliet, A., et al. 2016, *Astronomy and Astrophysics*, 595, A33
- Tran, A. & Sironi, L. 2019, in AGU Fall Meeting Abstracts, Vol. 2019, SH23B-3392
- Ulrich, R., Engel, R., & Unger, M. 2011, *Phys. Rev. D*, 83, 054026
- Urry, C. M. & Padovani, P. 1995, *Publications of the Astronomical Society of the Pacific*, 107, 803
- van den Eijnden, J., Degenaar, N., Russell, T. D., et al. 2021, *Monthly Notices of the Royal Astronomical Society*, 507, 3899
- van den Eijnden, J., Degenaar, N., Russell, T. D., et al. 2018, *Nature*, 562, 233
- van den Heuvel, E. P. J. 1992, Endpoints of stellar evolution: the incidence of stellar mass black holes in the Galaxy., In ESA, Environment Observation and Climate Modelling Through International Space Projects. Space Sciences with Particular Emphasis on High-Energy Astrophysics p 29-36 (SEE N93-23878 08-88)
- Verner, D. A., Ferland, G. J., Korista, K. T., & Yakovlev, D. G. 1996, *Astrophysical Journal*, 465, 487
- Vernet, J., Dekker, H., D'Odorico, S., et al. 2011, *Astronomy and Astrophysics*, 536, A105
- Volonteri, M. 2010, *The Astronomy and Astrophysics Review*, 18, 279–315
- Volonteri, M. 2012, *Science*, 337, 544–547
- Volonteri, M., Habouzit, M., & Colpi, M. 2021, *Nature Reviews Physics*, 3, 732–743
- Waggett, P. C., Warner, P. J., & Baldwin, J. E. 1977, *Monthly Notices of the Royal Astronomical Society*, 181, 465
- Wald, R. M. 1984, General Relativity (Chicago, USA: Chicago Univ. Pr.)
- Waxman, E. 1995, *Phys. Rev. Lett.*, 75, 386
- Webster, B. L. & Murdin, P. 1972, *Nature*, 235, 37

- White, G. L., Jauncey, D. L., Savage, A., et al. 1988, *Astrophysical Journal*, 327, 561
- Wilms, J., Allen, A., & McCray, R. 2000, *The Astrophysical Journal*, 542, 914
- Workman, R. L. et al. 2022, *PTEP*, 2022, 083C01
- Wright, E. L., Eisenhardt, P. R. M., Mainzer, A. K., et al. 2010, *Astronomical Journal*, 140, 1868
- Wulf, T. 1909, *Physikalische Zeitschrift*, 11
- Xue, R., Liu, R.-Y., Petropoulou, M., et al. 2019, *The Astrophysical Journal*, 886, 23
- Xue, R., Liu, R.-Y., Petropoulou, M., et al. 2019, *The Astrophysical Journal*, 886, 23
- Yuan, F. & Narayan, R. 2014, *Annual Review of Astronomy and Astrophysics*, 52, 529
- Zacharias, M., Reimer, A., Boisson, C., & Zech, A. 2022, *Monthly Notices of the Royal Astronomical Society*, 512, 3948
- Zatsepin, G. T. & Kuzmin, V. A. 1966, *Soviet Journal of Experimental and Theoretical Physics Letters*, 4, 78
- Zauderer, B. A., Berger, E., Soderberg, A. M., et al. 2011, *Nature*, 476, 425
- Zdziarski, A. A. 2014, *Monthly Notices of the Royal Astronomical Society*, 445, 1321
- Zdziarski, A. A. 2016, *Astronomy and Astrophysics*, 586, A18
- Zdziarski, A. A. & Böttcher, M. 2015, *Monthly Notices of the Royal Astronomical Society: Letters*, 450, L21

# Appendix A

## SED Data of All Sources

### A.1 SED Data After the Flare of TXS 0506+056 in 2017

Frequency (Hz)	Flux (erg/s/cm <sup>2</sup> )	Flux error (erg/s/cm <sup>2</sup> )	Instrument
4.224e+08	2.335e-14	1.884e-15	VLA
1.549e+10	8.509e-13	3.479e-13	VLA
4.138e+10	2.487e-12	1.345e-12	VLA
1.329e+14	4.423e-11	2.790e-13	UVOT
2.154e+14	4.310e-11	4.330e-13	UVOT
2.980e+14	4.096e-11	7.748e-13	UVOT
3.806e+14	3.890e-11	1.115e-12	UVOT
4.631e+14	3.708e-11	1.399e-12	UVOT
5.457e+14	3.551e-11	1.659e-12	UVOT
6.283e+14	3.416e-11	1.891e-12	UVOT
7.108e+14	3.300e-11	2.090e-12	UVOT
7.934e+14	3.198e-11	2.269e-12	UVOT
8.759e+14	3.109e-11	2.426e-12	UVOT
4.900e+14	3.858e-11	1.906e-12	UVOT
7.691e+14	3.606e-11	2.477e-12	UVOT
1.048e+15	3.440e-11	3.428e-12	UVOT
1.327e+15	3.318e-11	4.035e-12	UVOT
1.606e+15	3.223e-11	4.337e-12	UVOT
7.253e+16	2.281e-12	5.883e-13	XRT
1.209e+17	1.462e-12	2.539e-13	XRT
2.418e+17	9.226e-13	1.158e-13	XRT
3.143e+17	8.237e-13	8.246e-14	XRT
5.561e+17	7.446e-13	5.122e-14	XRT
7.979e+17	7.544e-13	4.630e-14	XRT
1.040e+18	7.845e-13	4.612e-14	XRT
1.281e+18	8.176e-13	4.645e-14	XRT
1.523e+18	8.485e-13	4.390e-14	XRT
1.765e+18	8.788e-13	3.986e-14	XRT
2.007e+18	9.046e-13	3.431e-14	XRT
2.249e+18	9.341e-13	3.622e-14	XRT
2.490e+18	9.633e-13	4.084e-14	NUSTAR

**Table A.1 continued from previous page**

Frequency (Hz)	Flux (erg/s/cm <sup>2</sup> )	Flux error (erg/s/cm <sup>2</sup> )	Instrument
4.666e+18	1.172e-12	1.026e-13	NUSTAR
7.084e+18	1.361e-12	1.897e-13	NUSTAR
9.502e+18	1.506e-12	2.613e-13	NUSTAR
1.192e+19	1.630e-12	3.214e-13	NUSTAR
1.434e+19	1.734e-12	3.687e-13	NUSTAR
1.676e+19	1.834e-12	4.269e-13	NUSTAR
1.917e+19	1.923e-12	4.774e-13	NUSTAR
2.159e+19	2.006e-12	5.221e-13	NUSTAR
2.401e+19	2.080e-12	5.603e-13	NUSTAR
4.280e+22	4.609e-11	7.300e-12	Fermi/LAT
1.344e+23	5.001e-11	5.813e-12	Fermi/LAT
4.219e+23	5.512e-11	7.088e-12	Fermi/LAT
1.324e+24	4.470e-11	1.043e-11	Fermi/LAT
4.157e+24	3.912e-11	1.769e-11	Fermi/LAT
1.912e+25	2.613e-11	6.685e-12	MAGIC
4.198e+25	5.962e-12	1.942e-12	MAGIC
9.792e+25	1.828e-12	5.954e-13	MAGIC

TABLE A.1 The data for the spectral energy distribution of TXS 0506+056 collected in the two weeks after the  $\gamma$ -ray flare and the neutrino detection in 2017 ([IceCube Collaboration 2018a](#)).

## A.2 SED Data for PKS 1424-418

For the second source, PKS 1424-418, there are multiple epochs for which there is SED data. These are referred to as the  $\alpha$ ,  $\gamma$ ,  $\delta$ , and  $\eta$  epochs throughout this thesis. There is also some archival data which was collected in a time window relatively close to the  $\alpha$  epoch during a quiescent state of PKS 1424-418.

### A.2.1 PKS 1424-418: Archival Data

Frequency (Hz)	Flux (erg/s/cm <sup>2</sup> )	Flux error (erg/s/cm <sup>2</sup> )	Instrument
3.030e+10	6.915e-13	1.089e-13	Planck
4.444e+10	1.124e-12	2.836e-13	Planck
7.071e+10	1.661e-12	2.282e-13	Planck
1.010e+11	1.911e-12	2.417e-13	Planck
1.444e+11	2.714e-12	3.468e-13	Planck
2.192e+11	3.080e-12	3.478e-13	Planck
3.566e+11	2.953e-12	4.630e-13	Planck
1.374e+13	1.279e-11	1.884e-12	WISE
2.524e+13	9.806e-12	1.428e-12	WISE

**Table A.2 continued from previous page**

Frequency (Hz)	Flux (erg/s/cm <sup>2</sup> )	Flux error (erg/s/cm <sup>2</sup> )	Instrument
6.603e+13	9.285e-12	1.357e-12	WISE
9.054e+13	8.188e-12	1.200e-12	WISE
1.396e+14	1.677e-12	1.538e-13	2MASS
1.814e+14	1.321e-12	1.522e-13	2MASS
2.441e+14	1.225e-12	1.133e-13	2MASS

TABLE A.2 The archival data for PKS 1424-418 used in addition to the data for the quiescent states of PKS 1424-418.

### A.2.2 PKS 1424-418: Alpha Epoch

Frequency (Hz)	Flux (erg/s/cm <sup>2</sup> )	Flux error (erg/s/cm <sup>2</sup> )	Instrument
6.700e+09	1.374e-13	9.466e-16	Ceduna
8.400e+09	9.682e-14	1.936e-14	VLBI
5.510e+14	5.054e-12	4.164e-13	UVOT
6.911e+14	4.054e-12	2.643e-13	UVOT
8.764e+14	3.124e-12	1.975e-13	UVOT
1.174e+15	1.658e-12	1.308e-13	UVOT
1.351e+15	1.031e-12	1.113e-13	UVOT
1.601e+15	5.056e-13	5.763e-14	UVOT
1.584e+17	3.640e-13	1.627e-13	XRT
2.164e+17	5.455e-13	2.500e-13	XRT
2.551e+17	6.551e-13	3.002e-13	XRT
2.926e+17	6.913e-13	3.168e-13	XRT
3.192e+17	2.035e-12	9.325e-13	XRT
3.421e+17	1.045e-12	4.788e-13	XRT
3.627e+17	3.775e-12	1.730e-12	XRT
3.893e+17	1.126e-12	5.034e-13	XRT
4.425e+17	1.033e-12	4.733e-13	XRT
5.453e+17	8.094e-13	3.709e-13	XRT
6.625e+17	1.871e-12	8.574e-13	XRT
7.858e+17	1.622e-12	7.247e-13	XRT
9.394e+17	2.007e-12	9.196e-13	XRT
1.120e+18	2.340e-12	1.072e-12	XRT
4.026e+22	4.709e-11	4.245e-12	Fermi/LAT
1.938e+23	4.262e-11	3.407e-12	Fermi/LAT
9.348e+23	2.651e-11	3.648e-12	Fermi/LAT
4.517e+24	1.252e-11	5.438e-12	Fermi/LAT

TABLE A.3 The data for the spectral energy distribution collected during the  $\alpha$  epoch of PKS 1424-418.

### A.2.3 PKS 1424-418: Gamma Epoch

Frequency (Hz)	Flux (erg/s/cm <sup>2</sup> )	Flux error (erg/s/cm <sup>2</sup> )	Instrument
6.700e+09	1.535e-13	9.280e-16	Ceduna
8.400e+09	1.241e-13	1.777e-14	VLBI
5.510e+14	6.056e-12	3.389e-13	UVOT
6.911e+14	4.642e-12	2.361e-13	UVOT
8.764e+14	3.802e-12	1.646e-13	UVOT
1.174e+15	2.036e-12	8.985e-14	UVOT
1.351e+15	1.102e-12	6.043e-14	UVOT
1.601e+15	6.442e-13	3.557e-14	UVOT
1.415e+17	5.133e-13	1.243e-13	XRT
1.910e+17	3.668e-13	8.794e-14	XRT
2.358e+17	7.074e-13	1.604e-13	XRT
2.660e+17	7.722e-13	1.803e-13	XRT
2.974e+17	7.218e-13	1.711e-13	XRT
3.313e+17	8.292e-13	1.966e-13	XRT
3.663e+17	9.458e-13	2.198e-13	XRT
4.074e+17	9.171e-13	2.182e-13	XRT
4.582e+17	1.280e-12	2.938e-13	XRT
5.126e+17	1.549e-12	3.686e-13	XRT
5.767e+17	1.629e-12	3.896e-13	XRT
6.928e+17	1.048e-12	2.485e-13	XRT
8.378e+17	1.611e-12	3.833e-13	XRT
1.006e+18	1.542e-12	3.687e-13	XRT
1.349e+18	1.680e-12	3.962e-13	XRT
4.005e+22	4.303e-11	3.296e-12	Fermi/LAT
1.910e+23	3.410e-11	2.418e-12	Fermi/LAT
9.138e+23	1.702e-11	2.180e-12	Fermi/LAT
4.387e+24	5.410e-12	2.553e-12	Fermi/LAT

TABLE A.4 The data for the spectral energy distribution collected during the  $\gamma$  epoch of PKS 1424-418.

### A.2.4 PKS 1424-418: Delta Epoch

Frequency (Hz)	Flux (erg/s/cm <sup>2</sup> )	Flux error (erg/s/cm <sup>2</sup> )	Instrument
5.688e+09	1.520e-13	5.386e-15	ATCA
6.700e+09	1.802e-13	7.543e-16	Ceduna
8.400e+09	1.600e-13	2.274e-14	VLBI
9.112e+09	2.619e-13	9.314e-15	ATCA
1.706e+10	5.331e-13	3.831e-14	ATCA
1.905e+10	5.972e-13	4.296e-14	ATCA

**Table A.5 continued from previous page**

Frequency (Hz)	Flux (erg/s/cm <sup>2</sup> )	Flux error (erg/s/cm <sup>2</sup> )	Instrument
5.510e+14	9.703e-12	3.173e-13	UVOT
1.342e+17	7.293e-13	2.051e-13	XRT
1.741e+17	4.185e-13	1.202e-13	XRT
2.152e+17	7.154e-13	1.968e-13	XRT
2.406e+17	8.569e-13	2.465e-13	XRT
2.624e+17	9.649e-13	2.755e-13	XRT
2.926e+17	5.702e-13	1.640e-13	XRT
3.216e+17	1.283e-12	3.660e-13	XRT
3.579e+17	6.933e-13	1.845e-13	XRT
4.026e+17	1.064e-12	3.062e-13	XRT
4.703e+17	7.040e-13	1.995e-13	XRT
5.537e+17	1.600e-12	4.533e-13	XRT
6.383e+17	1.414e-12	3.975e-13	XRT
7.314e+17	1.915e-12	5.510e-13	XRT
8.753e+17	1.231e-12	3.362e-13	XRT
1.165e+18	1.274e-12	3.582e-13	XRT
4.058e+22	5.316e-11	4.011e-12	Fermi/LAT
1.904e+23	4.650e-11	3.238e-12	Fermi/LAT
8.990e+23	2.493e-11	3.053e-12	Fermi/LAT
4.273e+24	7.711e-12	3.856e-13	Fermi/LAT

TABLE A.5The data for the spectral energy distribution collected during the  $\delta$  epoch of PKS 1424-418.

### A.2.5 PKS 1424-418: Eta Epoch (Flare)

Frequency (Hz)	Flux (erg/s/cm <sup>2</sup> )	Flux error (erg/s/cm <sup>2</sup> )	Instrument
5.495e+09	2.656e-13	7.931e-15	ATCA
8.400e+09	3.867e-13	5.740e-14	VLBI
8.996e+09	5.443e-13	1.615e-14	ATCA
1.701e+10	1.186e-12	6.021e-14	ATCA
1.900e+10	1.343e-12	6.796e-14	ATCA
3.800e+10	2.586e-12	2.352e-13	ATCA
4.004e+10	2.844e-12	2.620e-13	ATCA
3.430e+11	1.353e-11	6.821e-13	ATCA
2.398e+14	2.796e-11	1.398e-12	UVOT
4.677e+14	1.676e-11	8.382e-13	UVOT
5.501e+14	1.408e-11	7.042e-13	UVOT
5.510e+14	1.359e-11	7.953e-13	UVOT
6.845e+14	1.133e-11	5.667e-13	UVOT
6.911e+14	1.158e-11	6.720e-13	UVOT

**Table A.6 continued from previous page**

Frequency (Hz)	Flux (erg/s/cm <sup>2</sup> )	Flux error (erg/s/cm <sup>2</sup> )	Instrument
8.764e+14	1.232e-11	6.596e-13	UVOT
1.174e+15	5.755e-12	3.087e-13	UVOT
1.601e+15	1.569e-12	8.752e-14	UVOT
1.499e+17	6.331e-13	6.718e-14	XRT
1.983e+17	9.097e-13	9.599e-14	XRT
2.345e+17	1.046e-12	1.096e-13	XRT
2.684e+17	1.096e-12	1.171e-13	XRT
2.998e+17	1.413e-12	1.513e-13	XRT
3.288e+17	1.687e-12	1.755e-13	XRT
3.615e+17	1.535e-12	1.634e-13	XRT
4.014e+17	1.562e-12	1.696e-13	XRT
4.558e+17	1.623e-12	1.764e-13	XRT
5.283e+17	2.006e-12	2.149e-13	XRT
6.383e+17	1.747e-12	1.892e-13	XRT
7.750e+17	2.378e-12	2.578e-13	XRT
9.092e+17	3.115e-12	3.366e-13	XRT
1.126e+18	2.429e-12	2.637e-13	XRT
1.875e+18	3.358e-12	4.006e-13	XRT
3.761e+22	3.339e-10	1.770e-11	Fermi/LAT
1.156e+23	4.002e-10	2.063e-11	Fermi/LAT
3.559e+23	3.813e-10	2.016e-11	Fermi/LAT
1.096e+24	3.059e-10	1.802e-11	Fermi/LAT
3.378e+24	1.725e-10	1.528e-11	Fermi/LAT

TABLE A.6 The data for the spectral energy distribution collected during the  $\eta$  epoch of PKS 1424-418.

# Appendix B

## Jet Model Parameters

### B.1 Parameters of BHJet and HadJet

Name	Description
Source parameters:	
$M_{\text{BH}}$	Mass of the black hole in units of $M_{\odot}$ .
$\theta$	Viewing angle of the jet measured in degrees.
$D_{\text{lum}}$	Luminosity distance to the source measured in units of kpc.
$z_{\text{red}}$	Source redshift.
Main jet parameters:	
$N_j$	Power injected at the base of the jet measured in units of $L_{\text{Edd}}$ .
$R_0$	Radius of the jet nozzle/corona, described by an outflowing, magnetized cylinder of radius $R_0$ and height $2R_0$ . Measured in units of $R_g$ .
$z_{\text{diss}}$	Location of non-thermal particle injection region measured in units of $R_g$ .
$z_{\text{acc}}$	If $\text{velsw} > 1$ , this sets the location until which the jet is accelerating. It sets the jet speed and dependency of magnetic field with distance. Measured in units of $R_g$ .
$z_{\text{diss,max}}^*$	Max height up to which proton acceleration occurs in units of $R_g$ . Throughout this thesis this parameter was set to 0 to not set a maximum.
$z_{\text{max}}$	Sets the maximum length over which jet calculations are carried out measured in units of $R_g$ .
$\sigma_{\text{acc}}$	If $\text{velsw} > 1$ , it sets the value for the magnetization at $z = z_{\text{acc}}$ .
$p_{\beta}$	Plasma beta is the ratio between lepton and magnetic field energy density at the jet base. If $\text{velsw}=0$ or 1 this sets the equipartition value throughout the jet as well as the pair content, if $\text{velsw} > 1$ it only sets the pair content. If $\text{velsw} > 1$ , this can be set to 0 to always enforce one proton per electron.
$\text{velsw}$	Sets the jet velocity profile used by the code. If $\text{velsw} = 0$ or 1 the jet is pressure-driven and mildly relativistic ( <code>agnjet</code> flavor), otherwise the jet base is highly magnetized and the jet is magnetically driven ( <code>bljet</code> flavor).
Particle distribution parameters:	
$T_e$	Temperature of relativistic electrons in the jet nozzle/corona, measured in units of keV.

**Table B.1 continued from previous page**

$p$	Spectral index of the non-thermal electron distribution.
$p_p^*$	Spectral index of the non-thermal proton distribution.
$\eta_e^*$	The ratio between the number density of electrons and protons at the jet base. Throughout this thesis, $\eta_e$ was fixed to 1.
hadsw*	If hadsw=0, the model ignores hadronic acceleration. If hadsw $\geq 1$ , it is the minimum Lorentz factor of the accelerated protons at $z = z_{\text{diss}}$ .
$f_{\text{nth, e}}$	Fraction of thermal electrons accelerated into a powerlaw tail.
$f_{\text{nth, p}}^*$	Fraction of cold protons accelerated into a powerlaw tail.
$f_{\text{pl}}$	Reduces particle temperature and percentage of accelerated particles along the jet after $z_{\text{diss}}$ , resulting in an inverted radio spectrum. Throughout this thesis, it was set to 0 for a standard flat spectrum.
$f_{\text{heat}}$	Imitates shock heating such that at $z=z_{\text{diss}}$ it increases $T_e$ by a fixed factor $f_{\text{heat}}$ . Increasing values increase the radiative efficiency of the jet after $z_{\text{diss}}$ .
$f_b$	Sets the effective adiabatic cooling timescale, defined as $t_{\text{ad}} = r/f_{bc}$ . Throughout this thesis, $f_b$ was fixed to 0.1.
$f_{sc}$	If $f_{sc} < 0.1$ , it sets the maximum energy of non-thermal particles by parametrizing the acceleration timescale and therefore the acceleration efficiency. If $f_{sc} > 10$ , it sets the maximum Lorenz factor of the non-thermal particles.

Disk parameters:

$L_{\text{disk}}$	Sets the luminosity of the Shakura-Sunyaev disk in units of $L_{\text{Edd}}$ .
$R_{\text{in}}$	Inner radius of the disk measured in units of $R_g$ .
$R_{\text{out}}$	Outer radius of the disk measured in units of $R_g$ .

Inverse Compton parameters:

compsw	Sets the external photon fields to be used in the IC calculation. compsw=0 only includes SSC (+disk IC, if present) emission, compsw=1 adds a uniform external black body contribution (e.g. a host galaxy), and compsw=2 adds the BLR and DT of an AGN and ties their luminosity to that of the disk. Throughout this thesis, compsw=2 was used for all sources.
$f_{\text{BLR}}$	First parameter of the external photon field. Determines the fraction of disk photons reprocessed by the BLR.
$f_{\text{DT}}$	Second parameter of the external photon field. Determines the fraction of disk photons reprocessed by the DT.

TABLE B.1 Parameters of the multi-zone jet models **BHJet** and **HadJet** as used in this thesis. The parameters marked with \* only apply to the lepto-hadronic **HadJet** model version.

## B.2 Parameters of OneZone\_lep and OneZone\_lephad

Name	Description
Source parameters:	
$M_{\text{BH}}$	Mass of the black hole in units of $M_{\odot}$ .
$\theta$	Viewing angle of the jet measured in degrees.
$D_{\text{lum}}$	Luminosity distance to the source measured in units of kpc.
$z_{\text{red}}$	Source redshift.
Main jet parameters:	
$R$	Radius of the spherical single-zone region measured in units of cm.
$B$	Magnetic field strength in the single-zone region measured in units of G.
$\Gamma$	The bulk Lorentz factor of the single-zone region.
Particle distribution parameters:	
$n_e$	Electron number density in the single-zone region measured in units of $\text{cm}^{-3}$ .
$\gamma_{\min, e}$	The minimum Lorentz factor of the non-thermal electron distribution.
$\gamma_{\max, e}$	The maximum Lorentz factor of the non-thermal electron distribution.
$\gamma_{\text{brk}, e}$	If brksw=0, a normal powerlaw is used and $\gamma_{\text{brk}, e}$ sets the Lorenz factor where the exponential cutoff is. If brksw=1 or 2, a broken powerlaw is used where $\gamma_{\text{brk}, e}$ sets the position of the break.
$p_{1,e}$	Spectral index of the non-thermal electron distribution. If brksw=1, it is fixed to -2, but it is kept free to vary otherwise.
$p_{2,e}$	Spectral index of the non-thermal electron distribution after the break if $\text{brksw} \geq 1$ .
$n_p^*$	Proton number density in the single-zone region measured in units of $\text{cm}^{-3}$ .
$\gamma_{\min, p}^*$	The minimum Lorentz factor of the non-thermal proton distribution.
$\gamma_{\max, p}^*$	The maximum Lorentz factor of the non-thermal proton distribution.
$p_p^*$	Spectral index of the non-thermal proton distribution.
Disk parameters:	
$L_{\text{disk}}$	Sets the luminosity of the Shakura-Sunyaev disk in units of $L_{\text{Edd}}$ .
$R_{\text{in}}$	Inner radius of the disk measured in units of $R_g$ .
$R_{\text{out}}$	Outer radius of the disk measured in units of $R_g$ .

---

**Table B.2 continued from previous page**


---

Inverse Compton parameters:

<code>compsw</code>	Sets the external photon fields to be used in the IC calculation. <code>compsw=0</code> only includes SSC (+disk IC, if present) emission, <code>compsw=1</code> adds a uniform external black body contribution (e.g. a host galaxy), <code>compsw=2</code> adds the BLR and DT of an AGN and ties their luminosity to that of the disk. Throughout this thesis, <code>compsw=2</code> was used for all sources.
$f_{\text{BLR}}$	First parameter of the external photon field. Determines the fraction of disk photons reprocessed by the BLR.
$f_{\text{DT}}$	Second parameter of the external photon field. Determines the fraction of disk photons reprocessed by the DT.

TABLE B.2 Parameters of the single-zone jet models `OneZone_lep` and `OneZone_lephad` as used in this thesis. The parameters marked with \* only apply to the lepto-hadronic `OneZone_lephad` model version.